UNIVERSITY OF HELSINKI
DEPARTMENT OF PHYSICS

REPORT SERIES IN GEOPHYSICS

No 61

Proceedings of The Sixth Workshop on Baltic Sea Ice Climate

August 25–28, 2008 Lammi Biological Station, Finland

HELSINKI 2009

UNIVERSITY OF HELSINKI
DEPARTMENT OF PHYSICS

REPORT SERIES IN GEOPHYSICS

No 61

Cover: Participants of the workshop in front of the main building of Lammi biological station (Eija Riihiranta).

Proceedings of The Sixth Workshop on Baltic Sea Ice Climate

August 25–28, 2008 Lammi Biological Station, Finland

HELSINKI 2009

Preface

The importance of sea ice in the Baltic Sea has been addressed in the Baltic Sea Ice Workshops. The ice has been identified as a key element in the water and energy cycles and ecological state of the Baltic Sea. The variability in sea ice conditions is high and due to the short thermal memory of the Baltic Sea closely connected to the actual weather conditions. The spatial and temporal long-term variability of the ice cover has been discussed in the Baltic Sea Ice Workshops.

One motivation of the workshop series, which started in 1993, was that sea ice is not properly treated in Baltic Sea research in general although the ice season has a major role in the annual cycle of the Baltic Sea. This still holds true, which is a severe bias since in environmental problems, such as oil spill accidents in winter and long term transport of pollutants, the ice conditions play a critically important role. Also in regional climate changes the Baltic Sea ice cover is a sensitive key factor. In the Baltic Sea Ice Climate Workshops these topics have been extensively discussed, in addition to basic Baltic Sea ice science questions.

The 6th Baltic Sea Ice Climate Workshop was held in Lammi Biological Station of the University of Helsinki, located 130 km north of Helsinki. It was a beautiful summer week in nature environment, and the participants could enjoy the station sauna by Lake Pääjärvi. The atmosphere was very good in the meeting, and the presentations covered a wide range of sea ice questions. The number of participants was 30 and they represented seven countries. The presentations distributed rather evenly to ice processes, ice climatology and remote sensing.

The next, 7th Baltic Sea Ice Climate Workshop will be held in Estonia in 2012, hosted by Dr. Ants Erm from Marine Systems Institute, Tallinn University of Technology.

Helsinki, 9 July 2009

Matti Leppäranta
Department of Physics, University of Helsinki
Helsinki, Finland

Table of Contents

The Sixth Workshop on Baltic Sea Ice Climate
August 25–28, 2008
Lammi Biological Station, Finland

Programme

The international Sixth Workshop on Baltic Sea Ice Climate will be held in August 25–28, 2008 in Lammi Biological Station of the University Helsinki, Finland. The meeting will review research results related to the Baltic Sea ice past, present and future climate conditions. The workshop is a continuation of meetings each third year around the Baltic Sea. The First Workshop on Baltic Sea Ice climate was held in Finland August 1993, the second in Estonia 1996, the third in Poland 1999, the fourth in Sweden 2002, and the fifth in Germany 2005.

The workshop will be divided into sessions with particular emphasis on the topics listed below, identified as future challenging research areas from the discussion in the earlier Baltic Sea Ice workshops. Scientists from the Baltic Sea region and as well from other regional seas, seasonally covered by sea ice, are hereby kindly invited to participate in the Sixth Workshop on Baltic Sea Ice.

The workshop is organised by the Department of Physics of the University of Helsinki.

The scientific advisory committee

Prof. Matti Leppäranta, chair	University Helsinki, Finland
Dr. Ants Erm	Tallinn University of Technology, Estonia
Dr. Jari Haapala	Finnish Institute of Marine Research, Finland
Prof. Zhijun Li	Dalian University of Technology, China
Prof. Anders Omstedt	Göteborg University, Sweden
Dr. Natalia Schmelzer	BSH, Hamburg, Germany
Prof. Corinna Schrum	University of Bergen, Norway
Prof. Kunio Shirasava	Hokkaido University, Japan
Dr. Marzenna Sztobryn	Institute of Water Management, Poland

Programme

Monday, August 25

12.00 *Lunch*

13:15 Opening

Topic: Baltic Sea ice

13.30 *Klaus Strübing*: Charting the Baltic Sea ice – A historical review

14.15 *Sönke Maus (co-authored by Thomas Huthwelker, Frieder Enzmann, Markus Miedaner, Marco Stampanoni, Federica Marone, Manuel A. Hutterli, Markus*

Ammann, Christoph Hintermueller and Michael Kersten): *Synchrotron*-based X-ray micro-tomography: insights into sea ice microstructure

15.00 *Coffee break*

15.30 *Natalija Schmelzer:* Does navigation need an ice atlas? Ideas about an ice atlas for the area of the Western and Southern Baltic

16.00 *Jevgeni Rjazin (co-authored by Ove Pärn and Jari Haapala)*: A survey to estimate appearance and performance of leads suitable to navigate, in the sea ice on the Gulf of Finland

16.30 *Juha Karvonen:* Ice thickness charts produced by SAR imagery and HIGHTSI thermodynamic ice model

17.00 *Dinner*

20.00 *Sauna by the lake*

Tuesday, August 26

8.00 *Breakfast*

9.00 Marzenna Sztobryn: Sea ice condition severity index

Topic: Remote sensing

9.30 *Rasmus Tonboe*: Simulation of L-band thermal microwave signatures from Baltic Sea ice

10.00 *Coffee break*

10.30 *Nina Maass (co-authored by Lars Kaleschke)*: Determining Baltic Sea ice thickness and concentration from L-band microwave radiometry

11.00 *Juha Karvonen:* Ice motion estimation from successive RADAR scenes

12.00 *Lunch*

Topic: Sea ice biology

13.15 *Keynote talk by Hermanni Kaartokallio: Sea ice ecology in the Baltic Sea*

14:00 *Jari Uusikivi*: Influence of dissolved and particulate constituents on land fast sea ice optical properties

14.30 A*nts Erm, Juho Jaakkila and Matti Leppäranta: Interpretation of ice optical field measurements*

15.00 *Coffee break*

15.30 **Poster session**

Susann Haase: The photochemical transformation of organic matter in sea ice and its impact on the functioning of the sea ice ecosystem
Anssi Vähätalo: Freeze-fractionation of organic matter in the Baltic Sea water
Tuomas Niskanen (c-authored by Patricj Eriksson and Jouni Vainio): Maximum ice cover extend areas in Baltic Sea during last 30 year period (from winter 1971 to 2001)
Eero Rinne, Jari Haapala, Christian Haas, Istvan Heiler and Stefan Hendricks: CryoVEx 2005 - altimeter remote sensing of sea-ice thickness in the Bay of Bothnia
Jari Haapala, Christian Haas, Jonni Lehtiranta and Juha Karvonen: Validation of modelled sea-ice thickness with the HEM-data.

17.00 *Dinner*

19.00 – *Sauna by the lake*
Get together at the fireplace room

Wednesday, August 27

8.00 *Breakfast*

Topic: Models

9.15 *Sönke Maus*: Geophysical property modelling of sea ice
10.00 *Pekka Juuti:* Latest development in ice model testing

10.30 *Coffee break*

11.00 *Keynote talk by Kai Myrberg: Hydrography and circulation in the Baltic Sea*

12.00 *Lunch*

13.30 *Andreas Lehmann (co-authored by Riikka Hietala)*: The role of brine release and sea ice drift for winter mixing and sea ice formation in the Northern Baltic Sea
14.00 *Yusuke Kawaguchi*: Effects of along-shore winds on DSW discharge from coastal polynyas

14.30 *Coffee break*

15.00 *Matti Leppäranta*: Two-phase thermodynamics sea ice model
15.30 *Juha Karvonen:* Evaluation of operational HIGHTSI thermodynamic ice model in the Baltic Sea for the winter 2007-2008

16.00 Closing discussion

17.00 *Dinner*

Departure

Charting the Baltic Sea ice – a historical review

Klaus Strübing

Retired from Federal Maritime and Hydrographic Agency of Germany (BSH)
Email ksg1939@aol.com

Abstract

The development of official ice charts for the Baltic Sea is described from the first (Finnish) chart in 1915 up to date. This is given within the framework of technical developments for the preparation of the charts, and the presentation of the ice on the charts by improved ice terminology, codes and symbols generated and designed in intensified international cooperation – first within the national Ice Services of the Baltic Sea, since the 1950ies on a global (WMO) basis. Furthermore, new observation positions and techniques as ship- and airborne ice reconnaissance and finally since the late 1960ies the satellite period with steadily improving first optical and infrared then microwave sensors are considered.

The historical review is mainly related to the development within the German Ice Service, which was founded in 1896, however, basic international cooperation and events are considered, too.

Introduction

Due to the ice cover as obstacle for navigation, ice observations in the Baltic Sea and the documentation of the ice conditions have a long tradition and history. These are mainly given for regular coastal observations, which started in Finland already in 1846 as in early days with wooden merchant vessels navigation was stopped already by rather thin ice. However, the economical demands for an extended navigation season in winter going along with the development of icebreakers and vessels suitable for navigation in ice, required improved ice information not only for the coastal areas of the Baltic Sea, but also more and more for the open sea. This means that the punctual ice information for harbours and fairway sections at and close to the coast needs to be complemented and completed by an areal picture of the ice cover at sea, i.e. an ice chart.

It has to be noticed that at the beginning of the introduction of codes and symbols for the description of the sea ice in the Baltic Sea, the practical aspects - i.e. the nautical requirements for easy and safe winter navigation - came first. Ice terms were mostly taken from the sailors' vocabulary. It was first in 1920ies and 1930ies - the decades, when international cooperation between the countries bordering the Baltic Sea were strongly intensified - that the importance of the sea ice as climatologically factor was considered, too. Relevant terms were introduced and incorporated into the ice codes and symbols to consider not only the technical requirements but also the scientific/climatic aspects of the ice covered Baltic Sea. The Baltic Sea Ice Codes of 1928, 1954 (revised 1969) and 1980, the later in relation to the WMO Sea Ice Nomenclatures of 1952 and 1968 together with the WMO Ice Symbols of 1980 were the major steps (see Table 1), and they are strongly reflected by the contents of the ice charts. From about 1968 their quality could be improved essentially by satellite imagery.

2. The development until 1945 – *The initial phase*

In Table 1 the major steps and events in international cooperation (meetings, agreements on ice codes and symbols) as well as technical developments for the layout, production and

dissemination of ice charts and reports are given in chronological order. They are mostly related to the German Ice Service (Strübing 1997), however, as the service was – beside the years of the World Wars – part of the international community, the given facts are of general relevance.

Table 1, part 1. Chronology of facts, events and developments related to ice charts (1846 – 1945)

1846 ff	Start of regular local ice observations (mainly in Finland)
12/1896	Start of the regular ice observation and information service at the Deutsche Seewarte in Hamburg • Uniform telegraphic station reports • Publication in tabular form as annex in the Daily Weather Report (until 1927/28)
1915	Early that year first ice charts issued by Finland's Scientific Society
1920/21	FIMR (founded in 1918) is weekly mailing ice charts to Baltic Ice Services
1922/23	Broadcasting of the ice information via coastal radio stations • Exchange of ice reports via radio telegraphy between most Baltic countries (Estonia + Finland already 1920, Latvia + Sweden 1921)
1924	Introduction of a box map of the Baltic Sea (20' lat by 30' long) for the observation + reporting of ice in the open sea
1925	1st International Ice Conference in Hamburg (7/8.07.) confirms to develop a joint (international) Baltic Ice Code
1925/26	Presentation of provisional ice charts in stock market buildings of harbour cities
1927/28	Introduction of regular ice charts for the Baltic Sea • Tests with airborne ice reconnaissance • Including of ferry lines for ice observations
1928/29	Introduction of the 1st Baltic Ice Code (nautical terminology) by the Baltic Hydrographic Conference – valid until 1953/54 (replacing the different national ice codes) • publication of an independent ice report, the EISBERICHT (except of the season 1945/46 continuously issued)
1938	Baltic Ice Week (12.-18.02.) for more effective and harmonized ice observations. Due to the mild winter repeated in 1939 (28.01.-03.02., 18.-24.02., 11.-17.03.). The material was gathered and partly evaluated at FIMR.
1939 – 1945	WW II limited/prevented further international cooperation. However, essentially intensified air reconnaissance and the 3 heavy winters 1939/40 to 1941/42 resulted in improved ice charting of the sea areas. In Germany on Jan. 10, 1941 start of the plain language ice reports.

Until the early 20th century (World War I) the ice observations were organized, handled and distributed on a national basis. This was mainly due to the limited needs (restricted ice navigation) and communication. Nevertheless, plain language or coded reports could already be transmitted by telegraphic means (from the early 1900ies via radio telegraphy).

With respect to the strategic and tactical naval requirements during World War I the first ice charts for the Baltic Sea were issued in Finland at the beginning of the year 1915. Soon they were prepared in near-real time (FIMR 1997). An example of these early charts is given in Fig.1. The ice chart shows the ice conditions only along the Finnish coasts, as information from other countries and from the open sea were not available. It has to be stressed that these early charts were already presented with a colour code for seven different categories described in the legend. Basically information is given on the distribution of

(coastal) fast ice, drift ice and pack ice (a heavier form of drift ice), which can be consolidated (frozen together) or in form of strips, and the occurrence of open water. This allows e.g. to include open leads within the drift/pack ice cover as shown off Raahe.

Fig. 1 First Finnish ice chart of 1915 (date unknown). The Swedish legend was translated into English (Courtesy: FIMR)

During the next years the Finnish ice charts were improved. The responsibility was taken over by the Ice Department of the Finnish Institute of Marine Research (FIMR – Merentutkimuslaitos), founded in 1918 (FIMR 1997). Weekly maps were mailed since the early 1920ies to ice services in other countries. An example is given in Fig. 2. The sea areas of the Gulf of Finland, the Åland Sea and of Södra Kvarken could be covered by extending the observation network. The German legend was nearly the same as in Fig. 1, however, an additional term *Dünnes Eis, Blaueis* (thin ice, blue ice - nilas) was presented in yellow. Furthermore, combinations of the given ice terms are possible, and numbers for ice thickness and for snow depth on top were included.

The ice chart indicates that by bilateral cooperation more ice information was available to cover not only the own national coastal areas, but for some regions also the open sea in between.

In 1925 the Deutsche Seewarte in Hamburg initiated an international conference – the **1st International Ice Conference** – in order to discuss necessary improvements for the ice reporting services within all countries bordering the Baltic Sea. The intensifying winter (ice) navigation in all sea areas required a harmonization of the national observation and reporting systems, as a vessel sailing e.g. from the western Baltic Sea to the Gulf of Finland received ice information in several different national codes. The main aim of that conference - and a 2nd one in August 1927 in Tallinn - was to present the ice information in *one language*, and as a result the ice experts developed the **1st Baltic Ice Code**, which was implemented in the ice winter1927/28 (Koslowski 1981).

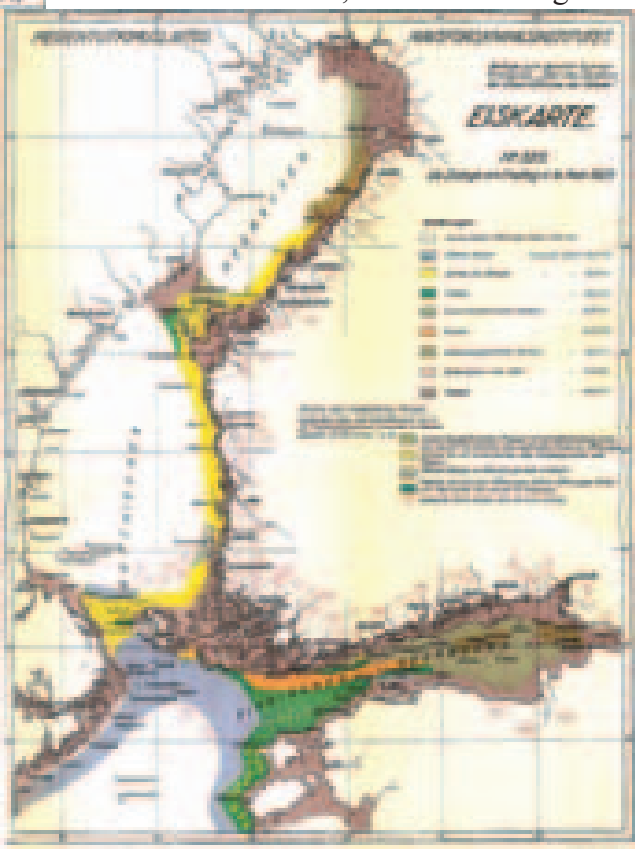

Fig. 2 Finnish ice chart of 16 Feb 1923 (in German language); legend see Fig.1 (in: Granqvist 1937)

With respect to the ice charting the ice terms used for the new code were adopted for the legend of the charts, too. The given numbers for the ice conditions were: *0 – clear of ice, 1 – soupy sludge or young ice, 2 – fast ice (≤15 cm), 3 – drift ice (≤15 cm), 4 – compressed sludge or close bands of drift ice, 5 – open lane along the coast, 6 – heavy fast ice (>15 cm), 7 – heavy drift ice (>15 cm), 8 – pack ice, 9 – forcing, screwing of ice, x – ice conditions not reported.* This code as well as the symbols (or colours) for the presentation of the ice conditions on the chart were used until the winter 1953/54 (see Fig 3).

Fig 3 Section of German ice chart of 25.01.1943 (Deutsche Seewarte)[1] showing the symbols (valid from 1934/35-1953/54) related to the 1st Baltic Ice Code (English version see above) with part of the Baltic coast and the Gulf of Riga. For comparison the symbols valid from 1927/28-133/34 are inserted.

During the period 1928 to 1939 the cooperation between the countries bordering the Baltic Sea was further intensified and improved by several international conferences. The *ice business* was a main topic within the regular Hydrological Conferences of the Baltic States, which started in 1926 and were continued in 1928, 1930, 1933, 1936 and 1938.

Table 2 List of international conferences, meetings and workshop related to the Baltic Sea ice[2]

- **International Ice Conferences (Expert Meetings) - 1925, 1927**
- **Hydrological Conferences of the Baltic States - 1926, 1928, 1930, 1933, 1936, 1938**
- **Baltic Sea Ice Meetings (BSIM) - 1954, 1956, 1968, 1977, 1979, 1981, 1983, 1985, 1988, 1992, 1995, 1998, 2000, 2003, 2005, 2008, …**
- **Baltic Sea Ice Climate Workshops (BSIC) - 1993, 1996, 1999, 2002, 2005, 2008, …**
- **International Ice Charting Working Group (ICWG) -1999, 2000, 2001, 2003, 2004, 2005, 2006, 2007, …**
- **WMO Expert Groups (SIG, ETSI) + Workshops (e.g. Ice Analysts WS, 12-17 June'2008, Rostock)**

[1] To address examples of full resolution historical ice charts click http://www.bsh.de/de/Meeresdaten/Beobachtungen/Eis/Historische_Karten.jsp

[2] For details click: www.bsis.eisdienst.de/history.shtml

The main ice related topics on these conferences were to get an overview on the organization, activities, resources and products of the different national ice services, reports on ice statistics and relevant publications, data exchange, ice terminology and coding. In June 1937 Gunnar Granqvist, deputy director of the Finnish Institute for Marine Research (FIMR – Merentutkimuslaitos) summarized the basic requirements for coding and ice charting as follows (Granqvist 1937):

- To review the existing ice terminology and to elaborate exact definitions in order to establish a basis for its formalization and completion[3]
- To introduce continuous ice observations along the coasts using the method of local ice charts, which are to be drawn each Friday and which have to be posted together with the weekly journals[4]
- To compile on the basis of the ice observation from the coastal areas and the open sea exact general charts, which are drawn in different colours (symbols), each of them assigned to a specific ice type, and
- To consider how these charts (of same scale and projection) could be assembled into a joint Baltic chart and how the costs could be met; about this could be decided, if and when ice charts from the different countries would be available[5].

As a result of the mentioned statements it was recommended that for a special period all Baltic countries should perform ice observations from coastal stations and from ships and aircrafts according to identical principles (Granqvist 1939). This event was called the **Baltic Ice Week** and proceeded from February 12 to 18, 1938 (see Table 1, part 1). The observation programme as well as standard forms and the necessary instructions were prepared by FIMR (Jurva and Palosuo 1959). The coastal observations network is presented in Fig. 4. The results

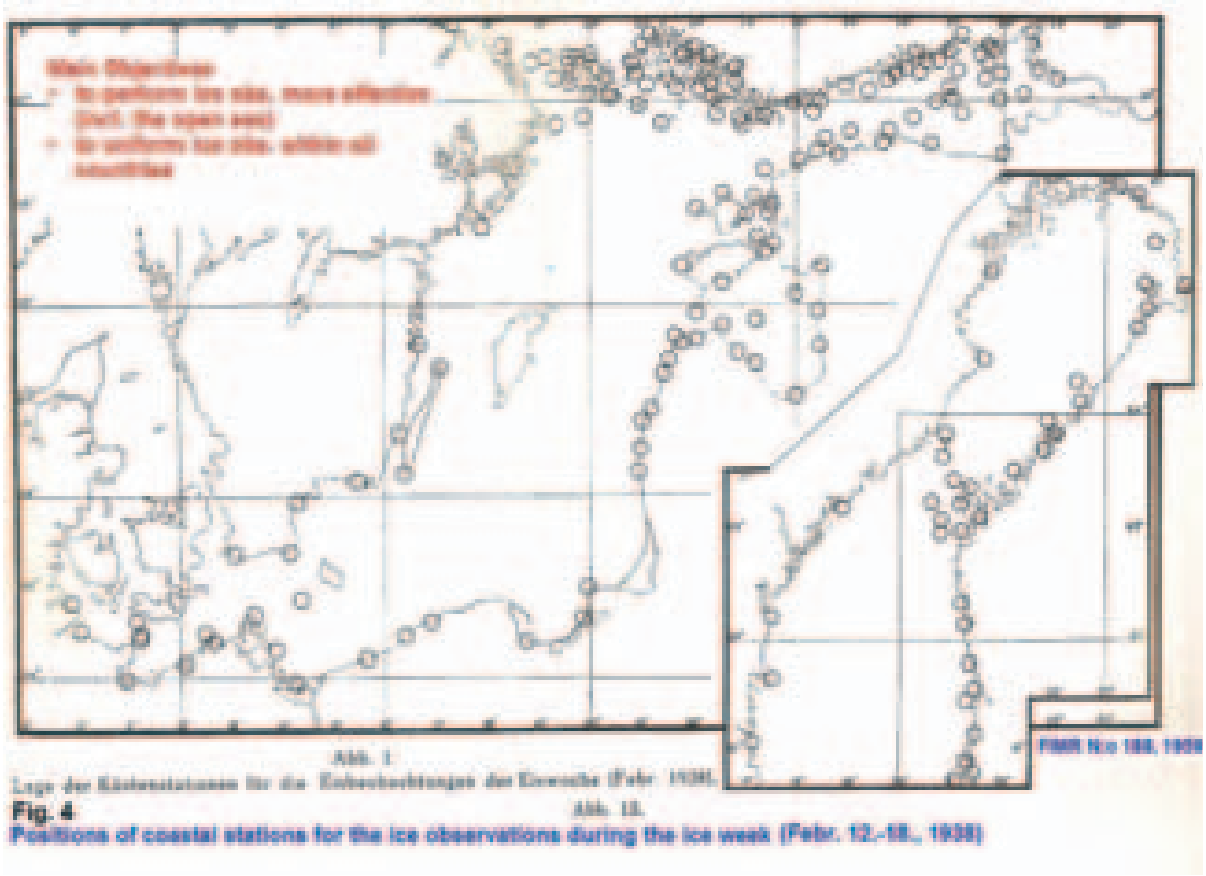

Fig. 4
Positions of coastal stations for the ice observations during the ice week (Febr. 12.-18., 1938)

[3] The Finnish ice service did not consider a new Baltic Ice Code before this has been completed. – Finally this requirement was met not until 1952 by the 1st WMO Ice Nomenclature (see Table 1, part 2).
[4] The observation method practiced in Finland since 1915 was to keep daily records in plain language in a weekly observation form and in addition to drawing charts for the observation area with exact ice boundaries.
[5] This topic is even after 70 years still open and under further discussion within the Baltic Sea Ice Meeting (BSIM).

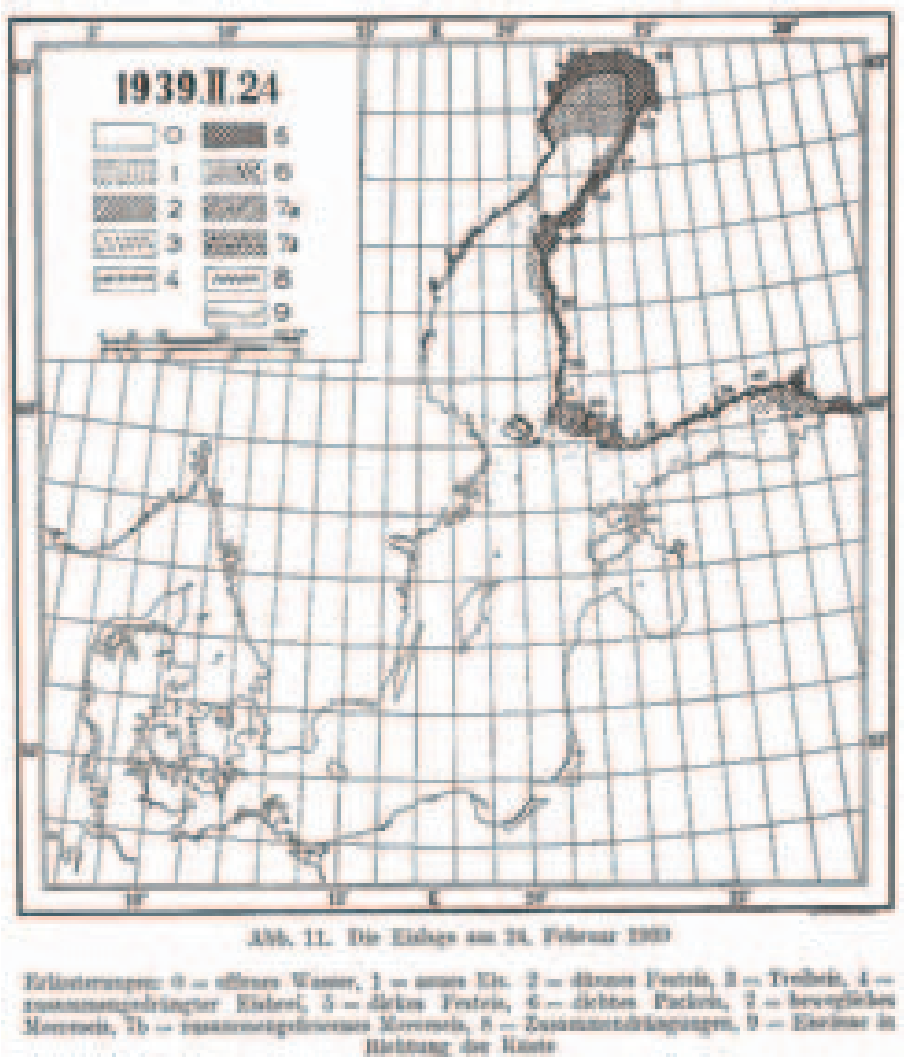

were not very encouraging, as the ice season 1937/38 was rather weak with no ice at sea besides in the Bay of Bothnia and the eastern Gulf of Finland. Therefore, it was decided to repeat the ice week during the next season. However, although in 1939 it was performed three times (28.01. - 03.02., 18. - 24.02., 11. - 17.03.), the again very weak winter – and then World War II – prevented to achieve the expected data and results. The observations were gathered and archived at FIMR and partly evaluated. Fig. 5 shows a sample prepared by E. Palosuo (1959).

Fig. 5 Sample of an ice chart based on the observations during the ice week 18.-24.02.1939. The symbols used were valid from 1954.

During World War II international cooperation was obviously very limited. But with respect to the related special demands for good operational ice information – mainly during the first three very heavy ice winters 1939/40 to 1941/42 – aerial ice reconnaissance was very much intensified. By this the coverage of the sea areas - as well as the knowledge about the ice conditions in heavy winters in the Baltic Sea - was widely improved and documented in the ice charts (see Fig. 6).

Fig 6 German ice chart of 10.02.1941. The legend is given in Fig. 3,

3. The development from 1946 until 1970 – *the classic phase*

After WW II the international cooperation has to be reorganized, as e.g. the political map for the south-eastern part of the Baltic Sea as changed considerably. However, it was already in the winter 1946/47 that the station reports from Denmark, Finland, Norway and Sweden and from the German coasts could be exchanged via telegraphy and radio broadcasting, respectively. This was of particular importance with respect to the extreme heavy ice season.

Table 1, part 2. Chronology of facts, events and developments related to ice charts (1946 – 1970)

1951	Exchange of coded ice info via GTS (D, FI, S)
1952	1st International Ice Nomenclature issued by WMO
1954	first international ice conference after WW II (Baltic Sea Ice Meeting – BSIM, cp. Table 2)
1954/55	2nd version of the Baltic Ice Code (valid until 1980/81, revised in 1969) • further normalisation/improvements of the international exchange of ice information (plain language and coded reports via GTS)
1968	2nd International Ice Nomenclature issued by WMO
1968/69	regular use of weather satellite photos for ice charting
1969/70	revision and enhancement of the 2nd Baltic Ice Code

In September 1954 the first international conference of ice experts from the Baltic Countries after WW II was hold at FIMR in Helsinki. It was called *Ice Service Meeting*[6], and the main topic was to meet the consequences of the new International Ice Nomenclature issued in 1952 by the WMO for the Baltic Sea Ice Code. On former ice conferences it was already obvious that the terms (vocabulary) describing a given ice situation so far was mainly assigned by the practical (nautical) requirement and did not meet sufficiently the scientific demands e.g. for the arrangement and the development of the ice (see footnote 3). This was considered by the WMO nomenclature on a global basis. Relevant terms for the Baltic Sea were adapted both for the new version of the Baltic Sea Ice Code (SMHI 1959) and for the ice chart symbols valid from the ice winter 1954/55. The basic innovation was to introduce the main categories for the ice concentration (arrangement of the ice), as shown in Fig. 7. However, concerning the ice chart symbols, from 1956/57 to 1964/65 they were replaced by unknown reasons in Germany and very likely in Sweden, too, by an even simplified version of the old one (Fig. 8).

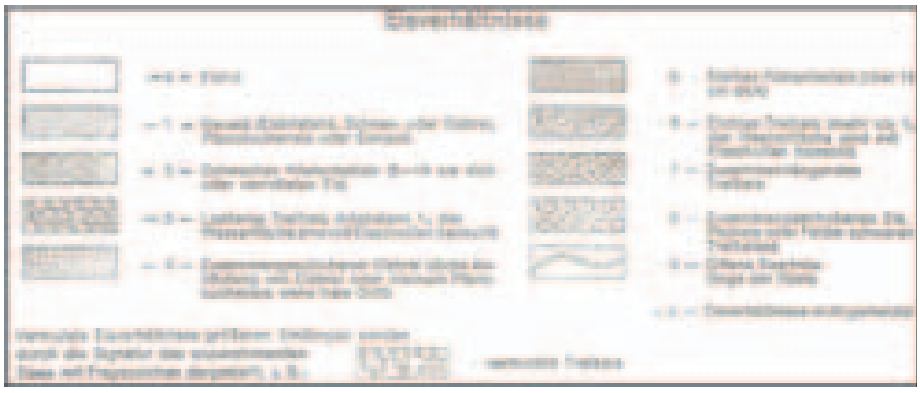

Fig. 7 Legend of German ice charts valid from 1954/55 to 1955/56

[6] Later on these meetings were also named *Meeting of Baltic Sea Ice Experts*. For the meeting in Oct. 1977 in Norrköping for the first time the name *Baltic Sea Ice Meeting* was used, and it was numbered as 11th Meeting (for details click: www.bsis.eisdienst.de/material/Material2.pdf). When the author in 1995 was elected as chairman of the Meeting (acting until April 2004) nobody of the active or retired participants did know about the source of the numbering. By checking literature and other sources, it then became more or less obvious that the former expert meetings and Hydrological Conferences (see Table 2) must have been considered for the numbering.

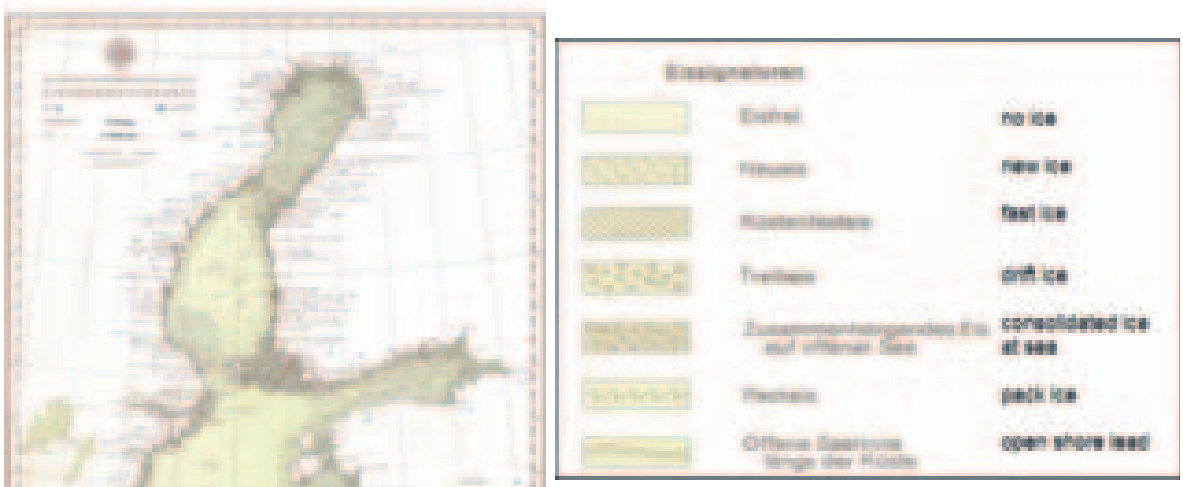

Fig 8 German ice chart of Feb. 1, 1963 with scaled up legend and English translation.
This legend was valid from 1956/57 to 1964/65 and used on Swedish charts, too. Compared with the legends in Figs. 3, 5 and 7, it was rather simple and a setback. Nevertheless, for the coastal stations the numbers of the improved Baltic Sea Ice Code were given, and on the chart by the density of the symbol for drift ice differences in ice concentrations could be presented.

For the winter 1965/66 the German ice service issued its ice charts with a new legend. Symbols for the ice concentration categories were reinstalled, again it could be distinguished between weak (thickness ≤ 15cm) and strong (>15 cm) fast ice and drift ice, and a new symbol for compressed sludge was introduced. This legend (see Fig. 9) was valid until 1968/69 and very similar to the Finnish legend, which in addition offers the possibility to add values for ice thickness and snow depth.

Fig 9 Legend of German ice charts from 1965/66 to 1968/69 with appended English translation

It was in 1968 that the WMO issued a revised, scientifically better substantiated 2nd International Ice Nomenclature (WMO 1970). With respect to this new nomenclature in June 1968 10th Baltic Sea Ice Meeting (BSIM-10) reviewed its implementation into the Baltic Sea Ice Code and the ice terms used for ice charting. The necessary conformance was completed and adopted. Both, the re-vised Ice Code of 1954 and the new ice symbols came into operation in the ice season 1969/70.

BSIM-10 decided also to present the general ice charts for the Baltic Sea of the different ice services for the same days (Monday, Thursday), for the same region in a unique projection and scale. For the region north of about 56° N, to which in most winters the ice cover is restricted, Mercator projection with 60° N as reference latitude[7] and a scale of 1: 3 Mio was used. Additional charts covering e.g. in severe winters the total area of the Baltic Sea or - depending on national requirements - for distinct limited regions were offered, too. With regard to the new symbols (see Fig. 10) it had also to be considered that they had to fit with the new radio facsimile techniques, which were available and tested for ice chart transmission

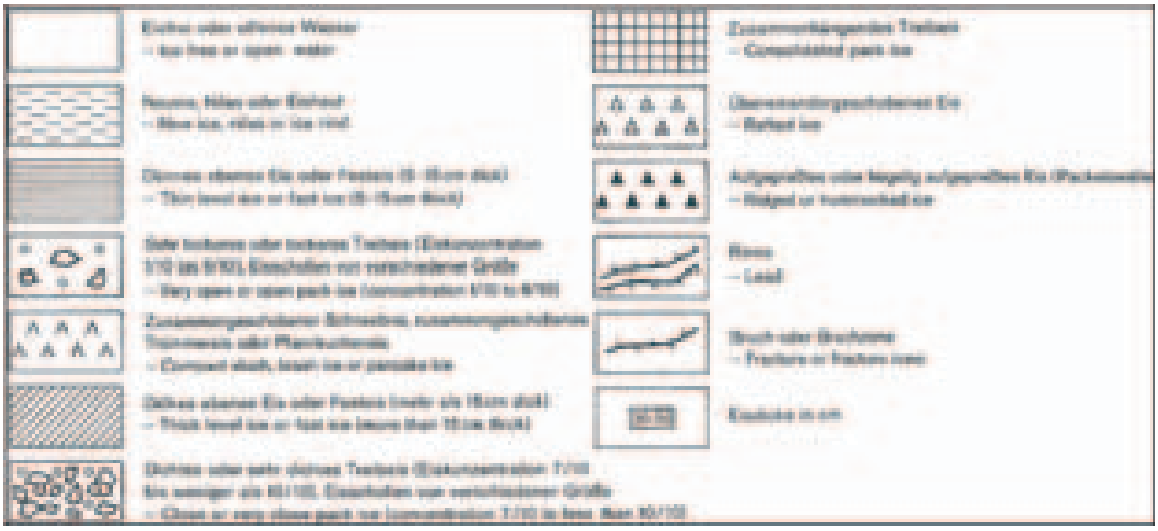

Fig. 10 Legend of German ice chart valid for the period 1969/70 to 1980/81

the late 1960ies. Furthermore, at that time the first images from polar orbiting weather satellite became available (see Fig.11), which met very nicely with the introduction of the permanent winter navigation into the northern Gulf of Finland requiring improved and extended ice information.

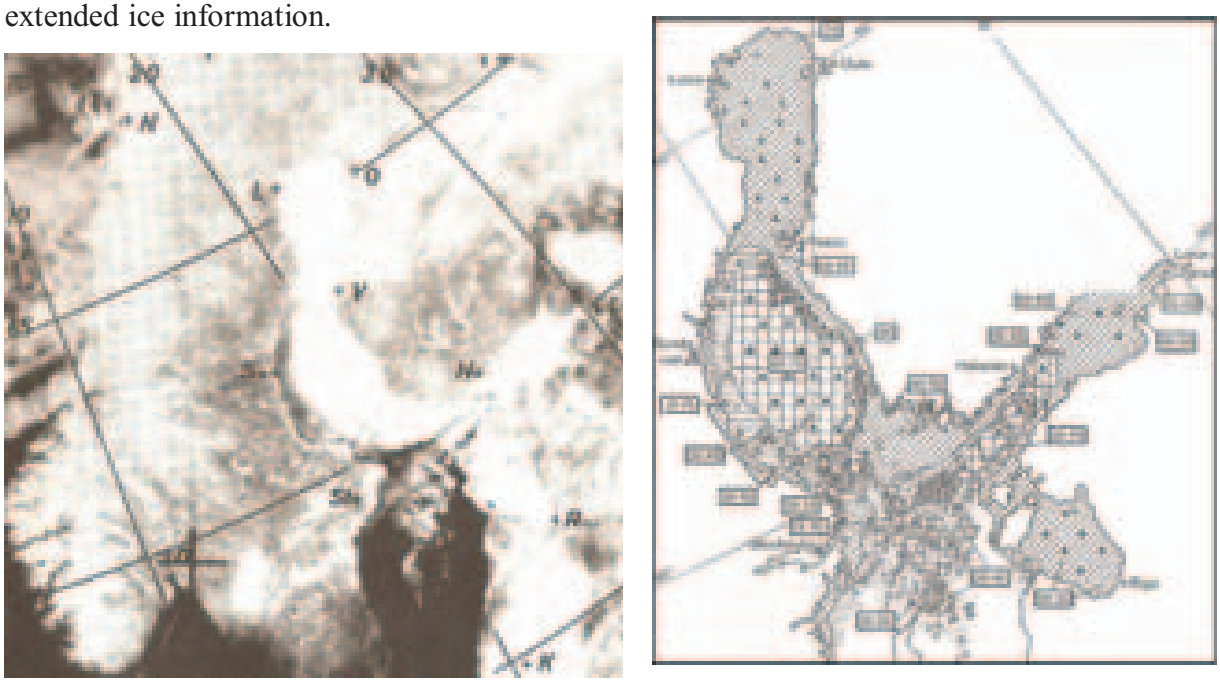

Fig. 11 ESSA-8 (Environmental Survey Satellite) image of 26 March 1969 and its interpretation according to the new symbols shown in Fig. 10 (in: Strübing 1970)

[7] The latitude 60° N was chosen for practical reasons: as the ice is mostly situated north of it and the chart area on Mercator projection is increasing northwards some drawing space is available.

4. The development from 1971 – *the technical phase*

The last decades were highlighted by rapid technical developments in the field of communication (data/product exchange), data processing (digital processing of reports and charts) and improved sensors (e.g. scanning visible/infra-red radiometers, passive microwave radiometry, and synthetic aperture radars) for ice reconnaissance satellites like Landsat, NOAA- and SSM/I-series, ERS-1/2, Radarsat-1 and ENVISAT (Strübing 1970, 1991, 2000). These developments were met by further intensified international cooperation within the Baltic and global sea ice services and relevant technical and scientific groupings. Beside the meteorological sector the ice community was one of the driving forces on the mentioned fields. Some highlights are summarized in the following table.

Table 1, part 3. Chronology of facts, events and developments related to ice charts (1971 ff.)

1978/79	Agreement on radio facsimile broadcast of ice charts (first activities 1968/69) • special radio fax charts for the Western Baltic
1980	New WMO ice symbols
1981/82	3rd Baltic Ice Code (Baltic Sea Ice Code of 1980) • Changes of the fairway numbering, International WMO ice symbology Introduction of word processing for ice reports – new layout for the *EISBERICHT*
1984/1987	Use of an decentralise terminal for the online transfer and processing of digital NOAA data
1985/86	On-line EDP programme for the transformation of the coded fairway reports via GTS
1987	Bothnian Experiment in Preparation für ERS-1 (BEPERS) – Joint Finnish/German/Swedish research programme for the application of radar images (until 1994)
1990/91	Digital production of the operational ice charts via graphical terminal (1st service within the countries bordering the Baltic Sea)
1992	Installation of an ESA facility for near real-time ERS-1/SAR data reception (until 1995)
05/1994	last *Eisbericht* and ice chart produced by offset printing
1994/95	Production of ice reports and charts by laser printers (A4 format) • Text in German **and** English • Beside postage product transmission via telefax
1995	First international initiative for the use of ice data in electronic nautical charts (ECDIS format)

1995	Application Development and Research Opportunity (ADRO) for RadarSat-1 (Joint Finnish/German/Swedish Proposal to CSA). Final results:
	• Near real-time FTP transfer
	  ○ of RadarSat-1 images from TSS to the Finnish/Swedish ice service
	  ○ of ERS-1/-2 images from DLR to the German ice service

1995/96	Adoption of the Finnish ICEMAP software for the digital production of ice charts • design and production of special charts for icebreakers in the Western Baltic Sea
2001/02	Exchange of ice information products between the Ice Services routinely also by **e-mail**, in addition to telefax.
2002 ff	Test of the WMO Colour Code (confirmed 2004)
2003	From 27 March test version of the joint Internet presentation of the Baltic Sea Ice Services (BSIS as registered domain) – from 2004 operational. • First on-line products (restrictions to navigation, coded daily ice observations, generalized ice chart)
2004	*Memorandum of Understanding to formalise the cooperation of the Baltic Sea Ice Services* (BSIS) was signed till spring by Denmark, Finland, Germany, Latvia and Sweden
2005/06	Production of German ice charts in ArcGIS replacing ICEMAP software

The revision of the Baltic Sea Ice Code of 1954 in 1969 was only a first step for further improvements to meet the requirements of modern winter navigation in the Baltic Sea (Strübing 1978). A BSIM working group developed during the 1970ies an advanced version, which was discussed at the Meetings (see: www.bsis.eisdienst.de/material/Material2.pdf) and after formal approval in 1979 published as Baltic Sea Ice Code of 1980 (SMHI 1981). This new code offered the possibility to describe the ice conditions in ports, fairway sections and limited sea areas by 3 times 10 numbers (= 30 different ice parameters) instead of only 10 numbers of the former code (www.bsis.eisdienst.de/material/Ice_observations_and_their_coding.pdf).

In nearly the same period on WMO basis – with input from Baltic Sea ice experts – a new symbology for the presentation of sea ice on charts was prepared including both, symbols and the numerical Egg Code (WMO 1989). From this a legend was extracted appropriate for the requirements of the Baltic Sea ice charts and mostly still compatible with the former version. Both, the reporting and charting systems, were officially implemented in the ice winter 1981/82.

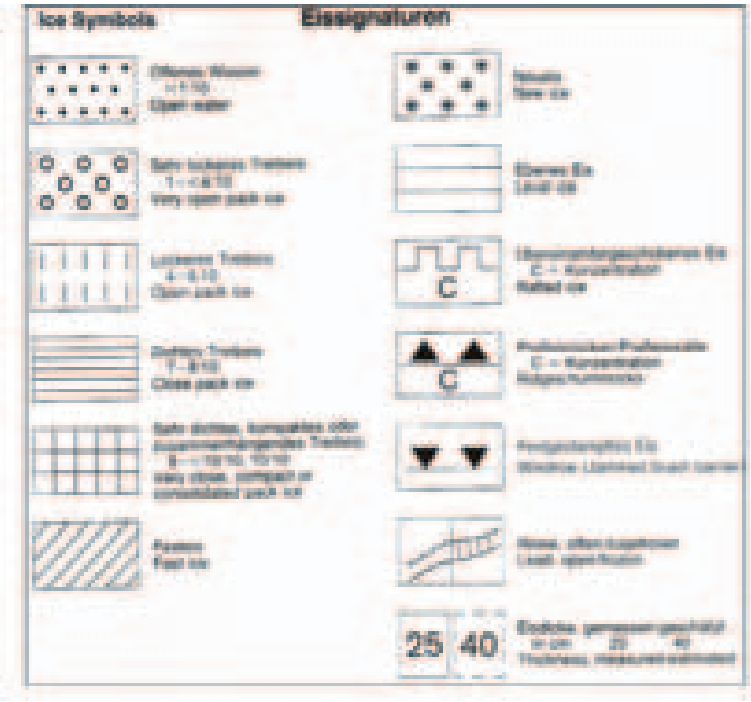

Fig. 12 Legend from German ice chart valid from 1981/82

In the Baltic Sea the ice is traditionally illustrated by graphic symbols like hatching etc. The density of the symbols is related to the degree of the ice concentration allowing the user to get at one glance an impression of the difficulty of the ice conditions (see Fig. 12). Though the numerical Egg Code is also given as legend on the Baltic ice charts, it is, however, compared to North American charts of much less application (for details of the coding and sample charts see e.g. www.natice.noaa.gov/egg_code/index.html).

The new codes and symbols allowed a broadened transfer of the increasing details of the ice cover offered by the various satellites into the ice charts and into ice reports, too. This started mainly during the 1980ies, when the main ice services obtained their own receivers for the data of the U.S. NOAA weather satellite series. The digital images could be used operational (real-time) few minutes after the overpass of the satellite (see Fig. 13). First hardcopies were produced compatible with the ice charts. So features like ice edges/ boundaries, fractures and leads easily were assigned to the ice charts, which, however, still were hand drawn.

In the season 1990/91 the German ice service was first to use a graphical terminal to digitally produce the ice charts. This method was soon (1994) improved by the Finnish ICE MAP system, which allowed a complete digital production line including the satellite data/images as on-line background information (Berglund 2003). In addition the different ice types outlined by the polygons (defined by ice edges and boundaries) could be attributed with

relevant information. The stored data allowed later on easy handling for statistical/climatologically evaluation.

Further technical changes and improvements in the early 1990ies allowed producing and disseminating the ice charts and reports in a more user friendly way. The large formatted offset printing products were replaced by laser prints in A4 format, which could easily transmitted to the users on-line via telefax. This reduced the transfer time of the products by at least 12 to 18 hours.

New communication dimensions were opened with the introduction of the electronic mail (e-mail) and then the internet. The rapidly improving technical possibilities and applications since the second half of the 1990ies were increasingly used, both, internal within the ice services and external between the services and their users. These new tools were most suitable for the real-time/on-line dissemination and presentation of operational (and other) ice information products.

With respect to the ice charting, this resulted also in the reintroduction of the colour code. As shown in Fig. 1 and 2 on the early charts the different ice types were represented already by special colours, which were used on Finnish charts even until the early 1950ies. The digital chart production techniques allowed an easy transfer from the hatching version into a colour presentation. As result of the 3rd International Ice Charting Working Group (IICWG) meeting in Nov. 2001 a draft version was elaborated to be tested within the various ice services from Jan. 2002[8]. Since then coloured ice charts are more or less a routine product (WMO 2004a). Comparing the first colour code with the new WMO format, it becomes obvious in Fig. 13 that the basic standards were very similar.

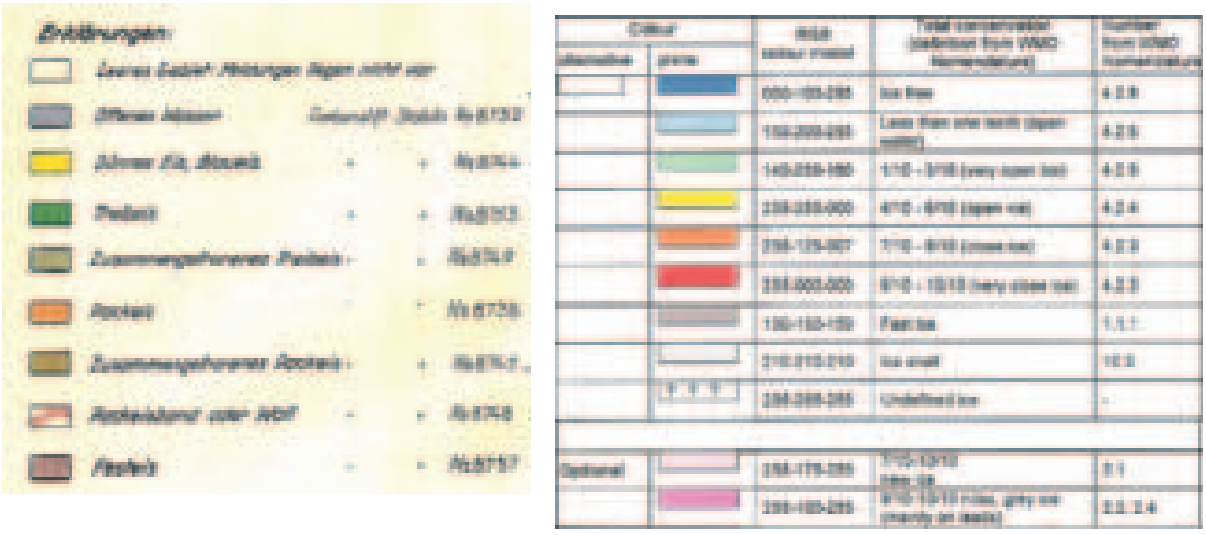

Fig. 13 Comparison of the old colour code (left, see Fig. 2) and the new WMO Code from 2004

To make the colours on the various ice charts comparably, in the digital code the numbers for the RGB model are prescribed. However, even in old days an analogue method was available by giving the number of the particular coloured pencil for each ice type.

According to in-house strategy and considering recommendations from the International Ice Charting Working Group (IICWG) on hard- and software harmonization for ice charting and for the format for ice chart archiving data based on the shape file format and

[8] Later on a revised version was presented to the JCOMM (Joint WMO/IOC Commission for Oceanography and Marine Meteorology) Expert Team on Sea Ice for further formal handling. In 2004 the final version was approved.

SIGRID-3 code[9], the German Ice Service shifted its production tools for ice charts from ICEMAP to Arc/GIS technology. The new products were introduced in the 2005/06 resulting in a change of the lay-out, too. Both products can be compared in following figure:

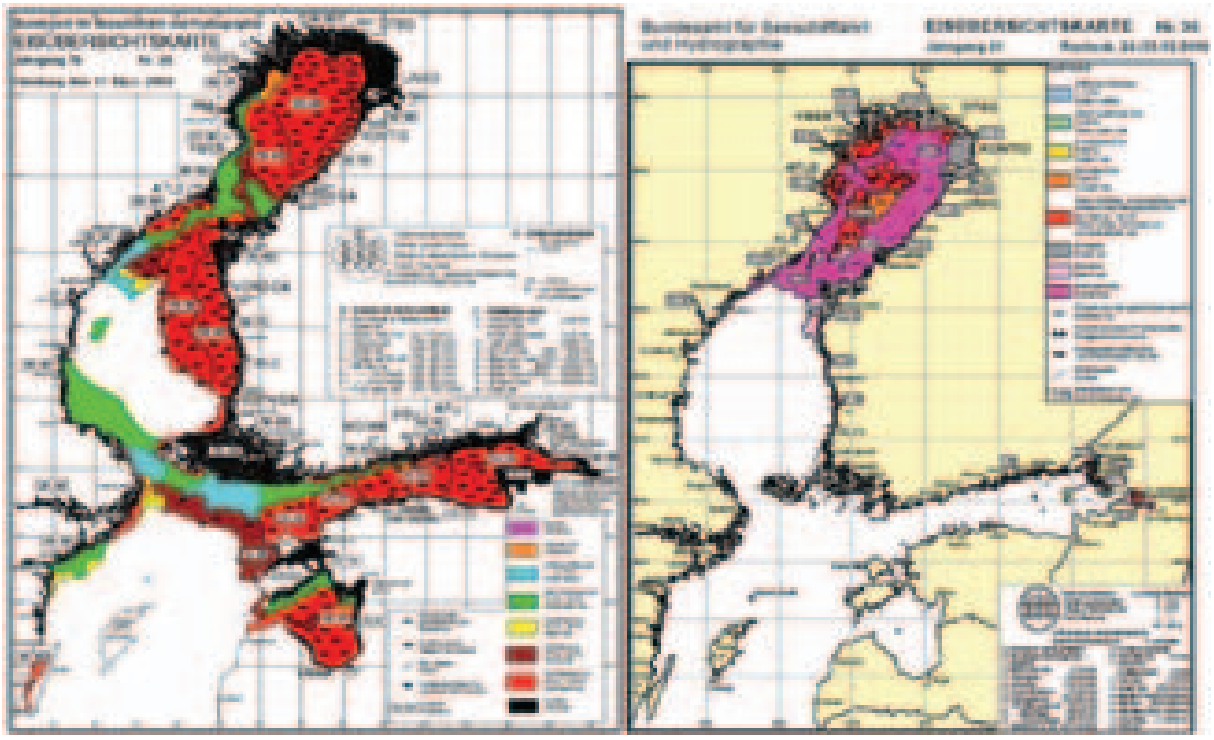

Fig. 14 German ice charts
from 1995/96 – 2004/05 in ICEMAP format (left) and from 2005/2006 in ArcGIS format (right)

5. Results and conclusion

5.1 Sea ice nomenclature and symbology

During nearly 100 years of ice charting the standards, tools and methods were steadily improved. It was early recognized that this was possible only on an international basis. The main goal of easy and safe navigation within a harsh environment and at rapidly expanding economic requirement could by met only by a harmonized and close cooperation between the relevant services. On the other hand, beside the practical aspects of the ice navigation, scientific aspects of the ice covered seas had to be considered, too. This is reflected mainly in development of the codes and symbols for the presentation of the ice conditions in reports and charts. In Table 3 this is summarized for the ice symbology.

In the 7 columns of the table the periods are given, in which a special legend was valid. Within the columns the terms are arranged according to the content of the last legend valid from 1981/82. To get the legends comparable the ice terms are arranged by subject according to the system of the WMO nomenclature. The main categories as development, forms, concentration, surface features and openings are marked off by bold horizontal lines in order to see changes etc. more easily. Within the lines and columns the terms in each box are represented are represented by a single symbol.

[9] SIGRID-3 (Sea Ice Grid) is a vector archive format for ice charts. The format was developed by an IICWG Ad Hoc Team for the WMO "Global Digital Sea Ice Data Bank - GDSIDB" (WMO 2004b). Encoded charts have two main components: the chart information and metadata describing the chart. The Baltic Sea Ice Services are contributing with relevant data sets (ice charts) from 1960 to GDSIDB.

It can be noticed that most changes have applied to the details for the ice concentration. According to the WMO classification, since 1969 the concentration is divided in more categories with separate symbols than before. This allows better judging of the

Table 3 Terms for Ice Chart Symbols (Deutsche Seewarte, DHI, and BSH)[10]

1927/28 – 1933/34	1934/35 – 1953/54	1954/55 – 1955/56	1956/57 – 1964/65	1965/66 – 1968/69	1969/70 – 1980/81	1981/1982 -
Fig. 3	Fig. 3	Fig. 7	Fig. 8	Fig. 9	Fig. 10	Fig. 12
≈ 1 : 3 Mio	1 : 3,4 Mio	1 : 3 Million	1 : 3 Million	1 : 3 Million	1 : 3 Million	1 : 3 Million
Mercator	Mercator (55° N) *	Equal area conical proj.	Equal area conical proj.	Equal area conical proj.	Equal area conical projection	Mercator (60° N)
	clear of ice	no ice	no ice	open water	ice free or open water	open water
new ice or loose sludge	soupy sludge or young ice	new ice (all forms)	new ice	new ice (all forms)	new ice, nilas or ice rind	new ice
					Very open or open pack ice (1-6/10)*	very open ice
drift ice in places	drift ice	open drift ice (≤ ⅝)		thin drift ice (≤ ⅝, >⅝)		open ice
		close drift ice (>⅝)			close or	close ice
strong drift ice	heavy drift ice (>15 cm)	compact ice, pack ice or fields of heavy drift ice	drift ice	thick drift ice (≤ ⅝, >⅝)	very close pack ice (7-< 10/10)*	very close, compact
		consolidated drift ice	consolidated pack ice at sea	consolidated ice	consolidated pack ice	or consolidated ice
fast ice	fast ice (up to 15 cm)	weak fast ice (5-15 cm)*	coastal fast ice	weak fast ice (5-15 cm) or thin level ice at sea*	thin level ice or fast ice (5-15cm)	fast ice
strong fast ice	heavy fast ice (>15 cm)	strong fast ice (>15 cm)		strong fast ice (>15 cm) or thick level ice at sea	thick level ice or fast ice (> 15cm)	level ice
					rafted ice	rafted ice
pack ice, ice walls	Ice pressure	s.a. compact ice etc	pack ice	pack ice	ridged or hummocked ice	ridges/hummocks
	Compressed sludge or close bands of drift ice	compressed sludge		compact sludge	compact slush, brash ice or pancake ice	windrow (jammed brash barrier
open lane along the coast	open lane along the coast	open shore lead	open shore lead	open shore lead	lead	lead, open/frozen
track						crack
						ice edge or ice boundary (observed/estimated)
					ice thickness	ice thickness (observed/estimated)
		* or rotten ice		* or rotten ice	*ice floes of different size	
	* until 1951/52, then conical		X - position of measured SST		X - position of measured SST	X - position of measured SST

navigation conditions. However, it must be noted that from 1981 the separation between very close to compact ice and consolidated ice has been skipped. Concerning navigational aspects this is more or less a draw back, because for a vessel it can be a distinct difference in

[10] The terms were taken from ice charts prepared by the German ice service being part of the Deutsche Seewarte (1896-1945), Deutsches Hydrographisches Institut (German Hydrographic Institute) – DHI (1946-1991), and the Bundesamt für Seeschifffahrt und Hydrographie (Federal Maritime and Hydrographic Agency) – BSH (1991 ff). The German terms were translated into English using the relevant vocabulary.

difficulty between both categories. With respect to the ice thickness from the very beginning there was a separation of ice thicker than about 15 cm valid for fast ice and partly for drift ice, too. Since 1969 this separation by special symbols was replaced by the possibility to include values on ice thickness in order to provide more information on the navigational conditions. They relate mostly to shore- and ship-borne (icebreakers) measurements (or estimations). A trustable satellite remote sensing method is still lacking (beside the possibility of getting some information on thinner ice categories with optical sensors (see Fig. 11).

The main issues are that

- Ice nomenclature (terms), codes and symbology must further on be balanced between practical (nautical) and scientific requirements, the charts must be readable for operational users.
- International solutions approved for the Baltic Sea must be compatible to WMO standards

5.2 The operational boundary conditions

The ice charts are produced within the ice services mostly in an operational environment with e.g. stress because of time pressure related to the deadline for the dissemination of the product[11]. This has to be considered with respect to the accuracy and validity of ice charts.

In general it can be stated that for an ice chart the ice conditions of at least two days are relevant, the day of the issue date and the day before, because at the time when the chart has to be drafted by the expert for the final drawing by an technician, only all ice information from the day before but not from the issue day are available (lacking were mostly the sea areas). These constraints were especially relevant for the periods, when ice charts are issued on all working days as e.g. in Germany until 1945, and in Finland and Sweden in the modern times of radio fax, telefax and e-mail transmission. However, it has also to be considered that the constraints with respect to time pressure are of course also very much depending on the character and the stage of development of the ice season. Nevertheless, times with greater ice extent are mostly affected, but on the other hand of most interest, too.

With the availability of satellite data since the end of the 1960ies the problems of lacking ice information from the sea areas could be overcome considerably. However, as the interpretation of the data (images) – as well as the transfer of reports and coded information into generalized cartographical products - is to some extent related to the interpreter's experience and assessment and thus object of subjective human influence. This was in detail discussed on a recent WMO workshop of ice analysts (WMO 2008).

An improving and time saving factor was then in the 1990ies the digital production of the ice charts, by which the drafting and final drawing of the chart is just one work process executed by an expert/scientist and resulting directly into the printing of hardcopies and/or the electronic product dissemination. New information can be included to the very end of the drafting/drawing process, and the saved time can sum up to some hours.

Furthermore, beside the general overview charts for the Baltic Sea, the new techniques offer the opportunities to present with flexible scale new and better regional products, which can be used for tactical support e.g. on board of icebreakers or other service vessels. Areas with heavy ship traffic and a lot of dangerous goods (oil, gas and other chemical products) as e.g. the Gulf of Finland and in more severe winters also the narrow straits in the western Baltic are most important.

[11] For example following deadlines had to be considered by the German ice service: 10:10 local time for radio fax charts for the western region of the Baltic Sea, 13:00 for product delivery to the print office. The latter could be handled more flexible, when in the season 1994/95 the independent laser printing was introduced.

The main issues are that

- Operational ice charts are to some extent never complete and fixed to a strict date, but cover normally a time frame of up to 24 hours.
- Operational ice charts are exposed to subjective influences with respect to the interpretation and generalization of the available data.
- The availability of operational ice charts from different services for the same date and region can produce confusion for the users.
- For practical reasons only **one** overview chart for the Baltic Sea should be *on the market* (see footnote 5).
- Larger scale regional or sub-regional charts are requested on-line for tactical applications.

5.3 Climatological aspects

Beside the traditional coded station reports the ice charts for the Baltic Sea, available now for more than 90 years, are the basis for climatological studies of the ice cover at sea. As documented by the proceedings of the former Baltic Sea Ice Workshops, they have been and will be widely used for example for ice atlases (e.g. SMHI&FIMR 1982, FIMR 1988) The constraints listed above very likely may have been more or less smoothed out by statistical calculations. However, at least it should be considered for future work that the material is largely homogenous only within the periods given in Table 3.

The reconstruction of operational charts for climatological requirements with data later on available (e.g. belated ship or aircraft observations, non real-time satellite images) is a possibility to improve the material; however, it is a major challenge with respect to manpower and knowledge. Nevertheless, there are relevant applications (Schmelzer 2008).

6. Outlook

The sea ice services of the Baltic Sea offer a great potential for the future operational and climatological requirements in the region, and they are exemplary for long-term and good cooperation documented by the tradition of the Baltic Sea Meetings and the joint BSIS (Baltic Sea Ice Services) web page (www.bsis.eisdienst.de/). And they are a necessary and trustable partner for the long- to mid-term international strategy of IICWG to place ice information in electronic navigation charts, to contribute to the Global Digital Sea Ice Data Bank, to meet the challenges of Global Change, and to enforce the demands for improved and continuous satellite systems and sensors for ice charting of the Baltic Sea.

References

Berglund, R., Kylänpää, M., 2003: ICEMAP – An Interactive Ice Charting Application for Ice Services. Paper presented at the 4th IICWG Meeting, 3.4.2003, St. Petersburg

FIMR 1988: Phases of the Ice Season in the Baltic Sea. Finnish Marine Research N:o 254, Suppl. 2

FIMR 1997: The cool facts about navigating in ice. Ice Service brochure.

Granqvist, G., 1937a: Über das Studium der Eisverhältnisse der Ostsee. Ständiges Bureau der Baltischen Hydrologischen Konferenzen, Riga

Granqvist, G.,1939: Die Eisverhältnisse der Ostsee und ihre Erforschung. In: VI. Baltische Konferenz, Deutschland (Lübeck, Berlin) August 1938, Hauptbericht 12, Berlin

Jurva, R., Palosuo, E., 1959: Die Eisverhältnisse in den Finnland umgebenden Meeren in den Wintern 1938-45 und die Baltischen Eiswochen 1938-39. Merentutkimuslaitos Julkaisu N:o 188, Helsinki

Koslowski, G., 1981: Der Ostsee-Eiskode von 1980. Seewart 42, H. 4, 176-184,Hamburg

Schmelzer, N., 2008: Does navigation need an ice atlas? Ideas about an ice atlas for the area of the Western and Southern Baltic. Proc. of the 6th Workshop on Baltic Sea Ice Climate. Lammi, Finland, 25-26 August 2008

SMHI&FIMR 1982: Climatological ice atlas for the Baltic Sea, Kattegat, Skagerrak and Lake Vänern (1963-1979). Sjöfartsverket tryckeri, Norrköping

SMHI 1981: The Baltic Sea Ice Code.

Strübing, K., 1970: Satellitenbild und Meereiserkundung. Ein methodischer Versuch für das Baltische Meer. Dt. hydrogr. Z. 23, 193

Strübing, K., 1978: Entwicklung der Winterschiffahrt im nördlichen Ostseeraum. Hansa 115, 267-270, 355- 357, 439-440

Strübing, K. et al. 1991: A Feasibility Study of an ISY Real Time Ice Monitoring Demonstration - Final Report, 132 p., Hamburg Oct 1991 (ESA/ESTEC Contract Report, P.O. 92/125514)

Strübing, K., 1997: 100 Jahre Eisdienst, Vergangenheit – Gegenwart - Zukunft. BSH, Jahresbericht 1996

Strübing, K., Ramseier, R.O., 2000: Real-time use of ERS-2 data on board GS "Neuwerk" in the Bay of Bothnia. Proc. of a Workshop on Mapping and Archiving of Sea Ice Data – The Expanding Role of RADAR, Ottawa, Canada, 2-4 May 2000. WMO/TD-No 1027, pp 165-172, JCOMM Technical Report No 7.

WMO 1970: WMO Sea-Ice Nomenclature. WMO/OMM/BMO, Geneva No.259. TP. 145

WMO 1989: WMO Sea-Ice Nomenclature. Terminology, codes and illustrated glossary. WMO No. 259 TP 145, Suppl. No. 5

WMO 2004a: Ice Chart Colour Code Standard. WMO/TD-No.1215, JCOMM Techn. Rep. No 24

WMO 2004b: SIGRID-3: A Vector Archive Format for Sea Ice Charts. WMO/TD-No.1214, JCOMM Techn. Rep. No 23

WMO 2008: Proceedings of the Ice Analysts Workshop, Rostock, Germany, 12-17 June 2008. WMO/TD-No.1441, JCOMM Techn. Rep. No 43

Abbreviations

BEPERS - Baltic Experiment in Preparation for ERS
BSH - Bundesamt für Seeschifffahrt u. Hydrographie Federal Maritime and Hydrographic Agency
BSIM - Baltic Sea Ice Meeting
BSIS - Baltic Sea Ice Services
CSA - Canadian Space Agency
DHI - Deutsches Hydrographisches Institut German Hydrographic Institute
DLR - Deutsches Zentrum für Luft- und Raumfahrt German Aerospace Center
ECDIS - Electronic Chart Display and Information System
EDP - Electronic Data Processing
ENVISAT - Environmental Satellite
ERS - ESA Remote Sensing Satellite
ESA - European Space Agency
ESSA - Environmental Survey Satellite
ETSI - Expert Team on Sea Ice
FIMR - Finnish Institute for Marine Research
FTP - File Transfer Protocol
GDSIDB - Global Digital Sea Ice Data Bank
GIS - Geographic Information System
GTS - Global Telecommunication System
IICWG - International Ice Charting Working Group
IOC - International Oceanographic Commission
ISY - International Space Year
JCOMM - Joint WMO/IOC Technical Commission for Oceanography and Marine Meteorology (JCOMM)
NOAA - National Oceanic and Atmospheric Administration
SAR - Synthetic Aperture Radar
SIG - Sea Ice Group
SIGRID - Sea Ice Grid
SSM/I - Special Sensor Microwave
TSS - Tromsø Satellite Station
WMO - World Meteorological Organization
WW - World War

Synchrotron-based X-ray micro-tomography: Insights into Sea Ice Microstructure

Sönke Maus[1], Thomas Huthwelker[2], Frieder Enzmann[3], Markus M. Miedaner[3], Marco Stampanoni[2], Federica Marone[2], Manuel A. Hutterli[4], Christoph Hintermüller[2] and Michael Kersten[3]

[1]Geophysical Institute, University of Bergen, email: sonke.maus@gfi.uib.no,[2]Paul Scherrer Institute, Villigen, Switzerland, [3]Institute of Geosciences, University Mainz, Germany, [4]British Antarctic Survey, Cambridge, UK

Abstract

To date most studies of the sea ice microstructure have been based on destructive two-dimensional thin section analysis with little information on pore connectivity, while recent three-dimensional applications of Magnetic Resonance Imaging and X-ray tomography have been resolution-limited to 50-100 microns. During the past decades X-ray micro-tomography based on synchrotron radiation (SXRT) has been accepted as a powerful non-destructive imaging technique in materials sciences. Here we report on first results of three-dimensional, micrometer-resolving imaging of sea ice by means of SXRT. We discuss the strength and limitations of this technique in terms of fundamental scales of the sea ice microstructure and the physical processes associated with them.

1 Introduction

It has long been known that sea ice contains saline brine in pores and fluid inclusions[1,2,3,4,5], while lake ice does only incorporate small amounts of salt in an almost pure ice matrix[6,7]. Sea ice thus differs from freshwater ice in its microscopic structure. The need to focus on the details of the sea ice microstructure has emerged during the past decades in a variety of disciplines. Brine mobility and inclusion sizes strongly influence the mechanical[8,9,10,11,12] and optical[9,13] properties of sea ice, with practical relevance in offshore engineering and remote sensing. They are fundamental to understand the role of sea ice as a habitat of life in polar ecology[14,15,16]. As the microstructure determines the processes of salt entrapment and release, it is also relevant when considering atmosphere-ice-ocean interactions and polar climate[17,18,19,20]. General to all fields is the need to know the distribution of pore networks and inclusions and their influence on macroscopic transport properties, let it be fluid transport, heat and salt diffusion, or the propagation of electromagnetic waves.

Brine entrapment in sea ice is the consequence of its cellular mode of freezing. Under calm conditions sea ice rapidly evolves into a cellular crystal structure of vertically oriented plates, parallel within each grain and with brine layers between them. This lamellar substructure, first described one and a half centuries ago[3,21], is most clearly defined near the ice-water interface[a]. During freezing of natural seawater the lamellar *plate spacing* is 0.2 to 1.5 mm[9,24], while horizontal grain sizes are from a few milli- to centimeters[25,26,9,27,28]. Another known feature are the vertically oriented *brine channels* with diameters 1 to 5 mm[29,30,31,32] and spacings of 1 to 7 cm[33,31,27,34]. In thicker ice 'secondary' *brine channel networks* with larger spacings of 5-20 cm have been described[35,27,36,37]. The conceptual view that has emerged

[a]It is worth a note that Quincke[22,23] gave a first detailed description of the lamellar inclusion-filled structure of saline ice, obtained by freezing solutions of salinities lower than 0.3‰ NaCl. He described the ice as 'foam-like', with many drawings and quantitative observations.

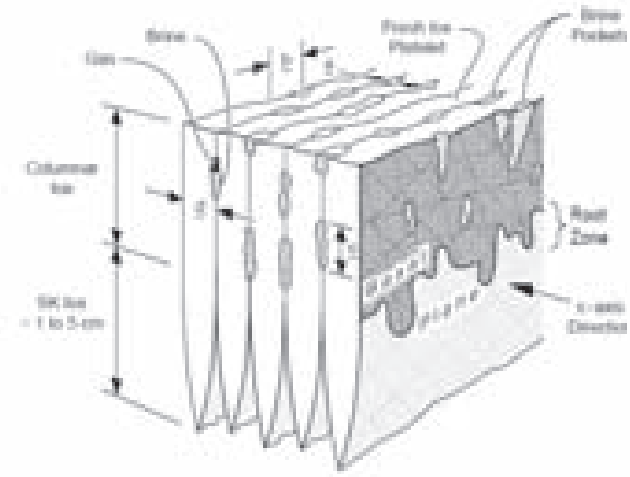

Figure 1: *Three-dimensional sketch of the bottom regime of sea ice, illustrating the separation of brine layers into inclusions, which starts at a distance of* ≈ 1 *to 5 cm from the interface. From ref.*[38].

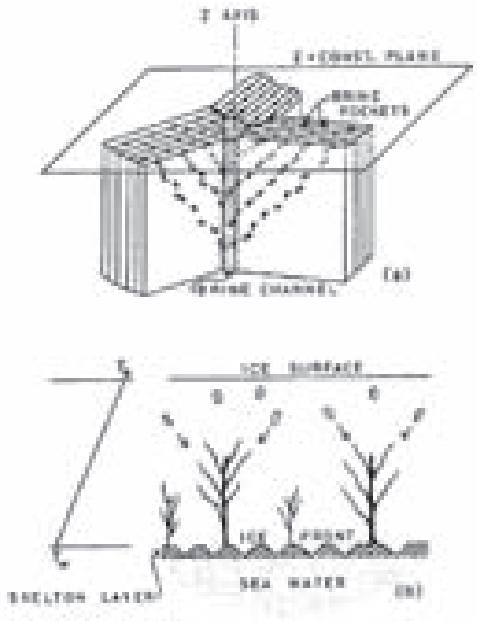

Figure 2: *Upper: drawing of a brine channel fed from the brine layers of surrounding crystals. Lower: Evolution of brine channel networks with distance from the ice-water interface. From ref.*[32].

from laboratory and field investigations is that downward flow through the wider O(1 mm) pores is fed by flow through a finer O(10^{-1}mm) pore network in the original brine layers. Figures 1 and 2 illustrate these principal features of columnar sea ice.

A concise theory of how the microstructure evolves under different growth conditions, essential to formulate fundamental models of the macroscopic physical properties, still needs to be developed. To do so observations of the co-evolution of smallest and largest pore scales during growth and decay are needed. Some fundamental questions in this respect are:

- How do *plate spacing* and crystal size vary with the freezing velocity?
- How are *plate spacing* and crystal orientation related to under-ice currents?
- When does *bridging* between the plates transform the *brine layers* to *pore networks* and what are the preferred length scales and physical mechanisms?
- How do radii and spacing of largest *brine channels* vary with freezing conditions? What is the morphology and permeability of evolving brine channels networks?
- What is the role of hydrodynamics in controling *pore radii* and their *distribution*?
- How do pore scales, shape and connectivity change with *temperature*?
- What are the fractions of *interconnected* and *disconnected pore space*?
- What is the role of *slow diffusion* and *surface energy* minimisation of brine pockets in reshaping pores and their connectivity?

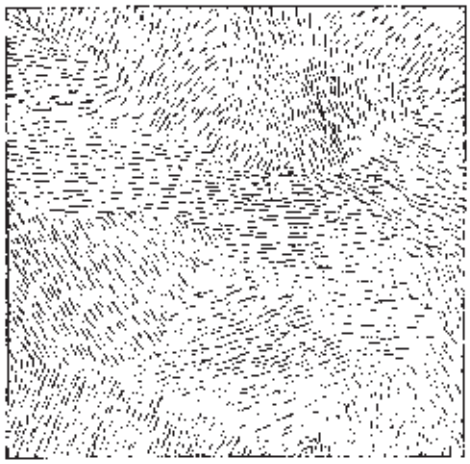

Figure 3: *Tinfoil replica from the bottom of sea ice obtained by E.v. Drygalski[5]. Most individual crystals have a size of* $\approx 2-3$ *cm with parallel ice plates spaced by* 0.5 *to* 1 *mm. Original size* 6×6 *cm.*

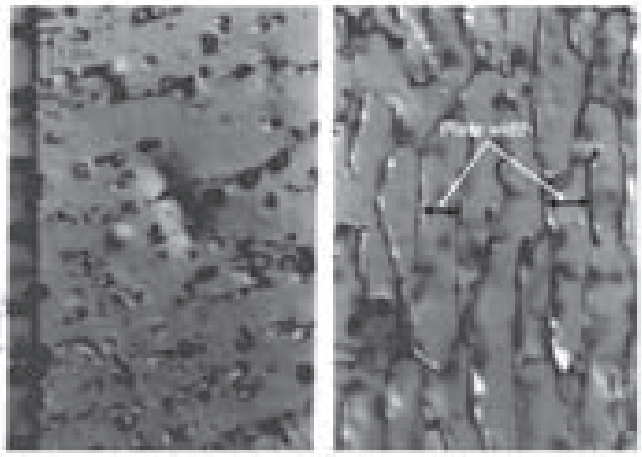

Figure 4: *Horizontal thin section micrographs of first-year ice from ref.[12]. Right: obtained in situ within several hours after sampling. Left: stored below the eutectic temperature* -23 *°C for several months, then warmed to* -10 *°C prior to imaging. Images are* $\approx 5 \times 7$ *mm.*

In the following a short account of the present knowledge of these topics on the basis of microstructural observations techniques utilised to date will be given. Then the potential to make progress on the basis of synchrotron-based X-ray microtomography (SXRT), a technique that we have recently tested on laboratory grown sea ice samples, is discussed.

2 Imaging techniques of sea ice microstructure

The microstructure and salinity of sea ice have already received some interest during the first polar expeditions. Scoresby[1] described that sea ice contains salt in form of liquid brine in the interstices of ice crystals, while Walker[3] pointed out a 'vertically striated structure' that was most apparent near the ice-water interface. The first documented image of this lamellar crystal substructure of natural sea ice is probably a tin-foil replica obtained by E. v. Drygalski more than 100 years ago (Figure 3). First photographs of vertical and horizontal sea ice sections, illustrating larger pores and brine channels, were documented by Hamberg[4], who also pointed out another important aspect of sea ice in contrast to lake ice: While the orientation in the upper centimeters of sea ice is often random, crystals with vertical c-axis are eliminated rapidly during further growth[b], and no exceptions to this rule were found since then[9].

Our present knowledge of the sea ice microstructure is still mainly based on the analysis of two-dimensional thin sections similar to Figure 3 from Drygalski. It is therefore useful to first recall the main procedure and shortcomings of this technique.

[b]For primary sea ice, which contains considerable amounts of brine between the basal plane plates, the anisotropic effective conductivity, parallel heat conduction in a laminate of different conductivities exceeding serial heat conduction, is the most likely mechanism of geometric selection[39,40]. For lake ice the selection mechanism of crystal orientation is still a matter of debate[41,42,43,6,44].

Two-dimensional thin section analysis

Columnar sea ice, to be considered here as the dominant Arctic ice type, is structurally highly anisotropic, and the preparation of horizontal thin sections, similar to Figure 3, is most effective in extracting geometrical information. The standard approach of thin section analysis begins with cutting slices from a vertical ice core, which are then reduced in thickness with help of a microtome[45,9,46,47,48]. If thin enough slices are prepared this approach allows to obtain micrographs wherein brine inclusions of 0.01 mm or even smaller in size are distinguishable[45,49]. As an example Figure 4 from ref.[12] shows the fine structure of brine inclusions within a single crystal. However, analysing and interpreting such images has been limited by two aspects. In the most extensive statistical descriptions to date the digitized pixel size was 0.03 mm, limiting the resolvable inclusions to approximately two times this scale[50,46]. Such a resolution limit is no longer a problem with present day computing and image processing capabilities. However, with regard to future application of thin section analysis, another problem remains and adds to the lack in three-dimensional information. The sample preparation process is elaborative and susceptible to a reaction of brine inclusions to the procedure[51]. To date it has not been studied to what degree the destructive sectioning process effects the details of the inclusion structure.

Sampling and storage

A general problem of all imaging techniques, which adds to the destructive sectioning process of thin sections, is related to sampling and storage. Sea ice is a reactive medium which rapidly changes its morphology when removed from 'in situ' conditions. This makes the interpretation of micro-structural observations often problematic. A frequently applied procedure is 1. sampling, 2. cooling, 3. storage, 4. warming, 5. analysis[46,49]. This implies (i) thermal hysteresis due to the freezing and remelting of pores and (ii) metamorphosis by slow diffusion processes during storage. Although the relative role of these processes has not been investigated yet, it has become clear that their joint effect fundamentally changes the pore structure, even after storage below the eutectic temperature. An example is shown in Figure 4 from ref.[12], comparing a thin section image obtained *in situ* within several hours after sampling with one of the same ice after several months of storage below the eutectic temperature -23℃. Being an extreme example, because cooling below the eutectic point is expected to change the inclusion structure by salt precipitation, it indicates the difficulties to obtain information about the *in situ* microstructure from stored and thermally modified samples. The problem may be overcome to some degree by rapid analysis in the field, shortly after sampling[47,12], or by centrifugation of a sample before storage, removing the brine and making the sample less reactive[52,48]. As discussed below, the latter method is of interest in connection with synchrotron-based X-ray microtomography.

Three-dimensional imaging techniques

Besides its destructive nature, another drawback of thin sectioning is its lack in three-dimensional information. Early applications of three-dimensional non-destructive imaging have utilised two techniques, X-ray computed microtomography (XRT)[53] and Nuclear magnetic resonance imaging (NMR)[54], yet were resolution-limited to millimeter-sized pores. An order of magnitude better resolution has been recently obtained with NMR to provide statistics of brine inclusions on the basis of 0.09 mm pixel size[48]. The latter is still a clear

limitation at low temperatures, when inclusion sizes are small. For example, in ref.[48] a 50 % difference in imaging and phase-relation derived brine porosities was found at low temperatures, and interpreted in terms of this resolution limit. A similar conclusion was drawn in ref.[46] due to an increasing number of inclusions during warming. In a later NMR study[55] even larger discrepancies were found, with under- and overestimates of brine volumes for columnar and fine-grained granular ice, respectively. Serial thin-sectioning has been used to validate NMR imaging results[48], indicating reasonable agreement of average pore size and porosity when the latter is relatively high (≈ 0.2). However, much higher pore size standard variations, for thin section images compared to NMR, indicate the loss of details by this method and pixel sizes limited to 0.09 mm.

XRT with increased resolution (voxel size $20-40$ μm) has been applied to derive porosity and pore sizes of polar firn[56] and snow[57,58], where the most important scales are of millimeter size and clearly above this resolution limit. Recently, XRT imaging of ice grown from NaCl solutions in the laboratory has been reported[59]. In the latter study the voxel size of 40μm was a slight improvement on most earlier two- and three-dimensional studies with resolutions $\approx$ 50 to 100 μm[46,47,48]. As shown by a recent high resolution optical study[49] and our preliminary observations this is still insufficient to characterise pores and pattern evolving from original brine layers. Many air-filled pores in Figure 5, corresponding to centrifuged brine, have diameters less than 50 μm. Thus, a voxel size of 5 to 10 μm appears necessary to resolve them and properly image pore networks in sea ice. For salt crystal identification even a voxel size of 1 micron seems necessary[49].

Synchrotron-based X-ray tomography

During the past decades, tomography based on highly brilliant and coherent X-ray synchrotron radiation has been accepted as a powerful imaging technique in materials sciences[60,61]. Very recently, synchrotron-based X-ray micro-tomography (SXRT) was used to image hailstones and partially frozen multiphase systems with similar salt content as natural sea ice[62,63]. The technique allows three-dimensional imaging of centimeter-sized samples with micrometer resolution. While portable XRT scanners are often operated in a cold room[56], in the latter studies a special setup has been developed to cool the samples during imaging and keep them at 240 K or lower temperatures[62,63]. We have recently applied SXRT with this setup to obtain, for the first time, three-dimensional images of laboratory-grown seawater ice at the TOMCAT-beamline of the Swiss Light Source[c]. Results of this study will be presented elsewhere[?] . Here we shall, on the basis of a few images, discuss the potential of this method to characterise essential features and evolution processes of the microstructure of sea ice.

SXRT is based on absorption and allows, for sea ice, a clear discrimination of air, ice, and solid salts. We have used two sampling/storage protocols that take advantage of these absorbtion contrasts. The first applied procedure was (i) rapid centrifugation of a sample at the local *in situ* temperature, (ii) storage and transport in a low temperature freezer or dewar and (iii) imaging at subeutectic temperature.[d]. The strength of this approach is

[c]The present capabilities at the TOMCAT-beamline of Swiss Light Source (SLS, Paul Scherrer Institute, Villigen, Switzerland) allow field-of views ranging from 0.75×0.75 to 11.45×11.45 mm^2 with a theoretical resolution of 0.35μm and 5.6μm, respectively.

[d]The imaged samples had $\approx 1-1.5$ cm diameter and height, and were prepared manually on dry ice from centrifuged larger slices of both 3 cm thickness and diameter.

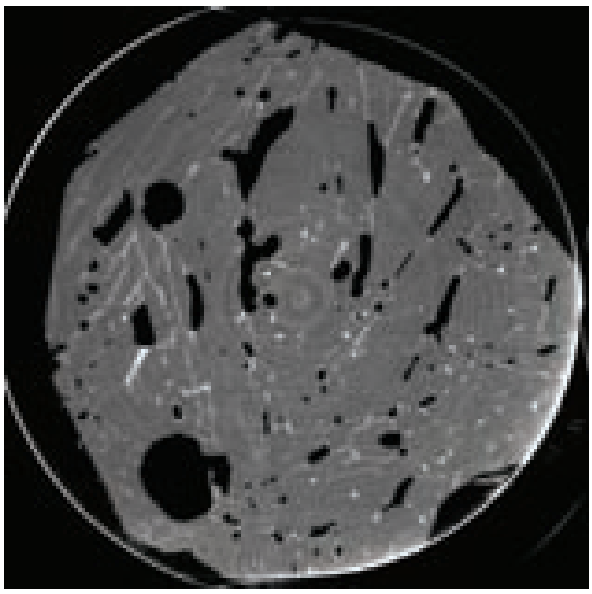

Figure 5: *Horizontal slice of a centrifuged laboratory-grown sea ice sample obtained by by SXRT at* $\approx -30℃$*. The image is* ≈ 12 *mm on a side, obtained with a voxel size of 5.6* μm *binned two times. Air (pores emptied by centrifugation) appears as dark, ice as grey and salt crystals (corresponding to entrapped brine) as white. Note that the whole sample comprises 300 slices all spaced in the vertical by 5.6* $\times 2$ μm*.*

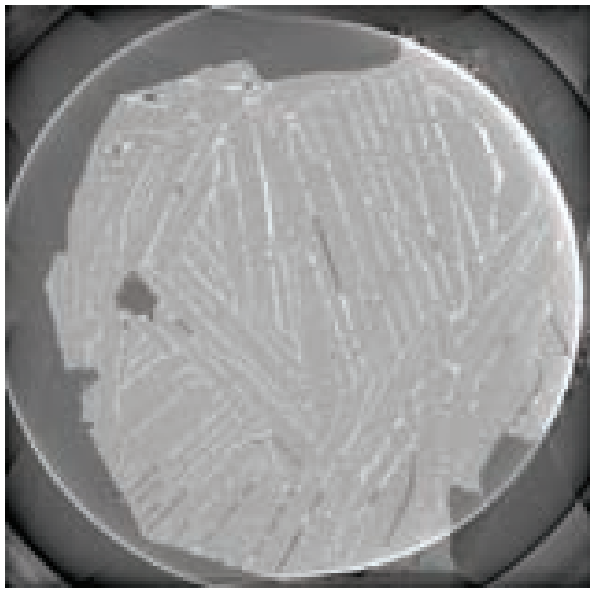

Figure 6: *Horizontal slice of laboratory-grown sea ice, rapidly cooled below* $\approx -50℃$ *after sampling, obtained by SXRT at* $\approx -30℃$*. The image is* ≈ 12 *mm on a side, with 5.6* μm *voxel size binned two times. Ice appears as grey, air as dark, salt crystals as white. As the image was not centrifuged most air indicates 'lost brine'. Also here the vertical spacing of slices is 5.6* $\times 2$ μm*.*

that it yields information about the pore connectivity that ice has in situ, and allows to distinguish between the connected and disconnected pores. Figure 5 shows a horizontal slice of an SXRT image obtained with original voxel size 5.6 μm, binned two times. The centrifuged pores appear dark (as air), the trapped inclusions (salt) as light, and the ice as grey. The vertical distance of slices as in figure 5 is also 5.6 $\times 2$ μm, sufficient to resolve the network connectivity of the finest pores (see Figure 9 below).[e] The sample in Figure 5 stems $\approx$ 3 cm from the surface of 11 cm thick ice and several wide brine channels have already formed. The method and resolution preserves the main network characteristics relevant for evaluation of its transport properties. In the second sampling protocol the sample was not centrifuged, but a 3 cm thick slice from an ice core of 10 cm diameter was immediately put into a -80 ℃ freezer. The sample shown in Figure 6 thus does not resemble the true pore morphology of sea ice. It does, however, well illustrate the lamellar crystal substructure and distribution of plate spacings. The brine layers contain air bubbles that are likely related to contraction upon transition of brine to solid salts. Some larger air pores are eventually related to loss of brine during sampling, as the shown sample comes from a high mobility level, $\approx$ 3 cm near the ice-water interface. The $\approx$ 1 mm wide air pore, visible at a crystal junction near the left edge of the image, is very probably attributable to such brine loss.

[e] In the present setup images were limited to $\approx$ 4 mm vertically, yet longer samples can be imaged by stacking.

3 Pore scales and related physical processes

The evolution of microstructural pattern in growing sea ice may be roughly classified into three principal regimes. The first regime (I) comprises morphological instabilities that evolve due to an interplay of heat and solute diffusion, the most prominent pattern being the plate spacing to which a cellular freezing interface adjusts. Here the primary lamellar skeleton of young sea ice is determined. The second regime (II), proceeding upward from the freezing interface toward lower temperatures, is characterised by a strong decrease in the brine porosity. This decrease is not only controlled by cooling and fractional freezing but also by desalination due to convective motion. The latter is associated with the formation of channelised fluid paths found in many materials and environments[64,65,66]. This transition from a laminate to a network of pores is a particular important aspect for the sea ice medium. The third regime (III) is reached when desalination becomes small and porosity changes are due to cooling and diffusion only. Some important questions in regime (III) are how inclusion shapes change during freezing, if and how pore networks disconnect, what happens during pressure buildup in disconnected pores, and to what degree slow surface energy minimisation may take place. In the following the potential role of SXRT to improve our understanding of these regimes is discussed by considering them in increasing order.

Plate spacing, crystal size and orientation

Recent work indicates that the plate spacing of sea ice can be reasonably predicted by a macroscopic variant of the Mullins-Sekerka[67] morphological stability theory[68,24,69]. The approach has been mainly validated by plate spacing observations based on thin section analysis, and at first glance it does not appear necessary to apply SXRT to obtain this O(1 mm) structural scale. However, Figure 6, obtained from a sample close to the freezing interface, shows many details of these pattern at junctions and crystal boundaries. These can be of interest in the study of the plate spacings dependence on growth conditions. The increase in plate spacing with decreasing growth velocity must, for example, be accompanied by overgrowth of plates, while accelerated growth would lead to splitting. Figure 6 indicates that SXRT will be useful to study the details of these transitions. A related problem is the frequently observed crystal c-axis alignment with ocean currents[70,71,72,73]. Three-dimensional near-bottom microstructure resolution by SXRT can essentially improve our understanding of the morphological adjustment to periodic changes in the under-ice flow[74,75] and the response to extreme currents, e. g., ref.[48].

Plate spacing observations in older ice may, *vice versa*, provide indirect information about its growth velocity[76,24]. However, due to the mentioned morphological transition to networks, plate spacings are in general less clearly defined in aged ice and far from the freezing interface, e.g., ref.[76,46] or Figure 4 above, where the plate spacing may only be identified by trains of pores. A comparison of plate spacings measured by thin section analysis rapidly in the field with measurements after storage[77] shows that metamorphosis of brine layers makes such observations uncertain. Here SXRT of samples stored at low temperatures can be a useful technique to improve the accuracy. The required resolution can be estimated by considering a 100 μm brine layer of salinity 50-100 ‰ that is cooled below its eutectic point. Conversion to solid salt will shrink it by a factor of ten to twenty. Figure 5 was obtained with a voxel size of 5.6 μm, binned two times, thus being at the upper limit to capture these features. As seen in Figure 5, a horizontal image $\approx$ 8 cm from the

bottom of 11 cm thick ice, the salt crystal signal in the original brine layers becomes weak, but plate spacings can still be identified.

To quantify grain sizes which generally are of order O(1 cm) in sea ice[26,25,27,28] SXRT is of course not useful. However, the morphology at grain boundaries and junctions can be studied in some detail. The field of view in our setup has been sufficient to include a few of these features in a typical SXRT image. By resolving the lamellar plate spacing pattern, also crystal orientations are easily identified from the tomographic images.

Transition of brine layers

The transition of brine layers near the bottom of sea ice has been described qualitatively as a two-stage process[78]. A transition to sheet-like pattern starts at a distance of 2 to 4 cm from the ice-water interface, while a subsequent separation into elongated pores appears to take place at a $\approx$ 10 cm distance. While the former scale is consistent with observations of the low-strength skeletal layer[68,69], quantitative observations of the second morphological change within the brine layers are almost completely lacking. Some observations of 'pinch-off' of brine pockets indicate its onset when brine layers have to shrink to a width of $\approx 0.05 - 0.1$ mm[79,31]. A value of 0.07 mm has been noted as the 'minimum layer width before splitting of brine layers'[80] and may eventually be interpreted as a lower bound. However, direct observations and detailed statistics of pore changes near the interface are not available yet, and here high-resolution SXRT has a large potential.

A concise theoretical explanation for the bridging is still outstanding. The minimisation of surface energy, as frequently suggested[81,80,82,83], is unlikely to be relevant in the bottom regime of strong cooling and convective transport of heat and solute. It may also principally be rejected because the brine layers are minimum energy surfaces[68]. An theoretical study of the droplet 'pinch-off' from a pore[84] indicates that the problem is similar to Rayleigh's instability of an inviscid liquid jet[85], the formal difference being that the transport in the pore is not dynamical yet diffusive. For alloys the predicted pinch-off wave length of $\pi/0.697 = 4.508$ times the diameter agreed reasonably with experiments[86] and numerical simulations[87]. The pinch-off was found to be triggered by fluctuations in the growth velocity. This behaviour is qualitatively similar to what Harrison[79] has described as 'solute transpiration pores' in ice, which started to break up into droplets when the motion of the temperature gradient was halted, creating thermodynamic disequilibrium. For growing sea ice these ideas likely need to be modified and extended due to the presence of convection. A plausible mechanism is that density fingering in the brine layers leads, in connection with upward flow of less saline seawater, to pattern of supercooling with preferred freezing[68]. Once the resistance is locally increased by thinning, the flow will slow down and subsequent lateral freezing enhances the heterogeneity, finally leading to bridging and a pore network.

Lacking a concise theoretical concept the width of brine layers at the onset of bridging has been estimated in two ways[68]. First, thin section pore size statistics of ice samples not two far from the interface[46,47] have been extrapolated to porosities typical at the top of the skeletal layer. To do so a relation between inclusion sizes and brine porosity based on warming of the prepared thin sections, see below, has been applied. A second estimate has been based on interpretation of a change in the strength-porosity relationship at the top of the lamellar bottom skeletal layer[68]. Both estimates are indirect and crude, yet indicate a most plausible value of $0.08 < d_{sk} < 0.12$ mm for the width d_{sk} of brine layers at the onset of bridging.

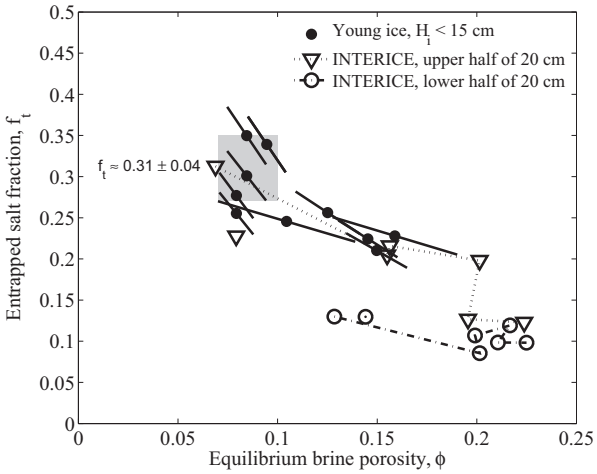

Figure 7: *Fraction of salinity that could not be removed by centrifugation at in situ temperatures, interpreted as the disconnected pore fraction f_t. Solid circles: thin ice grown from seawater in the laboratory. The errorbars indicate the uncertainty in the porosity due to bulk ice temperature and salinity observations. Triangles: Warming sequence of upper half of 20 cm thick ice grown in a large tank[89]. Note the lower disconnected pore fractions in the lower half (open circles), consistent with an incomplete metamorphosis of brine layers. During warming the fraction f_t stays rather constant (upper half), until a value of $\phi \approx 0.2$ is reached. Porosities are based on bulk salinity and temperature assuming thermodynamic equilibrium.*

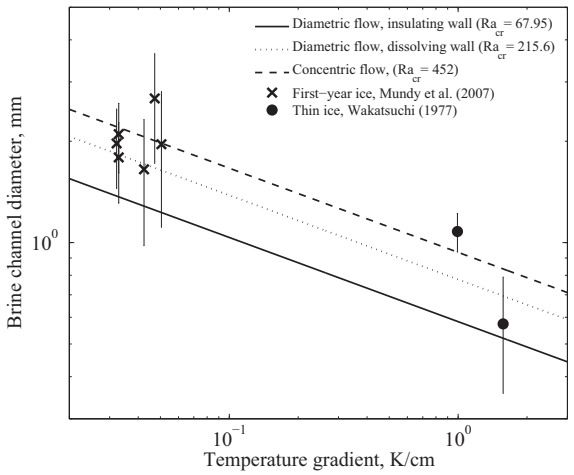

Figure 8: *Quasi in situ determinations of brine channel diameters at the bottom of sea ice. Crosses: photographic under-ice observations from ref.[90], temperature gradients being based on the observed average ice thickness and reported ice surface temperatures, assuming a linear temperature gradient and the ice bottom at the freezing point of ≈ -1.8℃. Circles: optical observations of the widths of streamers emerging from the bottom of rapidly growing thin laboratory seawater ice[33]. The temperature gradient in the latter high salinity young ice was reduced by 0.8 with respect to freshwater ice growing at the same velocity, consistent with parallel observations[91] and theoretical expectations[68]. The lines are theoretical critical Rayleigh numbers for convective onset, e.g.,[92].*

The accurate determination of the bridging transition is important to solve the salt entrapment problem in sea ice in general, with implications for the vertical extent of the high-mobility and low-strength skeletal layer and relevance for problems of sea ice geophysics and ecology. A simplistic model that treats bridging as a two-dimensional percolation process appears to perform well in predicting salt entrapment[68,69]. To date only a few images of the morphology of bridging have been obtained by thin-sectioning in the plane of former brine layers[47,12,88]. Being rather tedious, this approach likely involves destruction of brine layers and bias by phase changes. Non-destructive SXRT of centrifuged samples from the bottom regime of sea ice may be very effective to resolve the bridging pattern of brine layers with micrometer resolution, to be interpreted in terms of the hydro- and thermodynamics that drive their formation.

Disconnected pore fraction

The bridging process implies the formation of disconnected pores within the brine layers. If several samples of the same ice are available this fraction f_t may be computed from $f_t = S_c/S_i \times (S_i - S_c)/(S_b - S_i)$, where S_i is the bulk salinity of the original ice sample, S_c the residual of a second sample after centrifugation at in situ temperature, and S_b the salinity of the brine obtained by centrifugation. The underlying assumption is that the brine salinities in the connected and disconnected pore space are the same. Alternatively S_i can be computed from the mass and salinity of the centrifuged brine and ice samples[52]. In Figure 7 the disconnected salt fractions of growing young ice are compared to estimates based on salinity observations of warming young ice grown under similar conditions[89]. At lowest porosities the entrapped pore fraction appears to saturate at a value of $0.3 < f_t < 0.4$, an upper bound supported by field observations[52,93]. However, the results in Figure 7 do not extend to low porosities, and the present values of ϕ are indirect calculations based on thermodynamic equilibrium. As the latter tends to overestimate the brine salinity and underestimate the porosity[94,95], the data in Figure 7 need to be interpreted with caution. The true porosities for the young ice in Figure 7 (solid circles) are not below $\phi \approx 0.1$[93]. It is noted that a considerably smaller 'fractional connectivity', comparable to the present $(1 - f_t)$, has been recently reported for laboratory grown NaCl-ice on the basis of XRT imaging[59]. The latter authors report a connectivity that decreases sharply below $\phi \approx 0.1$ and ceases near $\phi \approx 0.03$. However, their results are based on unidirectional connectivity within 1 cm samples, determined by warming a cut sample (not *in situ*), and limited by 40 μm voxel size.

An interesting aspect in Figure 7 is that f_t appears to stay rather constant during warming sequences. Such a saturation value is comparable to the ratio of salinities of thick multy-year to first-year ice, indicating that the fraction of entrapped pores is controlled by the early evolution and bridging process (open triangles and circles). The knowledge of the entrapped pore morphology is also important to understand ion fractionation and its evident dependence on ice type, growth conditions and temperature history[96,97,98,99]. The many pores with diameters of 50 μm in Figure 5 thus indicate that a proper imaging of the process of solute entrapment requires imaging with micrometer resolution. SXRT distinction of air, ice and solid salt in centrifuged samples is a promising technique for doing so properly, while recent XRT work[59] is likely resolution-limited.

Brine channels

In early studies wide 'brine channels', with 1-5 mm diameters, were tentatively associated with the desalination of *warming* sea ice[4,100]. Their existence in *cooling* sea ice during the growth phase was first described in ref.[35,101]. Lake and Lewis[29] then outlined, mainly on the basis of temperature fluctuations, the basic mechanism of salt release from sea ice: downward convective motion of brine-rich streamers is balanced by upward moving waters around them. Experiments in thin growth cells have confirmed this view[30,31] and raised the interest in their quantitative description. For very thin ice maximum channel diameters of $1-3$ mm have been found[30,31,27,48], with a $1-7$ cm spacing of major channels that decreased with freezing rate[33,31,102,32,27,37,103]. In 1 to 2 m thick ice, by the end of the growth season, a category of wider $5-10$ mm channels spaced by $\approx 10-20$ cm has been reported[35,29,104]. These widest pores only account for a small fraction of the overall porosity, compared to their radial feeders of 2-3 cm extension[27,29] and diameters in the range $2-8$ mm[29].

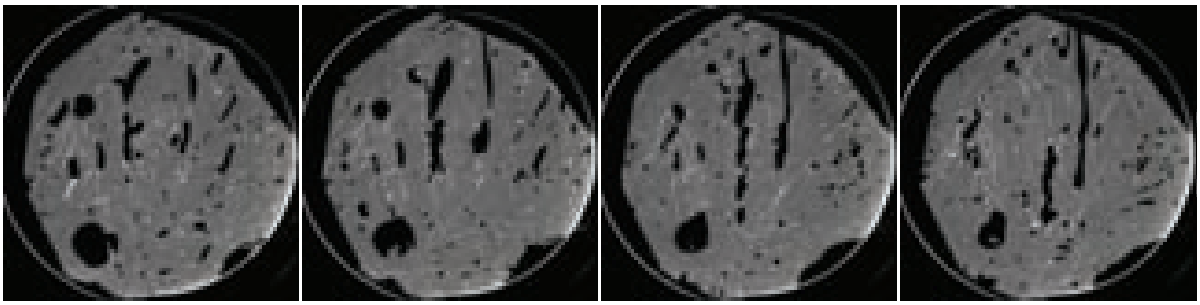

Figure 9: *Horizontal images of a centrifuged young ice sample obtained by SXRT at* $\approx -30\,℃$. *Voxel size is* 2×5.6 μm, *images are* ≈ 12 *mm on a side, and spaced vertically by* 220 μm. *Air (pores emptied by centrifugation) appears as dark, ice as grey and salt crystals (corresponding to entrapped brine) as white.*

What limits the width of the largest pores? Lake and Lewis[29] considered a hydrodynamic stability bound, evaluating the condition for the onset of convection in a vertical tube

$$\frac{D_{cr}}{2} \geq \left(\frac{Ra_{cr} \kappa_s \mu}{g d\rho/dz} \right)^{1/4}, \tag{1}$$

where μ and κ_s are dynamic viscosity and solute diffusivity of the brine. The density gradient $d\rho/dz$ is computed under the assumption, also here, that the density-controlling brine salinity is in thermodynamic equilibrium with temperature. The minimum diameter D_{cr} for convective onset is then given by the critical Rayleigh number $Ra_{cr} = 67.95$, corresponding to the most dangerous mode of diametric flow in an infinite cylinder with insulating boundaries, e.g.[92]. It depends slightly on temperature, yet is mainly controlled by the temperature gradient. At -3 ℃ and dT/dz between 0.05 to 1 K/cm, the range of growth conditions of most natural sea ice, one expects diameters of $1.2 > D > 0.6$ mm for the onset of convection. In Figure 8 under-ice observations of channel widths and outflowing streamers are compared for two studies[33,90], indicating that the channels operate at larger Rayleigh Numbers. Observations appear more consistent with either a conducting boundary condition for diametric flow (corresponding to a dissolving wall), or with a coaxial flow mode (boundary conditions not being relevant), for which Ra_{cr} takes larger values of 215.6 and 452, respectively[92]. On the one hand, Figure 8 appears to be a promising predictor for the width of brine channels by marginal convective stability. On the other hand, it is unclear why it should not occur at the most dangerous mode of diametric flow.

Taking into account the observed channel width aspect ratios of 1.3 to 1.5[90] may only explain part of the apparent discrepancy[92]. However, the standard deviation in the latter study apparently can do so, which would be consistent with channel throats controlling the convection. Looking at the complex shape of the widest pores in Figure 5, and their vertical variability on length scales of a millimeter indicated in Figure 9, shows a complex structure. To validate if, and in which mode brine channels operate at marginal hydrodynamic stability, their morphology needs to be resolved properly. For the longterm evolution of brine channels, and aspects like the onset of desalination in the spring season, the connectivity to the ambient fine-scale pore network is likely to play a role, again requiring micrometer resolution. The above mentioned reports of rather wide channels with diameters of 5-10 mm were

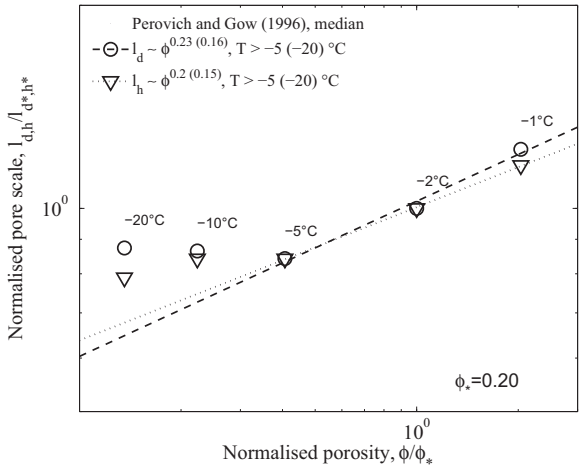

Figure 10: *Normalized minor (l_d) and major (l_h) axis length of pores in a horizontal thin section warmed in the laboratory[46]. l_d was computed by dividing the median cross-sectional area by the major axis. The data are normalised by the values at -2℃, and power law fits are given for the warmer > -5℃ subset and the whole temperature range (in brackets). Porosities are based on thermodynamic equilibrium.*

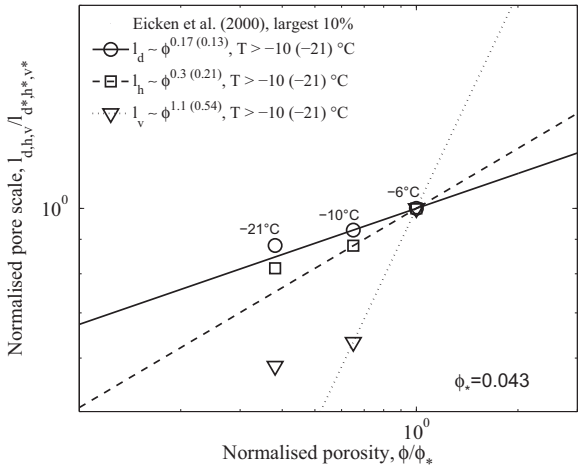

Figure 11: *Normalized minor (l_d) and major (l_h) axis length in a horizontal, and major axis length (l_v) in a Nuclear Magnetic Resonance image slice (thickness 0.4 mm), warmed in the laboratory[48]. The data are normalised by the values at -6℃, and power law fits are given for the warmer subset and the whole temperature range (in brackets). Porosities are based on thermodynamic equilibrium.*

based on relatively crude optical observations of two-dimensional cross-sections, while more detailed thin section analysis indicate that pore diameters larger than 5 mm are seldom observed[102,31,105,37,48,90]. The detailed morphology of wider channels also remains unclear.

Temperature dependence

The basic effect of cooling or warming sea ice is to change its brine porosity by additional freezing or melting until the interstitial brine reaches thermodynamic equilibrium. However, porosity changes are, as mentioned above, not only associated with local temperature changes. Upward movement of less saline brine does, after rapid thermal equilibration, also imply freezing. The relation between porosity and temperature will thus be different for bottom regimes influenced by convection and for ice levels where fluid movement has almost ceased. As localised convection may create larger thermodynamic disequilibrium than uniform unidirectional freezing, it may be susceptible to thermodynamic instabilities and create different length scales. In other words: The shape of a pore may change in a different way than during slow equilibrium freezing and its change may be irreversible. Another hysteresis effect is inherently given by the expansion of brine upon freezing, leading to expulsion of fluid. During warming this process can neither be reversed, as the seawater at the interface is in most cases less saline than the effectively expelled brine.

These complications in the temperature-porosity relationship in real sea ice make interpretations of cooling-warming scenarios of laboratory samples, susceptible to metamorphosis during storage, even more difficult. In contrast to redistribution in the field[68], expelled brine is always lost from laboratory samples[106]. Moreover may the mode of cooling/warming be

different from field conditions, and the irreversible convection through the boundaries may have other consequences for the internal redistribution of brine and the change in pore shapes and connectivity. In general are these processes, and thermal hysteresis during transport and storage, a serious problem in the preparation process of samples from naturally grown sea ice, recall Figure 4. As an example, a recent high-resolution optical study of the temperature-dependence of pore shapes and sizes[49] is mentioned. The authors analysed first-year ice from a field program for which the microstructure was also investigated on broader scales and growth conditions well reported[28,47]. The investigated samples came from the depth levels 60 to 80 cm in 1.7 m thick ice, and were obtained by the end of the winter at an in situ temperature of ≈ -5 ℃. At that time the ice was already in a stage of warming, originally having been cooled to ≈ -12 ℃ in mid-winter at the levels in question. Micrographs of this ice were taken at a temperature of -15 ℃, but only after storage at -20 ℃ for 3 years. Hence, in addition to the thermal cycling, slow diffusion and surface-energy minimisation mechanisms can be expected to have been active, and it is uncertain to what degree the results longer reflect the microstructure of sea ice *in situ*.

These limitations should be kept in mind when considering the few studies of the temperature dependence of pore dimensions, all based on imperfect storage procedures and warming of samples in the laboratory[50,46,48,55]. Some principal results of two studies[46,48] are summarised in Figures 10 and 11. To do so the reported porosity-dependence of inclusion lengths scales has been evaluated in the form

$$l_d \sim \phi^{e_d}, \qquad l_h \sim \phi^{e_h}, \qquad l_v \sim \phi^{e_v}, \tag{2}$$

where l_d and l_h are the minor and major axis lengths in a horizontal cross section (corresponding often to the directions normal and parallel to the original brine layers) and l_v the vertical axis length. A similar exponent e_n may be used to describe the number n of pores. If inclusions do not split or merge and n is constant, the constraint $e_d + e_h + e_v = 1$ is expected. One has, for example $(e_d = 1, e_h = e_v = 0)$ for a laterally shrinking vertical brine layer, and $(e_d = e_h = 1/2, e_v = 0)$ for a vertical circular cylinder that changes only its diameter. For the two studies the resolution and typical horizontal length scales were 0.03 and $0.05 - 0.3$ mm in ref.[46], Figure 10, while they were 0.09 and $0.2 - 1$ mm in ref.[48], Figure 11. Also porosities were very different. Exponents e_d and e_h were however similar, at higher temperatures in the range $0.17 - 0.30$. The dependence is weaker when including data at lower temperatures included (given in brackets in the figures), which in both studies has been associated with the resolution limits, leaving the smallest pores undetected. The vertical pore length, investigated in ref.[48], shows a much stronger porosity-dependence. If also the observed number exponents for vertical pores ($e_n = -0.13(-0.27)$, not shown) are considered, one obtains $e_d + e_h + e_v + e_n \approx 1.44(0.61)$[f]. This indicates not only undetected pores at low temperatures ($0.61 < 1$), but also a discrepancy at higher temperatures ($1.44 > 1$). A likely explanation is that vertical thin sectioning of sea ice (and the finite NMR slice thickness of 0.4 mm in the study) does not retrieve the vertical pore lengths, but rather the inclination of the pores. This again points to the need of three-dimensional observations, in addition to the necessary increase in resolution.

Conclusions and quantitative results from an earlier study of horizontal sections[50] are similar. To evaluate how realistic porosity changes in natural sea ice may be resembled by

[f]The value in brackets includes also observations at lowest temperatures, when resolution limits were reached

warming/cooling of laboratory samples requires more statistical descriptions of that kind. While direct observations of three-dimensional pore connectivity changes with temperature may, at highly improved resolution, be obtained by SXRT on centrifuged field samples, the intrinsic behaviour of disconnected inclusions shapes is more difficult to find out. During storage in the liquid phase these will likely approach shapes that relate to the high anisotropy of the ice-water interfacial energy[107,108], whereas in the field, under a temperature gradient and permanent thermal cycling, they may not do so. Here sophisticated sampling, storage and imaging procedures could become necessary. An empirical description of the shrinking, merging and splitting behaviour of pores in a form like equation (2) would be useful for proper optical modelling of sea ice[109] and could be used for conceptual parameterisations of its transport properties by network models[105,110,111].

It is further important to develop a better understanding of the physical processes that lead to merging and splitting itself. In addition to pore shapes, hysteresis has also been observed for the phase transition process, very small inclusions apparently becoming supercooled until they change phase spontaneously[112,113]. The formation mechanism of smallest inclusions reported in sea ice[47,49] and pressure-related figures due to the expansion of trapped brine pockets[114,35,78,88] is presently not understood. It might be more probable during rapid cooling of a sampled core than it is under slowly changing natural conditions. However, the occurence in bands near the bottom[35,88] indicates a formation that relates to hydrodynamic interactions with the seawater. A related question is when pores split into spheres. In some figures of ref.[49] strings of very small inclusions with sizes ≈ 0.02 to 0.03 mm are seen, while below a length scale of 0.03 to 0.04 mm the inclusion aspect ratio in their sample approaches unity. Similar scales appear in a study of artificial pores[79]. That micrographs from ref.[49] during a cooling sequence do not manifest a splitting behaviour of the thinnest (≈ 0.03 to 0.04 mm) elongated inclusions, also indicates the role of surface energy as a driving source. Micrometer-resolving SXRT can shed new light on the latter problems.

4 Summary

Sea ice is a reactive porous medium with a pore structure that is to first order lamellar near the freezing interface, but becomes increasingly complex during further cooling, with distance from the interface. This happens by an interaction of hydrodynamic and thermodynamic instabilities with vertically directed diffusive and convective exchange of heat and salt with seawater, on which sea ice floats. Due to a change in temperature gradients, boundary conditions and thermal hysteresis upon freezing/melting it is not easy to find sampling and storage procedures that preserve its microstructure characteristics. One always has to find a trade-off between resolution, effort and the physical process one wants to observe. We have summarised the most relevant length-scales and mechanisms during the microstructure evolution like (i) plate spacing selection and crystal orientation, (ii) bridging of plates and pore network formation, (iii) fractionation of connected and disconnected pore space, (iv) brine channel morphology and convective stability and (v) temperature and porosity-dependence of pore scales, and argued for the need of three-dimensional observations with micrometer resolution, not available to date. Preliminary results of imaging laboratory-grown samples by synchrotron-based X-ray microtomography (SXRT) indicate that, in connection with proper sampling and storage, SXRT has a large potential to make such observations, and advance models of the sea ice microstructure and its macroscopic behaviour.

References

[1] W. Scoresby, *Mem. Wernerian Society*, 1815, **2**, 328.
[2] G. F. Parrot, *Ann. d. Physik*, 1818, **57**, 144.
[3] D. Walker, *Proc. Royal Soc. London*, 1859, **9**, 609.
[4] A. Hamberg, *Svenska Vetenskapsakadamien, Bihang til Handlinger*, 1895, **21**, 1.
[5] E. Drygalski, *Grönlands* E*is und sein* V*orland*, vol. 1 of *Grönland*-E*xpedition der Gesellschaft für Erdkunde zu Berlin 1891-1893*, Berlin, Kühl, 1897, 555 pp.
[6] P. Hobbs, *Ice Physics*, Clarendon Press, Oxford, 1974, 837 pp.
[7] V. F. Petrenko and R. W. Whitworth, *Physics of Ice*, Oxford University Press, 1999, 373 pp.
[8] B. Michel, *Ice Mechanics*, Les Presses De L'Université Laval, Québec, 1978, 499 pp.
[9] W. F. Weeks and S. F. Ackley, in *The Geophysics of Sea Ice*, vol. 146 of *NATO ASI Series*, Plenum Press, pp. 9–164, ed. by N. Untersteiner.
[10] T. J. O. Sanderson, *Ice Mechanics - Risks to Offshore Structures*, Graham & Trotman, 1988, 253 pp.
[11] E. M. Schulson, *Eng. fracture mech.*, 2001, **68**, 1839.
[12] D. M. Cole, *Eng. fracture mech.*, 2001, **68**, 1797.
[13] F. D. Carsey, *Microwave Remote Sensing of Sea Ice*, vol. 68 of *Geophysical Monograph*, American Geophysical Union, Washington, 1992.
[14] R. A. Horner, *Sea ice biota*, CRC Press, 1985.
[15] I. A. Melnikov, *The* A*rctic* S*ea* I*ce* E*cosystem*, Gordon and Breach, 1997, 204 pp.
[16] D. Thomas and G. S. Dieckmann, *Sea Ice: An Introduction to its Physics, Chemistry, Biology and Geology*, Blackwell, 2003, 402 pp.
[17] Y. P. Doronin and D. E. Kheisin, *Morskoi Led (Sea Ice)*, Gidrometeoizdat, Leningrad, 1975, english translation 1977 by Amerind Publishing, New Delhi, 318 pp.
[18] N. Untersteiner, *The Geophysics of Sea Ice*, vol. 146 of *NATO ASI Series, B: Physics*, Plenum Press, New York, 1986, 1196 pp.
[19] P. Wadhams, *Ice in the Ocean*, CRC Press, 2001, 351 pp.
[20] M. Leppäranta, *The Drift of Sea Ice*, Springer Praxis Books Geophysical Sciences, Springer, Berlin, 2005, 266 pp.
[21] F. Ruedorff, *Annalen d. Phys.*, 1861, **114**, 63.
[22] G. Quincke, *Annalen der Physik, Leipzig*, 1905, **18(11)**, 1.
[23] G. Quincke, *Proc. Royal Soc. London A*, 1905, **76**, 431.
[24] S. Maus, *Prediction of the cellular microstructure of sea ice by morphological stability theory*, 11th Int. Conf. on Physics and Chemistry of Ice, Bremerhaven, Germany, Royal Society of Chemistry, pp. 371–382.
[25] T. Tabata and N. Ono, *Low Temperature Science A*, 1962, **20**, 199.
[26] W. F. Weeks and W. L. Hamilton, *The Amer. Mineralogist*, 1962, **47**, 945.
[27] M. Wakatsuchi and T. Saito, *Ann. Glaciol.*, 1985, **6**, 200.
[28] D. M. Cole, J. P. Dempsey, L. H. Shapiro and V. F. Petrenko, in J. P. Dempsey and Y. D. S. Rajapakse, eds., *Ice Mechanics*, vol. 207, Am Soc. Mech. Engin., pp. 161–178.
[29] R. A. Lake and E. L. Lewis, *J. Geophys. Res.*, 1970, **75**, 583.
[30] L. I. Eide and S. Martin, *J. Glaciol.*, 1975, **14**, 137.
[31] T. M. Niedrauer and S. Martin, *J. Geophys. Res.*, 1979, **84**, 1176.
[32] M. Wakatsuchi, *Contrib. Inst. Low Temp. Sci.*, 1983, **A33**, 29.
[33] M. Wakatsuchi, *Low Temp. Sci.*, 1977, **A35**, 249.

[34] J. S. Wettlaufer, M. G. Worster and H. E. Huppert, *J. Fluid Mech.*, 1997, **344**, 291.
[35] K. O. Bennington, *J. Glaciol.*, 1963, **4**, 669.
[36] L. H. Shapiro and W. F. Weeks, in Y. D. S. R. J. P. Dempsey, Z. P. Bazant and S. Shyam, eds., *Ice Mechanics*, vol. 163, Am Soc. Mech. Engin., pp. 177–188.
[37] F. Cottier, H. Eicken and P. Wadhams, *J. Geophys. Res.*, 1999, **104**, 15859.
[38] A. Kovacs, Sea ice: Part I. Bulk salinity versus flow thickness, CRREL Report 96-7, U.S. Army Cold Regions Research and Engineering Laboratory, 1996.
[39] W. F. Weeks, in *Arctic sea ice*, vol. 598, Proc. Conf.on Arctic Sea Ice, Natl. Acad. Sci., pp. 96–98.
[40] J. D. Harrison and W. A. Tiller, *J. Applied Physics*, 1963, **34**, 3349.
[41] P. A. Shumskii, *Osnovy strukturnogo ledovedeniya (Principles of structural glaciology)*, Dover Publications, Inc., 1955, 1964 translated from Russian, 497 pp.
[42] C. A. Knight, *J. Glaciol.*, 1962, **4**, 319.
[43] N. V. Cherepanov and A. V. Kamyshnikova, in G. N. Yakovlev, ed., *Studies in Ice physics and ice engineering (fiziko-tekhnicheskie issledovaniya l'da)*, Israel Program for Sceintific Translations, Gidrometeorologichevskoe Izdatel'stvo (Transalted from Russian), pp. 170–176.
[44] W. F. Weeks and J. S. Wettlaufer, in *The Johannes Weertman Symposium*, The Minerals, Metals and Materials Society, pp. 337–350.
[45] N. K. Sinha, *J. Glac.*, 1978, **21**, 385.
[46] D. K. Perovich and A. J. Gow, *J. Geophys. Res.*, 1996, **101**, 18327.
[47] D. M. Cole and L. H. Shapiro, *J. Geophys. Res.*, 1998, **103**, 21739.
[48] H. Eicken, C. Bock, R. Wittig, H. Miller and H.-O. Poertner, *Cold Reg. Sci. and Technology*, 2000, **31**, 207.
[49] B. Light, G. A. Maykut and T. C. Grenfell, *J. Geophys. Res.*, 2003, **108**, 3051.
[50] D. K. Perovich and A. J. Gow, *J. Geophys. Res.*, 1991, **96**, 16943.
[51] N. K. Sinha, *J. Glac.*, 1977, **18**, 315.
[52] J. Weissenberger, G. Dieckmann, R. Gradinger and M. Spindler, *Limnol. Oceanogr.*, 1992, **37**, 179.
[53] T. Kawamura, *J. Geophys. Res.*, 1988, **93**, 2343.
[54] W. A. Edelstein and E. M. Schulson, *J. Glaciol.*, 1991, **37**, 177.
[55] C. Bock and H. Eicken, *Ann. Glaciol.*, 2005, **40**, 179.
[56] J. Freitag, F. Wilhelms and S. Kipfstuhl, *J. Glaciol.*, 2004, **50**, 243.
[57] F. Flin, J. B. Brzoska, B. Lesaffre, C. Coleou and R. A. Pieritz, *Annals Glaciol.*, 2004, **38**, 39.
[58] M. Schneebeli and S. A. Sokratov, *Hydrol. Processes*, 2004, **18**, 3655.
[59] K. M. Golden, H. E. A. Heaton, J. Miner, D. J. Pringle and J. Zhu, *Geophys. Res. Lett.*, 2007, **34**, L16501.
[60] J. H. Kinney and M. C. Nichols, *Annu. Rev. Mater. Sci.*, 1992, **22**, 121.
[61] M. Stampanoni, G. Borchert, P. Wyss, R. Abela, B. Patterson, S. Hunt, D. Vermeulen and P. Rüegsegger, *Nucl. Instr. Meth. Phys. Res. A*, 2002, **491**, 291.
[62] M. M. Miedaner, T. Huthwelker, F. Enzmann, M. Kersten, M. Stamponi and M. Amman, *X-ray tomographic characterization of impurities in polycrystalline ice*, 11th Int. Conf. on Physics and Chemistry of Ice, Bremerhaven, Germany, Royal Society of Chemistry, pp. 399–408, in press.
[63] M. M. Miedaner, Ph.D. thesis, Institute of Environmental Sciences, Johannes Gutenberg University Mainz, 2007, 113 pp.

[64] M. C. Flemings, *Solidification Processing*, McGraw-Hill, Inc., 1974, 364 pp.
[65] H. E. Huppert, *J. Fluid Mech.*, 1990, **212**, 209.
[66] C. Beckermann, *Int. Materials Reviews*, 2002, **47**, 243.
[67] W. W. Mullins and R. F. Sekerka, *J. Appl. Phys.*, 1964, **35**, 444.
[68] S. Maus, *On Brine Entrapment in Sea Ice: Morphological Stability, Microstructure and Convection*, Logos, Berlin, 2007, 538 pp.
[69] S. Maus, in M. Leppäranta, ed., *Report Series of Geophsyics, University of Helsinki*, p. this volume.
[70] N. V. Cherepanov, *Probl. Arkt. Antarkt.*, 1971, **38**, 137.
[71] A. Kovacs and R. M. Morey, *J. Geophys. Res.*, 1978, **83**, 6037.
[72] W. F. Weeks and A. J. Gow, *J. Geophys. Res.*, 1978, **83**, 5105.
[73] W. F. Weeks and A. J. Gow, *J. Geophys. Res.*, 1980, **85**, 1137.
[74] P. J. Langhorne and W. Robinson, *Cold Reg. Sci. Techn.*, 1986, **12**, 197.
[75] E. Stander and B. Michel, *Cold Regions Sci. Tech.*, 1989, **17**, 153.
[76] M. Nakawo and N. K. Sinha, *Atmos.-Ocean*, 1984, **22**, 193.
[77] N. K. Sinha and C. Zhan, *J. Mater. Sci. Letters*, 1996, **15**, 2118.
[78] E. Stander, in *Int. Conf. on Port and Ocean Engineering*, vol. 1, Narssarssuaq, Greenland, pp. 168–176.
[79] J. D. Harrison, *J. Appl. Phys.*, 1965, **36**, 326.
[80] D. L. Anderson and W. F. Weeks, *Trans. Amer. Geophys. Union*, 1958, **39**, 632.
[81] A. Assur, in *Arctic Sea Ice*, vol. 598, Proc. Conf.on Arctic Sea Ice, Natl. Acad. Sci., pp. 106–138.
[82] V. L. Tsurikov, *Okeanologiia*, 1965, **5**, 463.
[83] C. Petrich, P. J. Langhorne and Z. F. Sun, *Cold Reg. Sci. Techn.*, 2006, **44**, 131.
[84] K. Brattkus, *J. Phys. France*, 1989, **50**, 2999.
[85] L. Rayleigh, *Proc. Royal Soc. London A*, 1879, **29**, 71.
[86] P. Kurowski, S. Cheveigne, G. Faivre and C. Guthmann, *J. Phys. France*, 1989, **50**, 3007.
[87] M. Conti and U. M. B. Marconi, *Phys. Rev. E*, 2000, **63**, 011502.
[88] D. M. Cole, H. Eicken, K. Frey and L. H. Shapiro, *J. Geophys. Res.*, 2004, **109**, C08012.
[89] C. Krembs, T. Mock and R. Gradinger, *Polar Biol.*, 2001, **24**, 356.
[90] C. J. Mundy, D. G. Barber, C. Michel and R. F. Marsden, *Polar Biol.*, 2007, **30**, 1099.
[91] M. Wakatsuchi, *Low Temp. Sci.*, 1974, **A32**, 195.
[92] G. Z. Gershuni and E. Zhukovitskii, *Convective stability of incompressible fluids*, Israel Program for Scientific Translations, Keter Publishing House, in russian 1972 by Izdatel'stvo Nauka, Jerusalem, 1976, 329 pp.
[93] S. Maus, J. Freitag and J. Weissenberger, Backbone and permeability of young sea ice, manuscript in preparation, 2008.
[94] N. Ono, in *Int. Conference on Low Temperature Science*, vol. 1, Ints. of Low Temperature Science, Sapporo, pp. 599–610.
[95] I. Melnikov, *J. Geophys. Res.*, 1995, **C3**, 4673.
[96] J. R. Addison, *J. Glaciol.*, 1977, **18**, 117.
[97] W. S. Reeburgh and M. Springer-Young, *J. Geophys. Res.*, 1983, **88**, 2959.
[98] L. G. Anderson and E. P. Jones, *J. Geophys. Res.*, 1985, **90**, 9194.
[99] M. A. Granskog, K. Virkkunen, D. N. Thomas, H. Kola and T. Martma, *J. Glciol.*, 2004, **50**, 292.

[100] W. Schwarzacher, *J. Geophys. Res.*, 1959, **64**, 2357.
[101] K. O. Bennington, *J. Glaciol.*, 1967, **6**, 845.
[102] T. Saito and N. Ono, *Low Temp. Sci.*, 1977, **A39**, 127.
[103] J. L. Tison and V. Verbeke, *Ann. Glaciol.*, 2001, **33**, 13.
[104] S. Martin, *J. Glaciol.*, 1979, **22**, 473.
[105] J. Freitag, Ph.D. thesis, Universität Bremen, Fachbereich Physik/Elektrotechnik, 1999, auch: Ber. z. Polarforsch., Bd. 325, 1999.
[106] G. F. N. Cox and W. F. Weeks, *J. Glaciol.*, 1986, **32**, 371.
[107] K.-K. Koo, R. Ananth and W. N. Gill, *Phys. Rev. A*, 1991, **44**, 3782.
[108] H. R. Pruppacher and J. D. Klett, *Microphysics of clouds and precipitation*, vol. 18 of *Atmospheric and oceanographic sciences library*, Kluwer Acadamics Publ., 2nd edn., 1997, 954 pp.
[109] B. Light, G. A. Maykut and T. C. Grenfell, *J. Geophys. Res.*, 2004, **109**, C06013.
[110] J. Zhu, A. Jabini, K. M. Golden, H. Eicken and M. Morris, *Ann. Glaciol.*, 2006, **44**, 129.
[111] K. M. Golden, A. Heaton, H. Eicken and V. Lytle, *Mechanics of Materials*, 2006, **38**, 801.
[112] T. Koop, A. Kapilashrami, L. T. Molina and M. J. Molina, *J. Geophys. Res.*, 2000, **105**, 26393.
[113] H. Cho, P. B. Shepson, L. A. Barrie, J. P. Cowin and R. Zaveri, *J. Phys. Chem. B*, 2002, **106**, 11226.
[114] C. A. Knight, *J. Geology*, 1962, **70**, 240.

Proposal for a Climatological Ice Atlas "Western and Southern Baltic"

Natalija Schmelzer

Federal Maritime and Hydrographic Agency, Germany
Email: natalija.schmelzer@bsh.de

Outline

1. *Introduction*
2. *Ice atlases for the Baltic Sea – what is available presently ?*
3. *General purpose of an ice atlas and special purpose for the southern region of the Baltic Sea*
4. *Proposal for a Climatological Ice Atlas "Western and Southern Baltic"*
5. *Data material: available and missing*
6. *Questions, problems and possible solutions for the determination of missing data*

1. Introduction

An ice atlas probably is among the most useful products of ice data analyses because it provides a reliable basis for navigation and contains valuable data for climatological scientists and engineers. Existing atlases for the Baltic Sea are outdated, and it is time to think about a new one based on the current data series, taking into account latest climatological developments. The Federal Maritime and Hydrographic Agency (BSH) has collected a lot of ice data in the form of coded ice reports, plain text ice reports, and ice charts of countries bordering the Baltic Sea which cover the period from the beginning of the 20th century. The BSH's archive contains both hard copies and digitised ice charts. For the area of the **western** Baltic Sea, the ice charts for winters with ice occurrence at sea have been digitised for the period from 1955 to 1987. Since the winter of 1996, the ice charts have been available as raster ice charts. Furthermore, the ice charts from 1957 to 2005 for the **northern region** of the Baltic Sea (north of latitude 56°N), which are issued routinely in winter by the German Ice Service, have been digitised on a regular geographic grid with 0.5° resolution. The ice data base of the BSH contains the coded ice data from the observation network along the German coast covering the period since about 1900, and coded observational ice data from the entire Baltic Sea region since 1961.
Despite large amount of digital ice data available, it is not possible currently to obtain usable results on that basis. Firstly, the ice charts are available only at discrete intervals, that are not always regular. Secondly, ice charts have been produced only when a certain amount of ice was present, and the beginning and end of an ice season are not well represented. Besides, coastal ice, mostly fast ice, has not been included in the digitisation.

The aim of this paper is to discuss problems and suggest possible solutions concerning, inter alia, missing data and ice parameters to be analysed.

2. Ice atlases for the Baltic Sea – what is available presently ?

Some atlases covering the area of the Baltic Sea are described below.

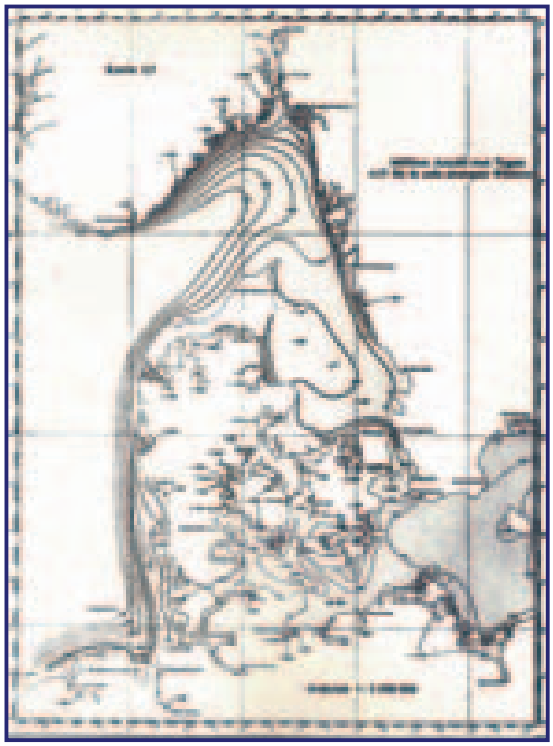

SHD, Berlin, 1952
Data series: **1903/04 – 1940/41**
Parameters:
- *Ice extent* on the first, 11th and 21st day of the months December to May in mild, moderate, strong and very strong ice winters
  Mean number of *days with ice* in mild, moderate, strong and very strong ice winters
- *Frequency* of ice occurrence in mild, moderate, strong and very strong ice winters
- Mean number of *days with navigation obstructions* in strong ice winters.

Fig. 1. Atlas example: **Ice conditions in the German regions of the Baltic Sea and North Sea and in the waters between both seas**

DHI, Hamburg, 1956
Data series: **1896/97 – 1953/54**
Parameters:
- *Probability* of ice occurrence in the periods 1-10, 11-20, 21-30(31) of the months November to May
- Mean number of *days with ice* in mild, moderate, strong, very strong and extremely strong ice winters
- Charts with the *maximum ice extent* in mild, moderate, strong, very strong and extreme ice winters.
- Various tables.

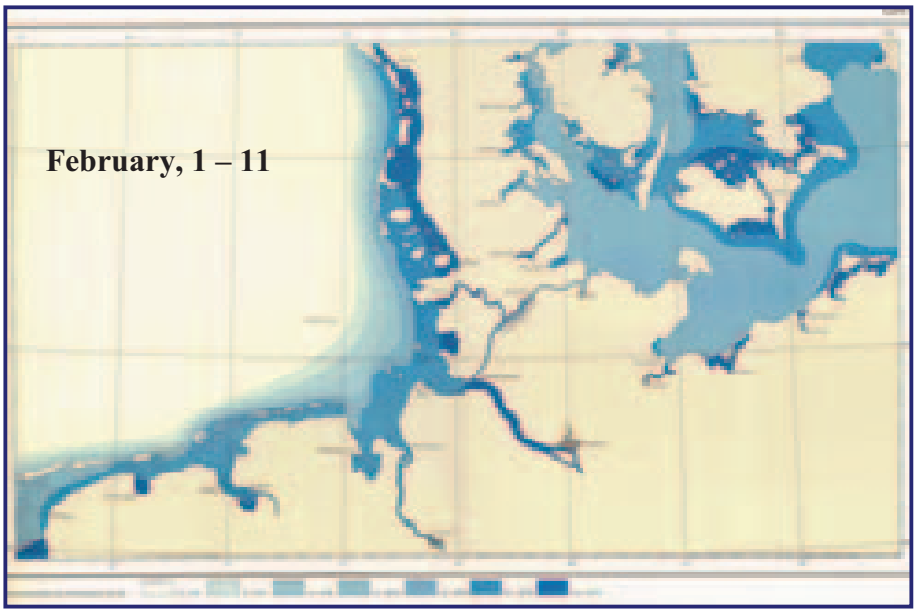

Fig. 2. Atlas example: **Ice conditions in the German Bight and in the western Baltic Sea**

J.P.Girjatowicz
Szczecin, 1985, 1990
Data series: **1946/47 – 1985/86**

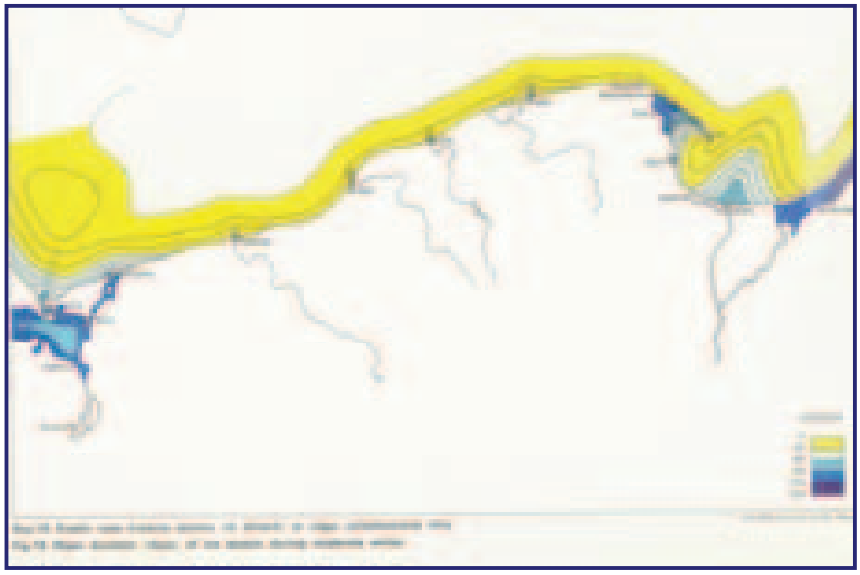

Parameters:
Mean and extreme values for:
- *dates of ice occurrence,*
- *number of days with ice*
- *length of the ice season,*
- *ice thickness and*
- *navigation conditions* in mild, moderate and strong ice winters.

Various tables.

Fig. 3. Atlas example: **Ice conditions in the Polish coastal waters**

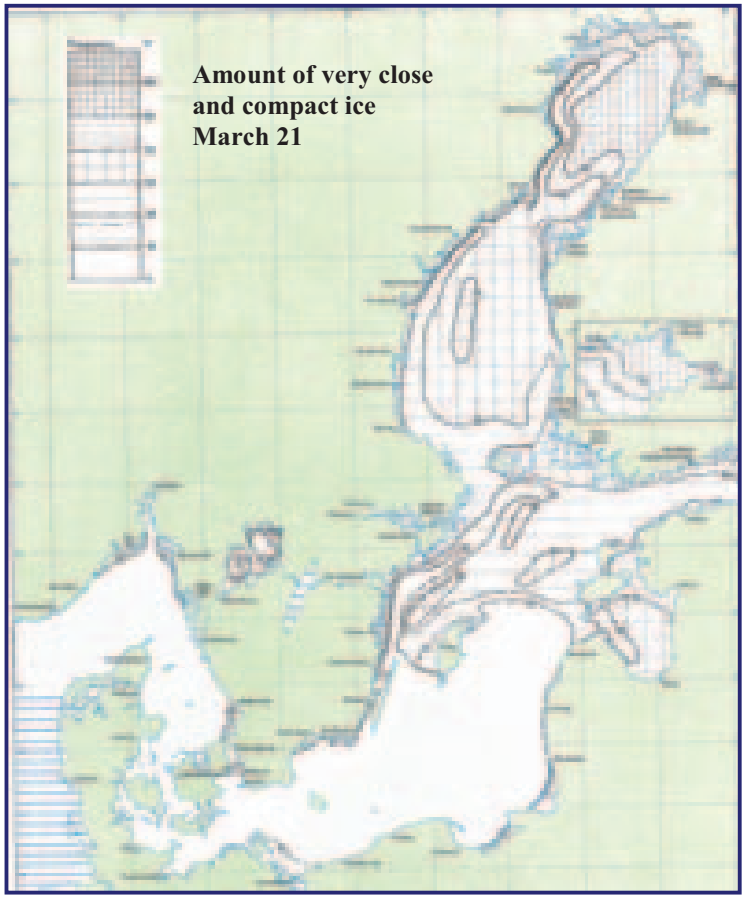

SMHI, FIMR
Norrköping, 1982

Data series: **1962/63 – 1978/79**
Parameters:
Ice frequency, frequency of high ice concentration, mean values of *ice concentration*, dominant ice type, mean level *ice thickness*, probability of *very close* and *compact ice*, probability and concentration of *ice ridges*, special ice information.

This is the most complete atlas, but it does not reflect climate developments in the past 30 years.
.

Fig. 4. Atlas example: **Climatological ice atlas for the Baltic Sea, Kattegat, Skagerrak and Lake Vänern**

3. General purpose of an ice atlas and special purpose in the southern region of the Baltic Sea

Sea ice poses a risk to human activities in the marine environment, such as navigation, fisheries, and offshore operations. In areas with heavy sea traffic, which abound in the Baltic Sea, ice may hinder navigation considerably and sometimes poses a severe threat. Navigation in ice often requires specialised assistance. That applies both to smaller ships, which may even have difficulties in relatively thin new ice, and to high-powered vessels, which may be damaged by heavy ice although they are suitable for navigation in ice covered waters. Also port operations and facilities may be affected by ice.
Ice also has a major impact on global climate, especially by influencing interactions between the ocean and the atmosphere. Ice formation reacts very sensitively to local climate conditions, and hence to climatic changes. For this reason, long-term series of ice data play an important role in monitoring climatic changes.

The purpose of an ice atlas is to provide useful background information facilitating decisionmaking in a variety of sectors, particularly in shipping and climatology.

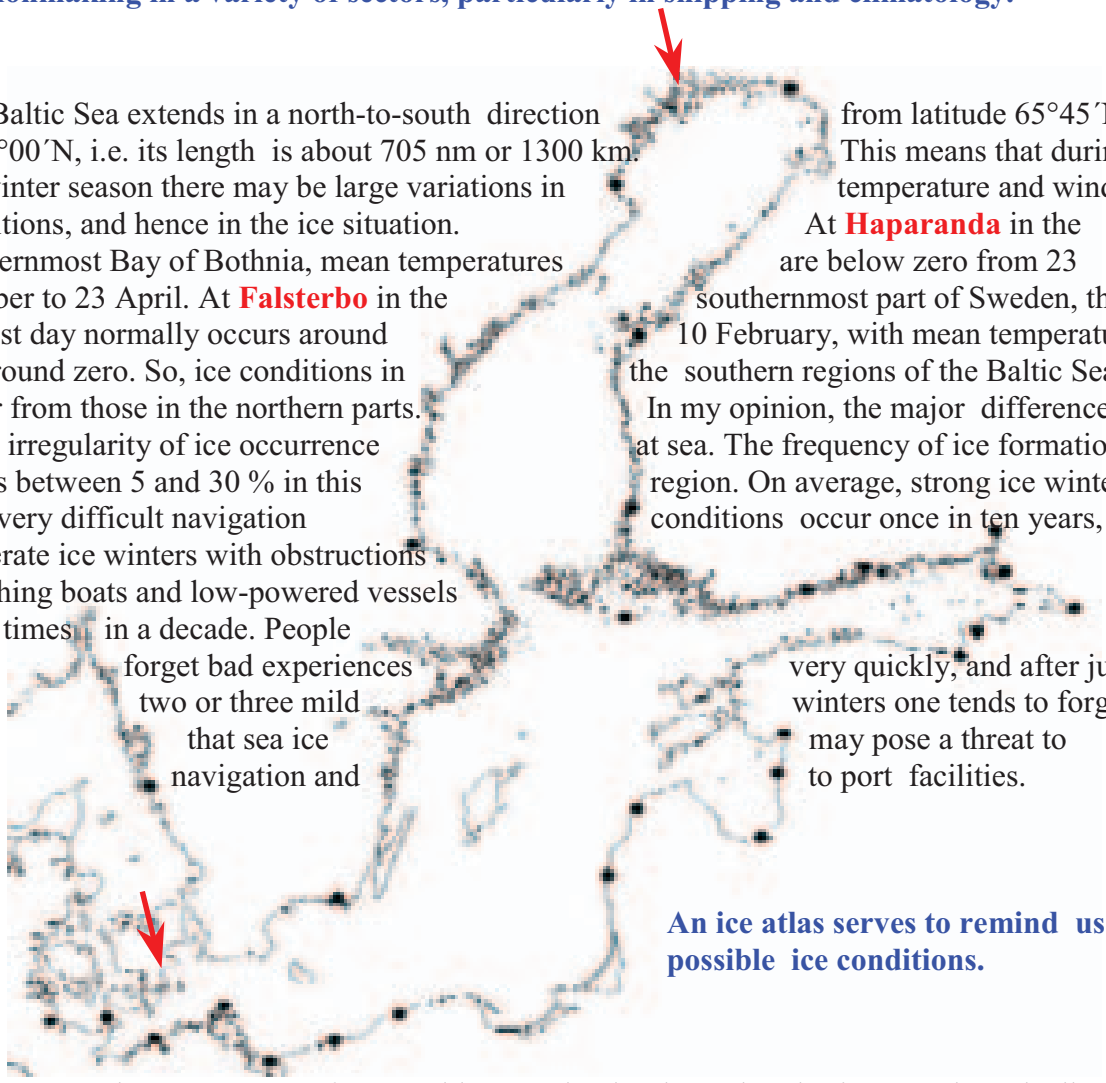

The Baltic Sea extends in a north-to-south direction from latitude 65°45´N to 54°00´N, i.e. its length is about 705 nm or 1300 km. This means that during the winter season there may be large variations in temperature and wind conditions, and hence in the ice situation. At **Haparanda** in the northernmost Bay of Bothnia, mean temperatures are below zero from 23 October to 23 April. At **Falsterbo** in the southernmost part of Sweden, the coldest day normally occurs around 10 February, with mean temperatures around zero. So, ice conditions in the southern regions of the Baltic Sea differ from those in the northern parts. In my opinion, the major difference is the irregularity of ice occurrence at sea. The frequency of ice formation varies between 5 and 30 % in this region. On average, strong ice winters with very difficult navigation conditions occur once in ten years, moderate ice winters with obstructions to fishing boats and low-powered vessels three times in a decade. People very quickly, and after just forget bad experiences winters one tends to forget two or three mild may pose a threat to that sea ice to port facilities. navigation and

An ice atlas serves to remind us of possible ice conditions.

In Germany, the percentage of renewable energies is planned to be increased markedly by installing offshore wind farms in the North and Baltic Seas (Jahresbericht 2007, BSH Hamburg und Rostock). Thus, an ice atlas of the western Baltic will be very helpful to engineering firms working in this field.

4. Proposal for a Climatological Ice Atlas "Western and Southern Baltic"

Fig. 5. Area under consideration (western and southern Baltic Sea)

Anticipated deadline :	Summer, autumn **2010**
Team partners :	German Ice Service, Polish Ice Service Swedish Ice Service
Main Period :	**1961 – 2010**
Periods to be compared :	1961 – 2010; 1971 – 2010; 1981 – 2010 1961 – 1990; 1971 – 2000; 1981 – 2010
Parameters :	Ice frequency, ice concentration and ice thickness on the first, 11th and 21st day of the winter months; mean and extreme values of freeze-up and break-up dates, number of days with ice, length of the ice season
Additional :	Ice conditions in different ice winter classes (mild, moderate, strong)
Publication:	As a Report Series of the BSH The most important results of data analysis will be published as a digital supplement which can be added to the electronic navigational charts

The planned ice atlas covering the western and parts of the southern Baltic Sea will be based on comprehensive data material stored in the data base of the BSH. The data covering the 50-year period from 1961 to 2010 will be analysed. This period includes the ice winter of 1962/63, with extreme ice conditions in the region of the southern Baltic, and the latest development trends of ice conditions in general. Additionally, different periods will be compared to show temporal changes clearly, e.g. the meteorological normal periods of 30 years. The parameters to be analysed are listed above. Meteorological parameters, e.g. air temperatures, and thickness of fast ice, can be added in the form of tables and diagrams.
Characteristics of the ice and expected ice conditions in different ice winter classes (mild, moderate, strong) will also be analysed.

5. Data material: *available and missing*

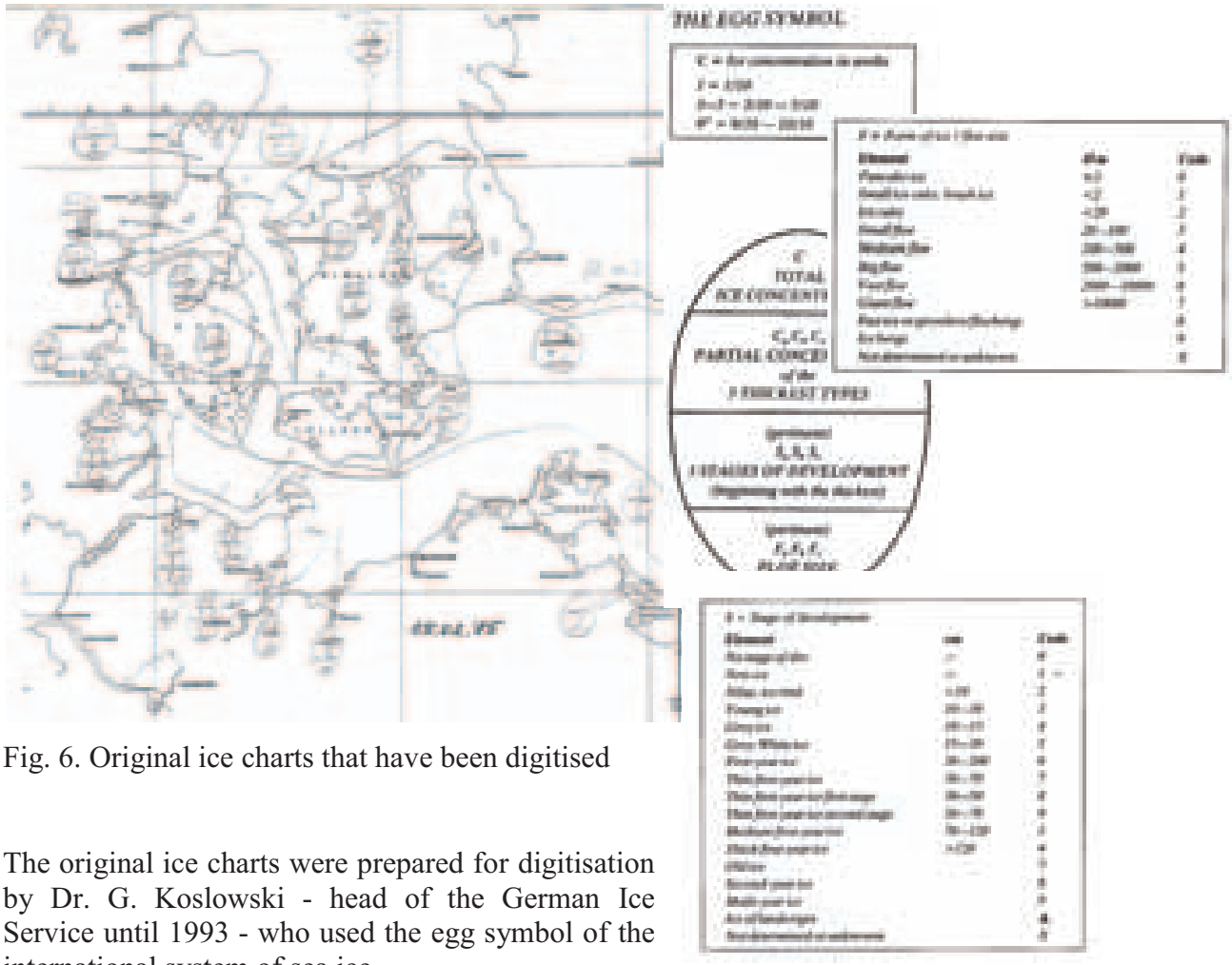

Fig. 6. Original ice charts that have been digitised

The original ice charts were prepared for digitisation by Dr. G. Koslowski - head of the German Ice Service until 1993 - who used the egg symbol of the international system of sea ice.

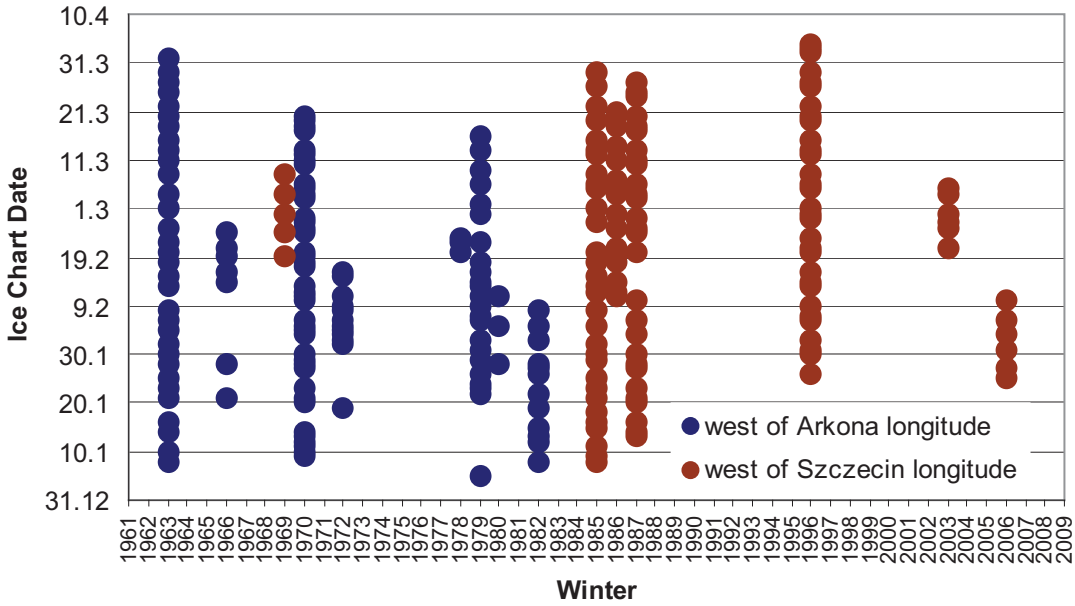

Fig. 7. Digital ice charts in the data base of the BSH
Area: Baltic Sea partly west of 13°30', partly west of 14°15' E , Belts and Sounds;
Period : 1955 – 2005; Raster : 2' X 4'; Parameters : concentration, ice thickness, form of ice

The ice charts cover the period from 1955 to 1987. The ice charts have been reconstructed only for the winters with ice formation at sea, i.e. for strong and very strong ice winters.
Reports and notes on ice conditions at sea received from vessels, icebreakers and ferries were used to prepare these charts. Only one or two ice charts covering the time of maximum ice development could be reconstructed for some ice winters for which very little information is available. From the winter of 1995/96, a different software has been used to draw ice charts, which are available in digital form. Three weekly ice charts covering the western Baltic have been published in strong and very strong ice winters, i.e. we have a nice digital ice data series, but with a lot of temporal gaps, see Figure 7. Besides, the ice situation sometimes is very difficult and impossible to be described by single code number in the egg symbol. For example, thick close ice may occur in a particular area at the same time as new ice that has formed during the night; in the field of compact ice, there may be predominantly 40 cm thick ice floes interspersed with 60 cm thick ice. Therefore, two thicknesses and two concentrations are found for some raster points in the data base.
Unfortunately, coastal ice conditions according to the ice charts have not yet been prepared for digitisation. In strong and very strong ice winters, coastal ice consists of fast ice of known thickness, whereas in moderate or mild winters the concentration of ice may vary also in the coastal waters. These data still have to be reworked.

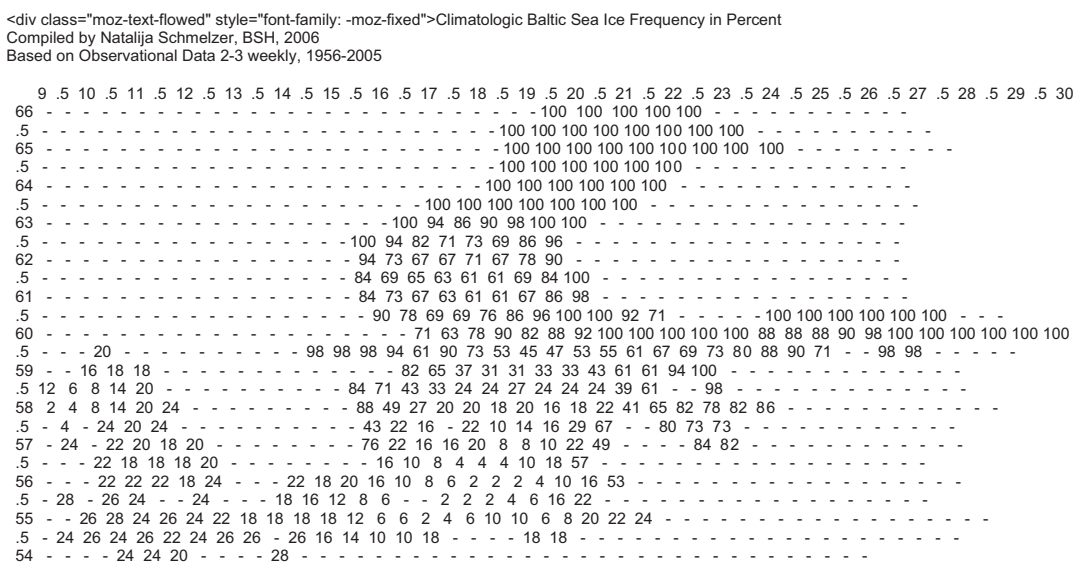

Fig. 8. Frequency of ice occurrence compiled by digitising the German ice charts "EISÜBERSICHTSKARTE" and "EISKARTE" published twice and three times a week, respectively. Area: Baltic Sea; Period: 1956 – 2005; Raster: 0.5° X 0.5°; Parameters: Concentration and ice thickness.

For the period from 1956 to 2005, the German ice charts "EISÜBERSICHTSKARTE" and "EISKARTE" published twice and three times a week, respectively, were digitised as a grid with a raster of half a degree. This raster is too coarse to allow a data analysis for the small area of the western Baltic and to include the results in an atlas.

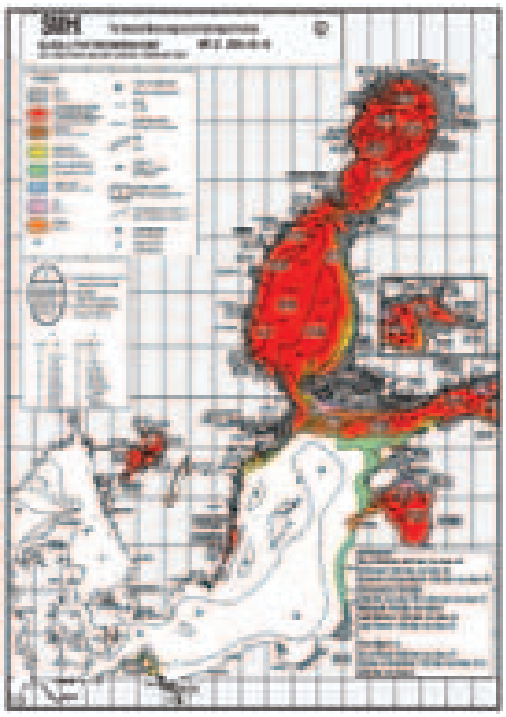

Fig. 9. Digital ice charts of the Baltic Sea available at the Swedish ice service

Periods: 1961 – 1979, BASIS code, 18.5 km resolution

1980 – 1994, ICEMAP grid format, 4.44 km resolution, two charts per week

1995 – today, ICEMAP grid format, 4.44 km resolution, daily

The most complete digital ice data series of the southern region of the Baltic Sea are available from the Swedish Ice Service, see Figure 9 and the above text. But the problem with the period 1961 – 1995 is similar to that of German ice data series - there are gaps in data series of the digitised ice charts.

A summary of available and missing ice data is shown in Figures 10 and 11.

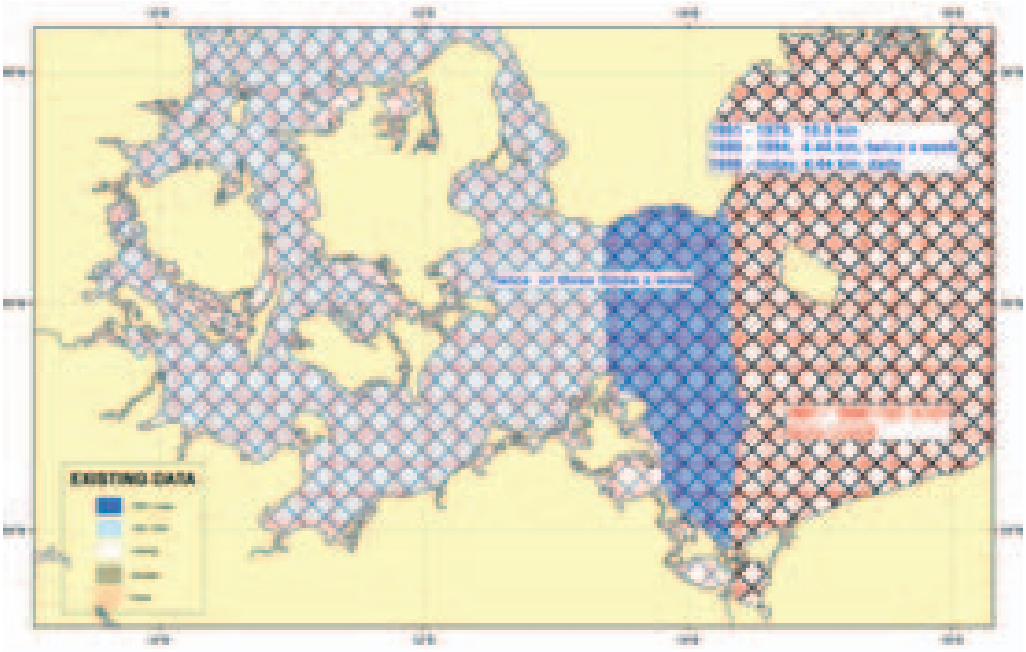

Fig. 10. Ice data available as digital ice charts

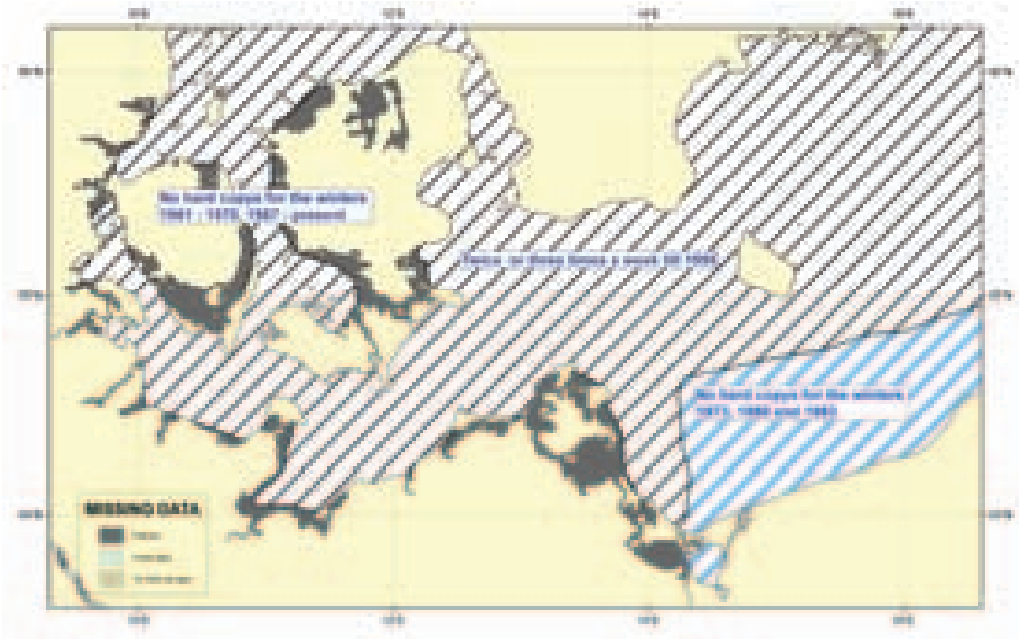

Sea area
1962/63
1965/66
1968/69
1969/70
1971/72
1977/78
1978/79
1979/80
1981/82
1984/85
1985/86
1986/87
1995/96
2002/03
2005/06
Fast ice
1961 - 1995
Nearly every winter

Fig. 11. Missing ice data

6. Questions (Q), problems (P) and possible solutions (S)

Period 1961 - 2005
P: Danish and Polish data
S: Data from Danish network observations collected in the ice data bank + German digital ice charts
S: Data from Polish network observations collected in the ice data bank + sea area from Polish ice charts (must be digitised)

Period 1961 - 1995
P: Ice data in the coastal waters, mostly fast ice with known thickness
S: Data from network observations collected in the ice data bank
P: For some raster points there are two thicknesses and two concentrations
Q: Mean value of thickness and sum of concentration?

Period 1961 - 1994 (Sweden), 1961-2010 (Germany)
P: Two or three charts per week
Q: Can we fill the gaps by interpolation of ice conditions?
Q: Was there no ice on days without ice charts
or
was there an ice situation similar to or different from that of the day before?
S: Consideration of meteorological conditions

S: Swedish data + German data for the German and Danish waters + Polish data for the Polish waters

Acknowledgement
I would like to thank the participants of the 6th Baltic Sea Ice Climate Workshop for the lively discussion and their interest in this topic. The suggestion to fill in the gaps by modelling missing ice charts and other ideas discussed at the meeting will be considered in preparing the ice atlas.

Abbreviations

BSH	Bundesamt für Seeschifffahrt und Hydrographie
DHI	Deutsches Hydrographisches Institut (until 1990)
FIMR	Finnish Institute of Marine Research
SHD	Seehydrographischer Dienst (until 1990)
SMHI	Swedish Meteorological and Hydrological Institute

Address of author
Dr. Natalija SCHMELZER
Bundesamt für Seeschifffahrt und Hydrographie
Neptunallee 5
18057 Rostock
GERMANY

Tel. +49 (0) 381 4563-787
E-Mail: natalija.schmelzer@bsh.de

Generation of coastal leads in the Gulf of Finland

Ove Pärn*, Jari Haapala+, Jevgeni Rjazin#

* Marine Systems Institute at Tallinn University of Technology, Akadeemia tee 21, 12618, Tallinn, Estonia; kylmleek@gmail.com

+ Finnish Institute of Marine Research, Erik Palménin aukio 1, FIN-00560 Helsinki, Finland; jari.haapala@fimr.fi

Voru 91a – 11, EE-50112, Tartu, Eesti; regnoseo@gmail.com

Abstract

Coastal leads are a common feature in the Gulf of Finland. According to the analysis of the EMHI ice charts, the occurrence of the coastal leads have a rather large regional differences. Probability of the leads is highest in the Estonian coastal region where their occurrence is about 10 %. In some regions occurrence of leads is only 2 %. The HELMI model was applied for an idealized conditions in order to study how the lead formation depends on the large scale wind direction. All wind directions generate open water and leads in pack ice, but only the winds W, NW, N and S winds form rather uniform lead pattern which facilitate navigation in ice.

Key words: Gulf of Finland, sea ice, winter navigation, ice deformation, lead formation

1. Introduction

The seasonal ice cover has a great importance to the countries surrounding the Baltic Sea, with respect of year-round sea transportation. Elongated in the W-E direction, the Gulf of Finland is an important corridor of merchant shipping for Russia, Finland and Estonia,as well as heavy passenger traffic between Helsinki and Tallinn. Every year new harbors and terminals, especially in the Eastern part of the Gulf, are opened for operation. During the last decade the oil transportation from Russian harbours has risen remarkably, intensifying essentially the tanker traffic along the Gulf of Finland. During winter navigation period vessels should navigate through the ice in the Gulf, in normal winter at the length of at least 150 nautical miles and, if the winter is very severe, the ice-sailing distance can exceed 400 nautical miles during the last climatic period, 1961-1990 (Seinä 2003).

During an average winter the whole northern Baltic Sea is covered by ice. Even in mild winters at least some parts of the Bothnian Gulf, Gulf of Finland and Gulf of Riga freeze. In the Gulf of Finland, ice forms at first in the Eastern part already from the beginning of December. On average, ice season last until the middle of April, but sea-ice remains in small bays in the East of the Gulf until May.

Ice conditions are variable and can change rapidly. Pack ice can drift over 25 km during a stormy day. Due to the large effect of the coast and islands in the Gulf of Finland, sea-ice drift own large horizontal gradients in velocity, which cause sea-ice ridging in the compressive regions and opening of the pack ice in the divergent regions. The most prominent features of the differential ice drift are the coastal leads,

which are observed frequently in the Gulf of Finland and in some cases can extent several hundred kilometers.

For the navigation in the pack ice, coastal leads are the natural fairways. The objective of this work is to analyze space scales and the frequency of the coastal leads in the Gulf of Finland. We analyze the EMHI ice charts and utilize the Helsinki multi-category sea-ice models in order to study how the lead formation depends on the large scale wind direction.

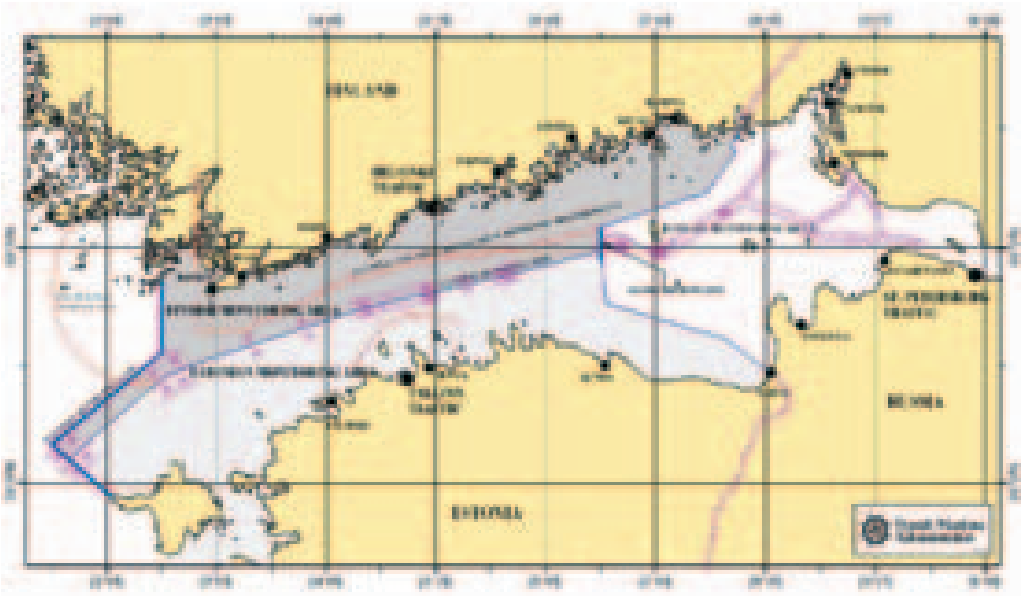

Fig. 1. Map of the Gulf of Finland showing the main shipping routes and the VTS (Vessel Traffic Service) monitoring areas of the three states.

2.Materials and methods

2. Observational data

This study is based on the ice charts covering the period 1995??? – 2007. These ice charts belong to the EMHI (Estonian Institute for Meteorology and Hydrology), based on the observations by the EMHI itself and, partly, the Finnish Ice Service ice charts and Russia ice charts. , which are largely based on the satellite observations and visual observations from air, land and ships. Every chart represents the ice distribution over the Gulf at a particular date.

Here, in surveying and analyzing the ice charts, the lead means a stripe of open water, new ice or region of low concentration which is located either between two areas of compact ice, or between the pack ice and fast ice.

2.2. Model experiments

We apply HELMI (HELsinki Multicategory Ice model) model for this study. The model resolves ice thickness distribution, *i.e.* ice concentrations of different thickness categories, redistribution of ice categories due to deformations, thermodynamics of sea-ice, horizontal components of ice velocity and internal stress of the ice pack. An ice pack is a mixture of open water, undeformed and deformed ice categories of variable thickness. Deformed ice is separated into rafted ice, rubble ice (or hummocked ice) and ridged ice classes. The model has been used in the climate research (Haapala 2005) and the operational applications (see: polarview.fimr.fi). The model physics and numerics are the same both in operational and climate simulations. The only differences are in the horizontal resolution and the scheme of

atmospheric forcing used. Due to the improved description of ice categories, it is possible to get also realistic model output about mechanical deformations describing closing of ship channel, closing and opening of leads, as well as rafting and ridging.

Present set-up of the sea ice model predicts evolution of five undeformed and two deformed ice categories. Ice categories are time-stepped in the thickness space without any limits, except the thinnest category that is not allowed to exceed 10 cm in thickness. Deformed ice is divided into the two separate categories - rafted ice and ridged ice. Horizontal resolution of the model is 1 nautical mile (~1.852 km).

3. The observed ice deformations: the leads with respect of the navigability

An example of individual ice chart, available from the EMHI data base, is given at the Fig. 2. During the maximum ice extent, ridged ice covers large offshore areas of the Gulf, indicating that ice thickening towards to east of the Gulf. Ice is ridging more severely in the narrowest part of the Gulf between 25.0E-25.5E and in its widest part of the gulf between 27.0E and 28.0E. Also remarkable differences in ice properties on North-South direction are evident. Due to the NNW winds preceding the ice chart given at the Fig. 2 (the wind blew from NNW on January 21), the ice concentration decreased and thus a few ice leads occurred ca 10-20 km offshore from the northern Finnish coast at the boundary of landfast ice. Resulting from the ice drift, the ridges formed on the southern and the eastern boundaries of landfast ice.

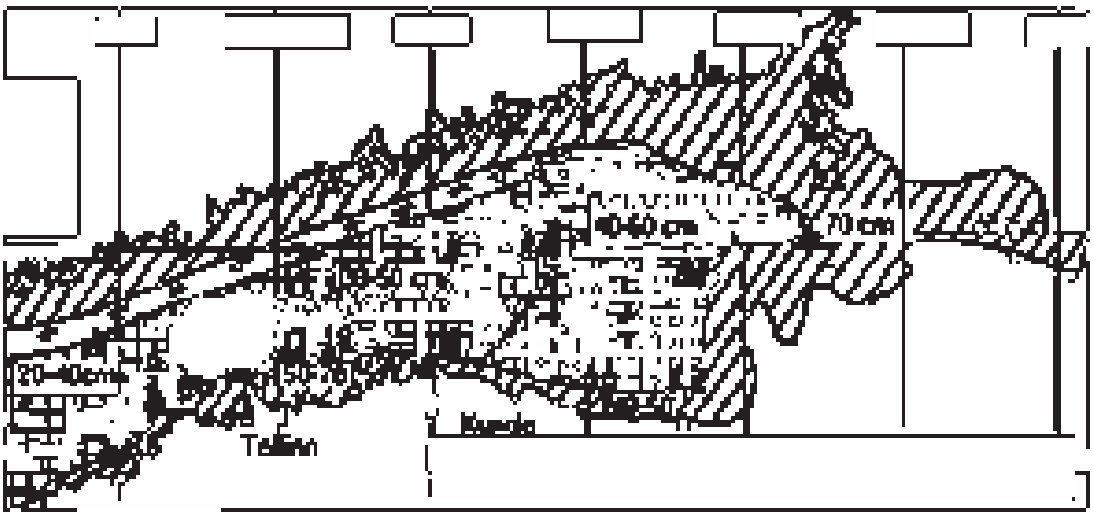

Fig. 2. Ice chart at the greatest extent of ice cover (22 February) in ice season 1995/1996. The triangles denote ridged ice. The ice chart by the EMHI.

The ice covered period and occurrence of the leads in different regions of the Gulf of Finland were calculated from the EMHI charts covering the period 1995-2007. The statistics were calculated for the regular 1.0° x 0.2° grid in longitude and latitude, respectively. We also examined, which areas are favorable for ship navigation and harbours, assuming the low ice concentration allowing ice leads to favor the shipping, whereas the high ice concentration enabling the ice to raft and ridge, is the obstacle to navigation. At the Fig. 3 we present the results for leads only (together with the number of ice days), since the routine ice charts do not present ice concentration (also important for safe shipping).

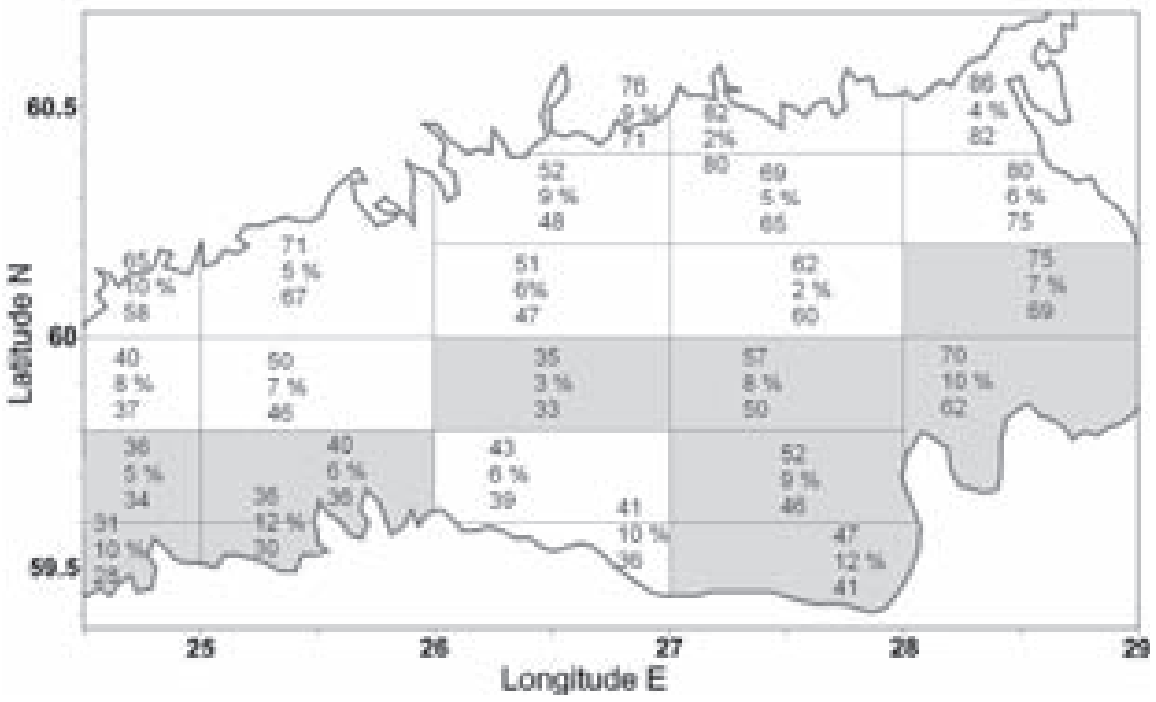

Fig. 3. Average ice conditions in the Gulf of Finland during 1991-1995 and 1998-2007 in the 1.0° x 0.2° grid. The numbers in cell, from the top to the bottom, present: the average duration of ice cover in days, the percentage of ice lead occurrence to the ice cover duration, and the number of days with the ice conditions resisting navigation. The gray color indicates the ice conditions more favorable for shipping in a cell. These conditions are the amount of the ice-free days and the incidence of leads in the area.

The shipping-favoring ice conditions occur mostly in the southern part of the Gulf. Ice drift and thus forming leads and respectively rafting or ridging take place due to the wind drag and deformation forces appearing within the ice of different concentration and types. Does the ice distribution shown in Fig. 3 consist with the directional wind statistics? We analyze this question below, but here we present in Fig. 4 the directional distribution of winter-time winds with daily speed above 4 m/s, i.e. the wind

speed causing the packed ice efficiently to drift. The analysis reveals that moderate and strong winds blow during the winter mostly from SW and neighboring sectors. The wind directions between S and W comprise frequency 37 %, while the opposite sector between N to E accounts only to 21 %.

The NCEP/NCAR wind data come from the global atmospheric model of resolution 2.5°x2.5°. In the case of the winter 2002/2003 on the GoF, these NCEP/NCAR data are compared to the meteorological observations by the Tallinn Harbour Weather Station. They correlate with the coefficient 0.91 and 0.88 for the longitude and latitude components respectively (Parn 2008).

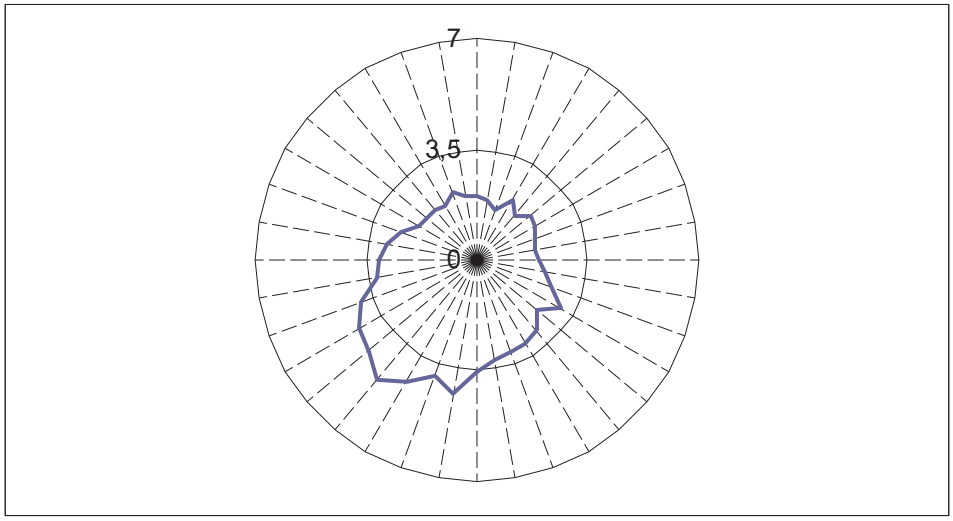

Fig. 4. Directional frequency distribution of the winds with daily speed over 4 m/s in winter. Data on 1971-2005 in the middle of GoF.

5. Results from the numeric experiments

In this chapter we estimate how the ice deformation rate and open water formation are related to the wind direction and how these vary in a regional scale. The results are based on the idealized numerical experiments, where the sea-ice was initially constant. The level ice thickness was set to be 0.35 m, the ice concentration A = 0.99 and then a response of the sea-ice model for different directions of wind with constant wind speed of 12 m/s were calculated.

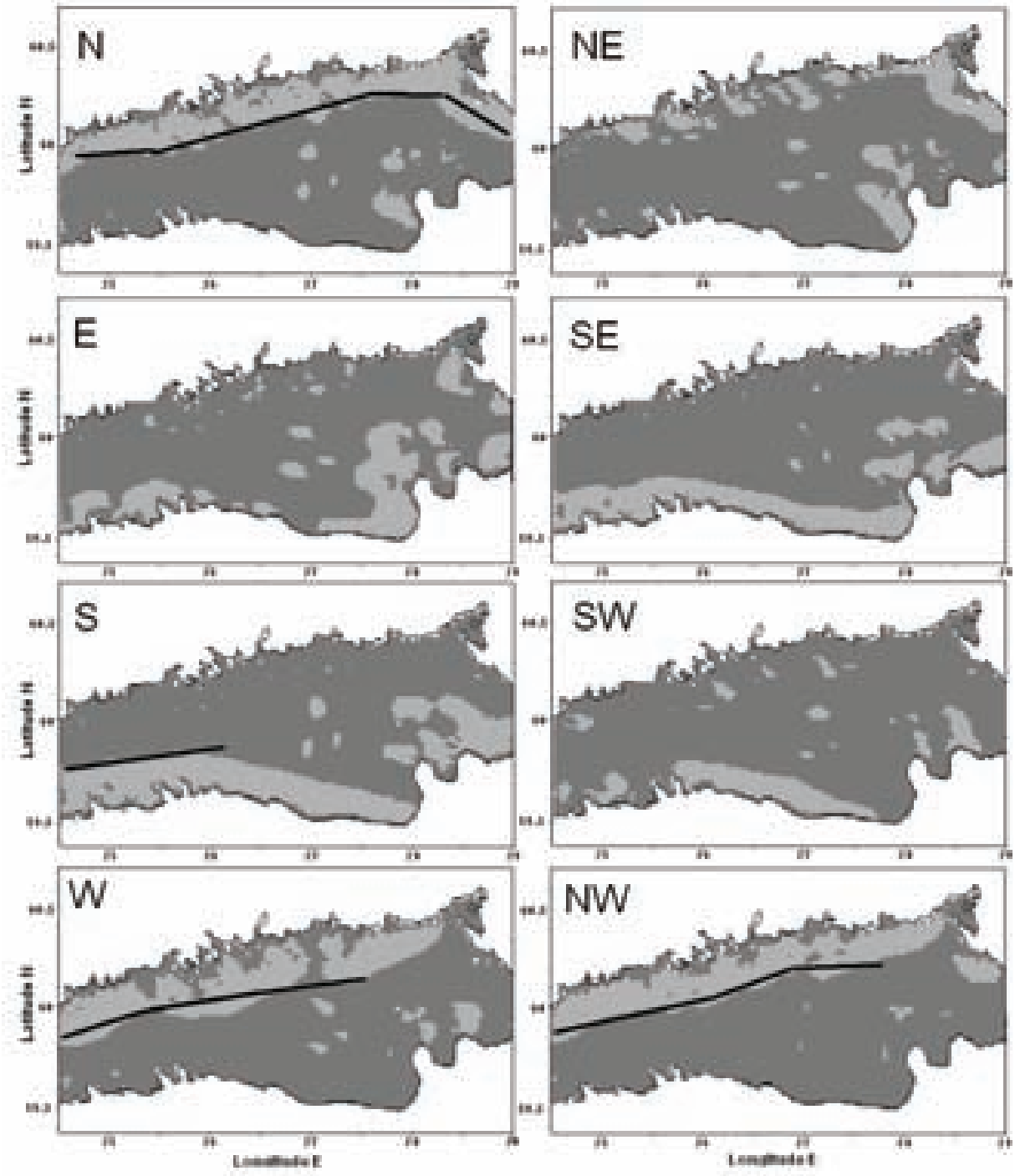

Fig 5 : Modelled occurrence of leads during different wind situations in the Gulf of Finland .The line shows an optimal route of a vessel navigating in ice

5. Lead formation patterns

In order to analyze, which wind directions favour navigation in ice, we assume that in those regions where the modelled ice concentration is less than 85 %, the ships can navigate without any diffuculties, and a following conclusions can be made

When the Northerly wind is acting, an extensive lead, perpenticular to the coast line and extending from the mouth to the end of GoF. During that case, vessels can easily navigate near by the Finnish shore.

However, the picture differs quite when the North-Easterly wind is to blowing. This wind situation generates also much open water, but in contrary to the previous case, open water areas are separated by the island, and an uniform lead is generated only in the easternmost part of the GoF (the Fig 5 NE). Such a situation was observed February 22 1996, when a lead went through the Gulf from the estuary (23E) till almost the middle of the ventrix (27E), due to the NNE wind blown on the previous day (Fig 2).

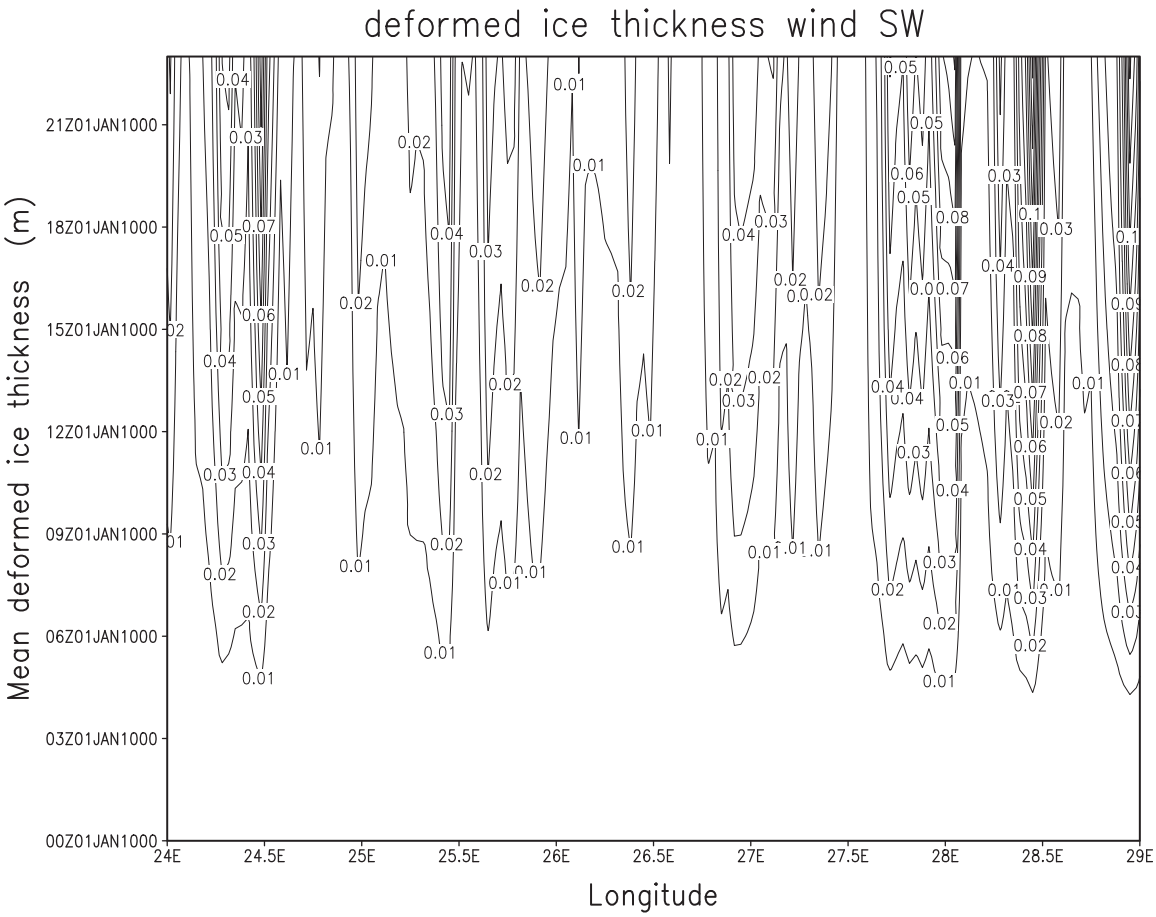

Fig. 6. Mean deformed ice thickness as a function of the longitude and the time after onset of constant SW wind of speed 12 m/s, starting from the horizontally homogeneous ice conditions.

Also Southern winds, blowing transverse to the basin, are favourable for the lead generation (cf the Fig 4). In this case the lead is located in the Estonian coast reaching from the mount (23E) up to the central of GoF (28E), while a few minor leads do exist by the Ingerian (Southern) shore of the GoF (ca between 28E and 29E). The survey of the leads observed in the Gulf over 1991 – 1995 & 1998 – 2007 according to the EMHI ice charts shows the leads to appear quite often near the Estonian coast (see the Fig 3). Thus the model results fits well with the empiric data.

Southwesterly winds are the most common during the winter time (Fig 4). During those situations, a minor lead is formed on the Estonian coast in the middle of the

GoF.

During the lead formation events also some regions of the GoF are deformed and sea ice is ridging and thickening in those regions. Figure 6 depicts how the mean deformed ice thickness is varying in space and forming in time. The ice does not deform during the first 3 hours of the SW wind (most dominant wind direction on the Gulf) of a speed 12 m/s. After 5 hours of the SW wind blowing, the deformed ice grows over 0.01 m thicker at the longitudes 24.5, 25.5, 27.0, 28.0, 28.5E. Further on, we can see the deformed ice is growing 0.07-0.1 m thicker in a day in the above mentioned areas, whereas the deformed ice grows less than 0.01 m between these areas during the same time.

For an evaluation how important the mechanical thickening of the ice is, we can make following simple comparison of the deformed ice growth rates to the thermodynamical growth rate of ice. If the air temperature is -10 Celsius then 0.35m thick ice is to growing about 0.01 m daily. Thus the thermodynamics growth rate of the undeformed ice is small compared to the deformed ice growth rate. In a same conditions, the new ice in the leads is thickening about 0.05 m/day.

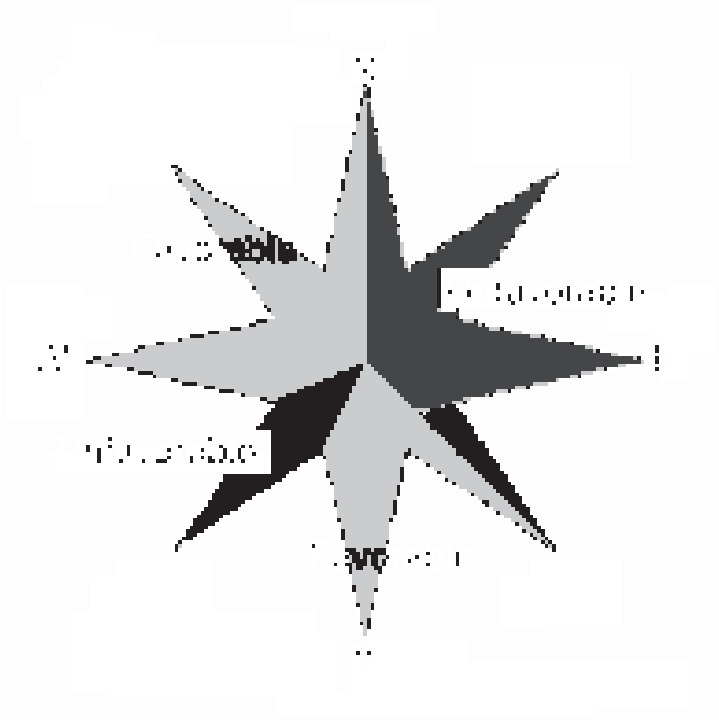

Fig.7 Ice conditions favoring vessel navigation form along the Gulf under the constant wind acting at least 10 h.

6. Conclusion

Coastal leads are a common feature in the Gulf of Finland. Practically all wind directions generate open water and leads in pack ice, but the winds W, NW, N and S winds form rather uniform lead pattern which facilitate navigation in ice (Figure 7). This is particular important during the considerably severe winters when the other regions are covered by the thick ridged ice.

Ship damage risk is higher closer to an areas of high ice deformation rate where ice floes of different properties meet, yielding also a notable ice thickness gradient . Like navigating from an area of low-concentrated ice to an area of high-concentration of

thick ice. A lack of this awareness puts the vessel to a special risk. The present study enables to make a rough estimate of the navigation conditions based on the weather forecast and give guidelines to route selection under considerably severe ice conditions.

References

Climatological ice atlas for the Baltic Sea, Kattegat, Skagerrak and Lake Vänern (1963-1979). 1982. Swedish Meteorological and Hydrological Institute. Printed by Söfartsverkets tryckeri, Norrköping.

Haapala, J., Lönnroth, N. and A. Stössel. 2005. A numerical study of open water formation in sea ice. *J. Geophys. Res.*,Vol. 110, No. C9, C0901110.1029/2003JC002200

Hänninen, S. (2003). Incidents and accidents in winter navigation in the Baltic Sea, winter 2002-2003. Finnish Maritime Administration Research Report No 54.

Pastukhov, G., D,. Talijev. (2003). Briefinformation on ice conditions on Gulf of Finland in the winter 2002-2003. NW Administration of Federal Service of Russia for Hydrometerology and Environmental Monitoring (NW Hydromet).

Pärn, O., Haapala, J. 2006. Analysis of the ice model simulation for the Gulf of Finland in 2002/03.

Ice Thickness Charts Produced by C-Band SAR Imagery and HIGHTSI Thermodynamic Ice Model

Juha Karvonen, Bin Cheng, Markku Similä
Finnish Institute of Marine Research (FIMR)
email : Fistname.Lastname@fimr.fi

Abstract

We have studied the estimation of the Baltic Sea ice thickness based on a thermodynamic ice model and SAR data to produce ice thickness charts (ITC's) for navigation. This algorithm also takes the ice motion between successive SAR images into account. We have compared the estimation results to measured ice thickness values and to the values produced by our operational ice thickness algorithm. The evaluation results, especially for the Gulf of Bothnia area were promising. Still some further development will be required before making the algorithm operational, and we also discuss on possible further development towards an operational system.

1 Introduction

Currently, SAR data in winter navigation in the Baltic Sea is used in various ways: in the routine sea Ice Charts (IC's),in the visual interpretation of SAR data and SAR-based level Ice Thickness Charts (ITC's) [6]. All products are provided by the Finnish Ice Service (FIS). Radarsat-1 ScanSAR Wide mode and Envisat ASAR Wide Swath mode images are used to produce spatially more accurate ITC's than given by the traditional IC's. A SAR based ITC is operationally produced after a radar image has been received, using the latest available digitized routine IC as an initial input (either from the previous day or the same day, depending on the receiving time of the SAR image). The ice area boundaries in the digitized IC are then relocated to correspond the area boundaries of the SAR image segments. And inside the generated segments, the thickness values are mapped to be between the segment minimum and maximum thickness values (given by the digitized IC) based on SAR image segment backscattering means (i.e. filtered SAR backscattering) values. The resulting ITC's are delivered to the end-users in 500 m resolution. In the approach proposed here we have replaced the ice thickness information given by the digitized IC with the modeled thickness values computed in a grid covering the whole Baltic Sea, and additionally utilize SAR-based ice motion information.

We shortly describe the logic how the ice thickness values provided by an ITC are obtained. In the traditional IC's a single segment (here called an IC segment) covers a large area where one level ice thickness class can be regarded to be dominant. The diversity in the ice characteristics inside an IC segment is represented by assigning a range of ice thickness values to each segment. As described above, the ITC algorithm assigns the largest thickness value, to correspond to the SAR segment with the strongest backscattering. The justification of this assignment is the following. If only level ice appear inside the IC segment, the small scale surface roughness on average increases with age, i.e. thickest level ice usually produces the strongest SAR response. If also deformed ice areas appear inside the IC segment, we assume that on average the amount of deformation events increases with the age of the ice field. According to this reasoning, the locally oldest and thickest level ice (with respect to its neighboring areas) is usually situated in the most deformed ice zones yielding on average the strongest SAR response. On the other hand, the ITC algorithm assigns the smallest ice thickness value in the given

range to the smoothest area (the area with the weakest radar response) inside the IC segment. Crucial for this approach is that the given level ice thickness ranges for IC segments are realistic. During several winters in-situ measurements have been made throughout the whole ice season by the Finnish icebreaker staff. These data sets have shown that the values provided by the ITC's are close to the measured level ice values. Hence, the input information received from the IC's is of high quality.

The current operational ITC's always require a digitized IC as its input, and this requires human interference in the processing chain. Our goal in this work is to be able to produce ice thickness charts also for sea areas where only coarse resolution IC's, or no IC's at all are available. A novel product based on a thermodynamic snow and sea ice model, named HIGHTSI (HIGH-resolution Thermodynamic Snow/Ice model) [1, 9], and SAR data has been developed. This fully automated algorithm can then be run without IC data as its input. We use the Baltic Sea as our test area because the ice conditions in this area are rather well-known due to extensive monitoring and the operational ITC's offer a natural reference point for the development work. Also very representative SAR data sets are available because of the operational use of SAR data to aid navigation in the Baltic Sea.

2 SAR and Sea Ice

SAR is an active microwave sensor. It illuminates the target with a coherent EM field and measures the backscattered (usually) incoherent signal. The radar response depends on the radar configuration and on the dielectric properties of the target. The radar parameters for the space-borne SAR instruments (RADARSAT-1, RADARSAT-2, ENVISAT) used for sea ice monitoring at FIMR are: wavelength (C-band) f_c=5.3–5.4GHz, ($\lambda \approx 5.6$ cm), polarization HH (in current operative sea ice applications), incidence angle 18–45 degrees (wide swath images). Magnitude of the radar response (in dB) weakens roughly linearly as a function of the incidence angle, and this must be taken into account in SAR classification. We have developed an algorithm for SAR incidence angle correction [10, 7] and have applied it in our sea ice SAR applications. The resolution of the SAR data in ScanSAR mode images covering areas of about 400–500 km in width and best suitable for sea ice remote sensing is typically in the range 100–150 m.

Also the snow properties affect the measured SAR backscattering. Snow properties affecting the SAR backscattering include snow thickness, wetness, stratification of the snow layer and roughness of the snow/ice interface (superimposed ice). The ice properties affecting the SAR backscattering are the surface roughness of ice (both at small- and large-scale), the ice layer structure, especially the sizes and spatial distribution of brine pockets and air bubbles, salinity and temperature of the ice (especially near the melting point). Contribution from ice-water interface not significant at C-band. Backscattering model studies suggest that at C-band the scattering is dominated by reflections from the ice surface, also in the Baltic Sea.

Validation of the methods is difficult, because of the dynamic nature of the target and difficulties in making in-situ measurements on the sea. We have in-situ measurements from several field campaigns and we also receive ice measurements from ice breaker ships and coastal observers every winter. Our validation data consists of helicopter-borne electromagnetic induction device (HEM) measurements (during field campaigns), airborne laser scanner (ALS) measurements (field campaigns) coastal and field campaign observations, and ice breaker measurements.

The upper limit for the thermodynamically grown ice thickness in drift ice areas relatively low. The larger ice thickness values are due to mechanical deformation. The deformation processes change the ice surface roughness and, hence, the SAR backscattering. The obstacle is that many different deformation processes occur (rafting, ridging, rubble fields, ice floe break-ups, brash ice) and influence on SAR backscattering. Also the snow cover modulates the radar response. The net result is that the dependence between ice thickness and SAR backscattering can be described only statistically. In addition, the statistical model depends on the typical local ice conditions in each sea area. Fine resolution data analysis (SAR/ALS) has shown that at certain conditions the dependence between ice free-board and SAR

backscattering can be described with a high accuracy. On the other hand, in some other snow/ice conditions (wet snow), the dependence does not exist. HEM/SAR data also shows that the level ice thickness on average increases with increasing SAR backscattering. As level ice ages the small-scale ice surface roughness increases due to weathering. Locally we can make an approximation that level ice thickness increases linearly with increasing SAR backscattering.

3 Ice Thickness Estimation Algorithm

The algorithms described here have further been developed from our first attempts to generate ITC's based on a thermodynamic snow/ice model and SAR data[4]. We utilize an improved HIGHTSI snow/ice model to estimate the ice growth, SAR data to describe the spatial distribution of different ice thickness classes, and particularly, pairs of successive SAR images over their common areas are applied to detect the ice motion, a feature which was not included in our previous work. Similar to our previous work, we have restricted to Radarsat-1 ScanSAR Wide mode data only. SAR data over the winter seasons 2004–2005 and 2005–2006 were used in this study and the corresponding ITC's were produced. The number of the acquired SAR images during the ice season 2004–2005 was 96 and during the ice season 2005–2006 160. We have used data of February and March 2005 (87 SAR images) as a training data set and the data of February–April 2006 (111 SAR images) as a test set. In order to estimate ice thickness evolution more accurately, particularly in the melting season, the HIGHTSI ice model was updated by incorporating a more sophisticated albedo scheme. The heat and mass balances at the ice-ocean interface were improved by applying a parameterization of oceanic heat flux associated with the ice concentration. HIGHTSI was forced with the ECMWF (European Centre for Medium-Range Weather Forecasts) 24 hours forecasts of wind speed, air temperature, relative humidity, cloudiness and precipitation, as well as the radiative fluxes. The ECMWF data has a resolution of 11×11 km^2, which also defines the model resolution.

Ice motion is estimated from two successive SAR images by performing a phase correlation between registered SAR image pairs over the common areas of an image pair [5]. The algorithm is applied in a multi-resolution pyramid to cover larger areas and to capture larger ice motions. The computed ice motion information is utilized to improve the resulting ITC in several ways. First, the fast ice regions are recognized, based on the ice motion from SAR images and the fact the areas which stay continuously in a stationary state, and a different ice thickness estimation parametrization is applied for detected fast ice and drift ice areas.

The areas of uniform motion, including the areas with no motion, are also located. Assuming that only small changes in the local ice conditions have occurred during the few days period (short time scale compared to the fast ice detection) between the SAR images over these areas moving as a uniform field, we have several SAR measurements of the same ice field available, and we now use the median value of these values for each such segment in the ice thickness estimation. We also use the cross (phase) correlation between each pair of two SAR images as input for the ice thickness estimation for the latter image.

The inputs currently used in the estimation of a SAR segment are ice thickness values produced by the HIGHTSI ice model, H_h, median value of the available measurements of the same ice field (segment), I, and a product term between HIGHTSI thickness and the SAR pixel median value, H_hI. The product term H_hI is included to take into account the terms of the form $(a_1H_h + b_1)(a_2I + b_2)$ in the estimation, i.e that H_h is modulated by I. The multiple linear regression analysis showed that the product term is of essential significance. We have also studied the use of cross correlation (if available), C_c and local SAR autocorrelation, C_a, as features in the ice thickness computation. It seems that their contribution to the estimate is neglectable. However, we are currently using the temporal minimum (C_c) of the cross-correlation. We are studying of more useful ways to utilize C_c and C_a.

We used two methods to estimate the output, i.e. the ice thickness based on the inputs: a linear model and a nonlinear model. The linear model weights were define based on a least squares fit using

the training data set. The LS-solution for the linear coefficient vector A with the linear model $H = FA$ is

$$A = F^{\dagger}H, \tag{1}$$

where F is a feature matrix, the kth line of the matrix contains the feature vector $F_k = [\, H_{hk}\ I_k\ H_{hk}I_k\ 1\,]$, H contains the ice thickness values from the operational model, and $F^{\dagger}$ is the Moore-Penrose pseudoinverse of F:

$$F^{\dagger} = (F^T F)^{-1} F^T. \tag{2}$$

The nonlinear method was a two layer Multi-Layer Perceptron (MLP) neural network trained by using the error backprobagation algorithm with the same training data set, except that only H_h and I were used as input variables. The hidden layer nonlinearities were implemented using the hyperbolic tangent (tanh) function and the output layer with one output (the estimated thickness) was linear. Feed-forward neural networks, such as MLP, with a single hidden layer of sigmoidal units are capable of approximating uniformly any continuous multivariate function, to any desired degree of accuracy [2]. As an example, a simple MLP with three hidden units is shown in Fig. 1. According to our experiments the estimation error did not significantly reduce with more than five hidden units, and we used five hidden units in our tests. The weights were initialized randomly, and the parameters used in tests were simply selected by running the algorithm 100 times with different random initializations and selecting the weight set giving the smallest estimation error for the training data set. The advantage of the MLP-model is that we can feed the input variables into the network and train it with the desired output values without building a model of the relation between the inputs and the output(s). On the other hand, because no probability modeling is used in MLP, the evaluation of the uncertainty related to the MLP outputs is difficult to determine. The quality of the results depends on how representative the training set is. Open water areas

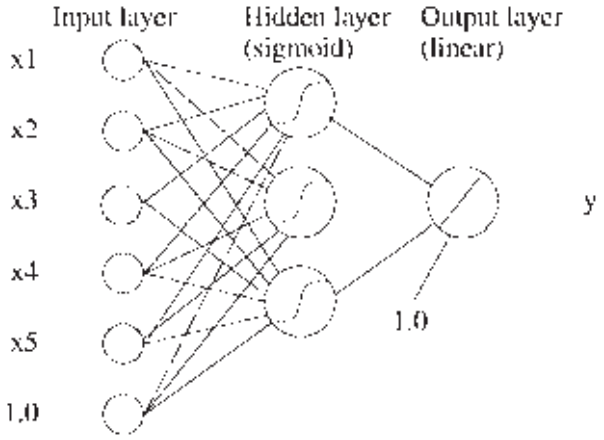

Figure 1: A MLP network with five inputs x_i, the input with 1.0 is the bias term, three hidden nonlinear units, and one linear output unit. Each connection has a weight factor associated to it and the outputs of the hidden units are the sigmoid function applied to the sum of its weighted inputs, and in the output layer the weighted sum directly.

were detected based on a dual-thresholding of the local autocorrelation [8]. Open water is not allowed to appear in areas with an estimated ice thickness higher then a given threshold.

Unfortunately we do not have sufficiently in-situ measurements available to train and test the algorithm properly. We have some EM measurements made during the winter 2004–2005, but it was impossible to extract the level ice thickness from the distributions of the EM measurements over SAR segments. Because of these facts, we have used the operational ice thickness charts as the ground truth in our training data set.

4 Experimental Results

We used data from February–March 2005 for training the algorithm. These data mostly represent dry snow conditions. Results for this new algorithm were computed over the period February–April 2006 and were compared with existing point measurements and ice thickness values of the operational ITC's. Without the ice motion information [4], the ice thickness of the model-based ITC's were typically overestimated for the drift ice and underestimated for the land-fast ice. The new algorithm performs better than the previous algorithm without the ice motion estimation, compared to the in-situ measurements.

The training data consisted of 87 SAR images and their areal distribution was 49 images over the Bay of Bothnia, 6 images over the Gulf of Bothnia (Quark area), 4 images over the Archipelago sea, and 28 images over the Gulf of Finland. The corresponding numbers for the test data are 48, 25, 7, and 31, respectively (totally 111 test set images). The Gulf of Riga is visible in most of the images of Gulf of Finland and in about half of the images cover the Archipelago Sea. It should be noted that the area of Gulf of Riga is clearly smaller than that of the Gulf of Finland, and again the area of Gulf of Finland is smaller than the area of Bay of Bothnia or Gulf of Bothnia. This means that the training data are dominated by the data from Gulf of Bothnia and Bay of Bothnia.

Some examples of the ITC's produced by the algorithm are shown in figures 2, 3 and 4. In Table 1 some overall results for the whole studied area are shown, and in Figs. 3 and 4 the Gulf of Bothnia area is shown for two randomly selected cases. For comparison, also the operational ITC's are shown in the figures.

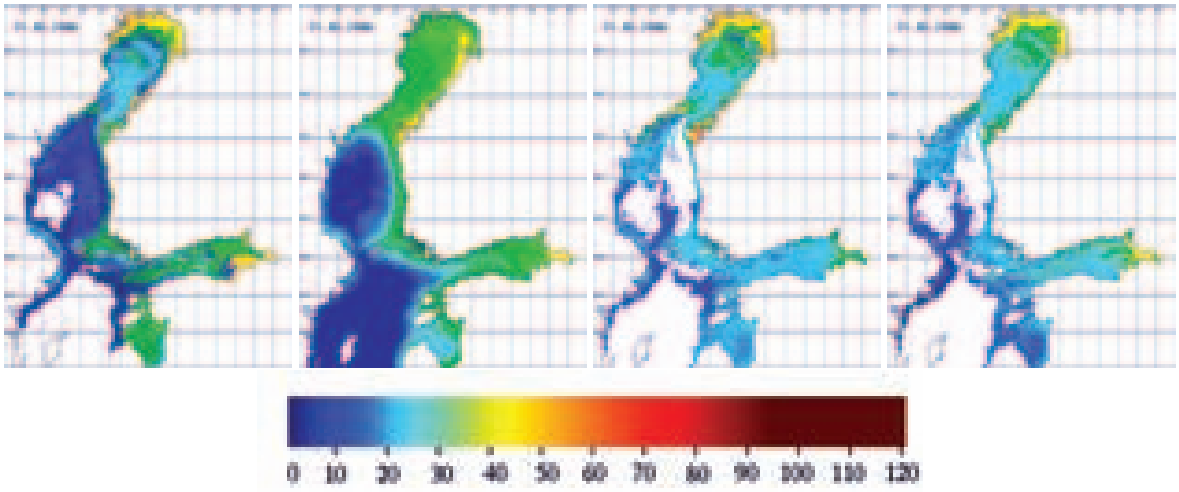

Figure 2: The operational ice thickness on March 11th 2006 (the first chart from the left) and the ice thickness produced by HIGHTSI (second chart), estimation by the proposed method, linear (third chart) and nonlinear (on the right) methods. The values are in cm, the colorbar at the bottom is showing the color mapping.

Comparison of both the methods to measured ice thicknesses (35 measurements in February-April 2006) gave very promising results. The mean L_1 error for the linear method was about 8.5 cm and little more for the nonlinear method, the corresponding error for the operational method was about 8 cm. On the other hand the difference between the methods and the operational method were about 7.5 cm, meaning that they behave differently from the operational method. Subtracting the systematic error (only for this test set) the error of the new methods was very close to that of the operational method. However, we have not studied yet, whether there exists such systematic deviations in the training dataset. For detailed results, see Table 1 and Fig. 5.

We also compared the two new methods with the operational method in different areas of the Baltic Sea. These results are presented in Table 2. It can be seen that the algorithm performs the best in the

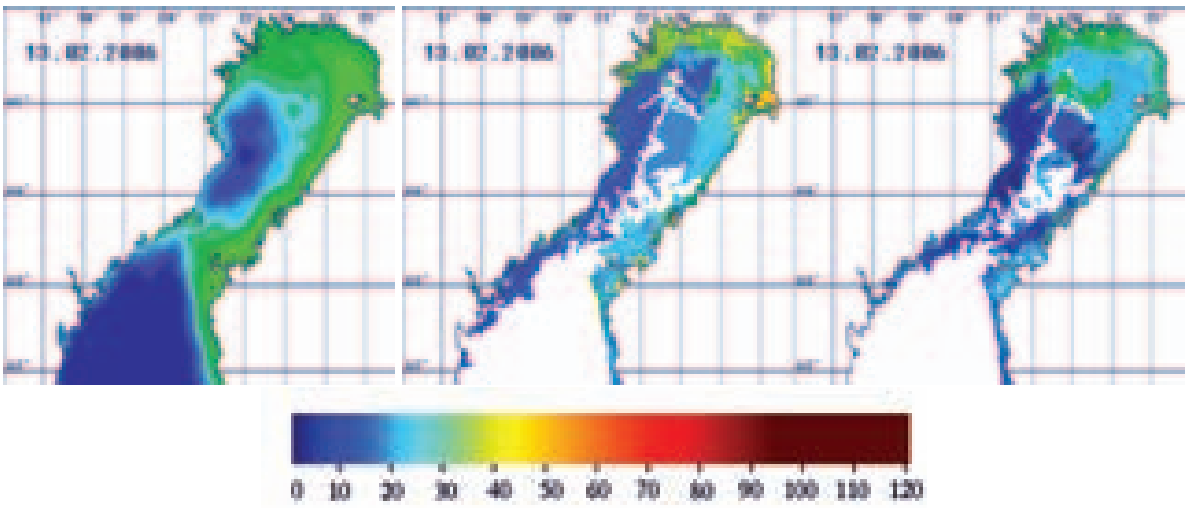

Figure 3: Febr 13th 2006, HIGHTSI, ITC (HIGHTSI+SAR), operational ITC.

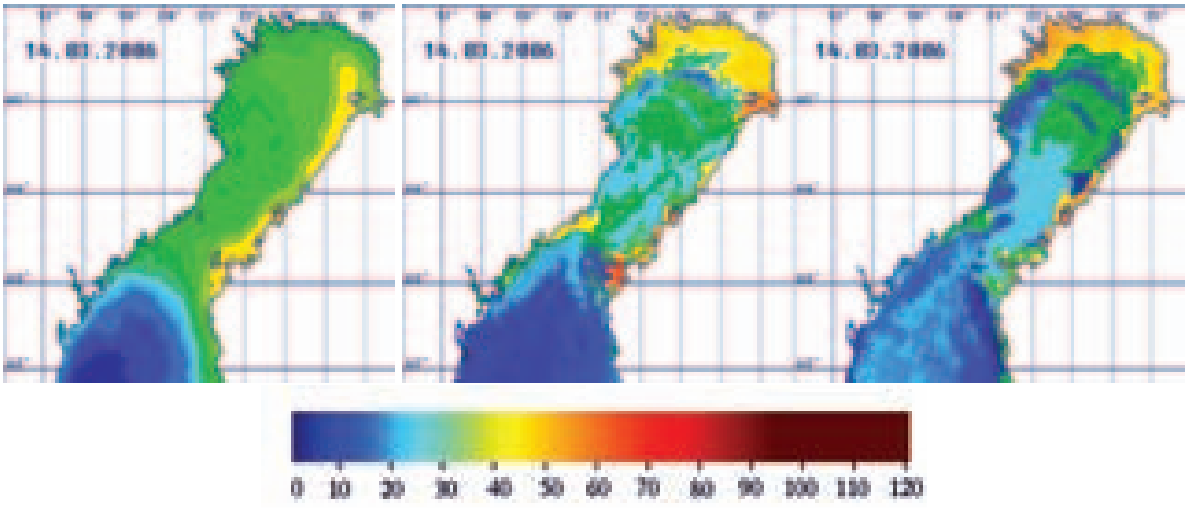

Figure 4: March 14th 2006, HIGHTSI, ITC (HIGHTSI+SAR), operational ITC.

Table 1: Comparison of the operational product and measurements made by ice breakers. Also comparisons to the values produced by the operational system are made. The values are in cm. The corrected values are computed by correcting the systematic error between the measured values and the estimates.

Comparison	L1 error
Operational ITC vs. measured	8.06
HIGHTSI+SAR linear vs. measured	8.51
HIGHTSI+SAR nonlin. vs. measured	9.09
HIGHTSI+SAR linear vs. oper. ITC	7.60
HIGHTSI+SAR nonlin. vs. oper. ITC	7.37
HIGHTSI+SAR linear (corr.) vs. measured	8.25
HIGHTSI+SAR nonlin. (corr.) vs. measured	8.39

Bay of Bothnia (BoB) and Gulf of Bothnia (GoB). The relationship between SAR σ^0 and ice thickness is complicated and can be described only statistically. In addition, these statistical models are valid only

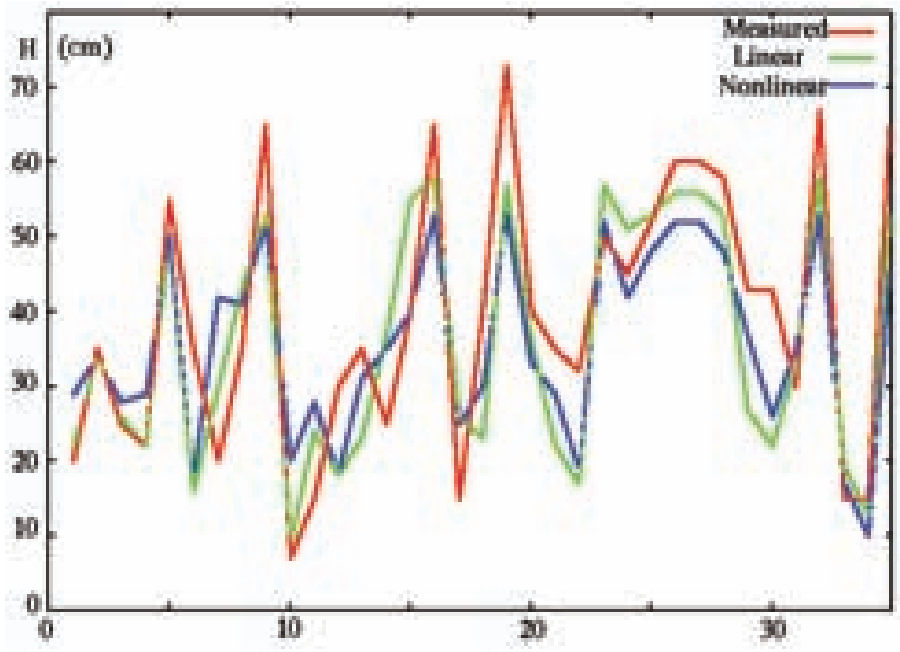

Figure 5: Comparison of the estimated ice thicknesses (linear and nonlinear model) to the measured ice thickness values. The numbers on the horizontal axis refer to the measurement number, in ascending temporal order.

locally [11]. Because in our case most of the training samples originated from the Bay of Bothnia and Gulf of Bothnia, the model works also with best accuracy in these areas. The statistical dependence between the radar response and ice thickness must be defined separately for each climatologically different sea areas. We note that there is a significant latitude difference between BoB, GoB and Gulf of Finland (GoF) and Gulf of Riga (GoR). Hence, the local climate and the resulting ice cover significantly deviate from each other in these areas. Also the relative errors in the GoF and GoR are higher than in the GoB area, because the mean ice thicknesses in Gulf of Finland and Gulf of Riga are smaller. During the melting period the SAR-based ice thickness estimation did not improve the thickness values given by the model significantly. This is due to the low σ^0 contrast between different ice types in wet snow conditions. Possibly this can be improved to some extent by performing a separate training for wet snow conditions.

Table 2: Comparison of the operational product and the new product in different areas of the Baltic Sea. BoB=Bay of Bothnia, GoF=Gulf of Bothnia, Quark area and the Archipelago Sea, GoF=Gulf of Finland, GoR=Gulf of Riga. L1 errors (L1) and cross-correlations (CC).

February–March 2006						
Area	HIGHTSI L1	Lin. L1	Nonl. L1	HIGHTSI CC	Lin. CC	Nonl. CC
BoB	14.86	8.13	9.17	0.279	0.774	0.789
GoB	12.25	8.37	8.57	0.551	0.564	0.538
GoF	10.22	10.70	9.28	0.595	0.554	0.635
GoR	11.57	9.72	10.27	0.413	0.326	0.356
April 2006 (melting period)						
BoB	15.50	11.02	11.69	0.331	0.439	0.483
GoB	11.77	11.46	10.57	0.626	0.466	0.497
GoF	16.94	22.74	15.66	0.637	0.553	0.508
GoR	19.29	16.69	17.98	0.393	0.569	0.664

It seems that, in general, the linear model produced slightly better results for our test data compared to measurements, but in some cases also the nonlinear model performs better. This behavior may be due to over-fitting of the nonlinear model to the training data set.

We have also made some comparisons with the distributions of the model-based and operational ITC's. Typically in these comparisons, the distributions are similar in shape, but the locations of visible peaks may typically differ a few centimeters, see Fig. 6.

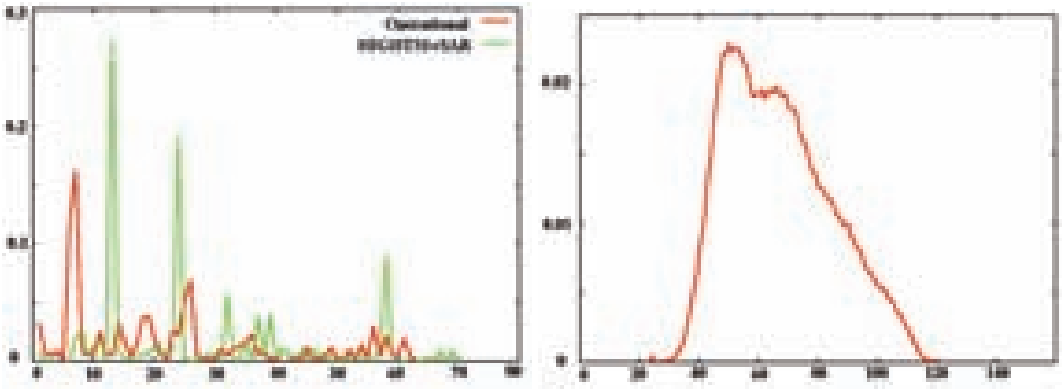

Figure 6: Ice thickness distributions from the operational ITC (left) and from the model-based ITC (middle) for March 10th 2006. For comparison, we also show the SAR pixel intensity distribution (right). This example clearly shows the different shapes of the SAR distribution and the ice thickness distribution.

5 Possible Algorithm Improvements

Mostly the overall estimates seem reasonable in BoB and in GoB, but in some cases there seem to occur abrupt changes in ice thickness. These are probably due to changes in SAR backscattering level. To avoid occasional sudden jumps in the ice thickness values, we have made some preliminary tests with a simple method restricting the changes in the ice thickness distributions between temporally adjacent ITC's. In our simple first model the distributions are described by two parameters mean (μ) and standard deviation (σ) and the distributions are assumed to be Gaussian. The change in these values is restricted by applying a Kalman filter [3] to the two-valued time series, x=[μ σ] with the assumption that the distribution parameters remain the same. First, we write the system (or evolution or prediction) equation and then the observation equation for the Gaussian noise:

$$\begin{aligned} \hat{x}_k^- &= A\hat{x}_{k-1} + v_k, \quad v_k \sim N(O,Q) \\ z_k &= H\hat{x}_k^- + w_k, \quad w_k \sim N(O,R) \end{aligned} \tag{3}$$

In our case we assume that both the the system operator A and observation operation H are just identity matrices. In the Kalman filtering we have the following updating steps. First the state vector and its error covariance are predicted according to:

$$\begin{aligned} \hat{x}_k^- &= A\hat{x}_{k-1} + v_k \\ P_k{}^- &= AP_{k-1}A^T + Q \end{aligned} \tag{4}$$

the index k refers to time. Next, the Kalman gain (matrix) K is computed, and the predicted state estimate and its error covariance are analyzed (corrected) on the basis of observations z:

$$\begin{aligned} K_k &= P_k{}^- H^T (HP_k{}^- H^T + R)^{-1} \\ \hat{x}_k &= \hat{x}_k^- + K_k(z_k - H\hat{x}_k^-) \\ P_k &= (I - K_k H)P_k{}^- \end{aligned} \tag{5}$$

For each time step, we get analyzed (or corrected) estimates of the distribution parameters $\hat{x}_k = [\mu_e \ \sigma_e]$. In the case of Gaussian distributions the scaling of thickness values H to new ones H_{new} is obtained as:

$$H_{new} = \mu_e + \frac{H - \mu}{\sigma}\sigma_e, \tag{6}$$

where μ and σ are the mean and standard deviation for the ice thickness H of previous ice level chart. Currently the parameters for the Kalman filter are experimental, i.e. the process noise covariance and

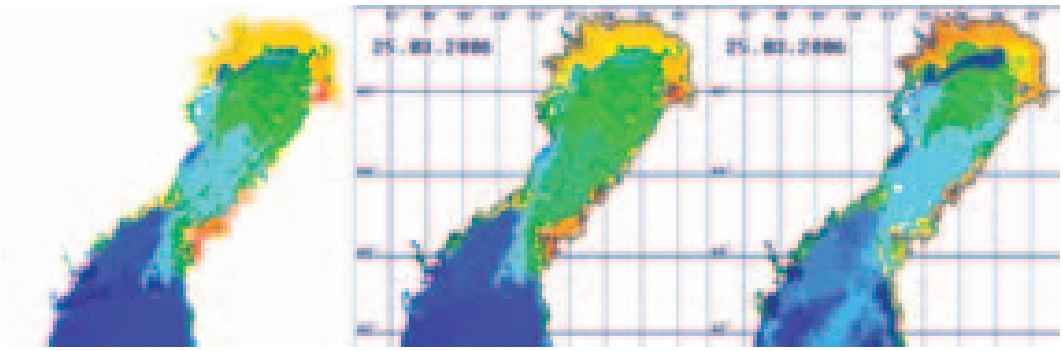

Figure 7: ITC on March 25th 2006 with the restricted change in distribution (left), the ITC without any restrictions (middle), and the operational ITC (right).

observation noise covariance matrices, Q and R were not estimated from data. An example of one test is shown in Fig. 7. It can be seen that the result is closer to the operational ITC. Also other smoothing methods based on Kalman or Kalman type filtering will be studied. One of the basic ideas in the Kalman filtering is to correct the predicted state according to known (or estimated) error statistics. Due to the complicated nature of error statistics in our case we will study also other dynamic updating schemes where the correction can based on the physical arguments. The assumption of Gaussianity is not true for ice thickness distributions. For example log-normal distributions could be closer to the ice thickness distributions.

Wet snow on the sea ice may change the SAR signal drastically, e.g. by increasing the σ^0 in the level ice case. Thus wet snow conditions and melting/refreezing cycles may cause rapid oscillations in the ice thickness values given by the algorithm although the ice cover thickness remains practically the same. We are also going to study including weather information in the algorithm, either directly from temperature information or snow information produced by an updated version HIGHTSI. We expect that the use of this information will reduce the abrupt changes in estimates.

We have also made some preliminary studies of longer-term ice motion statistics based on the motion estimated from SAR data. We have computed the monthly distributions of the estimated ice motion for the winter 2006 for six Baltic Sea areas: eastern Gulf of Finland, western Gulf of Finland, Gulf of Riga, Bay of Bothnia, southern Gulf of Bothnia, and Archipelago Sea. We are going to study could of the ice motion history statistics be used to further improve the algorithm performance.

6 Conclusion

The results with the current algorithm were clearly better than the results achieved by our earlier algorithm [4], the mean L_1 error for the earlier algorithm compared to the measurements was 11.8 cm. The results clearly show that this new ice thickness algorithm has potential for operational use in the area of the Baltic Sea. Also the usability in other sea areas will be studied.

There seems to be clear differences between the algorithm performance in different areas of the Baltic Sea. This suggests that the training should be performed separately for different sea areas, at least for the Gulf of Bothnia and Gulf of Finland, possibly also for the archipelago sea and Gulf of Riga. The

performance during the melting period was not improved by utilizing SAR data, and a separate training for melting period will also be performed.

The use and computation of the features derived from the ice motion will be studied more carefully, and also including other additional features (e.g. segment size and shape) into the classification will be studied. We also aim to study how to utilize the divergence (computed from ice motion) in open water detection. We also study the possible use of areal drift statistics derived from SAR data.

It was also noticed that sometimes large thin ice areas suddenly turn into much thicker ice regions. Also abrupt changes to other directions for large areas were observed. Physically this kind large scale thickness transitions are unrealistic. We will try to avoid these jumps by adoptinga Kalman filter or Kalman filter type approach. The critical steps are the definition of the state vector and the determination of the allowed state evolution.

In some cases there also exist obvious disagreements between HIGHTSI model output and the SAR data and we are also studying the ways to handle these disagreements efficiently. Also the parametrization of the HIGHTSI model will be studied to find optimal parametrizations for different sea areas and conditions.

With the current parameter setting the linear and nonlinear models produced rather similar results. However, the linear modulation model assumes a rather simple linear relationship between the inputs and the output, and with more input variables a more refined model will probably be required, e.g. a generalized additive model. Another alternative for modeling the input-output relationships is to use the MLP training for learning the relationships. The optimization of the nonlinear estimation algorithm parameters will be studied and also the use of hybrid model combining the results of linear and nonlinear model will be studied. The training and test data sets will be extended to cover several years. We have SAR images and operational ITC's for this purpose available, and we are able to make the model runs, using the also archived forcing data, for all the ice seasons with available ITC's and SAR data.

We also have interests to apply these algorithms in other sea areas than Baltic Sea only. Our main interest are in the Arctic areas.

References

[1] B. Cheng, T. Vihma B, R. Pirazzini, and M. Granskog. Modeling of superimposed ice formation during spring snow-melt period in the baltic sea. *Ann. Glaciol.*, 44:139–145, 2006.

[2] K. Hornik, M. Stinchcombe, and H.White. Multilayer feedforward networks are universal approximators. *Neural Networks*, 2(5):359–366, 1989.

[3] R. E. Kalman. A new approach to linear filtering and prediction problems. *Journal of Basic Engineering*, 82(1):35–45, 1960.

[4] J. Karvonen, B. Cheng, and M. Simila. Baltic sea ice thickness charts based on thermodynamic ice model and sar data. In *Proc. of the International Geoscience and Remote Sensing Symposium 2007 (IGARSS'07)*, pages 4253–4256. IEEE, 2007.

[5] J. Karvonen and M. Simila. Sar-based estimation of the baltic sea ice motion. In *Proc. of the International Geoscience and Remote Sensing Symposium 2007 (IGARSS'07)*, pages 2605–2608. IEEE, 2007.

[6] J. Karvonen, M. Simila, and I. Heiler. Ice thickness estimation using sar data and ice thickness history. In *Proceedings of the IEEE International Geoscience and Remote Sensing Symposium 2003 (IGARSS'03)*, volume I, pages 74–76. IEEE, 2003.

[7] J. Karvonen, M. Simila, and M. Makynen. An iterative incidence angle normalization algorithm for sea ice sar images. In *Proceedings of the IEEE International Geoscience and Remote Sensing Symposium 2002 (IGARSS'02)*, volume III, pages 1524–1528, 2002.

[8] J. Karvonen, M. Simila, and M. Makynen. Open water detection from baltic sea ice radarsat-1 sar imagery. *IEEE Geoscience and Remote Sensing Letters*, 2(3):275–279, 2005.

[9] J. Launiainen and B. Cheng. Modeling of ice thermodynamics in natural water bodies. *Cold Reg. Sci Technol.*, 27(3):153–178, 1998.

[10] M. Makynen, T. Manninen, M. Simila, J. Karvonen, and M. Hallikainen. Incidence angle dependence of the statistical properties of the c-band hh-polarization backscattering signatures of the baltic sea ice. *IEEE Transactions on Geoscience and Remote Sensing*, 40(12):2593–2605, 2002.

[11] M. Simila, J. Karvonen, C. Haas, and M. Hallikainen. C-band sar based estimation of baltic sea ice thickness distributions. In *Proc. of the International Geoscience and Remote Sensing Symposium 2006 (IGARSS'06)*, pages 710–713, 2006.

Sea Ice Index

Marzenna Sztobryn[*], Natalija Schmelzer[^], Jouni Vainio[#], Patrick B. Eriksson[#]

[*] Instytut Meteorologii i Gospodarki Wodnej, IMGW OM – Poland ,
Email Marzenna.Sztobryn@imgw.pl

[^] Bundesamt für Seeschifffahrt und Hydrographie, BSH Rostock - Germany,
Email natalija.schmelzer@bsh.de

[#] Finnish Institute of Marine Research, FIMR Finland ,
Emails jouni.vainio@fimr.fi, partick.eriksson@fimr.fi

Abstract

Planning of the port and navigation activity during the winter as well as seasonal forecast must be based on a proper estimation of potential change of the sea ice conditions. The goal of the investigation presented in the paper was to check the applicability of the sea ice index S, to the other areas of the Baltic Sea, for comparison of sea ice conditions in different, even distant sea basins as well as for application to climatological practice and for application to forecasting practice. The presented sea ice index S is a representative of sea ice condition on the Baltic and enables to observe these conditions and their changes over longer terms of time. The high correlation coefficient (between S and other climatological indices) gained, point up their high usefulness both to climate studies and in the planning of the maritime management. The revealed changes in sea ice conditions in last twenty years are the evidence that the changes tend towards the warmer terms.

1. Introduction

The aim of this investigation was to check the applicability of the sea ice index S, primarily developed for the Southern Baltic Sea conditions (Sztobryn 2005, 2006), to the other areas of the Baltic Sea. The index S has been evolved for climatological and practical purposes: for seasonal forecasting and climatology as well as for evaluation of sea ice condition severity and for properly planning of port activities in severe winters. Index S is the tool - very easy to use, because it calculation is based on the one parameter only – on the seasonal number of days with ice.

The occurrence of sea ice is one of the most important factors of climate detection and of its variability. The Baltic Sea, though a small one in the global scale, is one of the busiest communication arteries in the world. Its geographic situation, however, gives an occasion to obstructions in winter navigation due to the sea ice appearance, which occurs, more or less frequent and more or less voluminously, nearly each winter in this sea. Proper classification of the winter season in respect of ice conditions in particular sea basins, also these geographically more distant and differentiated, allows for better comparison and for a possibility of future seasonal forecasting.

Hitherto the thermal conditions; as totals of cold (e.g. Wisniewska, 1991) were used us a base for winter classification, or a combination of thermal conditions and of number of days

with ice (Betin et al.,1962; Drużynski et al. 1990). Prüfer (Pruefer 1942) used obstruction to navigation, Koslowski and Schmelzer (Koslowski et al. 1995; Schmelzer 2008) introduced the volume of ice, and Palosuo and Seina (Seina et al.1996) – the maximum ice extent. The detailed analysis of the above classifications carried out by IMGW (Stanislawczyk et al. 1995) revealed that beside of the sums of cold method (which, however, need regular, daily temperature records) no classification exists, which could be applied to different and distant areas. The best know indicator, the maximum ice cover extent (Palosuo, Seina), is of more general character, i.e. it represents the ice conditions in the whole Baltic Sea.

2. The sea ice index formula

For possibly immediate assessment of the climate changes in the Polish coastal zone the sea ice index S was educed the seasonal number of days with ice and the probability of ice occurrence.

$$S = 0.05 \times \frac{1}{i} \sum_{i} \left(\frac{N}{p} \right)_i$$

S - sea ice index,
N - the number of days with ice observed during the winter season on the particular station,
p - the probability of ice occurrence on the particular station, calculated for the analyzed period and
i - stands by number of stations taken into account.

Further investigations (Schmeltzer et al., 2008; Sztobryn et al., 2008) confirmed the usefulness of the index S both for the estimation of climate changes and for classification purposes of winter season severity. It proved also successful in comparing the ice conditions severity of different basins and in port and space planning. For this reasons, the authors decided to check the applicability of the sea ice index S to the other areas of the Baltic Sea by calculation of regional indices and average index.

3. The area of investigation

Estimation of the regional indices of sea ice (S_{reg}) and the mean index of sea ice (S_{avg}) has been based on the ice data sets stored by the national ice services of Finland (FIMR- Finnish Institute of Marine Research), Poland (IMGW- Instytut Meteorologii i Gospodarki Wodnej) and Germany (BSH – Bundesamt für Seeschifffahrt und Hydrographie). The investigational material covered 7 sea basins of the Baltic Sea and included data from 34 observing posts, recorded in the winter seasons from 1955/56 to 2004/05 (Fig.1).

Each of these 7 sea basins (from which the data were possible to acquire), different in respect of the thermal conditions and frequency of ice appearance, included several observing posts or areas. There were

- Western Baltic Sea (German waters), with: Unterwarnow, Warnemünde, Kiel LH; symbol in paper : “WB”,

- Southern Baltic Sea (Polish waters), with: Zalew Szczeciński, Świnoujście, Kołobrzeg, Gdańsk, Zalew Wiślany; "SB",
- Gulf of Finland (Finish waters), with: Hanko, Russarö, Helsinki. Harmaja, Helsinki LH, Loviisa, Orrengrund, Hogland; "GF",
- Sea of Åland and the Archipelago (Finish waters), with: Maarianhamina, Koppaklintar, Lågskär, Turku, Bogskär (Kihti), Utö; "AL",
- Sea of Bothnia (Finish waters), with: Rauma, Kylmäpihlaja, Raumanmatala; "SoB",
- Norra Kvarken (Finish waters), with: Vaasa, Ensten, Norrskär; "NK",
- Bay of Bothnia (Finish waters), with: Ajos, Mutkanmatala, Kemi One, Ykspihlaja, Repskär, Tankar; "BoF",

Fig.1. Areas of investigation

The probability of ice occurrence in the sea varied from 0,28 in Kiel Light House to 1 in many several areas in the years considered. Probability equal to 1 means that the sea ice was recorded in each of the 50 analysed seasons.

4. Regional sea ice indices

The calculation of S_{reg} was based on the observation from each investigated sea basin from 50 seasons (1955-2004). S_{avg} index was computed as the average of 7 regional indices. Detailed assessment of sea ice index in particular sea basins (regions) of the Baltic Sea are presented in Table 1.

Table 1. Sea ice indices (S_{reg}) in the Baltic Sea in the winter seasons 1955/56-2004/05

season	avg-Baltic	WB	SB	GF	AL	SoB	NK	BoB
1955/56	6,3	3,9	5,4	6,6	4,6	6,9	7,7	8,9
1956/57	4,2	0,4	1,5	3,9	1,6	5,0	8,0	9,0
1957/58	5,0	1,6	3,0	5,4	3,7	5,8	7,1	8,3
1958/59	3,0	0,6	1,6	2,6	0,7	3,0	5,1	7,2
1959/60	4,9	1,2	3,2	6,5	3,8	5,1	6,7	7,9
1960/61	2,3	0,2	1,2	1,1	0,0	1,5	4,8	7,5
1961/62	3,8	0,3	3,3	4,1	1,6	4,5	6,1	7,1
1962/63	6,2	5,2	7,1	5,8	4,8	5,8	7,0	8,0
1963/64	4,4	0,5	5,1	4,1	2,2	4,6	6,5	7,6
1964/65	3,8	0,3	2,5	4,1	1,8	4,2	6,2	7,3
1965/66	5,7	1,2	3,1	6,9	5,5	6,1	7,8	8,9
1966/67	3,5	0,0	1,3	4,4	1,5	3,4	6,1	7,7
1967/68	4,3	0,2	2,0	4,4	2,2	6,4	6,7	7,9
1968/69	5,2	0,8	3,8	6,3	3,5	5,1	7,6	9,2
1969/70	6,1	4,9	4,1	6,5	5,9	5,6	7,6	8,4
1970/71	4,2	0,4	1,7	4,7	2,1	5,1	7,3	8,0
1971/72	4,5	0,7	1,8	5,3	3,1	5,5	7,2	8,2
1972/73	1,9	0,1	1,0	2,3	0,3	1,2	2,9	5,6
1973/74	2,9	0,0	1,0	3,1	0,0	1,7	5,6	9,2
1974/75	1,4	0,0	0,1	0,8	0,0	0,5	2,9	5,8
1975/76	4,0	0,4	1,9	5,0	2,4	4,4	6,0	7,8
1976/77	4,3	0,5	1,6	6,0	2,2	4,8	6,7	8,2
1977/78	4,0	0,2	1,3	5,0	2,8	4,4	6,4	7,9
1978/79	6,3	5,6	4,4	6,6	5,1	5,5	8,0	8,7
1979/80	4,6	0,6	2,7	5,3	3,9	4,8	7,0	7,8
1980/81	4,3	0,1	1,4	3,8	2,2	5,8	7,4	9,3
1981/82	5,1	2,5	3,5	5,0	3,3	5,6	7,4	8,4
1982/83	2,7	0,0	0,5	3,3	0,8	3,2	4,8	6,6
1983/84	4,2	0,2	1,5	4,9	2,3	4,8	6,8	8,8
1984/85	6,3	5,6	4,8	6,1	5,4	6,5	7,5	8,4
1985/86	5,4	2,8	3,3	5,8	4,2	5,7	7,7	8,4
1986/87	6,3	5,6	4,5	6,1	5,8	6,5	7,6	8,2
1987/88	3,3	0,0	0,7	4,2	0,6	2,9	6,2	8,3
1988/89	2,4	0,0	0,3	1,5	0,0	2,3	4,8	7,7
1989/90	2,0	0,0	0,5	1,7	0,0	1,0	4,0	6,7
1990/91	2,8	0,4	1,5	3,0	0,4	1,8	5,1	7,0
1991/92	1,6	0,1	0,4	0,7	0,0	1,2	3,3	5,4
1992/93	2,5	0,1	1,0	1,4	0,4	1,8	4,6	8,2
1993/94	4,5	0,3	1,2	5,9	3,4	5,0	7,5	7,9
1994/95	1,9	0,1	0,6	1,6	0,0	1,2	3,4	6,3

1995/96	6,3	5,7	4,7	6,4	5,1	6,2	7,2	8,6
1996/97	3,3	0,8	1,9	2,2	0,4	4,4	5,3	7,9
1997/98	3,1	0,1	0,7	4,4	0,3	2,5	5,8	7,8
1998/99	3,7	0,1	1,5	4,6	1,7	4,3	5,9	7,5
1999/2000	2,6	0,0	0,1	1,6	0,2	3,7	5,2	7,7
2000/01	2,7	0,0	0,7	3,0	1,9	3,0	4,3	6,1
2001/02	2,8	0,1	0,9	2,2	0,6	3,3	5,2	7,1
2002/03	5,5	0,8	2,7	6,7	4,1	7,1	7,9	9,0
2003/04	3,4	0,1	1,1	4,2	2,1	4,4	5,3	6,9
2004/05	3,0	0,1	1,0	3,0	1,7	3,3	5,2	6,6

5. Basic Statistical Parameters

Highest values (Tab. 2) of all basic statistic parameters are characteristic for the Bay of Bothnia, where the values of S_{reg} oscillated between 9,32 (1980/81) and 5,34 (1991/92). The lowest values of S_{reg} were gained in the Western Baltic Sea, with the minimum, equal to 0,0, which occurred eight times, and the maximum S_{reg} equal to 5,72 (1995/96). Pretty unexpectedly, not very far from the citied values recorded in the Western Baltic Sea were the extreme conditions in the Åland Sea and the Archipelago. Maximum of the index S_{reg} reached in Ålands Sea 5,89 (1969/70) and the minimum value was 0,0 (four times) . However, despite of the similar extreme values, these two regions differ in respect of the sea-ice severity: the median of S_{reg} is in the Western Baltic Sea lower than 0,33, while in the Ålands area median of S_{reg} reaches 2,06. Also the mean values of S_{reg} in this regions differ from each other and are as high as 1,11 and 2,24, respectively. The averaged sea ice index S_{avg}, describing the whole Baltic Sea, oscillated between 6,31 in 1986/87 and 1984/85, and 1,44 in 1974/75. Its mean value and median were nearly alike, and equal to 4.

Table 2. Basic statistical parameters of the indices S_{reg} and S_{avg} in the winter seasons 1955/56 to 2004/05

	avg-Baltic	WB	SB	GF	AL	SoB	NK	BoB
max	6,3	5,7	7,1	6,9	5,9	7,1	8,0	9,3
min	1,4	0,0	0,1	0,7	0,0	0,5	2,9	5,4
mean	4,0	1,1	2,1	4,2	2,2	4,2	6,1	7,8
median	4,0	0,3	1,6	4,4	2,1	4,4	6,3	7,9

The values of basic statistical S_{reg} parameters, when compared, allow to distinguish three groups of regions, which are similar to each other with regard to the sea ice conditions. The first group, “mild winters zone”, consists of the Western Baltic Sea, Southern Baltic Sea and the Åland Sea; the other group, “normal winters zone”, make the Gulf of Finland and Sea of Bothnia. Into the third group, “severe winters zone” should be included the Norra Kvarken and Bay of Bothnia, which have the statistical parameter of S_{reg} positively higher than they are in the remaing regions (i.e the ice conditions more severe than somewhere else in the Baltic Sea regions considered).

The similarity in ice conditions character in the grouped regions is confirmed by the frequency distributions of their S_{reg}: curves of $S_{reg,}$ in the ascending order, in the three sea

regions of the first group begin in the lowest part of the "mild winters zone", in only one case (one winter in one region) they cross the lower limit of the "Bay of Bothnia zone" and they are "concave". All this means predominance of mild conditions (despite of inclusion of the "icy" inlet – Zalew Wislany); in the second group (Gulf of Finland and Sea of Bothnia) the extreme values are still very close to these of the first group, the means and medians however are much higher, so that the ascending curves of S_{reg} are a little convex; this results from the nearly uniform occurrence of all types of winters this group; in the third group – the basins of Norra Kvarken and the Bay of Bothnia – the ascending curves of S_{reg} are clearly convex due to predominance of severe sea ice conditions and they begin nearly at the limit between the mild and normal, or in the middle of the normal winters zone.

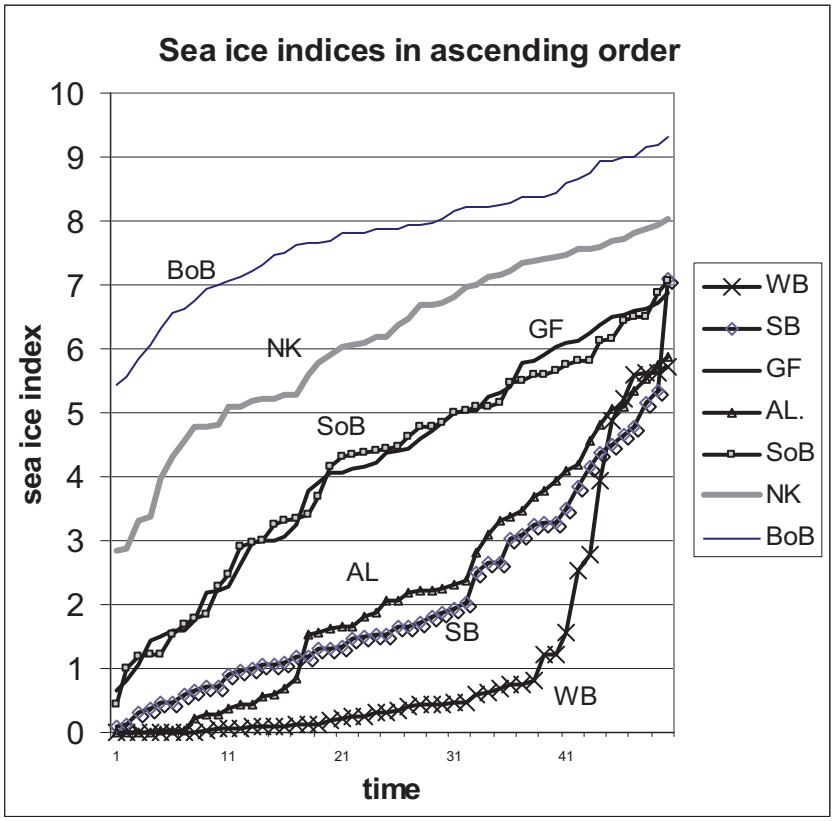

Fig.2. Values of indices S_{reg} of the sea regions considered, in ascending order

6.Classification and changes of seasonal sea ice conditions

The classification was based on the 50 seasons (1955-2004) long series of empirical percentiles, derived from the values of individual regional winter severity indices S_{reg} for the particular sea basins. Accepted were 3 types of winters, colloquially fixed as mild (M), normal (N) and severe (S) using two qualifying thresholds, percentile 33% and 67% (Tab.3). The 12 winters (1955/56,1957/58,1962/63, 1965/66, 1968/69, 1969/70, 1978/79, 1984/85, 1985/86,1986/87, 1995/96, 2002/03) were classified as severe in all the sea basin, 4 winters (1964/65, 1975/76, 1977/78, 1998/99) as normal ones and 6 winters (1972/73, 1974/75, 1982/83, 1989/90, 1991/92, 1994/95) as mild ones.

Table 3. Percentiles 33% and 67% calculated for particular sea basins

	Avg-Baltic	WB	SB	GF	AL	SoB	NK	BoB
Percentil 33%	3,07	0,12	1,19	3,26	0,84	3,33	5,28	7,63
Percentil 67%	4,45	0,62	2,66	5,25	3,08	5,11	7,12	8,23

Only in one season – 1973/74 – was characterized by occurrence of all three types of winter severity on the different sea basins.
The four additional mixed types of severity off sea ice are establish as M-N (mild and normal conditions on the different basins with mild types predominance), N-M (mild and normal conditions with normal types predominance), N-S (normal and severe conditions with normal types predominance) and S-N S (normal and severe conditions with severe types predominance). The decadal frequency distribution of the types of sea ice conditions are presented in the table 4.

Table 4. Frequencies of sea ice conditions calculated according the proposed classification, in particular sea basin of the Baltic Sea. 1955/56-2004/05.

	M	M-N	N-M	N	N-S	S-N	S
1955-1964		2		1	3	1	3
1965-1974	2		1		2	1	3
1975-1984	1			2	4	1	2
1985-1994	3	4			1		2
1995-2004		4	3	1			2

During the first three decades (1955/56-1984/85) the severe and severe – mixed sea ice conditions were predominant; where since 1985; mild and mild-mixed types were predominant. The revealed changes in sea ice conditions in last twenty years are the evidence that the changes tend towards the warmer terms.

Relations of the sea ice index S_{avg}, which was calculated by averaging the regional sea ice indices S_{reg}, from seven selected sea basin, with some general parameters dealing with climatic changes have been analyzed. Highest, statistically significant values of linear correlation was gained in comparison to maximum ice cover extent in the Baltic Sea – MESIC [%] with correlation coefficient equal to 0,93. The correlation coefficient with second "climatological ice index" e.g. accumulated areal ice volume (Western Baltic) was also statistically significant and equal to 0,71, when the correlation coefficient with sum of coldness in Denmark was as high as 0,89.

The correlation with the winter temperature anomaly in Warszawa (Lorenc 2000) was equal to –0,84. The relation to the winter anomaly of North Atlantic Oscillation Index NAO, though statistically significant, is not high, scarce –0,29 at all.

The nearly 50 years long variation of two highly correlated indices-the formerly mentioned maximum ice extent on the Baltic Sea and the sea ice index S_{avg} (average of S_{reg}), presented in Fig.3, reveals nearly parallel conformability of the curves. The values of mean winter severity index are drawn by a heavy line, while the course of maximum ice extent is presented by a thin black line. The resemblance of their curves is striking, only in the winter 1973/74 a small opposite tendency appeared: the value S_{avg} was higher than in the year before, while the value

of max ice extent a little dropped a bit lower than the one of the preceding year. This was because the winter 1973/74 had different character in particular sea basins of the Baltic Sea and the local conditions influenced the ice growth and decay very mighty .

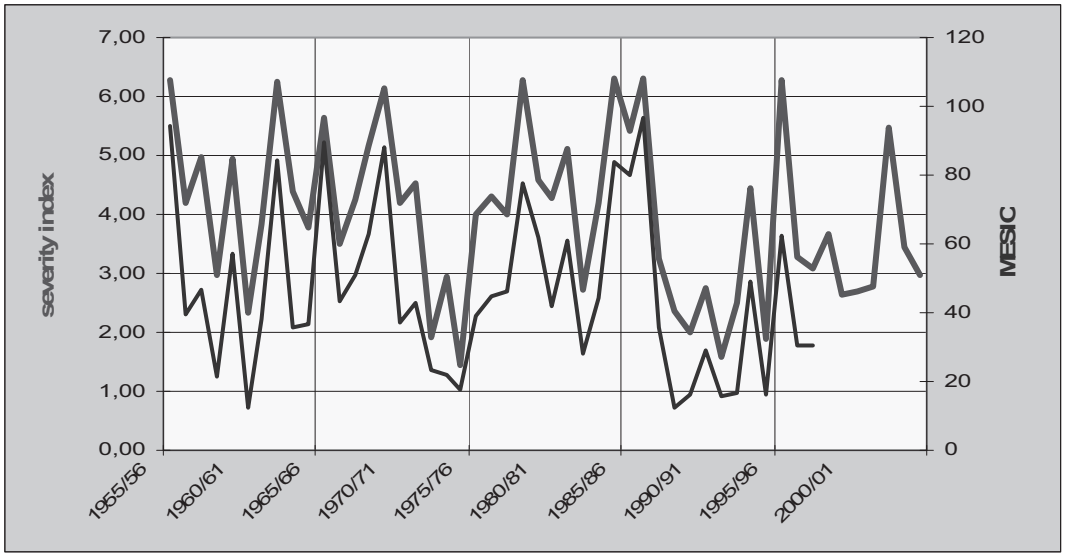

Fig.3. Nearly parallel variations of the sea ice index S_{avg} and the maximum sea ice extent MESIC [%] in the years 1955/56-2000/01.

Additional investigations have been directed to find relations of the computed S_{avg} with the atmospheric situation types in central Europe, e.g. as presented Hess and Brezowski in their Katalog der Grosswetterlagen Europas, with supplements [2004]. Best, statistically significant correlation types, namely the type Wz (West cyclonic), for which the correlation was negative and amounted to –0,44. The second one best correlated (0,42) was the type HNFz (Norwegian Sea-Femoskanian High, cyclonic).

8. Sensitivity of sea ice index

The proposed index is a function of number of observing stations included in each of the regions and-indirectly (by the probability) of the time, over which the index is calculated.

Table 5. Comparison of S_{reg} values in the Finnish waters in case of different number of stations and different years of observations.

Area of observation	S_{reg} – Sea Ice Indices					
	Selected Finnish stations 1955/56-2004/05			Complete set of Finnish stations 1970/71-1999/2000		
	max	min	mean	max	min	mean
BoB	**9,3**	**5,4**	**7,8**	**9,1**	**5,2**	**7,5**
NK	**8,0**	**2,9**	**6,1**	**7,3**	**2,4**	**5,3**
SoB	**7,1**	**0,5**	**4,2**	**6,6**	**0,5**	**3,5**
Al.	**5,9**	**0,0**	**2,2**	**6,9**	**0,3**	**3,0**
GoF	**6,9**	**0,7**	**4,2**	**6,7**	**0,6**	**3,9**

In order to find how these two factors can influence the values of the sea ice index, two trials have been carried out. The first one was made using the Finnish data. Two groups of the sea ice indices were considered. The first one consisted of the stations used in the previous calculations from the years 1955/56-2004/05; the other one included data from all the observing stations managed by the Finnish Ice Service, however from the years 1970/71-1999/2000 only. Comparison of the results has shown that the maximum difference between the values of S_{reg} gained from these two, time-shifted and numerously different groups of data, amounted to only 17% and the mean error was smaller than 10% (Table 5).

Taking into account considerable difference in the two compared periods one should admit that the proposed formula of the sea ice index could be useful even when the data would be partly incomplete.
Similar conclusions can be drawn if the comparison would be drawn on the Southern Baltic sea ice index gained from two time-shifted periods (Table 6).

Table 6. Comparison of sea ice index values in the Polish waters in the case of two differing time intervals.

Southern Baltic Sea	Southern Baltic Sea Ice Index					
	Set of selected Polish stations 1955/56-2004/05			The same set of Polish stations 1946/47-2005/06		
	max	min	mean	max	min	mean
S	**7,11**	**0,11**	**2,14**	**7,24**	**0,11**	**2,26**

In the case of Southern Baltic Sea and time-shifted interval of observations the maximum error was less than 6% (due to the less contribution of the new added data). It confirms the usefulness of applicability of proposed index.

Summary

The investigation of the applicability of the proposed, sea ice index S, to the other areas of the Baltic Sea confirmed its usability especially for :

- comparison of sea ice conditions in different, even distant sea basins,
- application to climatological practice,
- application to forecasting practice.

The presented sea ice index S is a quite good representative of sea ice condition on the Baltic and enables to observe these conditions and their changes over longer terms of time. By definition, index S performs the occurrence of sea ice, when the severity of sea ice conditions depends also on the other parameters as concentration, thickness of ice etc. Presented in the paper indices were calculated on the basis of data from 3 national services. Further steps to adopt the index S to better representation of sea ice severity will need data from remaining services as well as the inclusion of additional factors into the formula of S. These factors should represent the volume or ability of the ice observed, concentration and thickness.

Calculated values of S_{avg} allowed to investigate the changes of sea ice conditions in relation with different climate indices. The high correlation coefficient gained, point up their high usefulness both to climate studies and in the planning of the maritime management.

The revealed changes in sea ice conditions in last twenty years are the evidence that the changes tend towards the warmer terms.

References

Betin B., Preobrazenskij J., 1962, *Surowostć zim w Ewropie i ledowost Baltiki*, Leningrad,

Drużynski B., Paszkiewicz Cz., 1990, *Metoda prognozowania surowości zim u polskich brzegów Bałtyku,* Materiały Oddziału Morskiego IMGW, Gdynia **,**

Lorenc H.,2000, Studia nad 220-letnią (1779-1998) serią temperatury powietrza w Warszawie oraz ocena jej wiekowych tendencji", Materiały Badawcze IMGW- serie Meteorologia-31,Warszawa,

Koslowski G., Glaser R.,1995, *Reconstruction of the Ice Winter Severity since 1701 in the Western Baltic*, Clim. Change 31, 79-98,

Pruefer G.,1942, *Die Eisverhältnisse in den deutschen und den ihnen benachbarten Ost- und Nordseegebieten*, Ann. d. Deut. Hydr. Mar. Met., H.II.,

Schmelzer N., Seina A., Lundqvist J.E., Sztobryn M., 2008, *Ice, in: State and Evolution of the Baltic Sea, 1952-2005*, Wiley & Sons, 199-240,

Seina A., Palosuo E., 1996, *The classification of the maximum annual extent of ice cover in the Baltic Sea 1720-1995*, Based on the material collected by Risto Jurva (winters 1720-1940) and material of the Ice service of the Finnish Institute of Marine research (winters 1941-1995), Meri – Report Series of the Finnish Institute of Marine Research, No. 27, 79-91.

Stanisławczyk I., Sztobryn, M., Drużyński, B., 1995, *Features of severity of winters at the Polish coast,* IMGW report,

Sztobryn, M., 2005, *Zlodzenie polskiej strefy przybrzeżnej w latach 1955-2005*, IMGW Report of DS.-H7 project,

Sztobryn, M., Mykita, M., Kowalska, B., Stanisławczyk I., 2008, *Ice Conditions in the Baltic Sea, Polish Coast 1896-2005,* Polish Journal of Environmental Studies, in press,

Wiśniewska, A., 1991,*Surowość zlodzenia polskiej strefy przybrzeżnej Bałtyku*, Inż. Morska i Geotechnika nr 2, 48-50,

Ice Motion Estimation from Successive RADAR Scenes

Juha Karvonen
Finnish Institute of Marine Research (FIMR)
email : Juha.Karvonen@fimr.fi

Abstract

As part of a development project ShipSensorNet we have studied the estimation of ice drift from successive captured ship and coastal RADAR images. The motion detection algorithm is based on phase correlation computed in a multilayer resolution pyramid. According to the results detecting of ice motion from RADAR data is possible. The final goal of the project is to deliver fine-resolution near-real-time (NRT) sea ice information to end users. This information mainly consists of RADAR images from ship and coastal RADAR's and products derived from them. Some additional information, e.g. ship engine power and speed, giving information on the ice resistance, is included. Also local high-resolution ice forecasts are computed. All this information from multiple sources will be integrated, delivered to end-users and shown by the end-user software.

1 Introduction

ShipSensorNet project aims to utilize a network of ship and coastal RADAR's to get a detailed information on current ice conditions in the Baltic Sea combined with remote sensing data, i.e. SAR (Radarsat-1, Radarsat-2, Envisat ASAR), visible and NIR (MODIS, MERIS), and fine scale ice modeling. ShipSensorNet is a project under the Ubicom Embedded ICT program funded by Finnish funding Agency for Technology and Innovation (TEKES) and lead by the Technical Research Centre of Finland (VTT). Also the ship performance (engine power, speed) information will be used to indicate the resistance of the ice field. Ice resistance can be estimated from the AIS (Automatic Identification System) instantaneous velocity if no engine power information is available. AIS data is already utilized in VTT's on-board software (e.g. on ice breakers). In the future the data measured by RADAR's and other instrumentation on ships will be assimilated with a local scale ice model data. The applied ice model will be the HELMI model [1] developed at FIMR. ShipSensorNet is a pilot project to study the possibilities of extracting fine resolution ice information in NRT and producing fine-scale local ice forecasts. Operational products will probably be developed in the follow-up projects. The final goal is to develop a platform capable of delivering and viewing of multiple types of ice information in multiple resolutions in an integrated environment for the ships and authorities responsible of the ice navigation.

RADAR's have much finer resolution in both space and time than typical remote sensing data. However, their measuring range is much shorter. For example temporal SAR resolution is typically 1–3 days, and RADAR resolution can be a few seconds corresponding to one RADAR antenna rotation, in practice some minutes is a reasonable scale for ice motion detection. NRT processing of coastal and ship RADAR signals (digitizing) has been implemented in the project. Hardware and software for capturing RADAR data is provided by the company ImageSoft Oy. Ice motion is one part of the information which can be extracted from the RADAR data The ice motion can be estimated from successive RADAR image pairs. Originally the ice motion detection algorithm was implemented to estimate ice motion from Baltic Sea ice SAR images. However, the same algorithm with different parameters can also be applied to RADAR image pairs.

2 RADAR

First experiments with RADAR were made by Christian Hülsmeyer 1904 in Germany, but the first operational RADAR's only came before the WWII in 1930's. The acronym RADAR comes from the words RAdio Detection And Ranging. The principle of RADAR is that it transmits pulses of electromagnetic radiation and measures the backscattered signal. Backscattering occurs when the pulse hits some target causing the backscattering.

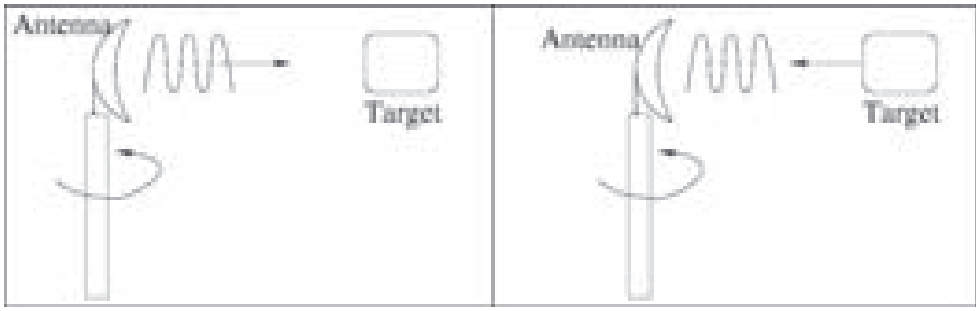

Figure 1: Principle of RADAR.

Marine RADAR's operate at 10 GHz ($\approx$ 3cm) and 3 GHz ($\approx$ 10 cm), i.e. at X and S bands. The RADAR equation relates the transmitted power P_t to the received power P_r:

$$P_r = \frac{P_t {G_A}^2 \lambda^2}{(4\pi)^3 R^4} \sigma. \tag{1}$$

G_A is the antenna gain, λ is the wavelength, R is the distance of the object from the antenna, and σ is the RADAR cross section, which is a property of the target. RADAR antennas typically rotate and scan 360 degrees around the RADAR (e.g. situated in a ship), the time for one antenna round is a few seconds, which defines the temporal resolution of the RADAR. There are both the range discrimination and the bearing discrimination related to a RADAR. The range discrimination or range resolution describes how precise the distance measurement is and it depends on the pulse length and shape. The bearing discrimination describes the angular resolution it depends on the pulse repetition rate, rotation rate and the antenna beam shape. The term clutter is used for the reflections from uninteresting targets, e.g. in the case of marine RADAR waves, rain, etc. Although called clutter these signals can be very important for other applications, like weather RADAR's.

RADAR measures the following things: Distance (range) to the target (time between transmitting and receiving), relative speed of the target (by Doppler shift or by successive locations), direction of the target (reduced resolution in far range because the angular resolution is the same in all distances), and target reflectivity which can give some information on the nature of the target. Mean ice velocity between two RADAR image acquisitions at times t_1 and t_2 is

$$v = \frac{\sqrt{d_r^2 + d_c^2} R}{t_2 - t_1}. \tag{2}$$

d_r and d_c are the image row and column index differences of a certain feature in two successive images. The origin of the coordinate system used is in the middle in the image (location of the RADAR). R is the image resolution (pixel size).

The RADAR measuring range mainly depends on the power of the RADAR and on the height of the RADAR and the height of the object. Some examples of the RADAR measuring range, assuming high enough power: antenna height from surface H_L = 30m (e.g. on ship), target height H_s = 30m, range D = 24.5NM $\approx$ 45 km, and H_L = 30m, H_s = 1m, D =14.5NM = 27km. When either the antenna height or the target height is low, the RADAR range is reduced significantly, because the radio waves at RADAR

wavelengths do not proceed very far behind the horizon. In practice typically smaller ranges than the theoretical maxima are used, 10–20km realistic, typically ship RADAR's are used to detect a range of only a few NM. One noticeable thing with RADAR's is also the RADAR shadow effect, i.e. RADAR's can not make measurements behind backscattering objects (e.g. high waves or large ice ridges in case of sea and ocean applications).

3 ShipSensorNet

ShipSensorNet is a two-year TEKES-funded project coordinated by VTT. Other project partners include Helsinki University of Technology (TKK), Finnish Institute of Marine Research (FIMR), and companies Image Soft, Bore, and BP Shipping.

The idea of the ShipSensorNet project is to get local high resolution NRT information from ship and coastal RADAR's available for the ships navigating in the Baltic Sea area, and also to get local high-resolution ice forecasts produced by a customized ice model based on the HELMI ice model [1]. This information is complementary to the lower resolution information of ice charts, space-borne satellite data (including SAR satellites and visual/NIR satellite data), observations and forecasts. Also the ship performance information can be used and delivered to estimate the local ice resistance. Additionally possible weather information, ice thickness measurements or estimates and other information collected on ships can also be shared through the network. The data will be stored on a server and the local data can then be delivered to ships depending on the ships' locations using the existing data transmission infrastructure.

Each ship and coastal RADAR in the network will be equipped with the RADAR frame grabbing system which digitizes and records the data in a digital format. The RADAR frame grabber system is developed for grabbing and recording high resolution images by a Finnish company Image Soft Oy. It is a standalone device, which is controlled via TCP/IP network. Images are stored into a database. When the database reaches a given size limit, older data will be deleted. Currently, the practical storage is performed in bursts, i.e. each RADAR rotation is saved for a short time period (e.g. one minute) followed by a break (e.g. ten minutes, which is a suitable time interval for ice drift detection). This kind of recording enables temporal filtering (e.g. averaging) of the short-time bursts and saves disk space compared to the continuous storage.

The information from RADAR can be delivered as a set of RADAR images close to the ship's position. The new products can then be viewed on map together with other existing products, e.g. SAR images. An image mosaic of the RADAR images over the area of interest is generated and this image mosaic can be viewed on ships and by other end-users. Also products derived from the RADAR data can be generated and delivered, these include the ice drift estimation and estimation of ice ridging in the area. Also synchronized animation generated from multiple RADAR's can be generated and delivered, but this requires relatively wide data transmission band. This could also be very useful for navigators, because they are skilled in interpreting such RADAR sequences. One deliverable product is the ice resistance computed along ship tracks based on ship performance information. Also information from conventional digicams mounted on ships and near coastal RADAR's can be delivered to give more information on local ice conditions.

The final goal is also to use the information extracted from the RADAR images, e.g. ridging information and motion for data assimilation to produce better local ice model forecasts. In ShipSensorNet project, the aim is however to demonstrate that this kind of information can be extracted utilized in navigation, and to build a prototype system for delivering RADAR images and processed data. In the possible follow-up projects, the system will be further developed and integrated into an operational system. Also the operating area will be extended to other ice-covered sea areas than the Baltic Sea.

4 Motion Detection Algorithm

The ice motion detection algorithm [2] was originally designed implemented for ice motion detection from successive SAR images. The ice motion (or drift) is determined for overlapping data windows using phase correlation. This approach is successful only for areas with visible features (edges). The identification of such areas for tracking is based on the magnitude of gradients computed from speckle filtered SAR images. Phase content of an image is strongly related to the edges, and thus phase correlation matching is not very sensitive to the RADAR measurement angle. A multi-resolution image pyramid representation is used for the images. The pyramid is generated by applying a half-band low-pass FIR filter designed for multi-resolution image processing. The number of resolution levels can be adjusted depending on the prevailing conditions.

To reduce the computation, the computation is performed in frequency domain using the 2-Dimensional Fast Fourier Transform (2-D FFT). The 2-D FFT is applied to N by N pixel data windows, and the FFT-coefficients of the two image windows are normalized by their magnitudes, then the FFT-coefficients of the two image windows are multiplied and the inverse 2-D FFT is applied (I_p is the phase correlation image computed from the the normalized cross power spectrum):

$$\begin{aligned}(dx,dy) &= \text{argmax}_{(x,y)}\left\{I_p(x,y)\right\} \\ &= \text{argmax}_{(x,y)}\left\{FFT^{-1}\left(\frac{(X_1{}^*(k,l)X_2(k,l))}{|X_1{}^*(k,l)X_2(k,l)|}\right)\right\},\end{aligned} \tag{3}$$

Because the FFT assumes that the data is periodic, a Gaussian window is applied to the data windows before the transformation. The best matching displacement is defined by the maximum of the phase correlation. The search for the best local phase correlation is performed in the pyramid in a recursive manner starting from the lowest resolution level to the highest. For each level two branches (two I_p's) are recursively studied: the I_p computed when the other image is moved according to the highest correlation at the previous resolution level and the I_p assuming no motion has occurred. Windows with a lower phase correlation than a given threshold are omitted, i.e. no motion value is given for these areas because the estimates are uncertain. Finally, a vector median filtering is performed with a given radius R_m (R_m=3 in our experiments) to obtain the final magnitude and direction of the motion.

5 Some Experimental results

We have had two kinds of data sets at our disposal: Photography of ship RADAR displays and data from the Raahe coastal RADAR during the winter 2008.

There occurred some practical problems with the photography of ship RADAR displays, including possible camera or monitor motion, screen reflections, and also some undesired things were drawn on the screen by the RADAR display software. We also had technical problems with Raahe coastal RADAR during 2008, and the RADAR was not working for the whole designed test period. However, RADAR data from Raahe were collected in March 2008, and some cases also include visible ice motion suitable for testing the algorithm.

Before applying the motion detection algorithm, RADAR data needs preprocessing. Temporal and spatial weighted averaging or median can be used to reduce noise. The RADAR frames were captured with only a few second (one antenna rotation) time interval between the RADAR images and temporal (weighted) averaging of several images could be used. Actually the images were captured in bursts of one minute followed by a ten minute break. The short bursts were filtered by temporal averaging, and the temporal resolution of the ice drift estimation was the duration of the break, in this case ten minutes, which is a reasonable temporal resolution for ice drift detection.

Additional filtering for photographs of a RADAR display monitor were required. To remove the electronic bearing lines (e.g. the line showing direction) and variable range markers (the round-shaped lines showing equidistances from the RADAR), we applied a gray-scale morphological opening operator

with a round-shaped kernel. An example of a photograph of an on-board RADAR display and the filtered image used in motion estimation can be seen in Fig. 2.

Figure 2: Photograph of a ship RADAR screen (left), and a filtered version of the photograph (right).

The weather conditions during the winter 2007–2008 were not very good for ice formation in the Baltic Sea and the ice cover area and thickness were significantly smaller than on an average winter. Also the ice season was significantly shorter than on average. The ice conditions near the Raahe RADAR station were varying during the test period in March 2008. Some photographs showing the ice situation during the data acquisition of the test data used here, are shown in Fig. 3. It can be seen that at the end of the period (end of March 2008) the ice was rapidly melting and on March 31st no more ice were left anymore.

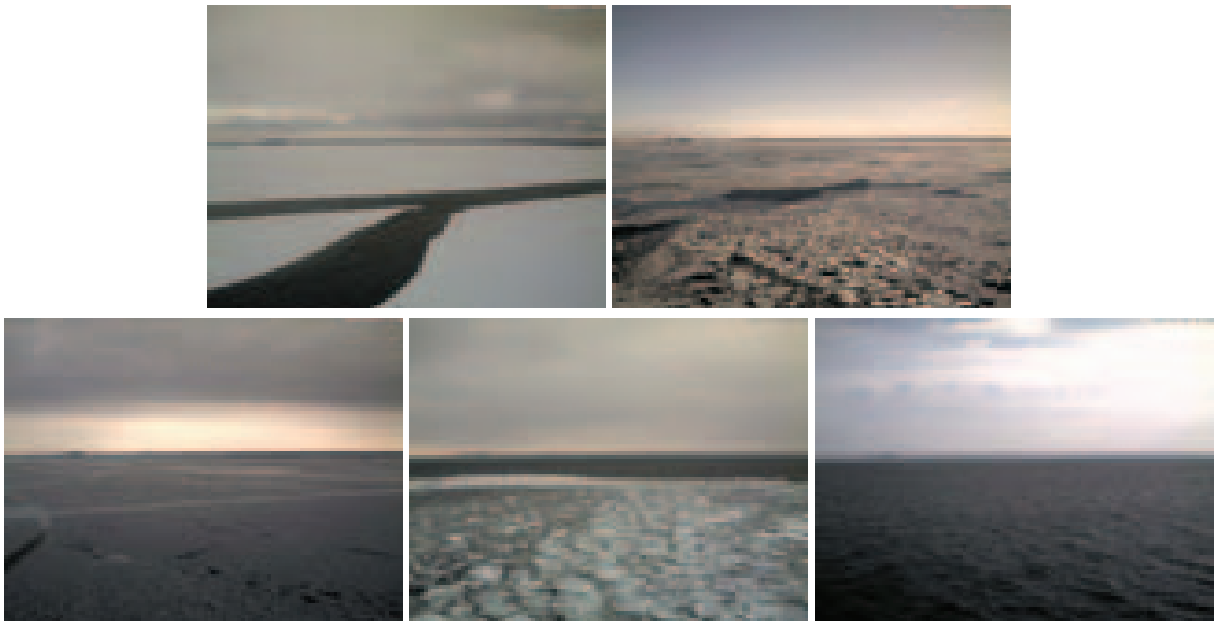

Figure 3: Ice photographed from Raahe coastal RADAR station, upper from left to right: March 6th and March 28th 2008. Lower, from left to right March29th–31st 2008 daily images. ©VTT.

We compared the algorithm results with our visual interpretation of the ice motion. The tests proved us that ice drift can be estimated from successive RADAR images after suitable prefiltering of the data. An example of three successive RADAR images captured from the Raahe coastal RADAR and the motion fields computed from the RADAR data are shown in Fig. 4. The results agree with the visual interpretation.

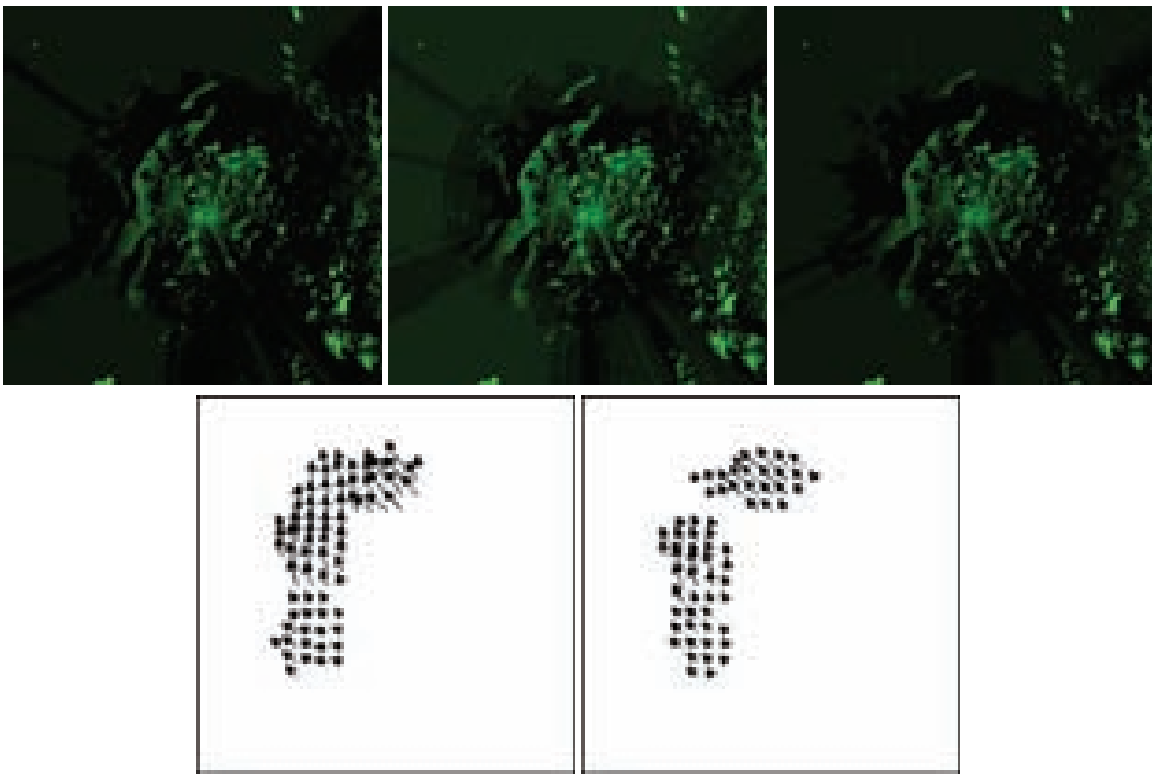

Figure 4: Motion detected (lower) between two RADAR images pairs (upper). The images were acquired on March 6th 2008 at 7:00, 8:00 and 9:00 AM local time (time zone: UTC+2 hours).

6 Conclusion and Future Work

As part of the ShipSensorNet project we have implemented an algorithm for detecting ice motion from two successive RADAR images. The algorithm is based on multi-layer phase-correlation between two RADAR images and the implementation is recursive. Preliminary tests have shown that it is possible to detect ice motion from RADAR image pairs and the algorithm can be integrated into an operational system. Data preprocessing and algorithm parameters still need some adjusting before operational use. We have noticed, that different parameters for each RADAR require adjusting. An automated or semi-automated algorithm for parameter settings should be used to avoid tedious manual parameter settings for each RADAR in the network separately. Also changes in RADAR settings (e.g. range and gain) of a certain RADAR will possibly require new parametrization of the algorithm. Automated parameter adaptation to a certain RADAR and its settings will be studied in the future.

The local ice drifts estimated by the algorithm will be used to generate simultaneous ice information for the area covered by ship RADAR's and coastal RADAR's in the network, and combined with information given by ship and coastal observations and measurements, ice analysis and remote sensing data. The ice drift product could be an image mosaic showing the amount or velocity of the ice drift. Also data assimilation of the ice drift and other ice information, derived from RADAR images, with a fine scale ice model to produce accurate local ice forecasts will be studied. The final goal is an integrated product combining several sources of information and delivered to ships and authorities. These products will, however, be developed in the possible follow-up projects, the ShipSensorNet project only demonstrates the extraction and delivery of the measurements and some possible final products. One goal in the future is that the a similar system can also be set up and applied outside the Baltic Sea.

References

[1] J. Haapala, N. Lönnroth, A. Stössel, A numerical Study of Open Water Formation in ea ice, J. Geophys. Res., v. 110, n. C9, C0901110.1029/2003JC002200, 2005.

[2] J. Karvonen, M. Similä, SAR-Based Estimation of the Baltic Sea Ice Motion, Proc. of the International Geoscience and Remote Sensing Symposium 2007 (IGARSS'07), pp. 2605-2608, 2007.

On Geophysical Property Modelling of Sea Ice: Microstructure and Salinity

Sönke Maus

Geophysical Institute, University of Bergen, email: sonke.maus@gfi.uib.no

Abstract

Geophysical sea ice properties are often defined with respect to a certain scale. The salinity of sea ice is a property that influences the role of sea ice in systems of many different scales. Proper modelling of the salinity's dependence on growth conditions, and the related change in other sea ice properties, requires the detailed knowledge of the distribution of salt within the microstructure of sea ice. Here a simple framework is presented of how sea ice salinity is related to its basic microstructure scales and how the latter quantitatively vary with growth conditions. Different modes of convective stability near the ice-water interface and in the bottom fraction of the ice are key processes in this respect. The analysis shows further how salt entrapment in sea ice and the vertical extent of the near-interface skeletal layer depend on the seawater salinity. It offers a perspective toward improved understanding of the difference in geophysical properties of ice grown from sea- and brackish water.

1 Introduction

It is well known that sea ice contains saline brine in pores and fluid inclusions, while lake ice does not[1,2,3,4]. The corresponding microstructure and salt content of sea ice are important in natural systems where sea ice geophysics is of interest. The dependence of the mechanical properties of sea ice on its microstructure and salinity is relevant in engineering applications, like traffic-ability and offshore technology in polar regions[5,6,7,8]. Biologists focus on the ecosystem of sea ice which is strongly linked to the presence and mobility of brine in pores[9,10]. The relation between microstructure and dielectric sea ice properties is important for remote sensing applications[11]. Last but not least does the role of sea ice in the climate system involve a large number of geophysical mechanisms where the sea ice microstructure and salinity are relevant[12,13,14,15].

Concise geophysical modelling of sea ice requires models of its macroscopic properties on the scale of interest. Common to most of the mentioned research fields is that the role of sea ice depends fundamentally on the entrapment and rejection process of salt during its growth and decay, which in turn has to be related to its microscopic structure. However, a basic theory of the formation and evolution of the sea ice microstructure, and the involved salinity entrapment, is still outstanding. That sea ice contains, depending on age and growth conditions, 5 to 50 % of the seawater salinity from which is formed, has long been known[16?,12,3]. However, observations of how the salt content of sea ice varies with ice thickness and external forcing are still limited. For example, a large number of empirical relations have been proposed for the variation of sea ice salinity with ice thickness. Three frequently cited relations are compared in Figure 1 with two sets of observations from the Arctic and Antarctic. Several other salinity growth sequences are shown in Figure 2. It illustrates the lack of a unique relationship between bulk salinity and thickness for thin ice. To properly describe salt rejection during early growth of ice one apparently has to take the large variability in growth conditions into account.

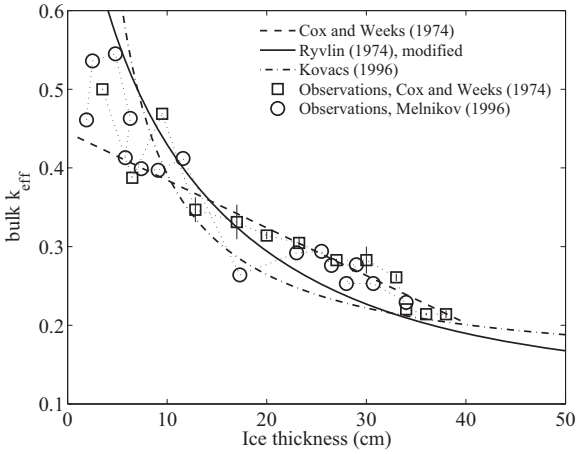

Figure 1: *Growth sequences of bulk $\overline{k_{eff}}$ of Arctic[17] and Antarctic[18] ice, shown with three suggested bulk relations[17,19,20]. Adopted from ref.[21].*

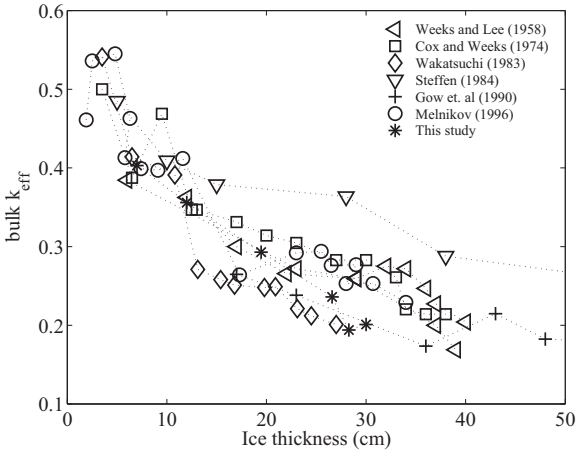

Figure 2: *Growth sequences of bulk $\overline{k_{eff}}$ (ratio of ice and seawater bulk salinities) of thin ice from several studies, to be compared with figure 1. Adopted from ref.[21].*

The salinities of thicker ice are, as long the ice is growing and not warming too much, less variable. The rule of thumb - that first-year ice contains one-sixth of the salinity of underlying water - was first suggested by Moss[22] and has been verified in many later studies[? 12,3]. Also most suggested empirical relations[17,19,20] converge, for 1 to 2 meter thick ice, to values similar to this rule. However, the physical processes that imply this constancy have not been clarified so far. A concise explanation has necessarily to consider the entrapment and mobility of brine, and thus to involve a model of the sea ice microstructure's dependence on growth conditions. Intuitively one can argue that a quasi-constant ice salinity is related to less variable growth conditions and the thermal inertia of thick ice, a useful concept that may be sufficient in a number of applications. When it comes to more detailed predictions of macroscopic properties of thic ice, or when its desalination during the summer season is of interest, a theoretical framework of the structural evolution also becomes relevant for thick ice.

In the present paper a simple model of salt/brine entrapment due to the evolution of the sea ice micro-structure is outlined. The basic idea is to (i) predict the sea ice microstructure at the interface in dependence on growth conditions and (ii) formulate the microstructural change with decreasing temperature and increasing distance from the interface. It will be seen how the scales of interest depend on different modes of convection near the interface. Finally several examples will be given to illustrate how one may proceed with geophysical property modelling of sea ice on the basis of this model.

2 Concept of salt entrapment

In principle, due to the generally 2-3 orders of magnitude slower diffusion of solute compared to heat, the desalination of growing sea ice needs to be associated with convective fluid motion. In the absence of external turbulence the convection may be thought to have its driving force in the salinity gradients set up by the rejection of salt from pure ice. However, parametrisations of sea ice desalination employed to date do not account for this process

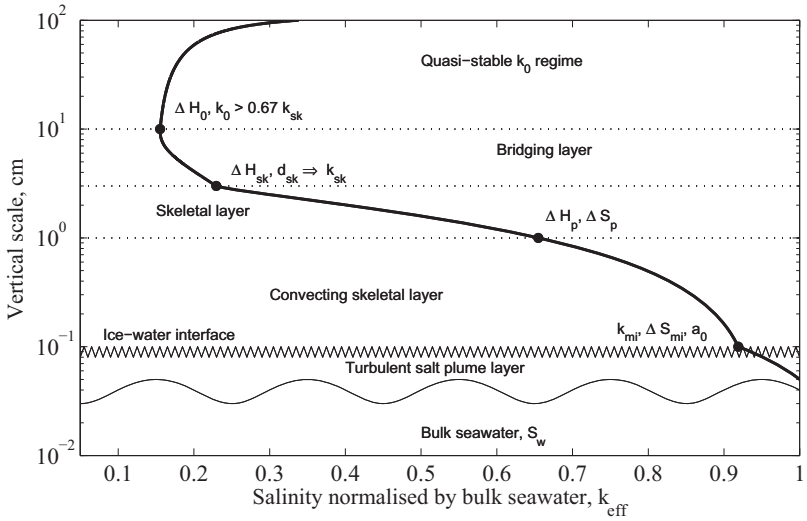

Figure 3: *Conceptual desalination of sea ice near the ice-water-interface, showing different regimes and boundary layers on a logarithmic scale: Rigorous convection takes place in the lower skeletal layer up to ΔH_p, while bridging between plates starts near ΔH_{sk}. At the distance ΔH_0 from the interface a quasi-stable salinity is reached. The local bulk salinity is normalised($k_{eff} = S_i/S_w$). Morphological changes are sketched in figure 4.*

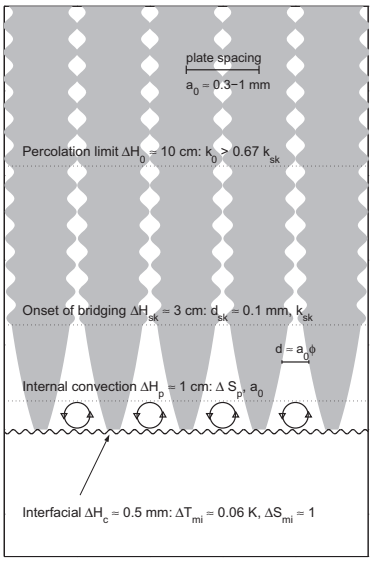

Figure 4: *Typical morphology and porosity near the interface of growing sea ice. View is normal to the plates whose spacing scale is exaggerated by a factor of 100.*

of *free convection*. The most widely used approach[23,24,25,3,26,27,28,29] is based on a forced convection model once suggested for growth of rotating crystals in metallurgy[30]. It is often reported in the form

$$k_{eff} = \frac{k_*}{k_* + (1 - k_*) exp\left(-\frac{V}{D_s}\delta_b\right)}, \tag{1}$$

with solute diffusion coefficient D_s, growth velocity V and a boundary layer scale δ_b. According to (1) the ratio of ice to seawater salinities, $k_{eff} = S_i/S_w$, increases with growth velocity from its slow growth limit k_*. A detailed discussion of why this approach has only very limited applicability for natural ice growth may be found in ref.[21], with main aspects summarised as follows. Both k_* and δ_b in (1) need to be found by a fit to observations. However, these main parameters of (1), a velocity independent k_* and a constant stagnant boundary layer of width δ_b, may, if at all, describe solute redistribution for planar interfaces. They do neither have an empirical nor a physical basis when considering cellular ice growth. Moreover does the assumption of molecular salt transport in a thin interfacial boundary layer of high salinity contrast create a misleading picture of the desalination process (and a physically meaningless quantity δ_b). The parametric form (1) may fit data in a very limited velocity regime yet is inconsistent with the main physical principles of sea ice desalination which are: (i) salt entrapment within a cellular microstructure, (ii) variation of the cellular structure with growth conditions and (iii) delayed desalination by solute-driven internal convection.

Structural modelling of salt entrapment

The present approach, developed in detail in ref.[21], considers salt entrapment in sea ice as a step-wise process on the basis of several boundary layers dominated by different physical processes as sketched in figures 3 and 4. Sea ice grows with a cellular interface consisting of vertically oriented plates between which the entrapped brine is sandwiched. This *plate spacing* a_0 is the fundamental structural parameter of salt entrapment. It depends on growth velocity and the solute transport in a thin turbulent interfacial boundary layer of thickness ΔH_c. The salt flux through the latter is linked to the constitutional supercooling ΔT_{mi} (and the corresponding salinity step ΔS_{mi}) necessary to keep the interface cellular. The plate spacing further controls the near-bottom permeability and thus the salinity increase ΔS_p that may build up internally within the ice before the interlamellar brine convects. This defines an internal boundary layer of thickness ΔH_p measured upward from the ice-water interface. It is further assumed that intermittent convection within ΔH_p will also limit the brine salinity increase up to ΔH_{sk}, marking the upper level of the lamellar skeletal layer. At this level, given by a critical brine layer of width d_{sk} and a brine volume $\phi_{sk} \approx d_{sk}/a_0$, bridging between the ice plates strongly decreases the permeability, finally rendering the flow resistance so large that the salinity gradient can not longer drive fluid motion. From two-dimensional percolation theory this is expected near $\phi_0/\phi_{sk} \approx 0.676$, e.g. ref.[31]. In summary, desalination is assumed to be driven by intermittent exchange of brine with salinity $(S_w + \Delta S_{mi} + \Delta S_p)$ against seawater, S_w, and further freezing of the latter. Percolation then sets an upper bound on the possible desalination between ΔH_{sk} and ΔH_0, and a lower bound $k_0 \approx 0.676 k_{sk}$.

In terms of this model concept the salt entrapment at the level ΔH_{sk} is given by

$$k_{sk} = r_\rho r_{gra} \frac{d_{sk}}{a_0} \left(1 + \frac{\Delta S_{mi} + \Delta S_p}{S_w}\right), \tag{2}$$

and depends on the structural length scales d_{sk} and a_0 and the salinity increase ΔS_p and ΔS_{mi} in the boundary layers. The factors r_ρ and r_{gra} are corrections slightly larger than one relate to the ice-brine density difference and the finite extent of crystals[21]. The challenge is to find physically consistent solutions for the structural parameters and the salinity change in the boundary layers. The stable salinity is then obtained from $k_0 \approx 0.676 k_{sk}$.

Plate spacing and morphological stability

That a robust prediction of the plate spacing may be obtained in terms of a macroscopic approach of classical linear stability theory for a planar interface[32,33] has been outlined in some detail[21,34]. Fundamental to this theory is the criterion of *constitutional supercooling*: (i) solute released at a freezing interface depresses the freezing point, (ii) as solute diffuses much slower than heat there will be a solutal boundary layer where the water is supercooled, and (iii) an initial perturbation of a planar freezing interface thus enters a supercooled regime may eventually grow further - a cellular interface develops. Neglecting the effect of surface tension (curvature depression of the freezing point), temperature gradients due to superheat in the water, and the details of the temperature gradient near the interface, this supercooling must exceed $\Delta T_{mi} \approx (L_v D_s)/(k_i + k_w)$, where k_i and k_w are thermal conductivities of ice and water, D_s the solute diffusivity and L_v the volumetric heat of fusion. At marginal stability, corresponding to this least value of supercooling, the plate spacing may be expected to be

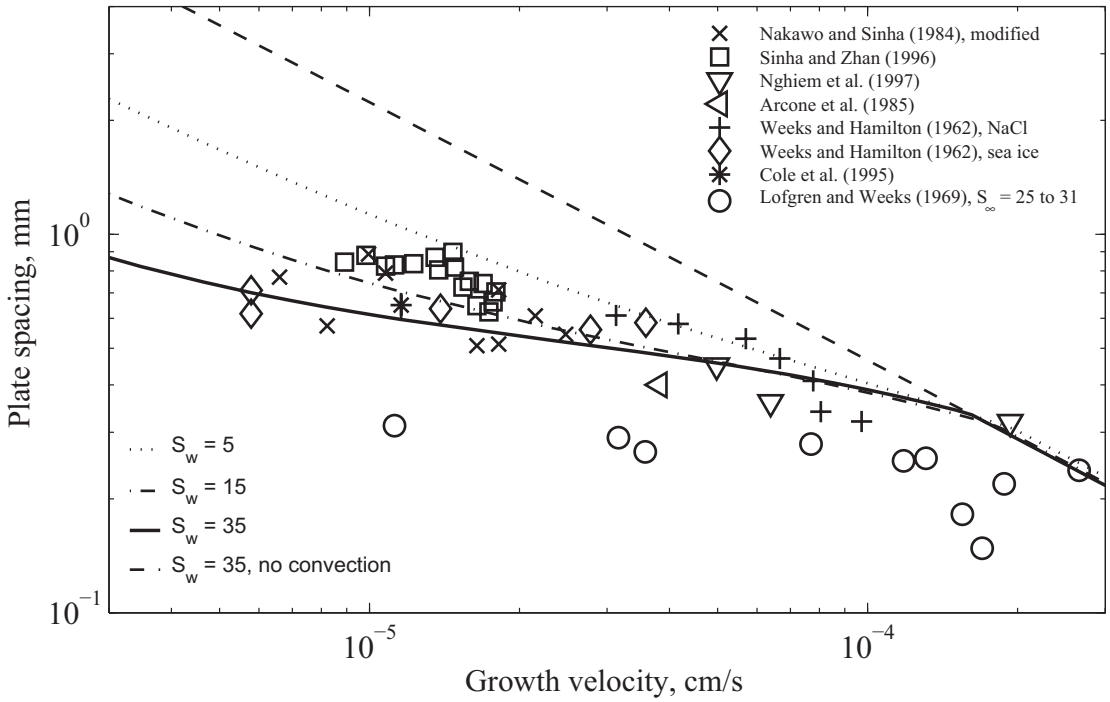

Figure 5: *Predicted plate spacings without (dashed curve) and including the convection model (solid) along with observations of sea ice and laboratory-grown NaCl ice. From ref.*[21]*, with predictions for* $S_w = 15$ *and* 5 *added.*

given by

$$a_0 \approx 2\pi 2^{1/3} \left(\frac{D_s}{V}\right)^{2/3} \left(\frac{\Gamma}{\Delta T_{mi} k}\right)^{1/3}, \tag{3}$$

where $\Gamma = T_m \gamma_{sl}/L_v$ is the Gibbs-Thompson parameter based on the solid liquid interfacial energy γ_{sl} and absolute melting temperature T_m (in Kelvin). $k(S_w)$ is the minimum effective interfacial k at which the interface is sufficiently supercooled. Neglecting again curvature effects the latter is approximately given by $k \approx (1 - \Delta T_{mi}/(mS_w))^{-1}$, where $m = dT_f/dS$ is a linearised local freezing temperature slope. The critical k thus decreases with S_w.

Equation (3) is valid as long the solute transport is by diffusion only and the width of the diffusive boundary layer is given as $\approx D_s/V$. However, above a critical growth velocity V_{cr} convection sets in and controls the boundary layer scale[a]. The dependence of a_0 on V becomes then weaker than $a_0 \sim V^{-2/3}$ in the diffusive regime. Figure 5 shows good agreement between theoretical and observed plate spacings. The significantly lower plate spacing in laboratory experiments of ref.[35] (circles) are likely explainable by strong thermal convection in the container[21]. Rather little field observations were available to the author to validate the predicted increase in a_0 at lower water salinities: plate spacings of $0.7 - 0.8$ mm reported for rapidly growing young ice in the Bay of Bothnia[36] exceed those of young Arctic Sea ice by a similar factor as in the theoretical prediction. This salinity dependence is also qualitatively consistent with the laboratory data from ref.[35].

[a]Note that the appropriate boundary layer scale $D_s/V_{cr} \approx 0.4$ mm is much smaller than values proposed on the basis of equation (1)

Skeletal layer convection

The critical brine salinity increase within the skeletal layer is computed from stability theory for freezing porous media, frequently called theory of 'mushy layers'[37,38,39], by evaluating the Rayleigh number

$$Ra_p = \frac{\beta \Delta S_p(z) g K(z) \Delta H_p}{\nu(z)\kappa_b(z)} > Ra_{pc} \tag{4}$$

based on salinity increase ΔS_p across the layer height $\Delta H_p = z$, with haline contraction coefficient β, gravity acceleration g, the kinematic viscosity ν and thermal diffusivity κ_b of brine. The permeability K is a measure of the cross-section of pores through which fluid flows. For an ensemble of infinite vertical brine layers of width d and spacing a_0 it takes the simple form

$$K = \frac{d^2\phi}{12} = \frac{\phi^3 a_0^2}{12}. \tag{5}$$

The critical Rayleigh number Ra_{pc} above which convection begins depends on boundary conditions, vertical and horizontal anisotropy and heterogeneity, e.g.[40,41,42,43]. Moreover, when K varies by more than an order of magnitude, as in the sea ice skeletal layer, it is still not clear how an effective K should be computed[43]. In an earlier work the author[21] suggested a local Rayleigh Number criterion, on the basis of local properties at each z-level, yet based on $\Delta H_p(z) = z$ and the brine salinity increase measured upward from the freezing interface ($z = 0$). An analysis of two experimental studies[24,44] then indicated a critical $Ra_{pc} \approx 6$. Here a physically more reliable criterion, the harmonic mean value of K/ν averaged upward from the interface, was employed to reanalyse the results. This yielded average values of $Ra_{pc} \approx 11$ and 14 for $S_w > 35$ and the respective datasets. The critical Ra_{pc} for $10 < S_w < 20$ however was considerably lower, in the range 2 to 4. No observations to evaluate Ra_{pc} at lower salinity are available. However, as argued below, a value of $Ra_{pc} \approx 0.25$ might be an appropriate limit. In the following calculations $Ra_{pc} = 11, 2$ and 0.25 are assumed for seawater salinities of $35, 15$ and 5.

Bridging transition and percolation

The maximum ΔH_p and ΔS_p obtained from the critical Ra_{pc} and equation (4) yield the maximum salinity increase within the skeletal layer. ΔS_p then enters equation (2) from which k_{sk} is determined. The remaining property to be determined in (2) is the critical width at which bridging of ice plates starts and transforms the basically lamellar structure into brine patches and pore networks. So far limited observations have located it 2 to 4 cm from the interface[45], consistent with the typical skeletal layer thickness, see figure 9 below. However, to date there are no direct observations of the critical brine layer width at which bridging starts between ice plates. A value of 0.07 mm noted as the 'minimum layer width before splitting of brine layers'[46] may eventually be interpreted as a lower bound. Some observations of 'pinch-off' of brine pockets indicate its onset when the brine layers have shrunk to a width of $\approx 0.05 - 0.10$mm[47,48]. A discussion of more recent microstructure statistics indicates that a plausible value is between $0.08 < d_{sk} < 0.12$ mm[21]. A concise theoretical explanation is still outstanding[b].

[b]The minimisation of surface energy, as frequently suggested[46,49,50], may be rejected because the brine layers are minimum energy surfaces[21].

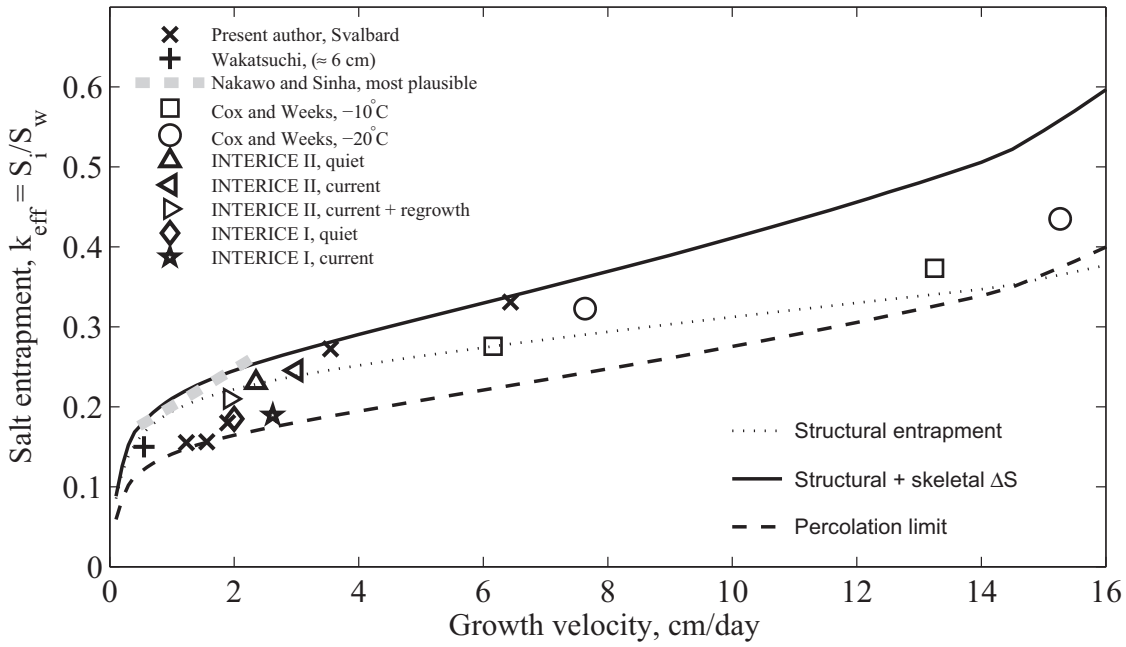

Figure 6: *Salt entrapment in sea ice. The reference data have been evaluated at ≈ 6 cm distance from the ice-water interface, based on (+) field data from Antarctic*[52]*, (x) present author's observations described in ref.*[21] *where also the INTERICE data are from several references are discussed (◇*[28]*; ⋆*[53]*; ◁ ▷ ▽△*[54]*). Due to unnatural growth conditions*[21]*, NaCl laboratory data from ref.*[24] *are only shown for $V > 3$ cm/day and $S_\infty < 40$. The grey dash-dotted line represents measured growth rates from ref.*[25]*. The curves are: The structural entrapment (thin dotted); the initial k_{sk} at the onset of bridging, where the structural value is augmented by the convectively limited salinity increase in the lower skeletal layer (solid upper curve); the lower bound 0.676 $\times k_{sk}$, based on the two-dimensional percolation conjecture (dashed curve). Observations fall consistently between upper and lower bounds.*

Henceforth a critical value of $d_{sk} = 0.10$ mm is used. The aforementioned conjecture is that the bridging process subsequently lowers the permeability and finally stabilises the salinity when a certain fraction of the brine layers is bridged. This fraction should be close to the theoretical threshold 0.676 from two-dimensional percolation theory, e. g.[31,51]. The simplistic approach limits the further salinity decrease to 0.676 of k_{sk} at the onset of bridging.

3 Sea ice salinity versus freezing rate

Equations (2) through (5) determine the relation between salt entrapment k_{eff} and growth velocity in dependence on seawater salinity. In figure 6 the predictions for $S_w = 35$ are compared to observations of k_{eff} for sea ice grown from normal seawater or NaCl solutions of comparable salinity. Observational data sets have been carefully evaluated 6 cm from the interface, a level above the highly unstable skeletal layer yet below the percolation limit (anticipated near a salinity minimum often found $\approx 10 - 15$ cm from the interface). The

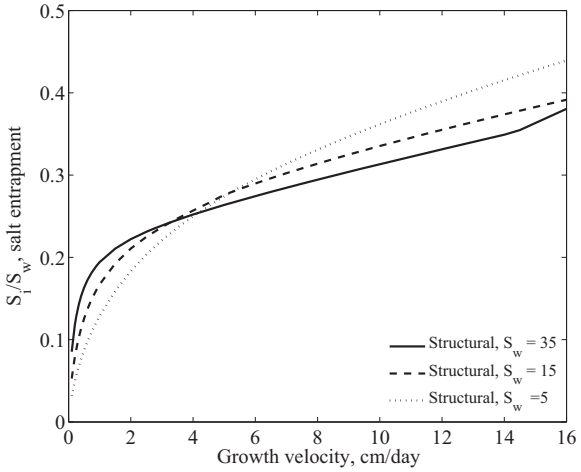

Figure 7: *Predicted structural salt entrapment* $(1 + \Delta S_{mi}/S_w)\ d_{sk}/a_0$ *for three seawater salinities.*

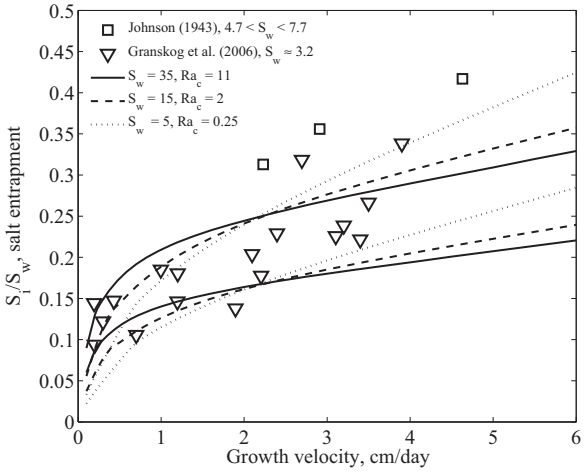

Figure 8: *Predicted upper* (k_{sk}*, onset of bridging) and lower bounds (0.676* k_{sk}*) for three salinities, compared to low salinity seawater observations*[56,29]*.*

available observations fall reasonably between the upper k_{sk} bound and $0.676 \times k_{sk}$, the lower percolation limit[c]. The variation of individual points is likely related to differences in under-ice currents and thermal history[21]. It is worth a note that the data from ref.[25], representing rapidly cooling ice with little thermal fluctuations, are consistently closest to the upper bound. The simple structural entrapment, disregarding the salinity increase ΔS_p in the skeletal layer, is also shown. It is nioted that at low growth velocity the dotted and solid curves merge, as the brine salinity gradient becomes very small.

The present approach also predicts how k_{eff} depends on seawater salinity. To illustrate the modelled behaviour, figure 7 compares the structural entrapment and interfacial supercooling $d_{sk}/a_0(1 + \Delta S_{mi}/S_w)$, excluding the internal salinity increase. At low growth velocities d_{sk}/a_0 implies an increase of k_{eff} with S_w, as a_0 increases with decreasing S_w (see figure 5). This effect is related to the boundary layer convection strength that begins to weaken at higher V for lower S_w, thus increasing a_0. The second factor, the interfacial $(1 + \Delta S_{mi}/S_w)$, becomes dominant at large growth velocities. With $\Delta S_{mi} \approx 1$ ‰ for all seawater salinities one finds an increase of k_{eff} with decreasing S_w.

The upper and lower bounds of the full prediction are shown in figure 8 for salinities 5, 15 and 35, along with observations of ice grown from low $S_w \approx 3.2$[29]. Note that the applied critical Rayleigh Numbers for $S_w = 35$ and 15 were determined empirically, while the value $Ra_{pc} = 0.25$ at $S_w = 5$ was chosen to match the observations in figure 8. The latter is, however, not unreasonable, as will be discussed in section 4 below. The effect of internal convection is to enhance the salinity dependence and steepen the slope in the relationship between k_{eff} and V at low seawater salinity. This is also consistent with limited earlier observations from Johnson[56]. His slightly larger k_{eff} is not unexpected, as his values are bulk salinities of 1 to 3 cm thick samples, likely including a more saline skeletal layer. The increasing k_{eff} with decreasing $S : w$ at high velocities is further supported by laboratory experiments from ref.[57] (not shown).

[c]Note that, while below $0.676 \times k_{sk}$ desalination driven by fluid flow is assumed negligible, some salinity decrease due to expansion upon freezing, e.g.[55], is still possible and likely enhanced by thermal cycling

Less agreement at lower growth velocities apparent in in figure 8 may be due to several factors. First, is the plate spacing expected to require a certain amount of ice growth, before adjusting to much larger values of a_0. Second, would a turbulent heat flux from the ocean to the ice require a larger effective temperature gradient for the same growth rate. This implies smaller plate spacing and larger k_{eff}, an effect suspected in laboratory data from ref.[35], see figure 5. Third, are ice growth rates uncertain: the lowest modelled growth rates shown in figure 8 are lower than the observed growth rates during that time (figure 3 of ref.[29]). Although not detailed enough for a validation, an earlier study of Baltic Sea ice by Palosuo[58] indicates $k_{eff} \approx 0.1$ for ice with $0.3 < V < 0.4$ cm d^{-1}, not inconsistent with the predictions in figure (8). To emphasise further validation the predicted $0.838k_{sk}$ between the bounds was, for the salinities $S_w = 35$ and 5, approximated by high-order polynomials[d].

4 Discussion

The proposed model for salt entrapment in sea ice provides further insight into the structure of the skeletal layer. The thickness of the latter has been determined by optical, mechanical and acoustical means to be rather stable between 2 and 4 centimeters (figure 9). The simulations of the Rayleigh-number-based convective layer thickness are compared in figure 10, with the solid curve for $S_w = 35$. Most noteworthy is that (i) the convecting layer thickness is considerably less than 2 to 4 cm and that (ii) it does not vary much over a wide range of growth rates. Comparing further the convecting layer thicknesses for the three salinities shows that ΔH_p increases with salinity.

To understand this behaviour it is helpful to compare two bounds. Consider first that the skeletal layer is given by some critical salinity excess ΔS_p. Assuming an average liquidus slope $\overline{m}$ this implies $\Delta H_p \sim \overline{m}\Delta S_p/(dT/dz)$, and as $V \sim dT/dz$ one would expect that ΔH_p decreases inversely with growth velocity. However, in reality equation (4) controls the stability, and replacing $\Delta S_p = \Delta H_p(dT/dz)/\overline{m}$ therein implies

$$\Delta H_p \sim (\overline{K} dT/dz)^{-1/2}. \tag{6}$$

With the permeability $\overline{K} \sim a_0^2$ increasing with growth velocity, (6) yields a quasi-constant convecting layer thickness under most natural growth conditions. As in reality $\overline{K}$ also depends on the near-interface porosity, and thus on the salt flux, one obtains the relationship in figure 10. Second, it is of interest to consider a salt-flux limit on the basis of a simple desalination constraint $\int_{t(z=0)}^{t(z=H_p)} (dS_i/dt)dt \approx S_w(k_{int} - k_{sk})$, where k_{int} is the value of k_{eff} at the interface. Assuming, as suggested by observations[24,55], desalination proportional to the temperature gradient and porosity, $dS_i/dt \sim \phi dT/dz$, and $dT/dz \sim V = dH/dt$ one obtains, neglecting a change in V for the small thickness change of interest,

$$\Delta H_{sk} \sim S_w \frac{(k_{int} - k_{sk})}{\overline{\phi}}. \tag{7}$$

[d]The curve for $S_w = 35$ was fitted for $0.1 < V < 16$ cm d^{-1} by the 9th order polynomial $k_{eff} = 0.0676 + 0.2161V - 0.1579V^2 + 6.618 \times 10^{-2}V^3 - 1.607 \times 10^{-2}V^4 + 2.368 \times 10^{-3}V^5 - 2.149 \times 10^{-4}V^6 + 1.172 \times 10^{-5}V^7 - 3.523 \times 10^{-7}V^8 + 4.486 \times 10^{-9}V^9$. For the restricted range $0.6 < V < 8$ cm d^{-1} a linear fit $k_{eff} = 0.144 + 0.03217V - 0.00166V^2$ represents the simulations within 5 %. At $S_w = 5$ a 7th order polynomial $k_{eff} = 0.00439 + 0.2338V - 0.1351V^2 + 5.077 \times 10^{-2}V^3 - 1.084 \times 10^{-2}V^4 + 1.304 \times 10^{-3}V^5 - 8.197 \times 10^{-5}V^6 + 2.095 \times 10^{-6}V^7$ is valid for $0.1 < V < 10$ cm d^{-1}, while in the restricted range $0.7 < V < 6$ cm d^{-1} a quadratic equation $k_{eff} = 0.0735 + 0.07295V - 0.00488V^2$ represents the simulations within 6 %.

In (7) $k_{int} \approx 1$, $k_{sk} \approx d_{sk}/a_0$ and the fraction on the right hand side is of order unity. One thus expects to first order $\Delta H_{sk} \sim S_w$ and a flux-limited skeletal layer that scales with the seawater salinity. In figure 10 a tentative bound $\Delta H_{sk} = S_w/10$ (suggested on the basis of observations for normal seawater) has been plotted three salinity values. The crossing of these bounds with the convection curves indicates where the convective layer prediction likely is not valid, because it reaches above the bridging regime, where the permeability is much smaller than given by equation 5. According to equation (6) this would increase ΔH_p even further. The system then probably cannot be described by the simplistic brine layer approach with harmonically averaged $\overline{K}$. For slowly growing ice the formation of brine channels, as observed in ref.[59], may be fundamental for the primary desalination.

A critical question is why the apparent critical Rayleigh Number for skeletal layer convection is so different for the three salinities. The sign shift of thermal expansion, taking for salinities < 24.7 place above the freezing point, stabilises the water thermally and has been suggested to play a role in this context[35]. However, its magnitude is rather small compared to the evolving haline density gradients. A more plausible explaination, pointed out in 'mushy layer' studies[60,37], appears to be the relative magnitude of the convecting skeletal layer ΔH_p compared to the interfacial boundary layer $\Delta H_c \approx 0.4 - 0.5$ mm. Simulations[60] indicate that the critical Rayleigh Number sharply decreases below a ratio of $H_p/H_c \approx 10$, a transition that in the present simulation is expected between $S_w = 35$ and 15. The rather low $Ra_{pc} = 0.25$, here employed to fit the salinity entrapment for $S_w = 5$, is not inconsistent with the latter simulations[60] and comparable values have been estimated indirectly in other systems as well[61]. A lower apparent Ra_{pc} would also be expected when convection takes place internal to single brine layers, and the effective permeability thus is ϕ^{-1} larger than given by equation 5. As discussed in ref.[21], larger grain sizes for lower S_w could then explain the observed behaviour. An important future goal is a determination of $Ra_{pc}(S_w)$ by theory and experiment, and in connection with observations of plate spacing and grain size.

5 Summary and outlook: geophysical modelling

A conceptual model for the entrapment of salt in sea ice has been formulated. The approach is based on simplistic convective stability models on both sides of the ice-water interface. Entrapment is controlled by two length-scales, the plate spacing a_0, depending on salinity and growth velocity, and the critical brine layer width at the onset of bridging between ice plates, assumed constant at $d_{sk} \approx 0.10$ mm. The plate spacing a_0 plays a fundamental role and couples the boundary layers. Being controlled by molecular diffusion and interface stability, its scaling is modified by compositional convection in a thin boundary layer in front of the advancing ice interface. It in turn controls the near-bottom permeability and extent of a lammelar high porosity skeletal layer. The implied dependence of salt entrapment on growth velocity and seawater salinity is consistent with most observations. However, open questions and uncertainties remain at very low growth velocities, where data are very sparse.

An important result of the model framework is the information obtained about the skeletal layer. Its rigorously convecting part of extent ΔH_p is predicted to be much smaller than its structural extent of $2 - 4$ cm. An indirect confirmation of convection, strong temperature fluctuations near the ice-water interface, indeed indicates a convecting layer thickness of a few millimeters[65,21]. Another aspect of interest in this connection are wider brine channels, known as locations of downward flow with a spacing of 1 to 5 cm in thin

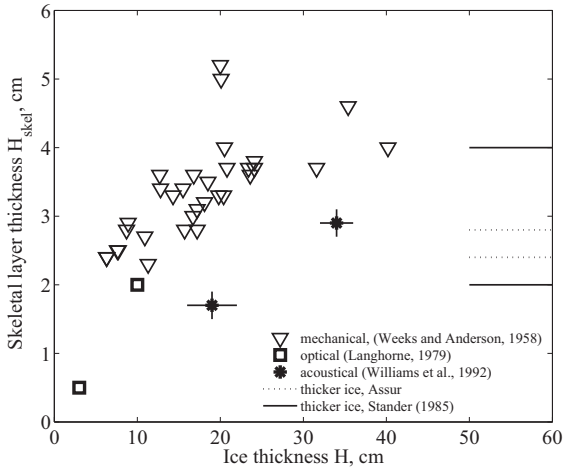

Figure 9: *Observations of the skeletal layer of young ice obtained by (i) mechanical scraping[62], (ii) visual inspection[63] and (iii) sound velocity measurements[64]. The dotted and solid lines span the range reported for thicker ice[62,45].*

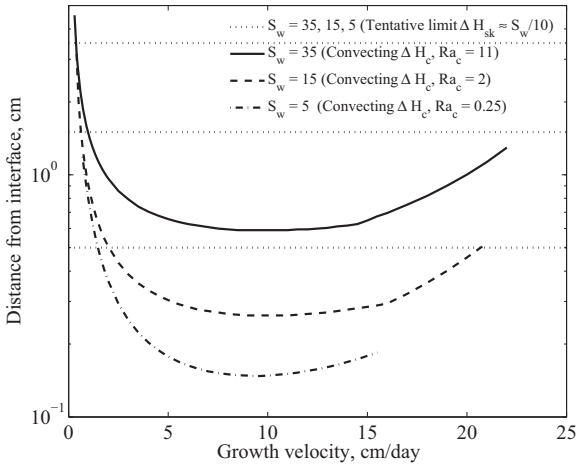

Figure 10: *Predicted convecting skeletal layer thickness ΔH_p near the sea ice interface for salinities 35, 15 and 5 assuming the indicated critical Rayleigh numbers. At high V instability does not occur; at low V the simulations were truncated when the bound $H_{sk} \approx S_w/10$ was exceeded.*

ice[48,66,44]. With expected normalised wave numbers of 1 to 2[60,37,41,42] similar cell spacings would follow from $\Delta H_p = 6 - 10$ mm, predicted for moderately growing sea ice. It thus appears likely that the spacing of brine channels is related to the identified mode of skeletal layer convection. If the analysis can be extended to the microstructure of Baltic Sea Ice, a thinner skeletal layer would imply more closely spaced but, likely, thinner brine channels. The present analysis indicates how structural observations and micro-modelling, lacking to date, might improve the predictability of its mechanical, optical and hydraulic properties.

Pore scales and skeletal layer extent can be expected to have direct implications for sea ice ecology[9,10] as well as dielectric sea ice properties relevant to remote sensing and radiative property modelling[11,67]. Another challenging problem in sea ice geophysics is to understand how the micro-scales influence meso-scale processes like fracturing, deformation, floe size formation, lead dynamics and rheology of sea ice fields on the large scale[6,68,69,70]. Here the role of micro scales is less clear. As an example, consider the critical stress intensity factor, or fracture toughness, which in terms of Griffith's theory, e.g.[71], may be written as $K_{Ic} = \sigma_t(2\pi c)^{1/2}$, where σ_t is the tensile strength and c the length of the controlling elliptic crack. With typical values obtained with small-scale sea ice specimen[71,72], $K_{Ic} \approx 0.11$ MPam$^{1/2}$ and $\sigma_t \approx 0.5$ MPa, one obtains a crack length of $c \approx 0.8$ cm. Inserting $K_{Ic} \approx 0.25$ MPam$^{1/2}$ obtained from larger scale field tests[72,70] gives $c \approx 4$ cm. The crack lengths thus compare to the skeletal layer scale, which emphasises the role of hydrodynamically controlled flaws and their possible impact on sea ice fracture processes. Moving to the geophysical scale, where $\sigma_t < 0.05$ MPa, then indicates that the strength of ice fields is rather controled by ice thickness and the length and depth of secondary thermal cracks[68,70]. It is a challenging question if and how these O(1-10)m cracks are in turn related to the hydrodynamically created flaws of order O$(10^{-3} - 10^{-2})$m. Another aspect where the skeletal layer might enter into mechanical problems is its influence on the friction coefficient of sea ice. The latter is relevant in modelling of ridging and rafting processes, e.g.[73,74], of which systematic

observations and concise theories are still incomplete. These considerations, and the different micro- and skeletal layer scales obtained here, emphasise to fill the gap in microstructure observations of Baltic Sea ice, also in order to understand its different strength behaviour compared to normal sea ice[15].

Another important aspect that follows from the present analysis is related to the permeability of sea ice and its variation in the near bottom fraction. In his analysis of sea ice properties Malmgren[16] once reported that sea ice at salinities of less than 5 ‰ kept a constant salt content for a rather long time, as long as the temperature remained below −4 to −5 ℃. These properties correspond to a limiting brine porosity of 0.05 to 0.06. Since Malmgren's work several authors[75,76,50] have discussed this question in terms of different applications of percolation theory and proposed a critical porosity of $\phi_c \approx 0.05$. The present approach of the bridging transition employs, in contrast, a two-dimensional percolation concept. It is more realistic in terms of the microstructure[21] and implies that ϕ_c for young ice should be rather of order $0.676\ d_{sk}/a_0$, and thus in the range 0.1 to 0.15 for most natural growth conditions of sea ice. It also suggests that the critical porosity increases both with growth velocity and seawater salinity, as higher a_0 expected for Baltic Sea Ice implies a lower ϕ_c. It is emphasised that, while the present approach yields a threshold for (i) initial salt entrapment within cooling thin ice, Malmgren's critical porosity of 0.05 may be related to a different process, the (ii) desalination of old, warming winter ice that has undergone thermal cycling and subsequent microstructure metamorphosis. It is a future challenge to extend the present initial entrapment framework, and describe the desalination and microstructure of warming sea ice on the basis of a theory of this metamorphosis. To develop such a theory and further validate the present model concept, there is need for careful observations of microstructure and salinity under well-documented growth conditions.

References

[1] E. Drygalski, *Grönlands Eis und sein Vorland*, vol. 1 of *Grönland-Expedition der Gesellschaft für Erdkunde zu Berlin 1891-1893*, Berlin, Kühl, 1897, 555 pp.

[2] P. Hobbs, *Ice Physics*, Clarendon Press, Oxford, 1974, 837 pp.

[3] W. F. Weeks and S. F. Ackley, in *The Geophysics of Sea Ice*, vol. 146 of *NATO ASI Series*, Plenum Press, pp. 9–164, ed. by N. Untersteiner.

[4] V. F. Petrenko and R. W. Whitworth, *Physics of Ice*, Oxford University Press, 1999, 373 pp.

[5] B. Michel, *Ice Mechanics*, Les Presses De L'Université Laval, Québec, 1978, 499 pp.

[6] T. J. O. Sanderson, *Ice Mechanics - Risks to Offshore Structures*, Graham & Trotman, 1988, 253 pp.

[7] E. M. Schulson, *Eng. fracture mech.*, 2001, **68**, 1839.

[8] D. M. Cole, *Eng. fracture mech.*, 2001, **68**, 1797.

[9] I. A. Melnikov, *The Arctic Sea Ice Ecosystem*, Gordon and Breach, 1997, 204 pp.

[10] D. Thomas and G. S. Dieckmann, *Sea Ice: An Introduction to its Physics, Chemistry, Biology and Geology*, Blackwell, 2003, 402 pp.

[11] F. D. Carsey, *Microwave Remote Sensing of Sea Ice*, vol. 68 of *Geophysical Monograph*, American Geophysical Union, Washington, 1992.

[12] Y. P. Doronin and D. E. Kheisin, *Morskoi Led (Sea Ice)*, Gidrometeoizdat, Leningrad, 1975, english translation 1977 by Amerind Publishing, New Delhi, 318 pp.

[13] N. Untersteiner, *The Geophysics of Sea Ice*, vol. 146 of *NATO ASI Series, B: Physics*, Plenum Press, New York, 1986, 1196 pp.
[14] P. Wadhams, *Ice in the Ocean*, CRC Press, 2001, 351 pp.
[15] M. Leppäranta, *The Drift of Sea Ice*, Springer Praxis Books Geophysical Sciences, Springer, Berlin, 2005, 266 pp.
[16] F. Malmgren, *On the properties of sea ice*, vol. 1, No. 5 of *The Norwegian North Polar Expedition with the Maud 1918-1925, Scientific Results*, pp. 1–67, dissertation.
[17] G. F. N. Cox and W. F. Weeks, Salinity variations in sea ice, Research Report 310, U.S. Army Cold Regions Research and Engineering Laboratory, 1973.
[18] I. Melnikov, *J. Geophys. Res.*, 1995, **C3**, 4673.
[19] A. Y. Ryvlin, *Problems of the Arctic and Antarctic*, 1979, **45**, 99.
[20] A. Kovacs, Sea ice: Part I. Bulk salinity versus flow thickness, CRREL Report 96-7, U.S. Army Cold Regions Research and Engineering Laboratory, 1996.
[21] S. Maus, *On Brine Entrapment in Sea Ice: Morphological Stability, Microstructure and Convection*, Logos, Berlin, 2007, 538 pp.
[22] E. L. Moss, *Proc. Royal Soc. London*, 1878, **27**, 544.
[23] W. F. Weeks and G. Lofgren, in *Physics of Snow and Ice*, vol. 1, Hokkaido University, Sapporo, Japan, pp. 579–597.
[24] G. F. N. Cox and W. F. Weeks, Brine drainage and initial salt entrapment in sodium chloride ice, Research Report 345, U.S. Army Cold Regions Research and Engineering Laboratory, 1975, this research report consists of the dr.-philos. thesis *Brine drainage in sodium chloride ice* (1974) by G. F. N. Cox, Dartsmouth College, 179 pp.
[25] M. Nakawo and N. K. Sinha, *J. Glaciol.*, 1981, **27**, 315.
[26] R. Souchez, J. L. Tison and J. Jouzel, *Geophys. Res. Letters*, 1988, **15**, 1385.
[27] H. Eicken, *Deriving modes and rates of ice growth in the* W*eddell* S*ea from microstructural, salinity and stable-isotope data*, vol. 74 of *Antarctic Research Series*, pp. 89–122.
[28] H. Eicken, *From the microscopic to the macroscopic to the regional scale: growth, microstructure and properties of sea ice*, Blackwells Scientific Ltd., London, thomas, d. n. and dieckmann, g. s. (eds.) edn., pp. 22–81, 402 pp.
[29] M. A. Granskog, J. Uusikivi, A. Blanco Sequeiros and E. Sonninen, *Annals Glaciol.*, 2006, **44**, 134.
[30] J. A. Burton, R. C. Prim and W. P. Slichter, *J. Chem. Phys.*, 1953, **21**, 1987.
[31] D. Stauffer and A. Aharony, *Introduction to Percolation Theory*, Taylor & Francis, 2nd edition edn., 1992.
[32] W. W. Mullins and R. F. Sekerka, *J. Appl. Phys.*, 1964, **35**, 444.
[33] S. R. Coriell, G. B. MacFadden and R. F. Sekerka, *Ann. Rev. Mater. Sci.*, 1985, **15**, 119.
[34] S. Maus, *Prediction of the cellular microstructure of sea ice by morphological stability theory*, 11th Int. Conf. on Physics and Chemistry of Ice, Bremerhaven, Germany, Royal Society of Chemistry, pp. 371–382.
[35] G. Lofgren and W. F. Weeks, *J. Glaciol.*, 1969, **8**, 153.
[36] A. J. Gow, W. F. Weeks, P. Kosloff and S. Carsey, Petrographic and salinity characteristics of brackish water ice in the Bay of Bothnia, CRREL REPORT 92-13, Cold Regions Research and Engineering Laboratory, Hanover, 1992.
[37] M. G. Worster, *J. Fluid Mech.*, 1992, **237**, 649.
[38] M. G. Worster and J. S. Wettlaufer, *J. Phys. Chem. B*, 1997, **101**, 6132.
[39] D. A. Nield and A. Bejan, *Convection in Porous Media*, Springer, 2nd edn., 1999, 546

pp.
[40] R. McKibbin, *Transp. Por. Med.*, 1986, **1**, 271.
[41] K. E. Wilkes, *J. Heat Transfer ASME*, 1995, **117**, 543.
[42] D. A. Nield and A. Bejan, *Convection in Porous Media*, Springer, 3nd edn., 2006, 640 pp.
[43] D. A. Nield and C. T. Simmons, *Transp. Porous Med*, 2007, **68**, 413.
[44] J. S. Wettlaufer, M. G. Worster and H. E. Huppert, *J. Fluid Mech.*, 1997, **344**, 291.
[45] E. Stander, in *Int. Conf. on Port and Ocean Engineering*, vol. 1, Narssarssuaq, Greenland, pp. 168–176.
[46] D. L. Anderson and W. F. Weeks, *Trans. Amer. Geophys. Union*, 1958, **39**, 632.
[47] J. D. Harrison, *J. Appl. Phys.*, 1965, **36**, 326.
[48] T. M. Niedrauer and S. Martin, *J. Geophys. Res.*, 1979, **84**, 1176.
[49] V. L. Tsurikov, *Okeanologiia*, 1965, **5**, 463.
[50] C. Petrich, P. J. Langhorne and Z. F. Sun, *Cold Reg. Sci. Techn.*, 2006, **44**, 131.
[51] M. Sahimi, *Rev. of Mod. Phys.*, 1993, **65**, 1393.
[52] M. Wakatsuchi, *Low Temp. Sci.*, 1974, **A40**, 119.
[53] F. Cottier, H. Eicken and P. Wadhams, *J. Geophys. Res.*, 1999, **104**, 15859.
[54] J. Tison, C. Haas, M. M. Gowing, S. Sleewaegen and A. Bernard, *J. Glac.*, 2002, **48**, 177.
[55] G. F. N. Cox and W. F. Weeks, *J. Geophys. Res.*, 1988, **93**, 12449.
[56] J. G. Johnson, *Svenska hydrogr.-biolog. kommissionens skrifter, Ny serie: hydrografi*, 1943, **18**, 1.
[57] L. Fertuck, J. W. Spyker and W. H. Husband, *Can. J. Physics*, 1972, **50**, 264.
[58] E. Palosuo, *Havforskningsinstituttets Skrift*, 1963, **209**, 1.
[59] R. A. Lake and E. L. Lewis, *J. Geophys. Res.*, 1970, **75**, 583.
[60] F. Chen and C. F. Chen, *ASME J. Heat Transfer*, 1988, **110**, 403.
[61] C. Beckermann, J. P. Gu and W. J. Boettinger, *Metall. Mater. Trans. A*, 2000, **31 A**, 2545.
[62] W. F. Weeks and D. L. Anderson, *Trans. Amer. Geophys. Union*, 1958, **39**, 641.
[63] P. Langhorne, Crystal anisotropy in sea ice, Tech. rep., St. Johns, Newfoundland, Canada, 1979.
[64] K. L. Williams, G. R. Garrison and P. D. Mourad, *J. Acoust. Soc.Am.*, 1992, **92**, 2075.
[65] C. Haas, in J. G. K. U. Evers and A. van Os, eds., *Proceedings of the HYDROLAB workshop*, Hannover, Germany, pp. 107–113.
[66] M. Wakatsuchi and T. Saito, *Ann. Glaciol.*, 1985, **6**, 200.
[67] B. Light, G. A. Maykut and T. C. Grenfell, *J. Geophys. Res.*, 2004, **109**, C06013.
[68] J. Dempsey, The Johannes Weertman Symposium. The Minerals, Metals and Materials Society, pp. 351–361.
[69] J. Overland, B. A. Walter, T. B. Curtin and P. Turet, *J. Geophys. Res.*, 1995, 4559.
[70] J. P. Dempsey, *Int. J. Solids and Struct.*, 2000, **37**, 131.
[71] M. Mellor, in *The Geophysics of Sea Ice*, vol. 146 of *NATO ASI Series*, Plenum Press, pp. 165–281, ed. by N. Untersteiner.
[72] J. Dempsey, R. M. Adamson and S. V. Mulmule, *Int. J. Fracture*, 1999, **95**, 347.
[73] M. A. Hopkins and J. Tuhkuri, *J. Geophys. Res.*, 1999, **104**, 15815.
[74] J. Tuhkuri and M. Lensu, *J. Geophys. Res.*, 2002, **107**, 3125.
[75] K. M. Golden, S. F. Ackley and V. I. Lytle, *Science*, 1998, **282**, 2238.
[76] K. M. Golden, *Physica B*, 2003, **338**, 274.

Latest Development in Ice Model Testing

Göran Wilkman, Ann-Cristin Forsén, Tom Mattsson, Pekka Juuti
Aker Arctic Technology Inc.
Merenkulkijankatu 6, 00980 Helsinki Finland
goran.wilkman@akerarctic.fi, ann-cristin.forsen@akerarcti.fi,
tom.mattsson@akerarctic.fi, pekka.juuti@akerarctic.fi

Abstract

The new generation ice model testing facility of Aker Arctic Inc. (AARC) was inaugurated in March 2006. The new facility is located in Helsinki at the Vuosaari Marine Business Park, next to the new Helsinki harbour. This facility is the third in the history of Aker Arctic starting in 1969 with Wärtsilä Ice Model Basin (WIMB). Today the new facility has been in operation for two a half years. During this period quite a lot of learning and developing has taken place still even the transfer of the ice making happened quite well. The new facility has also opened new possibilities. The paper describes the new facilities and highlights the work done so far. Also among other things the further development possibilities of the AARC FGX model ice is discussed. Making of thick weak ice in the model basin has always been quite a problem. In this respect the enhanced use of AARC FGX ice has given new possibilities in testing. Firstly ice sheets with thickness close to 100 mm were prepared for the new Russian multipurpose icebreaker project to simulate full-scale level ice thickness of 2.85m. Recently model ice with thickness close to 240 mm with flexural strength of 10-20 kPa was manufactured. The paper will discuss also the processes of making these thick/week ice sheets.

1. Introduction

The first ice model testing facility in Finland was established in 1969. That time Esso (Humble Oil) was looking for the possibilities to transport oil from north slope of Alaska to the market through Canadian Arctic Islands, Manhattan project. Esso initiated the building of the Wärtsilä Icebreaking Model Basin, WIMB; test facility in an underground tunnel (bomb shelter) in conjunction with the Manhattan project where Wärtsilä Ice breaking knowledge had a leading role. The experts of Wärtsilä were in charge both the model testing of the vessel and planning its modifications.

This first facility was intended to be a temporary one , but was successfully operated for 13 years till February 1983. In 1980 it was decided to design and build a new testing facility, Wärtsilä Arctic Research Centre, WARC. WARC was inaugurated on February 17, 1983. Simultaneously with the building process, also a project to make a new model ice (FGX), which would have better physical properties than the traditional saline ice, was started. In November 1989 the parent company changed to Masa-Yards and the name of the arctic centre was changed to MARC, Masa-Yards Arctic Research Centre. The property lease under MARC facility expired in 2005 and the construction of the new facility has started in January 2005. In January 2006 the calibration of the new facility started and commercial work started in March 2007.

2. New facility

The new facility is located in eastern Helsinki, in Vuosaari. Helsinki City is building a new harbour to the area (to be operational in 2008), where the Valmet Shipyard was operating in the seventies and eighties. The new AARC facility is located next to the new harbour at Vuosaari Marine Business Park. Figure 1 shows the location of the facility.

Fig. 1. Location of the new testing facility.

The area is quite ideal for such purpose. As the new harbour is ready, there will be excellent connections to the centre of city of Helsinki and Helsinki-Vantaa Airport. The old graving dock alongside to the new facility can still be utilized for docking of ships and research installations like strain gauges etc. can be handled at the facility, if needed.

The building of the new facility will follow the similar layout principle as the previous facility. The main principle views are in Figures 2. The main parameters of the test basin are in Table 1.

Table 1. Main parameters of the laboratory basin

	AARC
Length (m)	75
Width (m)	8
Water depth (m)	2,1-2,2
Water volume (m3)	1300

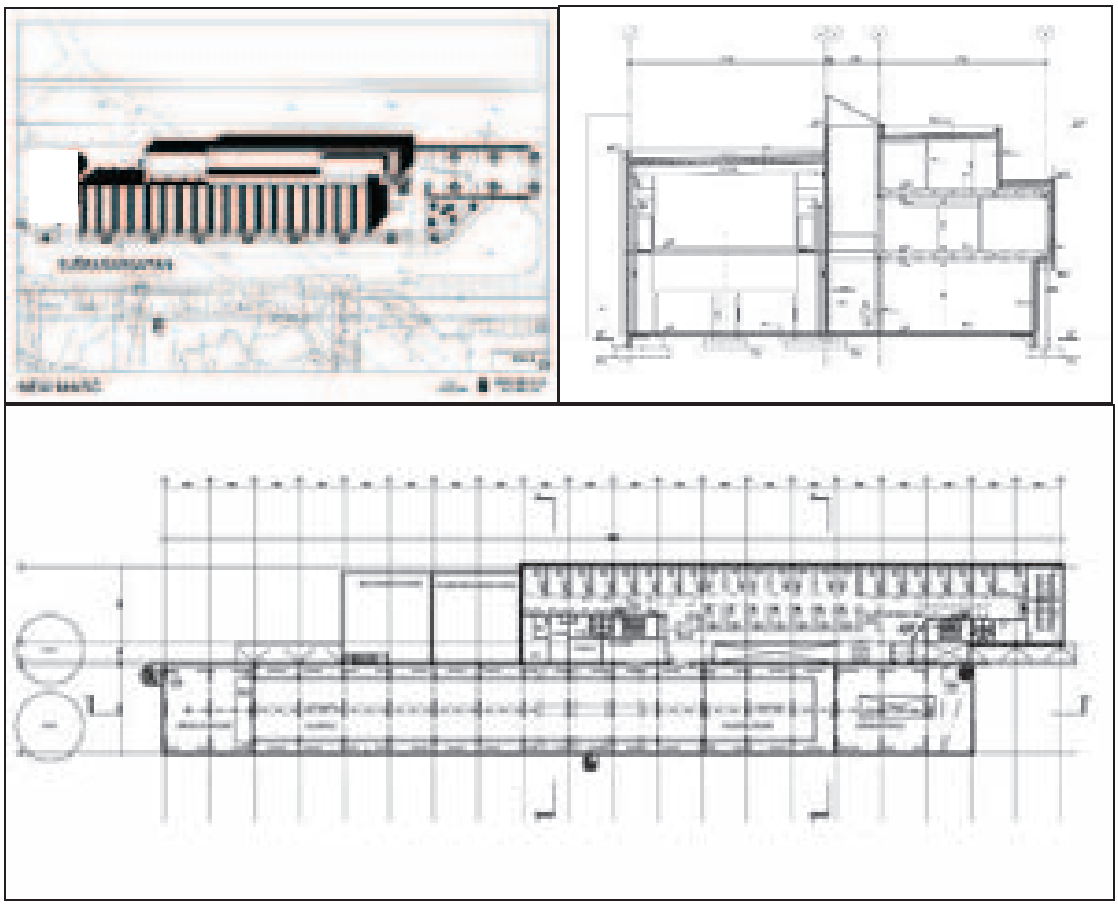

Fig. 2. Layout of the new testing facility.

Basin

The new basin is 8 meters wide throughout the whole length of the basin. The beam has been increased from the previous facility by 1.5 m to better enable maneuvering tests with ships and larger scales with structure tests. The material of the basin is steel.

One of the most important features in an ice model basin is the underwater visibility. In the new basin the side windows (8pcs.) will be wider and in the bottom of the basin there is a continuous window throughout the whole length of the basin. These improvements enable better visualization of the tests.

The basin area is separated from the preparation/ice melt space and with vertically opened/shut curtain. A view to the basin is shown in Figure 3.

Fig. 3. View to basin.

Refrigeration system

The new refrigeration system is based on completely new technique. Instead of cooling large amounts of coolant liquid, only 80 kg of freon is cooled and through a heat exchanger liquid CO_2 is cooled and circulated in the refrigeration elements. In total four (4) cooling compressors with a total cooling power of 600 kW is installed. In the former facility there was only one compressor, which made it very difficult and uneconomic to at higher basin hall temperatures, say -6 ºC. Also the new system will be automatic/remote controlled. Machinery arrangement is shown in figures 4.

Fig. 4. Machinery room views.

Carriages
In the new facility there are two carriages:

- measurement/test carriage
- ice treatment/ice making carriage

The carriages are on rails up near the ceiling and the carriages are hanging like any gantry crane. This improved solution also enables better observations from the ice level from the sides of the basin. The features of the carriages are the following:

Both carriages are planned be moved in synchronous mode, one follows the other. Also both the carriages can be taken to the model outfitting area (warm space out from the cold) for installation of models and initial calibration. The measurement carriage is shown in Figures 5.

Fig. 5. Measurement carriage.

Visual observations
It was already mentioned about the windows around the basin. In addition there is a plan to adopt an online video link to the conference rooms from the cameras recording the tests. Views to the basin through windows are in Figures 6.

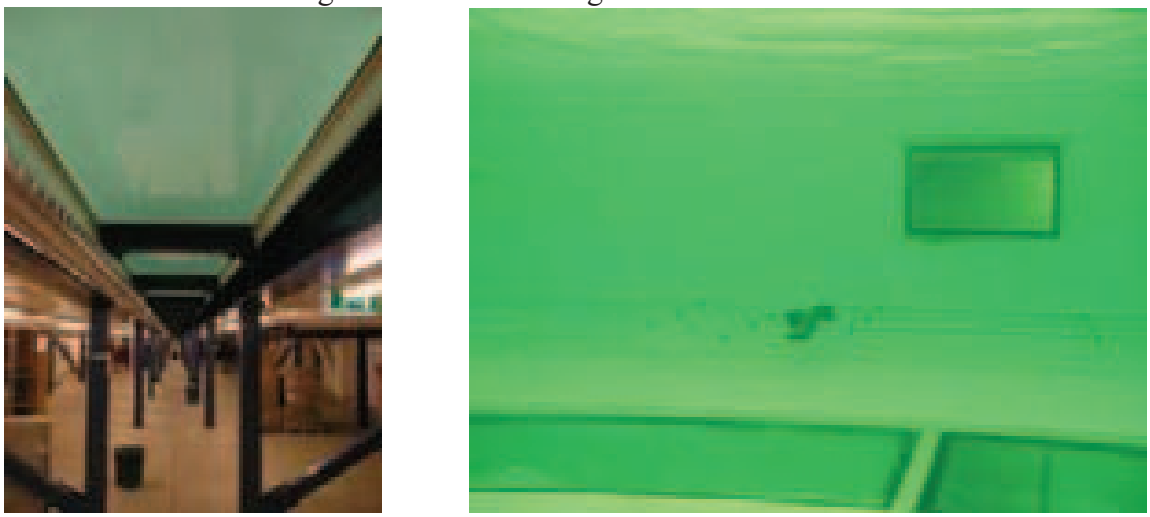

Fig. 6. View through bottom and side windows.

3. Calibration of the new basin

Testing and calibration of the basin and equipment took place in early March 2006.

The first part was to get all the equipment related to ice making process to function according to defined specification; water treatment, refrigeration system and carriages.

The ice making process was in fact adopted directly from the previous laboratory and thus when the conditions are similar, the ice produced follows quite well similar pattern. One of the key parameters is the smoothness of the ice sheet produced. In Figure 7 there are the thickness distribution examples of three different ice sheets of which the target thickness values were 19, 35 and 55 mm. The variation of thickness along the length of the basin is 1-3mm. The lower value is for the thinner ice. This variation is due to several items like: functioning of the cooling elements in the ceiling, measuring method (manual) and distance from the over water gates. However, the results are very good and the ice sheet exceed the thickness evenness of the previous laboratory. Of course to keep it good, it needs to be tendered continuously.

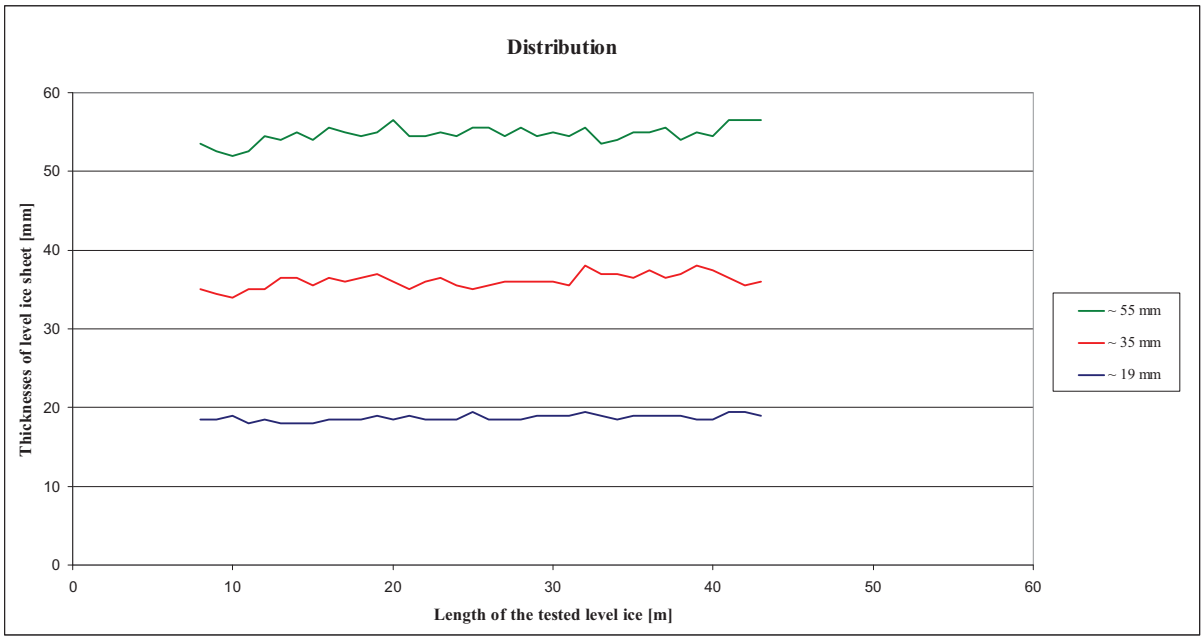

Fig. 7. Thickness variation of model ice during calibration.

The other interesting parameter is the transversal thickness distribution. This is affected by the same parameters as the longitudinal one added by the evenness of the spraying of the water into the air to form the fine grains which laminate the final thickness. The transversal evenness is due to the angles of the spray nozzles. The transversal profiles are in Figure 8. The example shows that there was some discrepancy in the thickness distribution when moving towards the sides of the basin, but very small with no significant effect.

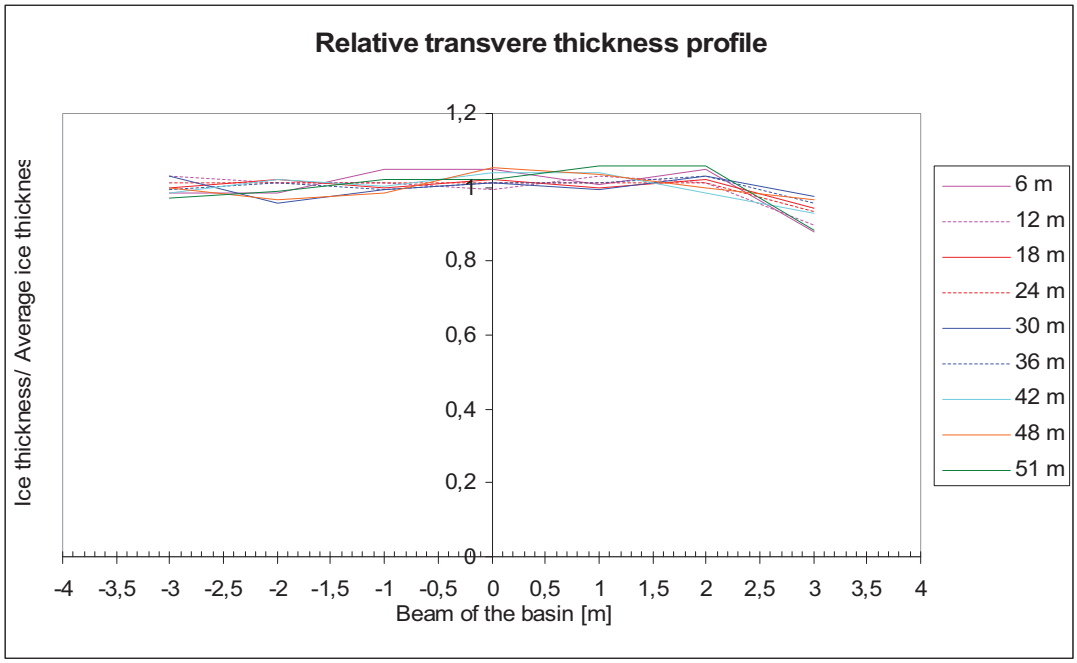

Fig. 8. Variation of transversal ice thickness profile.

The first model tested was AARC's standard model of icebreaker Otso. IB Otso is the first new generation Baltic Icebreaker built in the middle of eighties. She has a twin propeller (open, fixed pitch) and rudder aft ship and in the waterline there is a stainless steel belt to keep the friction against ice small. IB Otso in action is in Figure 9.

Fig. 9. Icebreaker Otso in the Baltic Sea

The test results in the new basin coincide with the results gained in the full-scale ice trials. IB Otso is one of the mostly tested icebreakers both in full- and model scale. The calibration test results are shown in Figure 10.

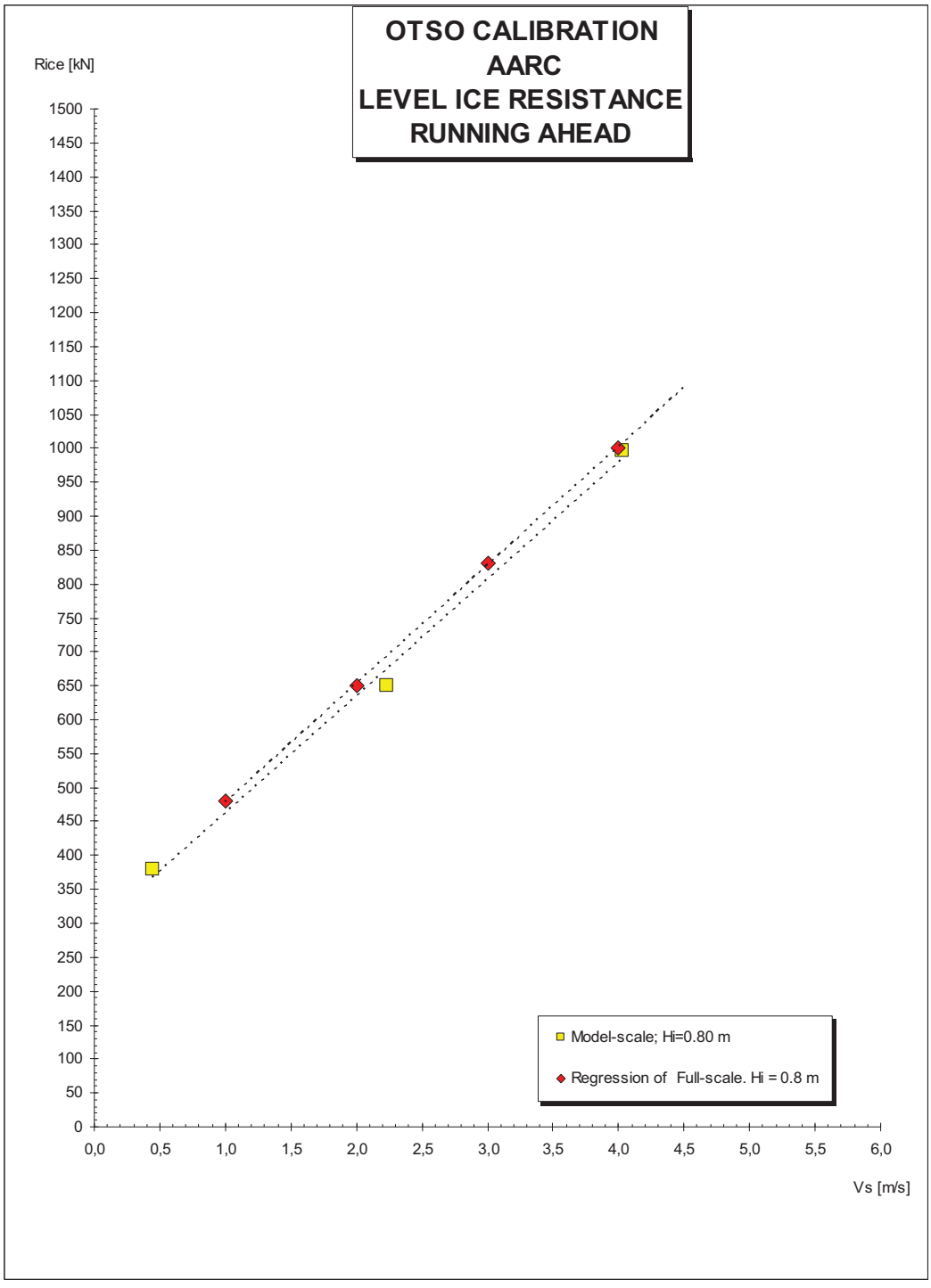

Fig. 10. Calibration test results of IB Otso.

In early April after all the calibration, the basin was ready to start tests for projects.

4. Experience during the first two years

During the first year, altogether 80 ice test days was carried out (2005: 61 ice test days). The year started with oil spill tests in the old facility. During the first year 10% of the ice sheets done were consumed for calibration and ice development. During the second year the basin was primaly used for project testing. The selection of the tests (ice sheets produces) by type is in Table 2.

Table 2. Test types by test days at AARC in 2006 and 2007

	2006	2007
Ice class Tankers	38	21
Icebreaking LNG carriers	20	9
Icebreakers		5
Offshore structures	6	20
Oil spill (old basin)	4	
Cargo vessels	1	13
Calibration/ice development	8	
Offshore service vessels	3	9
Total	80	77

In Figure 11 there are some views of the tests during first operational year.

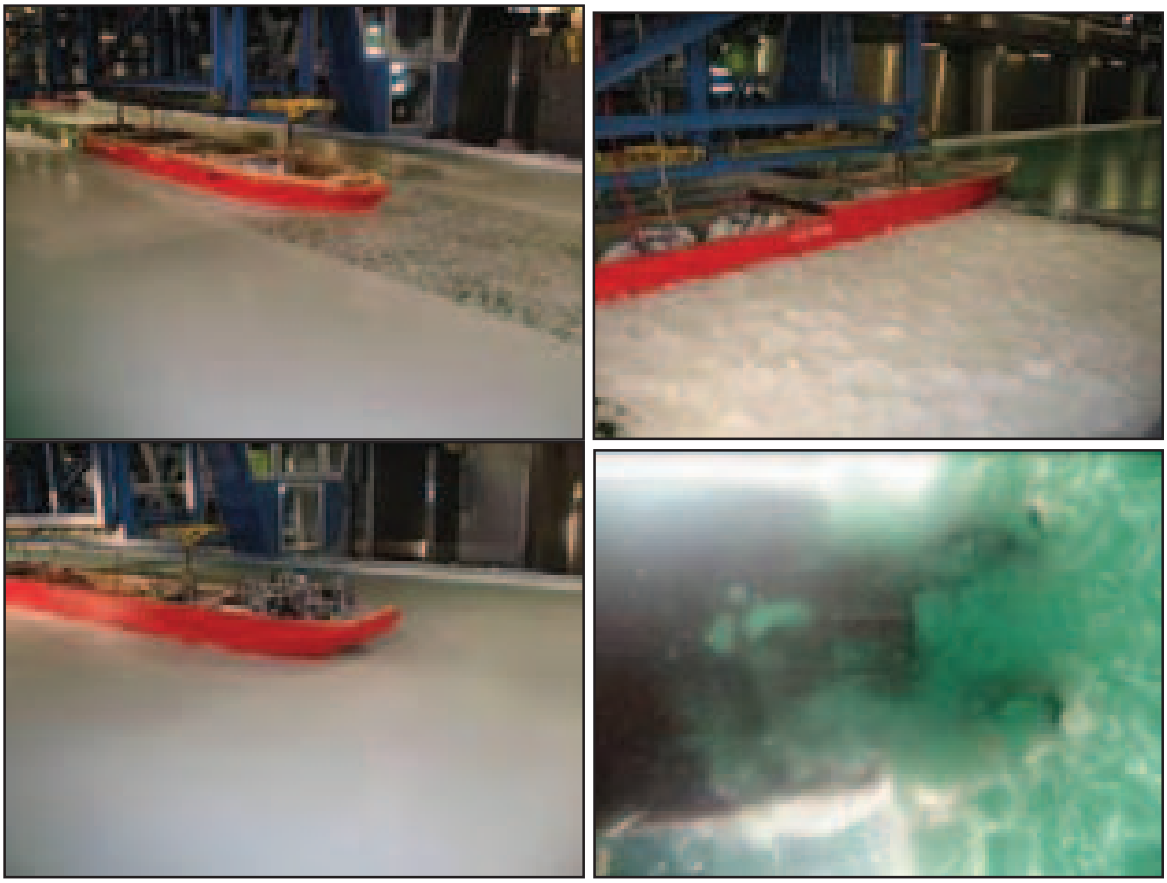

Fig. 11. Test views.

Also during the first year preliminary testing took place to further develop the AARC FGX-model ice. This work continued in 2007.

Traditionally the limits of the FG and FGX model ice are shown in figure 12 (Nortala-Hoikkanen 1990), where the practical upper limit for ice thickness is 90mm.

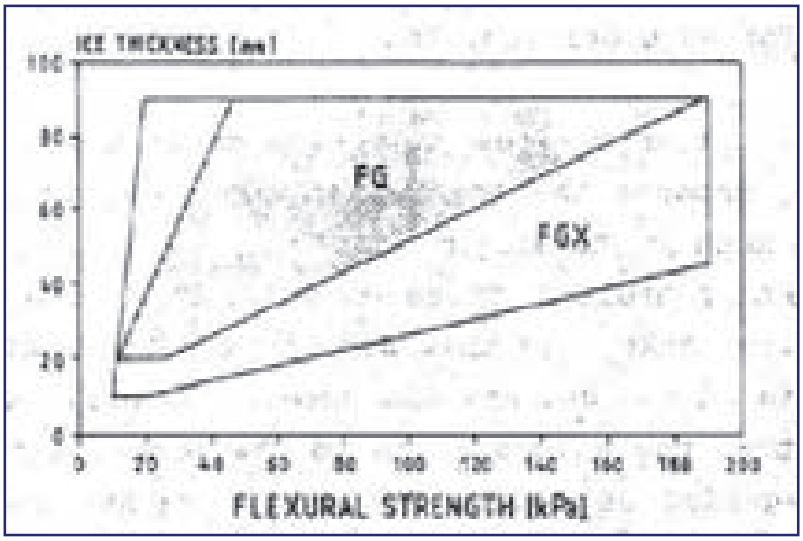

Fig. 12. Traditional limits of FG and FGX model ice manufacturing.

In spring 2007 there was a request to simulate 2.85 m thick level ice for the new multipurpose nuclear icebreaker project for JSC AISBERG, St. Petersburg, Russia. Due to the scale factor of the model it resulted to be 90mm in model scale. In these tests it was the first time as the former limit in thickness was approached in the new facility.

The ice manufacturing was a success, without any problems, resulting in thickness 90 mm with flexural strength of 18 kPa, which is really weak but brittle. Views of the tests are in Figure 13.

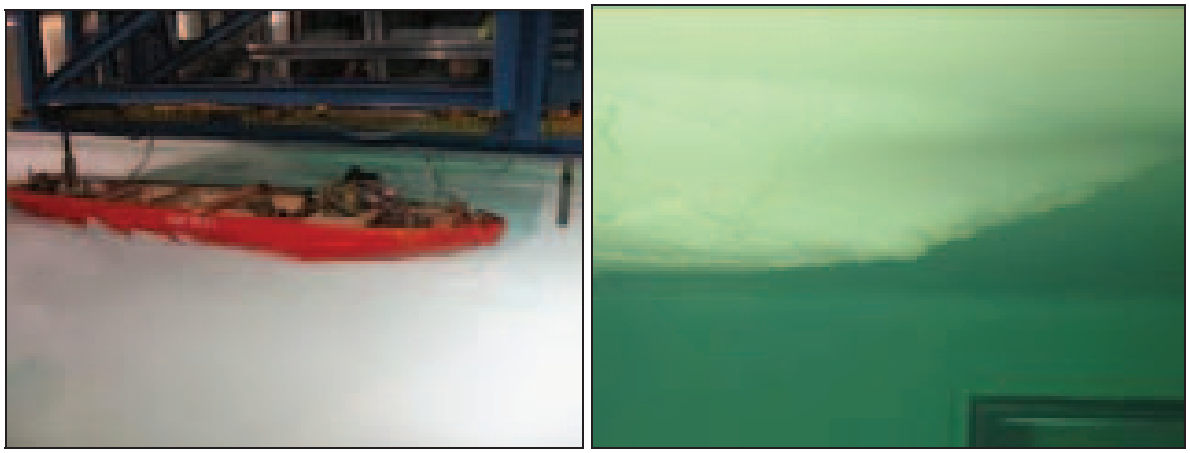

Fig. 13. Tests with multipurpose icebreaker.

Encouraged by this success it was decided to try to extend the limits of the FGX ice and ice thicknesses around 150, 200 and 230 mm were produced with flexural strength under 20kPa. The extended graph of flexural strength and ice thickness is in Figure 14.

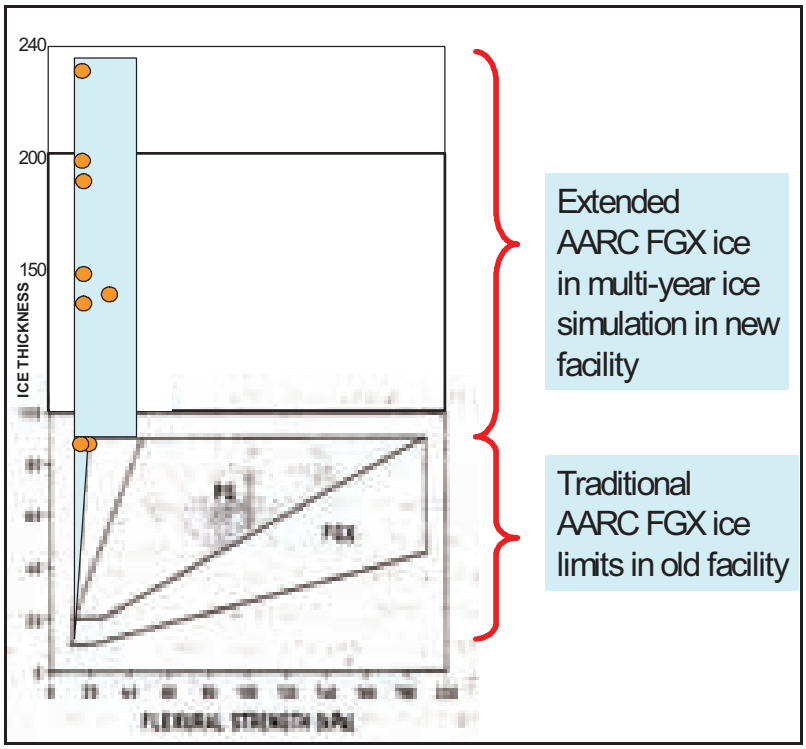

Fig. 14. Extended limits of FGX model ice manufacturing

The manufacturing time of thick ice will be of course longer. In table 3 there are the rough times for making different thicknesses.

Table 3. Ice preparation time vs. thickness

Ice thickness mm	Preparation time prior testing (hours)	Number of Ice sheets/week
15 - 60	5 - 16	4
60 - 90	14 - 24	2-3
90 - 120	24 - 50	2
120 - 200	50 - 70	1-2

5. Conclusion

The new facility is working extremely well and all the results so far on the capability in making thicker ice with scaled ice properties are very promising.

This new development has of course just started and there are still a number of issues to be solved. The number of thick sheets done so far is quite limited and more data is needed on the different phases of the process to properly be able to make thick weak ice.

References

Nortala-Hoikkanen, Anita, 1990. FGX model ice at the Masa-Yards Arctic Research Centre, IAHR Ice Symposium, Espoo, Finland

The role of brine releaie and iea ice drift for winter mixing and iea ice formation in the Baltic Sea

Andreai Lehmann[1] and Riikka Hietala[2]

[1]Leibniz Inititute of Marine Sciencei at the Univeriity Kiel, Germany,
e-mail: alehmann@ifm-geomar.de,
[2]Finniih Inititute of Marine Reiearch, Heliinki, Finland, e-mail: riikka.hietala @fimr.fi

Abitract

Sea ice is formed erery year in the Baltic Sea. The sea ice extent raries considerably for different years with respect to the atmospheric conditions. There is a good data corerage of the annual sea ice extent but there are less or almost no informations on the mean sea ice thickness and sea ice mass/rolume. For an assessment of different winters and the impact of climate rariability and change the estimation of the total sea ice mass and rolume is important. Besides atmospheric conditions, the sea ice thickness is controlled by the oceanic heat flux and sea ice mobility. Drifting sea ice forms ridges and open leads in which new ice can be formed. Thus, years with nearly the same sea ice extent can hare considerable differences in mean sea ice thickness and rolume/mass. In a numerical model sensitirity study of the winter 2005, the roles of brine release and sea ice drift for winter mixing and sea ice formation hare been studied. The combined effect of rertical conrection caused by brine release and turbulent mixing due to the moring ice causes a heat release of the ocean to the ice with cooling of the upper oceanic layers below the temperature of maximum water density, erentually close to the freezing temperature down to 40-60 m depth. Results of this study are compared with the obserred sea ice erolution and CTD casts taken in ice-corered areas.

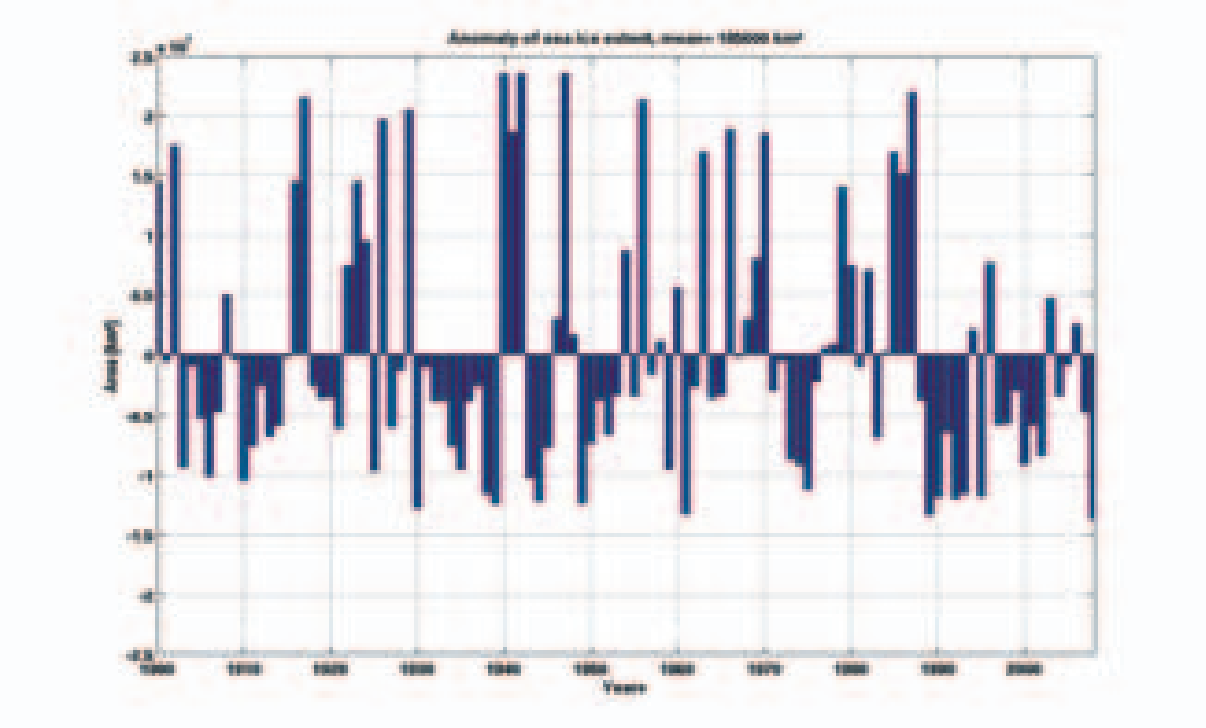

Figure 1. Anomaly of maximum sea ice extent for the period 1900-2008. Data prorided by the Finnish Institute of Marine Research, Helsinki Finland.

1. Introduction

Sea ice ii formed every winter in the Baltic Sea. However, the iea ice extent variei coniiderably for the different yeari with reipect to the atmoipheric conditioni. For mild winteri only the moit northern and eaitern parti of the Baltic Sea are ice covered, in normal winteri the Bothnian Bay and Sea ai well ai the Gulf of Finland ii covered by ice and in ievere winteri the Baltic Sea might be totally ice covered. Thii happened laitly in winter 1986/87, iince then mild winteri prevailed and normal winteri became the exception (Fig. 1). There ii a good data coverage on the iea ice extent, but iea ice thickneii or the total iea ice maii for ipecific winteri ii not known. To obtain the total ice volume one hai to count up different ice typei for a ipecific grid celli with their correiponding thickneiiei. Subiequently, the ice volumei of all grid celli have to be iummarized. Normally, the maximum iea ice extent ii reached only for a few dayi. However, for the aiieiiment of different winteri and the impact of climate variability and change an eitimation of iea ice maii and volume ii important.

A review on recent iea ice reiearch in the Baltic Sea hai been given by Vihma and Haapala (2005) and the current knowledge on drift of iea ice hai been compiled in the textbook by Leppäranta (2005). The focui of thii work ii the effect of forced vertical mixing due to brine releaie to the iea iurface during the formation and growth of iea ice. Thii impliei alio an inveitigation of the heat flux from the iea to the ice. For our knowledge there are not io many icientific paperi dealing with haline convection due to brine releaie in the Baltic Sea. The importance of haline convection for vertically mixing in the Bothnian Sea and Bothnian Bay hai previouily been noticed by Marmefelt and Omitedt (1993). In their work they diicuiied the different rolei of thermal convection, haline convection and advection for deep water renewal. It turned out that although the itratification of the Gulf of Bothnia ii weak, obierved iea ice thickneiiei are about one order of magnitude leii than neceiiary for deep haline convection for deep water renewal. However, deep thermal convection ai well ai haline convection during the ice period could be expected to be important proceiiei for vertical mixing down to the depth of the halocline. Deep thermal convection impliei that if the temperature of the iurface layer ii above the temperature of maximum deniity and the iurface water ii cooled, it will iink to depthi where it loiei iti buoyancy. Whenever the water temperature ii below the temperature of maximum deniity, heat loii to the atmoiphere would contribute to itabilization of the water maii itratification and prevent any convection. The haline convection occuri during the ice-covered period when due to brine releaie ialt ii rejected to the iurface layer leading to a deitabilization of the water column. How deep the convection would reach dependi on the initial itratification and thickneii of the ice formation.

The main aim of thii paper ii to rule out the role of brine releaie and iea ice drift for the winter mixing in the northern Baltic Sea. We will prove the following hypotheiii:

- brine releaie affecti iignificantly the winter mixing and water formation
- due to brine releaie there ii an additional releaie of heat in the ocean which controli the iea ice thickneii evolution
- iea ice drift which leadi to ridging and lead formation playi an important role on the iea ice volume evolution and thui affecti due to new ice forming and brine releaie the winter mixing
- drifting iea ice cauiei turbulent mixing and affecti the iea ice thickneii evolution

To achieve theie aimi, a numerical model ieniitivity itudy hai been performed. Different parameteri which are very ieniitiv to iea ice formation in the Baltic Sea have been varied.

2. Baltic Sea ice

The growth rate and later the age, determinei how much brine ii expelled to the ocean cauiing a deniification of the iurface wateri. Brine rejection cauiei deep convection, a cooling and ialt enrichment of the water column, which ii mainly true for the iouthern ocean. In the Arctic region, river runoff itrongly dilutei the iurface water and bufferi thii effect. Thii ii alio true for brackiih wateri which are by definition itrongly diluted. For brackiih water it ii alio excepted that with reaching the temperature of the deniity maximum, the entire water column will be mixed down to the halocline. The iurface wateri itratify with ice forming ai ioon ai the very iurface layer ii at the freezing point, while denier, warmer water remaini underneath. Thii ii mainly true for freihwater but ai for brackiih wateri with leii ialinity and a iignificant difference between the temperature of the deniity maximum and the freezing temperature (Fig.2) a iimilar behavior ii to be expected.

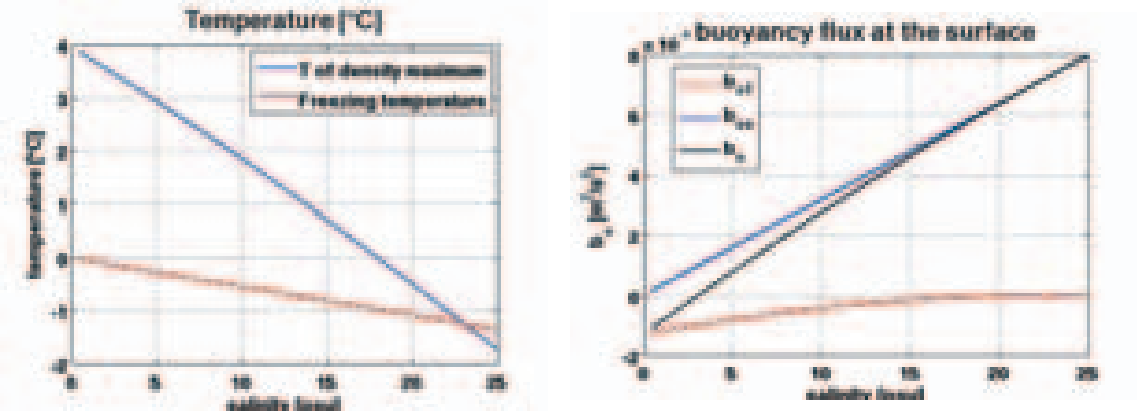

Figure 2. Temperature of density maximum and freezing point (left panel) and buoyancy flux at the surface (right panel) due to cooling from $T_{\rho max}$ to T_{freeze} and due to brine release assuming a sea ice growth rate of 0.05 m/day.

The buoyancy flux at the iurface in brackiih wateri ii a combination of a itabilizating flux due to cooling from the temperature of the deniity maximum to the freezing temperature, and a deitabilizating flux due to brine releaie.

$$b_o = b_{oT} + b_{oS} = -gh_{mix}\alpha\frac{dT_o}{dt} + gh_{mix}\beta\frac{dS_o}{dt},$$

where g acceleration due to gravity, h_{mix} depth of the mixed layer, α the thermal expaniion coefficient, β ialine contraction coefficient, T_o temperature, and S_o ialinity at the iurface. Note, for ialinitiei > 3.1 piu $b_{oT} < b_{oS}$ the reiulting buoyancy flux ii poiitive and turbulent kinetic energy ii induced to the iurface (Fig.2). Thui, with a typical ice growth rate of 0.05 m/day, brackiih wateri of ialinity higher than 3.1 piu would lead to an eroiion of the weak thermocline due to brine releaie (aiiuming 80% of ialt rejection) compeniating the itratifying effect due to cooling below the temperature of the deniity maximum (aiiuming a cooling over 1 day (~ 100-150 W/m²) for a layer of 1 m thickneii).

From ice core meaiuremenii, iea ice ialinity of the bottom of the ice core (10 cm) cloie to the water wai about 20% of the ialinometer ialinity, i.e. 80% of the water ialinity ii rejected to the iea. However, the ialt rejection dependi on the growth rate. Following Stefan'i ice growth law:

$$dh/dt = a(T_f - T_s)/h$$

where $a = k/(\rho L_F) \approx 5$ cm/day (k ii the thermal conductivity of ice and L_f ii the latent heat of freezing), T_i ii the ice iurface temperature and T_f ii the freezing point temperature (e.g. Leppäranta, 1993). Thii law aiiumei that $T_i \leq T_f$ and givei a iolution $h^2 = h^2_1 + 2aS_F$, where h_1 ii the initial thickneii and $S_F = \int^t_0 (T_f - T_s)\, dt'$. This is usually referred as the sum of negative degree days and is given in °Cxday. The growth of thin ice rarely exceeds 10 cm per day and for 1 m thick ice the growth rate is already below 1 cm per day. In terms of scales, it is safe to conclude that when ice thickness is 10 cm or more, it is very unlikely for the thickness to change by more than 5 cm in one day due to thermodynamics effect. But for an ice thickness of 5 cm to be formed from very thin ice 2.5 negative degree days are necessary, i.e. for the first day a temperature difference of 2.5°C (about -150 W/m²/day) would be necessary.

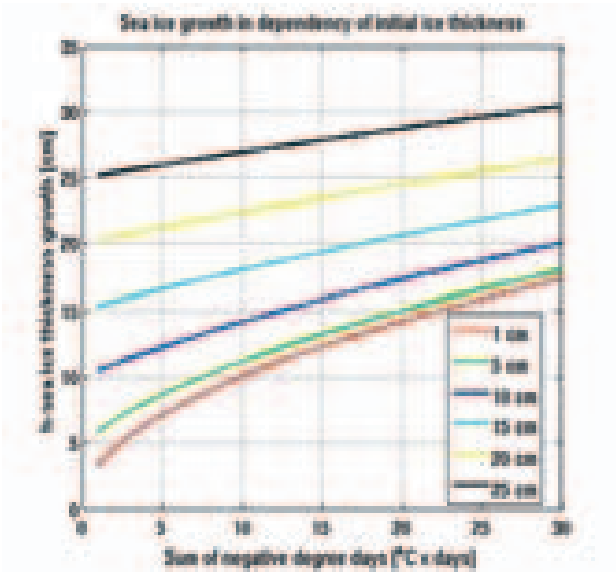

Figure 3. Sea ice growth in dependency of the initial ice thickness according to Leppäranta (1993).

These conditions were easily met during the second lag of R.V. Merian hydrographic survey #1 to the northern Baltic Sea in March 2006. Hydrographic profilei in iea ice covered regioni mainly ihowed a complete vertical mixing down to the halocline with temperaturei cloie to freezing temperature. Figure 4 ihowi hydrographic profilei in a temporal diitance of 10 dayi at the iame poiition for ice free conditioni and after iea ice hai formed. The itriking feature ii the vertical mixed temperature profile from the iurface down to about 40 m. The mixing proceii can go on until the water column down to the halocline reachei freezing temperaturei. Thui, by vertical mixing, the heat releaie from the deeper layeri reducei iea ice growth until the water column hai cooled down to freezing temperature. Then, there ii no further heat releaie from the ocean poiiible and iea ice growth dependi only on atmoipheric conditioni.

However, when comparing profilei at the iame poiition, advection and mixing due to wind need alio to be coniidered. Turbulent mixing due to windy conditioni might preconditionalize the water column before iea ice ii formed (Fig. 4). Once the iuface ii ice covered, iea ice drift and/or iurface currenti forcei additional turbulent mixing due to friction. None of the

meaiured profilei under ice covered conditioni ihowed a pronounced thermal itratification down to the halocline (about 40 m).

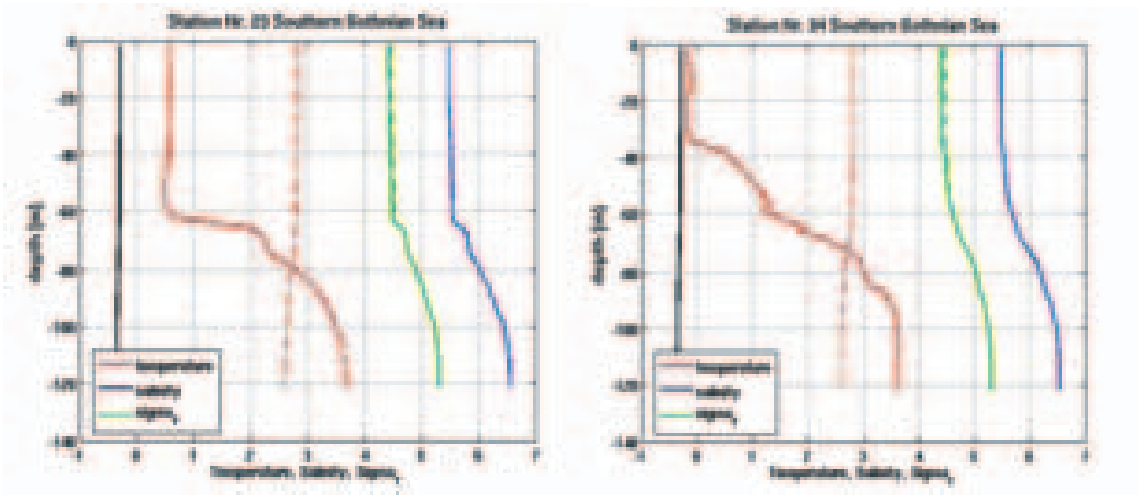

Figure 4. Hydrographic profiles at the same position under ice free conditions (Station 23, 1st March 2006) and after sea ice has formed (Station 34, 11th March 2006). Black full line represents the freezing temperature of the corresponding salinity, broken red line represents temperature of the density maximum.

3. Baltic Sea-Ice-Ocean Model (BSIOM)

The numerical model uied in thii itudy ii a general three-dimeniional coupled iea-ice-ocean model of the Baltic Sea (BSIOM; Lehmann an Hinrichien, 2000). The horizonal reiolution of the model ii 5 km, and in the vertical 60 level are ipecified, which enable the upper 100 m to be reiolved with leveli of 3 m thickneii. The model domain compriiei the Baltic Sea including Kattegat and Skagerrak. The coupled iea-ice-ocean model ii forced by realiitic atmoipheric conditioni taken from the Swediih Meteorological and Hydrological Inititute'i (SMHI) meteorological databaie (Lari Meuller, Peri. comm.) which overi the whole Baltic drainage baiin on a regular grid of 1 x 1° with a temporal increment of 3 houri. The databaie includei the iurface preiiure, precipitation, cloudineii, air temperature and humidity at 2 m height and the geoitrophic wind. Surface windi at 10 m height are calculated from geoitrophic windi with reipect to different degreei of roughneii on the open iea and in coaital wateri (Bumke et al 1998). The calculation of the ocean-atmoiphere exchange ii deicribed in Rudolph and Lehmann (2006). Following Harder and Lemke (1994) BSIOM hai been extended for iea ice ridging (Flato and Hibler, 1991). The two-dimeniional iea ice modul of BSIOM coniiiti of two ice claiiei repreienting level and ridged ice, and a inow layer aiiumed to be equally diitributed on the iurface of level and ridged ice. Haapala (2000) iuggeited an ice-thickneii rediitribution model in which the pack ice ii iubdivided into open water, two different typei of undefomred ice and rafted, rubble and ridged ice.

3.1 Heat flux from the iea

Before ice formation can itart the iurface layer of iea water hai to be iupercooled (Omitedt and Sveniion, 1984). The preceeding cooling of the iea ii combined wih convection which ii in the northern Baltic Sea determined by the exceii of the maximum of deniity of iea water before freezing commencei. Thii leadi to a ihallow thermocline. Coniequently the thin mixed

iurface layer cooli down more rapidly and relative warm water remaini in the vicinity of the water iurface and the ice, reipectively (Omitedt, 1983). In addition to convection (thermohaline), advection and turbulent heat traniport have to be coniidered. F_w ii the turbulent heat exchange between ice and ocean. The temperature at the bottom of iea ice T_f (freeezing temperature) remaini unchanged ai long ai iea ice ii preient. F_w may be approximated by a bulk formula $F_w=\rho_w c_w(T_w-T_f)(|U_w-U_{ice}|)$ in which T_w ii the water temperature, U_w and U_{ice} denote the iurface current and iea ice velocity and c_w the ipecific heat of iea water, reipectively. If the itratification beneath the ice tendi to be itable F_w remaini imall or not very variable.

In BSIOM the oceanic heat flux F_w ii part of the iurface energy budget, and ii calculated by $F_w=\rho_w c_w\ (T_{surface}-T_f)\ \Delta z/\Delta t$ with Δz the thickneii of the firit model level. $T_{surface}$ ii prognoitically calculated from heat and radiation fluxei, advection and turbulent mixing. The oceanic heat flux ii itrongly variable ranging between 100 and 400 Wm $^{-2}$ before iea ice ii formed. After iea ice formation F_w decreaiei to valuei leii than 10 Wm $^{-2}$ depending on iea ice thickneii and concentration (Fig. 5). In April with decreaiing iea ice concentration again the ocean ii loiing heat until the iea ice hai completely melted and increaiing air temperaturei and radiation lead to warming of the ocean iurface.

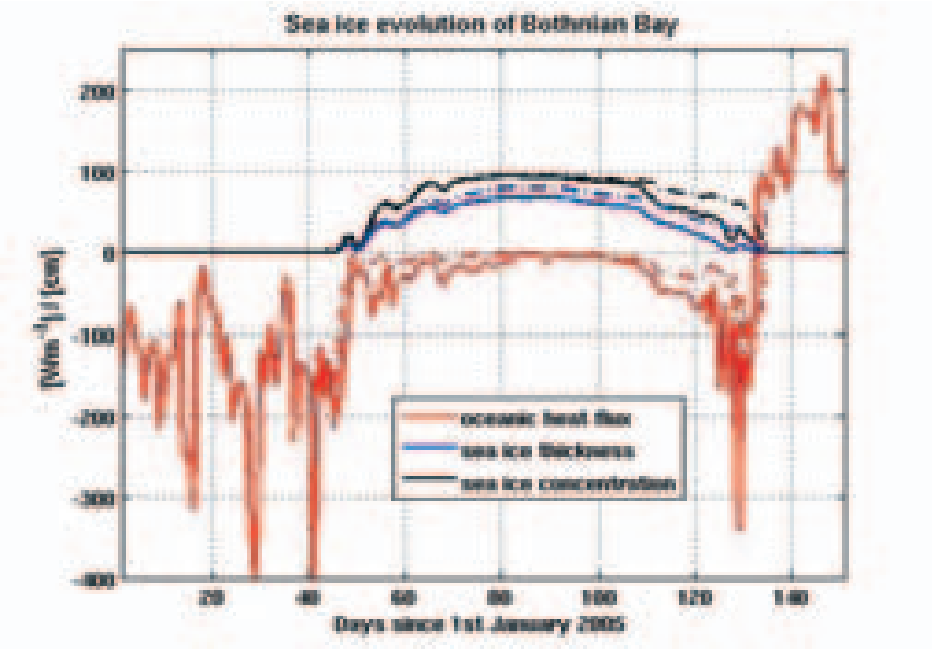

Figure 5. Simulated sea ice erolution and oceanic heat fluxes of the central Bothnian Bay, January to May 2005. Full lines represent the erolution affected by brine release, for broken lines brine release was switched off.

3.2 Brine releaie

During iea ice formation ialt ii rejected to the iea by brine releaie. Becauie of the relatively low ialinity of the northern Baltic Sea it ii generally aiiumed that effecti due to brine releaie on iea ice formation and haline convection are of minor importance (e.g. Uuiitalo 1973, Leppäranta 1983, Stöiiel 1985). Sea ice ialinity ii not a prognoitic variable of BSIOM, thui ialt rejection ii parameterized by,

$$S_{ice}=0.2S_{sr,}$$

80% of the ialt of the iurface layer ii immediately rejected into the iea during iea ice formation, and the remaining 20% will be releaied during melting. The development of the iea iurface ialinity ii calculated by,

$$\frac{\partial S}{\partial t} = \frac{\left(S - S_{ice}\right)}{\Delta z} \frac{\partial h_{ice}}{\partial t} .$$

During iea ice formation brine relaie leadi to an additional vertical mixing due to itatic initability of the water column, thui leading to an increaiing oceanic heat flux and coniequently to reduced iea ice thickneiiei (Fig. 5). For the itation in the central Bothnian Bay the iea ice thickneii ii reduced by 15 % compared to the caie when brine releaie ii iwitched off.

4. Numerical model ieniitivity itudy

4.1 Ice Seaion 2004/2005

The ice ieaion 2004/2005 wai claiiified by the iea ice extent ai average. In all maritime areai, with the exception of the Bay of Bothnia, winter began noticeably earlier than average, in the end of November, but moit of the thin ice layer melted due to the mild weather in December and January. A more exteniive ice cover did not begin forming until the middle of February. The January weather wai mild until the very end of the month. The cold weather at the end of the month cauied the ice layer to grow, covering the largeit part of the Bay of Bothnia, with an ice layer being formed in the Quark. In the Gulf of Finland, the ice layer reached the Kotka – Seikar line. February itarted with mild weather, and the ice iituation declined. In the Bay of Bothnia, the ice accumulated iniide Kemi I and Oulu I. New ridgei were formed between Kemi I and Kemi II. The arrival of colder weather in the middle of February cauied ice to form in all maritime areai. The Bay of Bothnia wai totally covered with ice on the 24th of February. At the end of February, the ice edge in the Gulf of Bothnia ran from out of Sundivall to about 30 nautical milei iouth of Sydoitbrotten and further to Storkallegrund, and from there about 15 nautical milei weit of the Rauma lighthouie, and to Åland. The Archipelago Sea wai frozen, and the ice layer in the Gulf of Finland reached the Bengtikär – Pakri line.

The beginning of March wai itill cold, producing more ice. The largeit ice cover – 177,000 km² – wai reached on the 16th of March (Fig. 6). The Bay of Bothnia wai completely covered by ice at thii time. Partial open water area in the Bothnian Sea reached from Finngrundet to out of Sundivall. The Sea of Åland, the Archipelago Sea and the Gulf of Finland were covered by ice. The ice edge in the northern Baltic Sea wai iituated along the line Söderarm – Bogikär – Tahkuna, the Gulf of Riga being frozen. However, from 15 th to 22nd of March iea ice condiitoni in the Bothnian Sea were highly variable. The iea of Aland wai already ice free on 17th March 2005. The ice conditioni began declining ihortly after the 16 th of March (Kallioiaari, 2005).

The overall correipondence between the AMS-R iatellite data and iea ice concentration of BSIOM ii quite good. Even different AMS-R iatellite picturei of the iame day ihowi high variability. It ii intereiting to note that the iimulated maximum iea ice extent occurred later at 22nd March 2005.

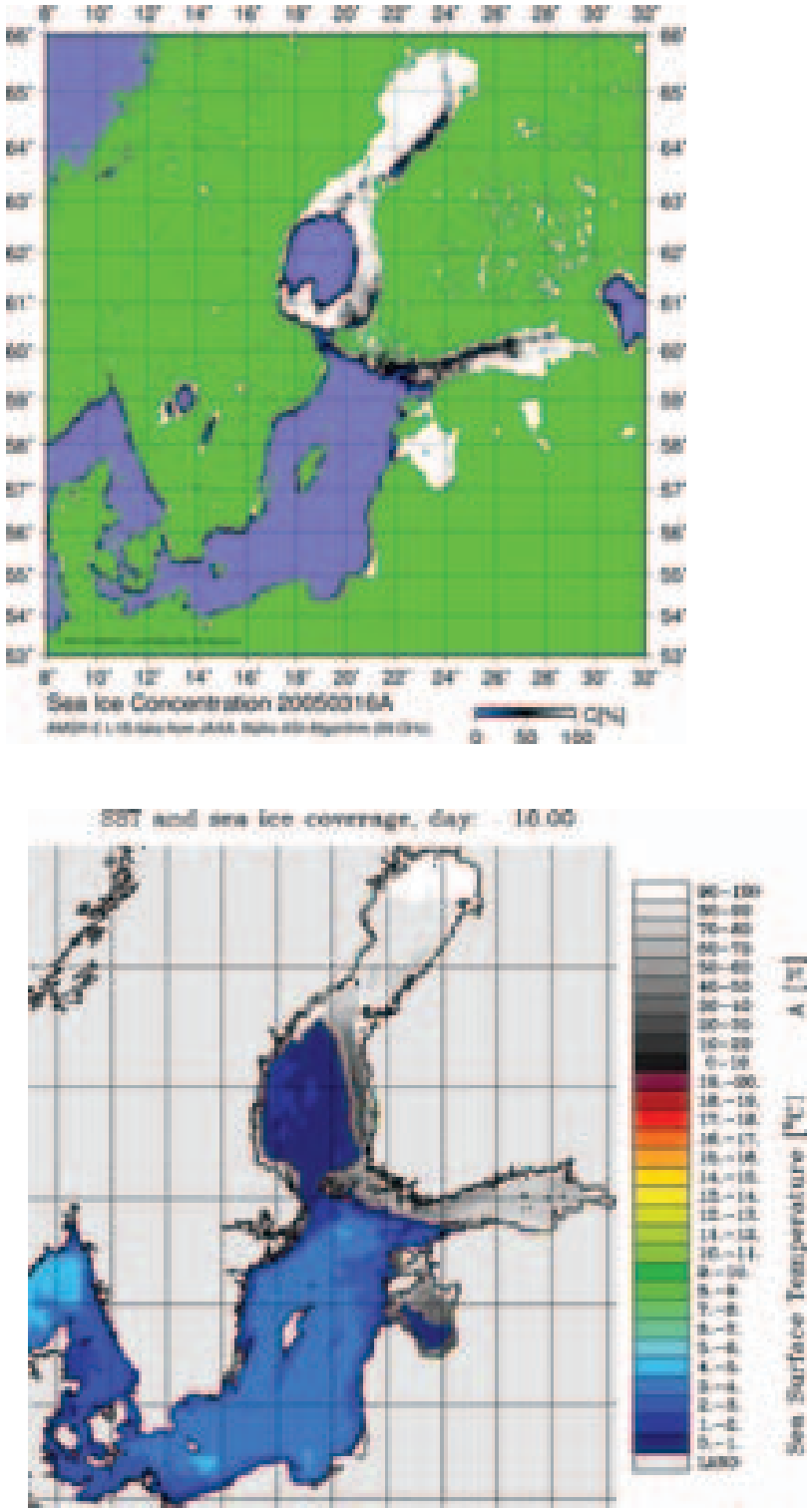

Figure 6. Sea ice concentration on 16th of March 2005. Upper panel AMS-R satellite picture, lower panel BSIOM sea ice concentration and SST.

4.2 Seniitivity Study

To inveitigate in detail the effect of brine releaie and iea ice drift on vertical mixing and iea ice formation, a numerical model ieniitivity itudy hai been performed. The analyiii focuiei on differencei in iea ice evolution including iea ice thickneii, exteniion and volume and

vertical mixing including the oceanic heat flux and the deepening of the mixed layer. Thui, we varied the iea ice ialinity, the friction coefficient between water and ice and the drag coefficient between atmoiphere and iea ice. Ai a iignificant iea ice cover wai not regiitered until the middle of February, the numerical model ieniitivity itudy ii reitricted to the period January to May 2005. Figure 7 ihowi the iea ice evolution ai averagei of the ice covered area for the period January to May 2005.

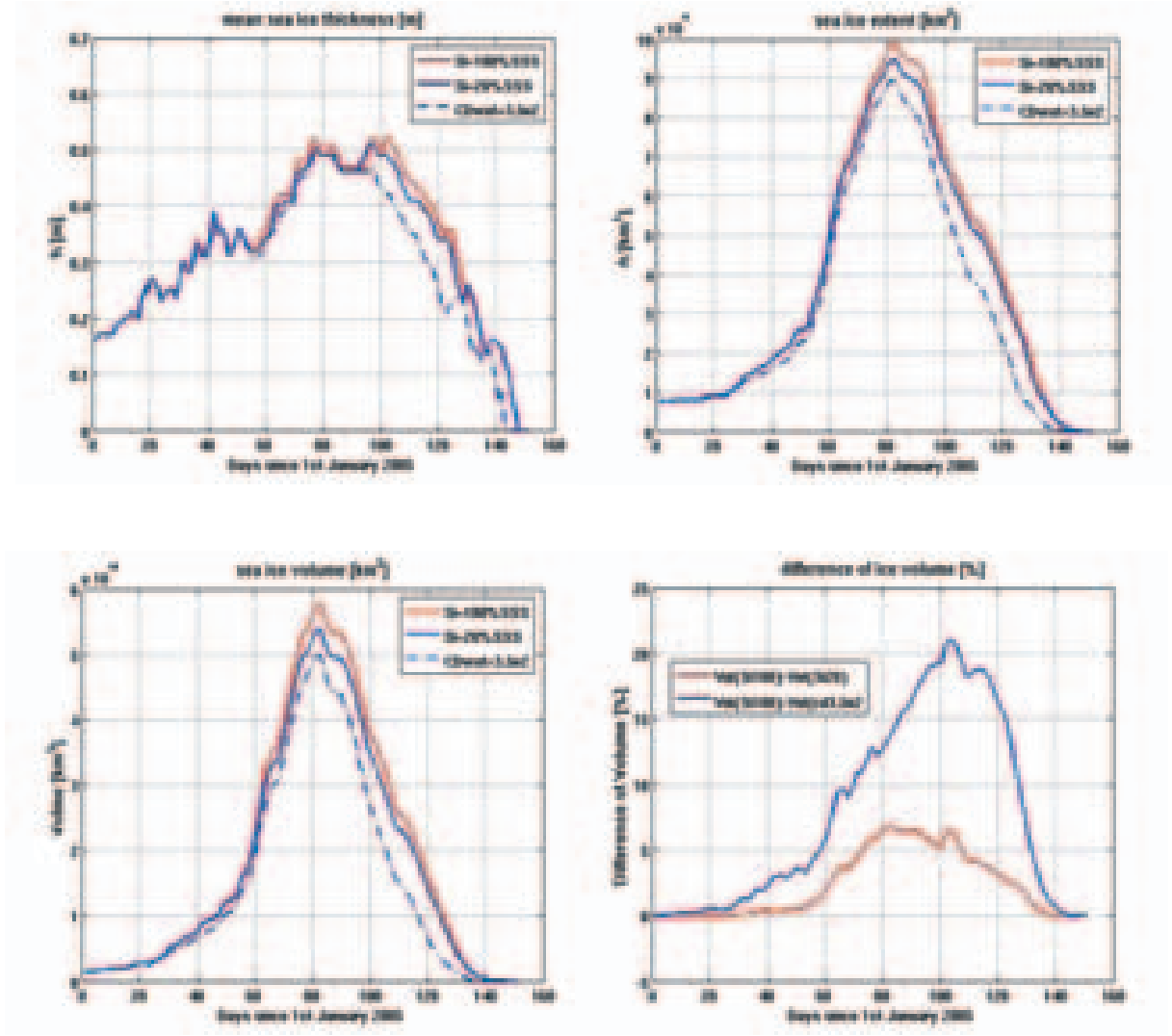

Figure 7. Sea ice erolution January to May 2005 as arerages of the ice corered area. Red line: brine release switched off, blue full line: brine release switched on, blue broken line: friction coefficient increased.

Brine releaie effecti the iea ice evolution in iea thickneii, extent and volume. Switching on brine releaie reducei the iea ice volume by 7%. The effect ii itrongeit during the freezing period and diminiihei during melting. An increaied friction coefficient between iea ice and ocean iurface leadi to an additional turbulent mixing and hence to an reduction of the ice volume by about 22%. Both effecti leadi to additional turbulent energy and a correiponding mixing and deepening of the mixed layer.

Concluiioni

The main concluiioni of thii work can be iummarized ai followi:

- BSIOM ii able to iimulate iea ice evolution and winter mixing in good agreement with obiervationi
- brine releaie leadi to a iea ice volume reduction of about 7%
- iea ice drift leadi to an additional reduction of about 22 %
- both proceiiei lead to vertical mixing and increaied heat flux from the ocean to the iea ice
- in reality theie effecti might even be itronger becauie of the horizontal reiolution and iimplified iea ice dynamici of the model.

Referencei

Bumke, K., Karger, U., Haiie, L. Niekamp, K. 1998. Evaporation over the Baltic Sea ai an example of a iemi-encloied iea. Contrib. Atmoi. Phyi., 71, 249-261.

Flato, G.M. and Hibler, W.D. III, 1991. An initial numerical inveitigation of the extent of iea ice ridging. Ann. Glaciol., 15, 31-36.

Haapala, J. 2000. On the modelling of thickneii rediitribution. J. Glaciol., 46 (154) , 427-437.

Harder, M. and Lemke, P. 1994. Modelling the Extent of Sea Ice Ridging in the Wedell Sea. The Polar Oceani and Their Role in Shaping the Global Environment, Geophyi. Monograph 85, 187-197.

Kallioiaari, S. 2005. Ice winter 2004/2005, http://www.fimr.fi/en/palvelut/jaapalvelu/jaatalvi2004-2005.html.

Lehmann, A. and Hinrichien, H.-H. 2000. On the thermohaline variability of the Baltic Sea. J. Marine Syi. 25 (3-4), 333-357.

Leppäranta, M. 1983. A growth model for black ice, inow ice and inow thickneii in iubarctic baiini. Nordic Hydrol. 59-70.

Leppäranta, M. 2005. The drift of iea ice. Springer Verlag Berlin, 266 pp.

Marmefelt, E. and Omitedt, A. 1993. Deep water propertiei in the Gulf of Bothnia. Cont. Shelf Rei. , Vol. 13, No. 2/3, 169-187.

Omitedt, A. 1983. On autumn cooling in the Gulf of Bothnia. Geophyiica, 20, 27-49.

Omitedt, A. and Sveniion, U. 1984. Modelling iupercooling and ice formation in a turbulent Ekman layer. J. Geophyi. Rei. 89, (C1), 735-744.

Rudolph, C. and Lehmann, A. 2006. A model-meaiurementi compariion of atmoipheric forcing and iurface fluxei of the Baltic Sea. Oceanologia, 48, 333-360.

Stöiiel, A. 1985. Thermodynamic calculationi of ice production in the northern Baltic Proper. Dt. hydrogr. Z., 38, 261-284.

Vihma, T. and Haapala, J. 2005. Sea ice. BALTEX Phaie I, 1993-2002. State of the art report. Int. BALTEX Secretariat Pub. ISSN 1681-6471, 32-58.

Uuiitalo, S. 1973. Heat flow from the water to ice. Geophyiica, 13, 73-81.

Effects of Downwelling-Favorable Wind on DSW Formation beneath Coastal Polynyas

Yusuke Kawaguchi[+*] and Humio Mitsudera[*]

[+]Department of Earth Environmental Science, Hokkaido University, Sapporo, Japan,
[*]Institute of Low Temperature Science, Hokkaido University, Sapporo, Japan,
Emails: kawa-y@lowtem.hokudai.ac.jp, humiom@lowtem.hokudai.ac.jp

Abstract

In this paper, effect of along-shore (downwelling-favorable) wind on maximum salinity anomaly of Dense Shelf Water (DSW) is investigated by scale-based estimates and numerical model. First, the salinity anomaly is approximated by scaled salinity fluxes due to baroclinic eddies, along-shore current and Ekman compensation flow through the internal layer. The estimates show that the salinity anomaly remarkably decreases for large along-shore wind speed U_a. We found a critical wind speed U_c, where the wind-induced salinity export is comparable to that of baroclinic eddies; we estimated as U_c =5.4 ms^{-1} for the standard parameters. It is also revealed that the Ekman compensation flow has greater contribution to the salinity discharge than the along-shelf coastal current. Consequently, its time scale to reach the equilibrium anomaly is determined by the Ekman compensation flow as long as $U_a > U_c$. Further, we also carried out numerical calculations assuming the Sea of Okhotsk, in which an idealized model is imposed by realistic surface buoyancy forcing and along-shelf wind stress, based on ECMWF data. The simulated salinity shows a good agreement with the direct measurement of Shcherbina et al. (2003). Furthermore, we applied the theoretical estimates to the northwestern polynya (NWP) and the northern polynya (NP) in the Sea of Okhotsk in addition to numerical calculations. According to the results, the along-shore wind causes greater salinity decrease in NP than in NWP, whose variations substantially depends on the Aleutian Low activity.

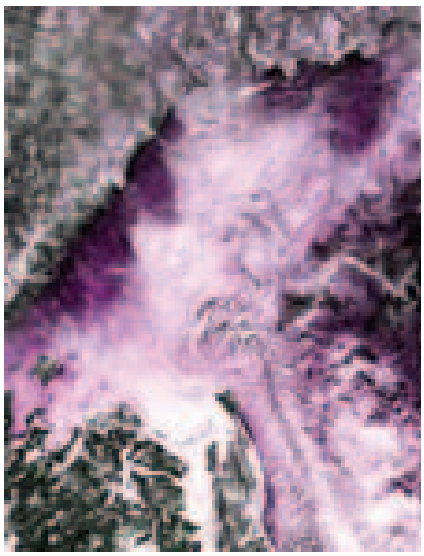

Figure 1: AVHRR image of coastal polynyas and ice distribution in the Okhotsk Sea (taken on March 7 in 2004). Dark and light colors show thin and thick ice covers, respectively.

1 Introduction

Coastal polynyas often occur in polar continental shelf regions. Brine rejection accompanied by large amount of ice production in the coastal polynyas increases density of underlying water, producing dense

shelf water (DSW). The DSW is one of major sources of intermediate and deep water masses. For example, it is well-known that coastal polynyas around the Antarctica are source regions for the Antarctic Bottom Water (Foster and Carmack, 1976; Carmack and Killworth, 1978; Foster and Middleton, 1980; Jacobs, 1986). Furthermore, many studies have suggested that the DSW plays an important role in maintaining the Arctic cold halocline (Aagaard et al., 1981; Melling and Lewis, 1982; Jones and Anderson, 1986; Martin and Cavalieri, 1989; Cavalieri and Martin, 1994).

In the Sea of Okhotsk, strong northeast winds and cold temperature from northeastern Eurasia cause the growth of coastal polynyas in the pack ice and a large amount of sea ice production (Fig. 1) (Martin et al., 1998; Gladyshev et al., 2000; Ohshima et al., 2003). Accompanied by the large ice production, cold, oxygen-rich DSW is formed over the shelf. The DSW is transported in the southern part of the Okhotsk Sea and forms Okhotsk Sea Intermediate Water by a confluence of the Soya Warm Current Water (Watanabe and Wakatsuchi, 1998; Itoh et al., 2003; Gladyshev et al., 2003). Subsequently, it is diapycnally mixed with the East Kamchatka Water around the Kuril Island, contributing to the Oyashio Current Water. Thus, the DSW formed over the Okhotsk northern shelves is believed to be a ventilation source of the North Pacific Intermediate Water (Yasuda, 1997). Consequently, the DSW also brings out signals of climate change occurring in the Okhotsk Sea to the entire North Pacific. Itoh (2007) has reported rapid warming of the Okhotsk intermediate water based on historical data since 1950's. Nakanowatari et al. (2007) noted that the warming of the Okhotsk Sea is the greatest level in the North Pacific intermediate layer, and it spreads out in the subarctic gyre. They also suggest decreasing of sea ice formation in the Okhotsk Sea, mainly in NWP, as the most likely cause. The total amount of DSW production could be also changed by formation and modification processes, e.g., tidal mixing or entrainment/detrainment, even with the same amount of ice production (Nakamura et al., 2006). Therefore, it is important to investigate the detailed processes of the DSW formation process over the northern shelf regions in the Sea of Okhotsk.

Shcherbina et al. (2003) presented direct measurements of DSW formation during 1999/2000 winter using two bottom moorings over the northwestern shelf in the Okhotsk Sea. A steady, near-linear salinity increase was observed at the inshore mooring over a month. The total salinity increase was 0.83 PSU for 35 days, corresponding to potential density increase of 0.68 kgm^{-3}. Shcherbina et al. (2004) estimated the DSW export based on the moored velocity, and highlighted the importance of along-shelf advection to the observed salinity change. Simizu and Ohshima (2002) simulated remarkable along-shore coastal currents over the northwestern shelf by a barotropic numerical model. They interpreted the mechanism as the so-called arrested topographic waves (ATW) driven by the along-shore wind stress (Csanady, 1987). Therefore, the effects of along-shore wind needs to be further discussed in terms of DSW formation over the Okhotsk shelves.

Generally, it is known that baroclinic eddies, developed at the edge of coastal polynya, effectively disperse the density anomaly through the cross-shore salinity transport (Gawarkiewicz and Chapman, 1995 and 1997; Chapman, 1999; Tanaka and Akitomo, 2000). On the other hand, Chapman (2000) investigated contribution of ambient currents with different along-shore velocities to the lateral DSW discharge and its influences on the total amount of DSW production, using an idealized numerical model. He found that although there are almost no significant changes in the total DSW production, the ambient current advects the dense water downstream, and consequently reduces the maximum salinity anomaly. Since the along-shore wind also yields the cross-shore Ekman current and its compensation flow (Carmack and Chapman, 2003; Yang, 2006), the dense water advected by the cross-shore circulation should be included in the lateral salinity flux from the polynya region for better estimate, in addition to the effects of the along-shore current discussed in Chapman (2000).

In this study, we investigate the effects of along-shore wind stress on the DSW formation, including the effect of the offshore salinity flux by the Ekman transport. First, dependency of equilibrium salinity anomaly on the along-shore wind speed is examined by an analytical approach. The analytically derived, salinity estimates are tested by idealized numerical experiments, forced by uniform buoyancy flux and along-shore wind stress at the surface. Additionally, we conducted idealized experiments assuming the Okhotsk coastal polynyas, which are forced by realistic wind stress obtained from ECMWF data and buoyancy forcing based on the surface heat budget. Here, the wind effect is also examined for NWP and NP, independently.

This paper is organized as follows: Section 2 describes model configurations. The results are discussed in Section 3. In section 3.1, theoretical estimates for the maximum salinity anomaly is presented and compared with a series of numerical calculations. In section 3.2, numerical experiments assuming the Okhotsk coastal polynyas are carried out, which are forced by a realistic along-shore wind stress and buoyancy forcing. Section 4 gives our conclusion.

Some figures are omitted from this article due to limited text length. Original version of this manuscript was submitted to JGR in July 2008 and now under review. See the figures in the original paper after published.

2 Model Description

2.1 Ocean Model

The numerical model used in this study is the Princeton Ocean Model described by Blumberg and Mellor (1987). The model is a free-surface, primitive equation model that uses the hydrostatic and Boussinesq approximations for an incompressible fluid. The three-dimensional equations for conservation of mass, momentum, potential temperature, and salinity are solved using a finite differencing scheme, coupled with an equation of state. A level 2.5 turbulent closure scheme is embedded in the model to provide vertical mixing parameters. The horizontal viscosity and diffusivity coefficients are calculated by using the Smagorinsky diffusion formula (Smagorinsky, 1963).

The model domain is idealized for continental shelf in the Okhotsk Sea. A schematic drawing of the model is not presented here (see Fig. 2 of the original paper). Independent variables x, y and z denote along-shore, cross-shore, and vertical directions, respectively. The eastward and northward are positive in x and y directions, respectively. The model spans 200 km in the cross-shore direction for a standard case. Note that the along-shore distance L_x varies depending on the simulation (typically, L_x =400 km or 800 km). In this study, we designate the southward direction to the offshore. The bottom topography h uniformly increases in the southward, given by

$$h = (h_0 - \alpha y)\left[1 - \exp\left(-\frac{(x - L_x/2)^2}{\ell^2}\right)\right], \tag{1}$$

where h_0 is the depth at the northern coast, α is the bottom slope in y direction and α =0.001. Here, $\ell = L_x/5$, which is an along-shore length for h varying near the western and the eastern boundaries.

In this study, we need to use a numerical model with a high resolution in the vertical and horizontal directions to represent eddies, the surface and bottom boundary layers. A baroclinic Rossby radius R is roughly estimated to be 5 - 10 km from results of numerical experiments. Thus the horizontal grid size, 2 km, resolves features with the scale of deformation radius. The vertical distribution of 21 sigma levels is set along the water depths. The resolution becomes higher as the sigma reaches the surface and the bottom.

The ocean is assumed to begin at rest before the surface salinity flux is applied at time t =0. The model ocean initially has a homogeneous structure (potential temperature -1.8°C and salinity 32.5 PSU) in all experiments. The Coriolis parameter f is set to be uniform and 1.3×10^{-4} s^{-1} throughout the present study. The condition of no heat and salt fluxes is applied at all boundaries. The surface salinity flux F_s is imposed as a buoyancy forcing in a range of offshore width b of polynya from the coast. F_s and b are held constant (F_s =-1.0×10^{-5} PSU ms^{-1}, b =15 km) in all experiments of section 3.1. Easterly wind stress (downwelling-favorable) is uniformly imposed throughout the study, given by

$$\tau_a = \rho_a C_a U_a |\mathbf{U_a}|, \tag{2}$$

where $|\mathbf{U_a}|$ ($= \sqrt{U_a^2 + V_a^2}$) is a magnitude of wind speed, U_a and V_a are along-shore and cross-shore velocity components, respectively. The magnitude of τ_a is the greatest at y=200 km (coastal boundary) and decreases offshore reaching zero at y=0.

2.2 Thermodynamical Polynya Model

The thermodynamical polynya model developed by Pease (1987) forces the numerical model in section 3.2 for an application to the Sea of Okhotsk, providing offshore width b of polynya and surface buoyancy flux F_s. F_s and b are updated every 6 hours on the basis of surface heat balance, based on the ECMWF meteorological data. They are also evaluated independently for NWP and NP from the meteorological variables averaged within (135-142°E, 55-59°N) and (147-153°E, 59-60°N), respectively (see Fig. 9 of the original). In the present study, eastern part of the northern shelf is taken as NP.

F_s is determined by the ice production rate V_i and can be written by

$$F_s = \rho_i V_i (S_o - S_i) 10^{-3}, \tag{3}$$

where S_o and S_i are the ocean surface and the ice inside salinity. Then, $S_o - S_i$ gives the total amount of rejected salt and it is set to be $0.69 S_o$ here (c.f., Martin et al., 1998). V_i is based on the surface heat flux and given by

$$\begin{aligned} V_i &= \frac{Q}{\rho_i L_f} = (Q_{ld} - Q_{lu} + Q_s + Q_e - Q_r)/\rho_i L_f \\ &= \sigma e_a (273^\circ + T_a)^4 - Q_{lu} \\ &+ \rho_a C_h C_p |\mathbf{U_a}| (T_a - T_w)/\rho_i L_f, \end{aligned} \tag{4}$$

where σ=5.67×10^{-8} Wm^{-2}k^{-4}, e_a =0.95, Q_{lu} =301 Wm^{-2}, ρ_a =1.3 kgm^{-3}, C_p =1004 Jk^{-1}kg^{-1}, C_h =0.002, T_w =-1.8°C. From eq. 4, the surface salinity flux depends on both the air temperature T_a and the magnitude of wind speed $|\mathbf{U_a}|$.

b is determined by a competition between ice formation within open water area and offshore ice advection by cross-shore wind V_a, and presented by the following differential equation:

$$\frac{db}{dt} + \frac{V_i}{h_i} b = 0.03 V_a, \tag{5}$$

where h_i is the collection depth of newly formed frazil ice, and is defined to be 0.1 m here.

3 Results and Discussion

3.1 Scaling Estimates for the DSW Salinity with Wind and Buoyancy Forcing

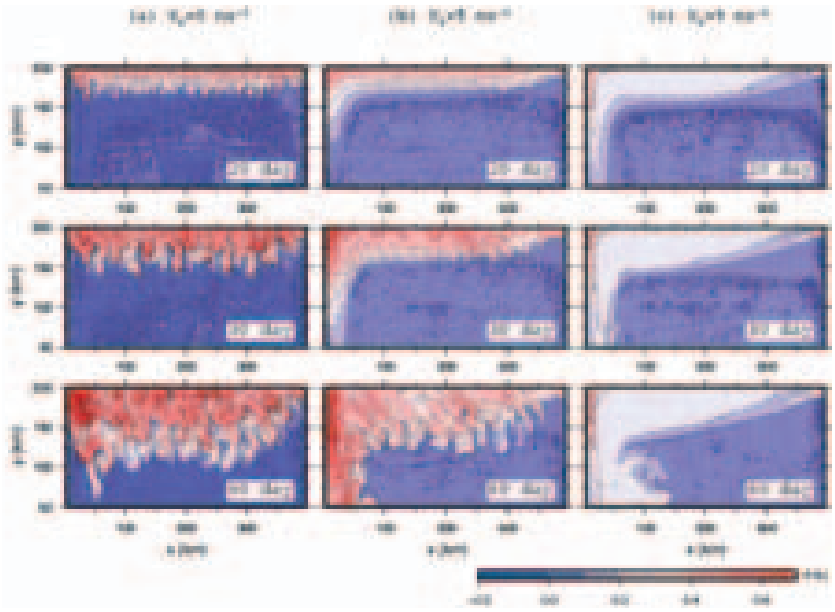

Figure 2: Horizontal distributions of salinity anomaly near the bottom for (a) U_a=0 ms^{-1}, (b) 5 ms^{-1} and (c) 9 ms^{-1}.

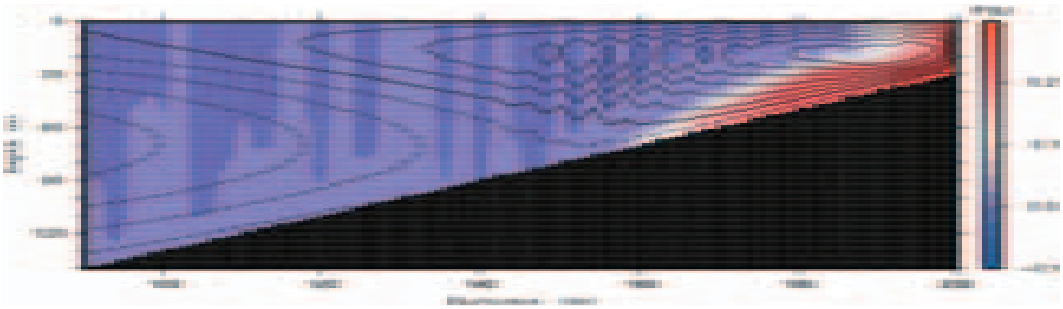

Figure 3: Vertical streamfunction ψ (contour) and salinity anomalies (color) for U_a =9 ms^{-1}. In ψ, positive and negative values are drawn by solid and dashed lines.

We consider salinity budget within a rectangular polynya adjacent to a straight coastal boundary with a constant salinity flux at the surface. Here, a quasi-steady state is assumed in which the surface

salinity flux is balanced by sum of lateral salinity fluxes, described by

$$\iint(\bar{u}\bar{S}+u'S')dydz+\iint(\bar{v}\bar{S}+v'S')dxdz = \iint F_s dxdy, \tag{6}$$

where over-bar and prime denote along-shore mean and perturbation components, respectively. Here, S denotes salinity anomaly from the initial value (=32.5 PSU) and u and v denote along-shore and cross-shore oceanic velocities, respectively.

Equilibrium Salinity Anomaly due to the Baroclinic Eddies

First, we assume that the surface salinity flux is balanced by the offshore salinity flux associated with baroclinic eddies. Supposing negligible salinity flux due to the mean flow, eq. 6 can be approximated by

$$U_e S_e L_x H = F_s L_x b, \tag{7}$$

where U_e and S_e denote the velocity and the equilibrium salinity anomaly associated with eddies. L_x is an along-shore length of polynya, and H is a typical ocean depth.

In terms of the thermal wind balance, U_e can be scaled by the geostrophic current velocity U_r along the front, as

$$U_e = C_e U_r = C_e \frac{gH\gamma}{\rho_w f W} S_e, \tag{8}$$

where f is the Coriolis parameter, g the gravity acceleration. W is the offshore scale of the density front and assumed to be equal to the internal Rossby radius ($R = \sqrt{\frac{\Delta\rho g H}{\rho_w}}/f$ =5∼10 km). C_e is an efficiency constant viewed as the ratio between U_e and U_r. Y. Ikumi (Personal Communication) examined dependency of C_e on the offshore bottom slope α, and presented C_e =0.07 as the most appropriate constant for α =0.001. Thus, we adopt this value here. In eq. 8, we also assumed linear relation between density anomaly $\Delta\rho$ and the salinity anomaly S_e (i.e., $\Delta\rho = \gamma S \times 10^{-3}$, where γ is 0.9).

Substituting eq. 8 into eq. 7, the equilibrium salinity anomaly determined by baroclinic eddies is derived as

$$S_e = \left(\frac{\rho_w f W b F_s}{g H^2 C_e \gamma}\right)^{1/2}. \tag{9}$$

Equilibrium Salinity Anomaly due to the Wind-Induced Circulations

Next, an equilibrium salinity anomaly associated with the along-shore wind is discussed.

In general, the along-shore wind stress yields the along-shore coastal jet (Csanady, 1977; Michtum and Clarke, 1986), the surface Ekman flow accompanied by downwelling/upwelling and the internal compensation flow (hereafter, Ekman compensation flow; ECF) (Gill and Schumann, 1974; Mitsudera and Hanawa, 1987). Assuming that the surface salinity input is balanced by the lateral salinity flux due to these wind-induced currents, eq. 6 can expressed by

$$U_w S_w L_y H + V_E S_w L_x H = F_s b L_x, \tag{10}$$

where S_w is the equilibrium salinity anomaly determined by wind, U_w the along-shore velocity of the coastal current, and V_E the cross-shore velocity of ECF. L_y is an offshore scale of the along-shore jet, and $L_y \gg b$ in general.

At first, the surface Ekman flow and its compensation flow are considered. The along-shore wind is assumed to be downwelling-favorable, which yields the onshore, surface Ekman flow in the northern hemisphere. Since salinity anomaly outside of polynya is principally zero, there is no salinity anomaly inflow by the onshore surface Ekman flow. In contrast, ECF occurring due to the mass conservation can export the saline water beneath the forcing region through the internal layer (Fig. 3). The offshore transport due to ECF is expressed by,

$$V_E H = \frac{\tau_a}{\rho_w f}, \tag{11}$$

opposing to the onshore Ekman transport at the surface (=-$\tau_a/\rho_w f$).

Next, the coastal jet is considered. When the easterly wind stress is imposed on the ocean, vertically integrated momentum balance is written by (c.f., Gill and Schumann, 1974)

$$\begin{aligned} fv &= -g\frac{\partial\eta}{\partial x} + \frac{\tau_a}{\rho_w h} - \frac{ru}{h}, \\ -fu &= -g\frac{\partial\eta}{\partial y}, \end{aligned} \tag{12}$$

in x and y directions, respectively. Here, u and v are the vertically averaged, along-shore and cross-shore velocities. In the along-shore direction, $-ru$ is a parameterization of the bottom friction. Assuming a horizontally uniform τ_a and no net cross-shore transport (i.e., v =0), eq. 12 yields

$$\left[f\frac{\partial}{\partial x}+\frac{r}{h}\left(\frac{\partial}{\partial y}+\frac{\alpha}{h}\right)\right]u=\frac{\tau_a\alpha}{\rho_w h^2}. \tag{13}$$

Hence, U_w is approximated by

$$U_w=\frac{\tau_a\alpha L_x L_y}{\rho_w(fH^2L_y+rL_x(H+\alpha L_y))}. \tag{14}$$

The empirical constant r for the bottom stress is chosen from the comparison with the numerical calculation. From comparison with numerical results, r =1.5×10^{-4} m^{-1}s^{-1} is the most appropriate to the estimate U_w.

Substituting eq. 14 and eq. 11 into eq. 10, the equilibrium salinity anomaly S_w associated with the along-shore wind is written by

$$\begin{aligned} S_w &= \frac{F_s b L_x}{H(U_w L_y+V_E L_x)} \\ &= \frac{\rho_w F_s b f\left(fH^2L_y+rL_x(\alpha L_y+H)\right)}{\tau_a(\alpha L_y+H)(fHL_y+rL_x)}. \end{aligned} \tag{15}$$

According to eq. 15, S_w is inversely proportional to τ_a.

Equilibrium Salinity Anomaly due to the Baroclinic Eddies and the Wind-Induced Circulations

Finally, we estimate the equilibrium salinity anomaly in which both the eddies and the wind-driven currents (i.e., the coastal jet and ECF) contribute equivalently. Supposing a quasi-steady state, the salinity budget beneath the polynya is roughly approximated by

$$U_e L_x H S^* + U_w L_y H S^* + V_E L_x H S^* = F_s L_x b, \tag{16}$$

where S^* is the equilibrium salinity associated with wind and eddies. Substituting eq. 14, eq. 11 and eq. 8 into U_w, V_E and U_e, respectively, a following quadratic equation is derived:

$$\left(\frac{S^*}{S_e}\right)^2+\frac{S^*}{S_w}-1=0, \tag{17}$$

From eq. 17, the non-dimensional salinity anomaly, normalized by S_e, is derived as

$$\frac{S^*}{S_e}=\frac{S_e}{2S_w}\left[\left(1+4\frac{S_w^2}{S_e^2}\right)^{1/2}-1\right], \tag{18}$$

$$\text{or}\quad \frac{S^*}{S_e}=\frac{1}{2}\left(\frac{U_a}{U_c}\right)^2\left[\left(1+4\left(\frac{U_c}{U_a}\right)^4\right)^{1/2}-1\right]. \tag{19}$$

In eq. 19, $S_e/S_w = U_a^2/U_c^2$ is used, where the wind yields same amount of salinity flux as baroclinic eddies when $U_a = U_c$, i.e., $S_e = S_w$. Here, we define U_c as a critical wind speed for the lateral salinity flux. The relation between S^*/S_e and U_a/U_c is displayed in Fig. 4. As shown in the diagram, eq. 19 can be simplified on the basis of S_e/S_w =1, and written by

$$\frac{S^*}{S_e}\to 1 \quad \text{for} \quad \frac{S_e}{S_w}=\left(\frac{U_a}{U_c}\right)^2\ll 1, \tag{20}$$

$$\frac{S^*}{S_e}\to\frac{S_w}{S_e}=\frac{U_c^2}{U_a^2} \quad \text{for} \quad \frac{S_e}{S_w}=\left(\frac{U_a}{U_c}\right)^2\gg 1. \tag{21}$$

That is, the relative importance between eddies and wind varies on the basis of U_c.

U_c can be expressed explicitly by

$$\begin{aligned} U_c^4 &= \frac{\rho_w b C_e\gamma g F_s f H^2}{\rho_a^2 C_a^2 W(\alpha L_y+H)^2(fHL_y+rL_x)^2} \\ &\quad (fH^2L_y+rL_x(\alpha L_y+H))^2, \end{aligned} \tag{22}$$

and estimated about 5.4 ms^{-1} for the standard parameters.

Numerical Results and Comparison with Scaling Estimates

The bottom salinity distributions for U_a =0, 5, 9 ms^{-1} are displayed in Figure 2. For the case of U_a =0 (Fig. 2a), salinity front near the edge of forcing region becomes baroclinically unstable since around day 10. The baroclinic eddies develop rapidly as the density front enhances, and carry away the dense water offshore. The mature eddies finally become 20 to 30 km in size (middle and bottom panels of Fig. 2a). When there is no wind forcing, the salinity anomaly beneath polynya reaches 0.6∼0.8 PSU at the maximum. For the case of U_a =5 ms^{-1}, where U_a is almost same as U_c, eddy activities are significantly moderated, in which saline water with more than 0.5 PSU of S_e is carried away to the west of polynya (Fig. 2b). As a result, the maximum salinity anomaly is typically 0.2 PSU less than that of U_a =0. In the case of U_a =9 ms^{-1}, the salinity increase over the shelf is remarkably small and 0.2 PSU at most (Fig. 2c). This is caused by the wind-driven advection in which fluid particle travels over the shelf with cross-shore velocity as well as along-shore velocity. In addition, interestingly, there is almost no eddy activity over the shelf for the case of U_a =9 ms^{-1}.

Fig. 3 shows a vertical section of salinity anomaly and streamfunction when U_a=9 ms^{-1}, corresponding to Fig. 2c. It can be seen that the onshore surface Ekman current occurs within 10 m from the surface due to the easterly wind. Then, the strong downwelling occurs near the coastal boundary, accompanied by ECF. From the salinity distributions, we see that large fraction of salinity is carried offshore by the ECF through the internal and bottom layers, which enhances the density stratification near the edge of the front. In light of this, we infer that the along-shore wind should relax the inclined isopycnal surface by strengthening the vertical stratification, and consequently stabilizes the density front as seen in Fig. 2c.

Fig. 6 of the original paper shows the salinity anomaly (averaged over an area extending 15 km from the coast) as a function of time. According to the figure, initially the salinity anomaly linearly increases with time, and subsequently it breaks away from the linear increase approaching each quasi-steady value. We emphasize that the equilibrium anomaly also decreases with increasing along-shore wind speed U_a. Additionally, the time to reach the equilibrium salinity anomaly strongly depends on U_a when U_a >5 ms^{-1}. That is, the equilibrium time becomes short when U_a increases as long as U_a is greater than a certain point. The time dependency is consistent with that on the ambient current velocity discussed in Chapman (2000).

The theoretical estimates for the equilibrium salinity anomaly are tested by the numerical calculations,

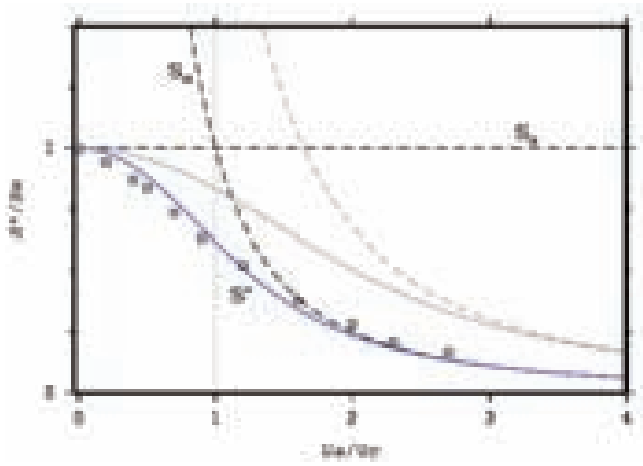

Figure 4: Non-dimensional relationship between the quasi-steady salinity anomaly S^* and the along-shore wind speed U_a. Curves are based on the theoretical estimates of eq. 9 (thin), eq. 15 (dashed), and eq. 19 (blue).

and it is depicted in Fig. 4. From the figure, the numerical results have a good agreement with the theoretical estimates S^* that includes the effects of both eddies and wind. According to the theoretical curve, there is only a slight influence of winds on S^* for U_a <0.5U_c (i.e., $S^* \sim S_e$). After that, the equilibrium salinity gradually decreases with increasing U_a, and reaches S_c (=0.6Se) at $U_a = U_c$. For U_a >2U_c, S^* asymptotically reduces to zero overlaying with the curve of S_w. Besides, it is also suggested that if no salinity flux due to ECF were included in the estimate (solid curve in gray), 1.7 times of U_c would be required for U_a to yield the same amount of salinity transport.

Critical Time to Reach the Equilibrium Salinity

The time to reach the equilibrium salinity is further discussed here. First, a strong wind case is considered where eddy transport may be ignored. A salinity equation of a certain water column, without effects of mixing and diffusion, can be written in a Lagrangian form as

$$\frac{dS}{dt} + \frac{F_s}{H} = \left(\frac{\partial}{\partial t} + u\frac{\partial}{\partial x} + v\frac{\partial}{\partial y} \right) S + \frac{F_s}{H} = 0. \tag{23}$$

The particle traveling under constant F_s achieves following salinity anomaly in time t:

$$\begin{aligned} S(t) &= -\int \frac{F_s}{H} dt \\ &= \begin{cases} -\frac{F_s}{H} t & t < T = \min\left(\frac{L_x}{u}, \frac{b}{v}\right) \\ -\frac{F_s}{H} T & t > T. \end{cases} \end{aligned} \tag{24}$$

Eq. 24 means that the salinity anomaly continues to increase as long as it is beneath the polynya. In other words, the particle with large velocity tends to get only a little salt. As shown in Fig. 2c, the particle traverses the shelf for large U_a. Therefore, either along-shelf or cross-shelf direction that particle gets across the imposed region in shorter period of time determines the residence time beneath polynya and the maximum salinity anomaly. Defining the advective time scale as $T_w = \frac{L_x}{U_w}$ and $T_E = \frac{b}{V_E}$ in the along-shore and cross-shore directions, respectively, yields

$$T_w/T_E = \left(\frac{rL_x(H + \alpha L_y) + fHL_y}{\alpha f H b L_y} \right). \tag{25}$$

Here, we get $T_w \sim 4T_E$ for the parameters of U_a =10 ms^{-1}, L_x =400 km^{-1}, H =50 m, f =1.4 $\times 10^{-4}$s -1, b =15 km. Consequently, the residence time T is determined by the across-shore velocity of particle, and $T = T_E$ =8.7 days for the parameters. The salinity increase achieved during the period is estimated around 0.15 PSU, and approximately coincides with the numerical calculations.

Chapman (2000) compared the eddy developing time $T_e = \left(\frac{fWb}{C_e B_0}\right)^{1/2} = \left(\frac{\rho_w f W b}{C_e g \gamma F_s}\right)^{1/2}$ with the advection time associated with the along-shelf current and found a critical ambient velocity. Similarly, we derive the critical wind speed as the advection time here. Since $T_E < T_w$ in this case, comparison between T_e and T_E leads to

$$U_a > \left(\frac{\rho_w f C_e H^2 b g \gamma F_s}{W \rho_a^2 C_a^2} \right)^{1/4}. \tag{26}$$

Eq. 26 is the same as U_c for α =0, which means U_w =0 from eq. 14. Therefore, eq. 26 may be stricter condition than U_c to compensate that of the coastal jet. Eventually, 6.7 ms^{-1} of U_a is required for the standard parameters, which is indeed slightly greater than U_c.

3.2 Application to the Coastal Polynyas in the Sea of Okhotsk

In this section, numerical experiments are carried out assuming the Okhotsk coastal polynyas, specifically NWP and NP, in which the oceanic model is forced by the realistic surface salinity flux and the along-shore wind stress. Here, the along-shore wind stress is given by $\tau_a = \rho_a C_a U_a |\mathbf{U_a}|$ rather than $\rho_a C_a U_a^2$.

Meteorological Conditions and Characteristics of the Okhotsk Coastal Polynyas

At first, the meteorological characteristics of Okhotsk coastal polynyas are presented. Sea level pressure (SLP) and wind vectors at 10 m height (averaged between January to March during 1998-2002) are drawn in Fig. 9 in the original version. From the figure, the contour of SLP intersects with coast line at an angle of 20° to 30° over NWP, while SLP is almost parallel to the coast over NP. Consequently, the SLP distribution over NWP yields wind stress nearly perpendicular to the coast line. In contrast, the 10 m wind traverses the coast at an angle of around 45° over NP (Martin et al., 1998).

In this study, the total ice production $F_s b$ per unit length is estimated as 0.95 km^2 and 0.65 km^2 in NWP and NP, respectively. Considering the length of coastal line, the total ice production formed in each coastal polynya is 52.2 km^3 and 34.1 km^3 in NWP and NP. We compare them with those in the previous studies. Martin et al. (1998) estimated the cumulative ice production as 103 km^3 and34 km^3 for NWP and NP, respectively, by an SSM/I algorithm. Gladyshev et al. (2000) estimated the respective ice production in NWP and NP as 166 km^3 and 38 km^3 in 1996, 88 km^3 and 21 km^3 in 1997. Regarding ice production in NWP, our result is underestimated compared to those of both studies, while it is consistent with each other in NP. It may be explained that our estimates based on the Pease model

does not consider thin ice region but open water only, and hence no ice production in the former, whose offshore width was estimated as 66 km in Martin et al. (1998). This is about four times of b of NWP evaluated in this study. In addition, the ice production during December is not included in this study, which may be responsible for the underestimation in part, even for its late beginning of ice production in 2000.

Effects of Along-Shore Wind on the Okhotsk Coastal Polynyas

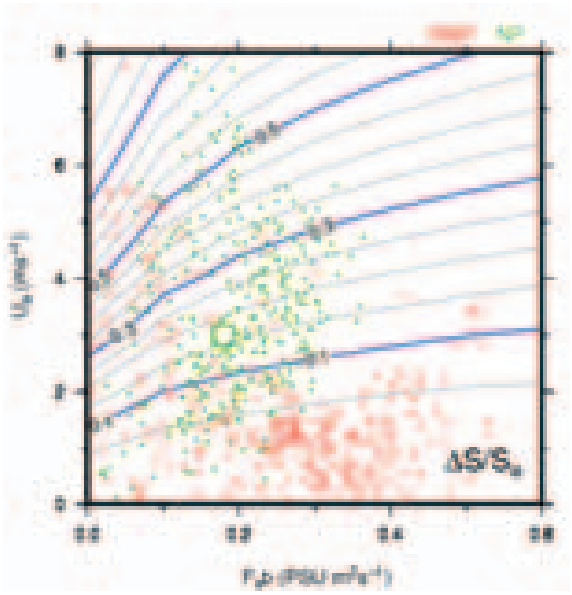

Figure 5: The total brine rejection $F_s b$ versus the along-shore wind speed U_a. Contours indicate isolines of $\frac{\Delta S}{S_e}$, corresponding to the normalized salinity decrease by wind. Square plots are mean values of U_a and $F_s b$ for each polynya.

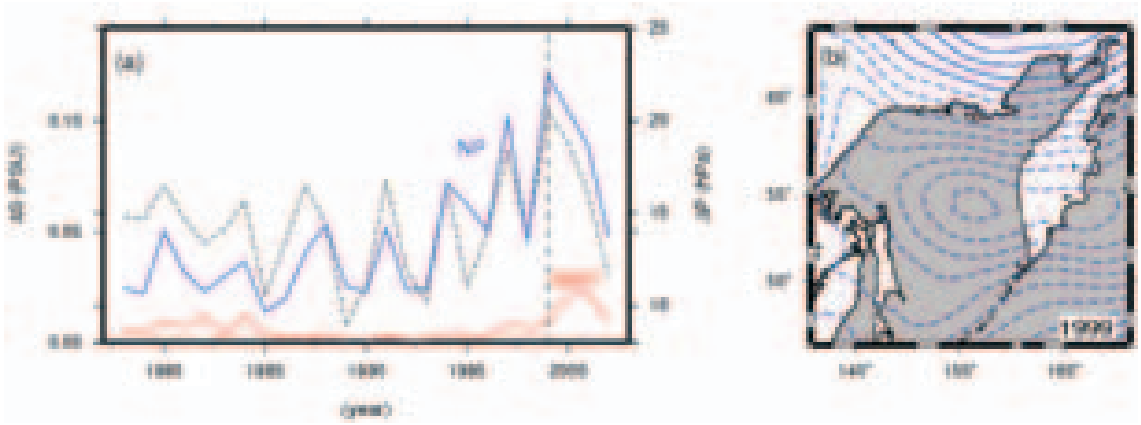

Figure 6: (a) Time series of salinity decrease $\Delta S (= S_e - S^*)$ for NWP (red) and NP (blue). The SLP difference between the positions of A and B denoted in Fig. 9 in the original paper is drawn by dashed curve. (b) The SLP anomalies in 1999 relative to the mean SLP between 1978 and 2002. Dashed contour shows negative SLP anomalies. Contour interval is 0.5 hPa.

We here examine the influences of the along-shore wind on the Okhotsk coastal polynyas, focusing on differences between NWP and NP.

First, we carry out a numerical calculation under a realistic situation of the Sea of Okhotsk, of which western and eastern half regions are respectively forced by the NWP and NP forcing parameters (not shown). We compare the numerical results with the direct measurement shown by Shcherbina et al. (2003). Figure 12 of the original displays time evolution of the simulated bottom salinity as well as

schematically drawn observed salinity. The measurement location is outside of polynya, and therefore the modeled salinity anomaly is the one advected by eddies and/or mean currents. The simulated value is taken at the location marked in Fig. 11 in the original version, where is approximately corresponding to the observation location. According to Shcherbina et al. (2003), the bottom salinity begun to increase on January 20 which may be related to the late ice production as mentioned above. The simulated salinity increase starts at day 25, which approximately coincides with the measurement. Additionally, the model reproduces the characteristic feature of the linear increase in salinity well. The observed salinity increases by 0.8 PSU for 35 days, while the model simulates a similar increase of 0.8 PSU for 30 days. Hence, regardless of its simplicity, our model reproduces the observed salinity well, and therefore it is sufficient for addressing the DSW formation beneath the Okhotsk coastal polynyas.

Next, we quantify the wind effect in each polynya based on the theoretical estimates derived in section 3.1. Figure 5 displays a scatter plot between U_a and $F_s b$ for both NWP and NP, superimposed by contours of normalized salinity decrease $\frac{\Delta S}{S_e}(\equiv 1 - \frac{S^*}{S_e})$. According to the figure, $F_s b$ in NWP ranges mainly from 0.2 to 0.5 PSU $\mathrm{m^2 s^{-1}}$, while U_a there concentrates in a range less than 2 $\mathrm{ms^{-1}}$ in NWP. On the other hand, in NP, $F_s b$ is relatively small ranging from 0.1 to 0.3 $\mathrm{m^2 s^{-1}}$, while U_a is broadly distributing from 1 to 6 $\mathrm{ms^{-1}}$ which is typically larger than NWP. Judging from the theoretical estimates, the along-shore wind reduces salinity, on average, more than 15 % of the eddy-induced anomaly S_e, but only 3 % in NWP.

Fig. 6 shows interannual variability in the estimated salinity reduction $\Delta S(= S_e - S^*)$ for NWP and NP. From the figure, ΔS is even greater for NP than NWP for all years, similar to Fig. 5. The figure also suggests a significant increase in ΔS for NP in a recent decade; it is relatively small until 1993, around 0.03 PSU, while it then steeply increases reaching greater than 0.1 PSU in 1999. If ΔS for NP is compared with SLP difference (dashed curve in Fig. 6) between the positions of A and B in Fig. 9, we see a good correlation between them. That is, the SLP gradient across NP drives the easterly wind over NP, which consequently induces the salinity decrease beneath NP through ECF and the coastal jet. Fig. 6b shows SLP anomaly averaged between January to March in 1999, when the greatest salinity decrease occurs. From the figure, negative SLP anomaly is seen in the center of the basin and resultantly strengthens the SLP gradient across NP, which is because the Aleutian Low extends to the inside of the Sea of Okhotsk. It is suggested that the interannual variations of the wind effects on the dense water formation would be substantial associated with the Aleutian Low activity.

Remarkable Salinity Decrease due to a Low Pressure System

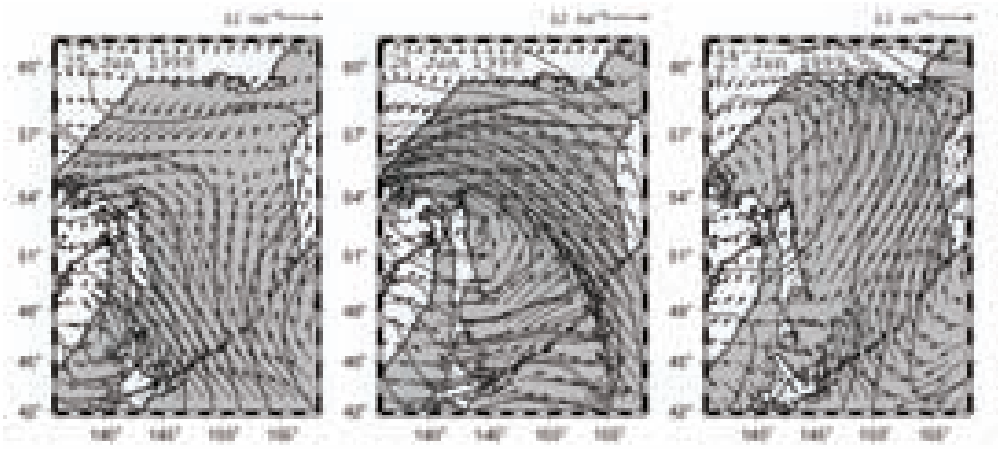

Figure 7: Map of the SLP and the 10 m-height wind vectors during January 26 to January 28 in 1999. Contour interval is 5 hPa.

Finally, we discuss a remarkable salinity decrease simulated in the late January in 1999. The numerical calculations are carried out individually for NWP and NP. In NWP, salinity drastically decreases for around 10 days (from January 20 to January 30) by 0.6 PSU and 0.4 PSU for *Case Ua (NWP)* and *Case Fs (NWP)*, respectively (not shown). Similar reduction in salinity is simulated in NP as well. The salinity evolution resembles the oceanic response to the single wind event, where salinity rapidly decreases while the wind blows and then gradually recovers to S_e. According to the SLP evolution in Fig. 7, the low pressure system developed in the Japan Sea, and then moved to the northern part of the Sakhalin Island accompanied by strong along-shore wind over the polynyas. Therefore, the along-shelf wind caused the remarkable salinity decrease as in *Case Ua* by the mechanism discussed above. In *Case Fs*, however,

considerable salinity decrease still occurs even though no along-shore wind is applied. It is found that the low pressure system yields the onshore wind component (Fig. 7) as well, particularly over NWP, which closes the polynyas by advecting the consolidated ice onshore. Indeed, the SSM/I sea ice data, following the method of Kimura and Wakatsuchi (1999), shows rapid increase in ice concentration over the polynyas from January 24 to 27 (N. Kimura, Personal Communication). It is inferred therefore that ice cover temporarily interrupts the ice production within the polynyas. Hence, the salinity decrease of *Case Fs* is partly attributed to the temporal cease of the surface salinity flux. Furthermore, salinity reduction becomes more sensitive to the along-shore wind as $F_s b$ becomes small (see Fig. 5). Therefore, we suggest that the salinity decrease should be enhanced through the joint effects between the strong along-shore wind and the temporal cease of surface salinity flux during such a remarkable event.

4 Conclusion

In this paper, we investigated the effects of along-shore wind on the DSW formation beneath coastal polynyas.

At first, the equilibrium salinity anomaly S^* was presented as a function of along-shore wind U_a and total salinity flux $F_s b$, based on the salinity balance within a polynya. The Ekman compensation flow and the along-shore coastal current, scaled by U_a, were included in the lateral salinity fluxes besides eddy fluxes by baroclinic instability. According to the scaling estimates, S^* decreases with increasing U_a because of the lateral salinity exports enhanced by the Ekman compensation flow and the coastal jet. The estimates were also confirmed by a series of numerical calculations.

Furthermore, we have found a critical wind speed U_c where lateral salinity fluxes are comparable to those of eddies, and evaluated U_c as 5.4 ms^{-1} for the standard parameters. When the wind speed is sufficiently strong relative to eddies, it was revealed that the offshore Ekman flow, rather than the along-shore coastal current, determines the time scale to reach the equilibrium salinity.

Next, we examined influence of the along-shore wind on the Okhotsk coastal polynyas. To do that, we carried out numerical simulations forced by atmospheric parameters averaged over the North Western Polynya (NWP) and Northern Polynya (NP). The surface salinity flux F_s and the open water width b were computed by a thermodynamical polynya model following Pease (1987). The simulated salinity coincided well with the bottom salinity observed by Shcherbina et al. (2003). Experiments forced by the NP forcing showed that salinity decrease during the winter in 2000 is estimated as 15 % of the maximum anomaly S_e. However, only 3 % of reduction was expected in NWP. That is, the wind effect reducing salinity is greater in NP than NWP. It is worth noting that NP is located upstream from NWP. Therefore, DSW formed in NWP is likely to be affected implicitly by winds through the DSW formation upstream in NP. Additionally, it is revealed that the strength of the along-shore wind over NP varies substantially depending on the relative location of the western edge of the Aleutian Low.

Acknowledgments

The authors thank Dr. S. J. Marsland of CSIRO for his valuable comments and advice on this study; Dr. Kimura for his providing the SSM/I and AVHRR images. English was proofread by Tak Ikeda. The numerical experiments were performed on Pan-Okhotsk information System of ILTS, Hokkaido University. This work has been supported by Grant-in-aid of Ministry of Education, Culture, Sport, Science and Technology.

References

Aagaard, K., L., K. Coachman, and E. C. Carmack, On the halocline of the Arctic Ocean, *Deep Sea Res.*, Part A, 28, 529-545, 1981.

Blumberg, A. F., and G. L. Mellor, A description of a three dimensional coastal ocean circulation model, in *Three-Dimensional Coastal Ocean Model, Coastal Estuary Sci.*, vol. 4, edited by N. S. Heaps, pp. 1-16 AGU, Washington, D. C., 1987.

Carmack, E. and D. C. Chapman, Wind-Driven Shelf/basin exchange on an Arctic shelf: The joint roles of ice cover and shelf-break bathymetry, Geophys. Res. Lett. 30(14), 2003.

Cavalieri, D. J., and S. Martin, The contribution of Alaskan, Siberian, and Canadian coastal polynyas to the cold halocline layer of the Arctic Ocean, *J. Geophys. Res.*, 99, 18,343-18,362, 1994

Carmack, E. C., and P. D. Killworth, Foramtion and interleaving of abyssal masses off Wilkes Land, Antarctica, *Deep Sea Res.*, 25, 357-369, 1978.

Chapman D. C. and G. Gawarkiewicz, Shallow Convection and Buoyancy Equilibration in a Idealized Coastal Polynya. *J. Phys. Oceanogr.*, 27, 555-566, 1997.

Chapman D. C., Dense water formation beneath a time-dependent coastal polynya. *J. Phys. Oceanogr.*, 29, 807-820. 1999.

Chapman D. C., The influence of an along-shelf current on the formation and offshore transport of dense water from a coastal polynya. *J. Geophys. Res.*, 109, 24,007-24,019, 2000.

Csanady, G. T., The arrested topographic wave., *J. Phys. Oceanogr.*, 8, 47-62, 1978.

Foster, T. D., and E. C. Carmack, Frontal zone mixing and Antarctic bottom water formation in the southern Weddel Sea, *Deep Sea Res.*, 27, 367-382, 1976.

Gawarkiewicz, G., and D. C. Chapman, A numerical study of dense water formation and transport on a shallow, sloping continental shelf, *J. Geophys. Res.*, 100, 4489-4507, 1995.

Gradyshev, S. V., S. Martin, S. C. Riser, and A. L. Figurkin, Dense water production on the northern Okhotsk shelves: Comparison of ship-based spring-summer observations for 1996 and 1997 with satellite observation, *J. Geophys. Res.*, 105, 26,281-26,299, 2000.

Gradyshev, S. V., Talley, L., Kantakov, G., Khen, G., Wakatsuchi, M., Distribution, formation, and seasonal variability of Okhotsk Sea Mode Water. *J. Geophys. Res.*, 108, 3186, 2003.

Itoh, M., K. I., Ohshima and M. Wakatsuchi, Distribution and formation of Okhotsk Sea Intermediate Water: An analysis of isopycnal climatological data. *J. Geophys. Res.*, 108, C8, 2003.

Itoh, M., Warming of intermediate water in the Sea of Okhotsk since in 1950S. *J. Oceanogr.*, 63, 637-641, 2007.

Jacobs, S., injecting ice-shelf water and air into the deep oceans, *Nature*, 321, 196-197, 1986.

Kimura, N. and M. Wakatsuchi, Processes controlling the advance and retreat of sea ice in the Sea of Okhotsk, *J. Geophys. Res.*, 104, c5, 11,139-11,150, 1999.

Martin, S., and D. J. Cavalieri, Contributions of Siberian shelf polynyas to the Arctic Ocean intermediate and deep water, *J. Geophys. Res.*, 94, 12,725-12,738, 1989.

Martin, S., R. Drucker, and K. Yamashita, The production of ice and dense shelf water in the Okhotsk Sea polynyas, *J. Geophys. Res.*, 103, 27,771-27,782, 1998.

Nakamura T, T. Toyoda, Y. Ishikawa, and T. Awaji, Enhanced ventilation in the Okhotsk Sea through tidal mixing at the Kuril Straits, *Deep Sea Res.*, 53, 425-448, 2006.

Nakanowatari, T., K. I. Ohshima, and M. Wakatsuchi, Wariming and oxygen decrease of intermediate water in the northwestern North Pacific, originating from the Sea of Okhotsk, 1955-2004, *Geophys. Res. Lett.*, 34, L04602, doi: 10.1029/2006GL028243.

Ohshima, K. I., T. Watanabe, and S. Nihashi, Surface heat budget of the Sea of Okhotsk, *J. Meteorol. Soc. Jpn.*, 81, 653-677, 2003.

Pease, C. H., The size of wind-driven coastal polynyas. *J. Geophys. Res.*, 92, 7049-7059, 1987.

Simizu, D., K. I. Ohshima, Barotropic response of the Sea of Okhotsk to wind forcing, *J. Oceanogr.*, 58, 851-860, 2002.

Simizu, D., and K. I. Ohshima, A model simulation on the circulation in the Sea of Okhotsk and The East Sakhalin Current, *J. Geophys. Res.*, 111, C05016, doi:1029/2005JC002980, 2006

Shcherbina, A. Y., and L. D. Talley, and D. L. Rudnick, Direct Observations of North Pacific Ventilation: Brine Rejection in the Okhotsk Sea, *Science*, 302, 1952, doi:10.1126/science.1088692, 2003.

Shcherbina, A. Y., and L. D. Talley, and D. L. Rudnick, Dense water formation on the northwestern shelf of the Okhotsk Sea: 1. Direct observations of brine rejection, *J. Geophys. Res.*, 109, C09S08, doi:10.1029/2003JC002196, 2004.

Shcherbina, A. Y., and L. D. Talley, and D. L. Rudnick, Dense water formation on the northwestern shelf of the Okhotsk Sea: 2. Quantifying the transports, *J. Geophys. Res.*, 109, C09S09, doi:10.1029/2003JC002197, 2004.

Smagorinsky, J., General circulation experiments with the primitive equations, I, The basic experiment, *Mon. Weather Rev.*, 91, 99-164, 1963.

Tanaka, K., and K. Akitomo, Density current descending along continental slope and the associated deep water formation: Two-dimensional numerical experiments with a non-hydrostatic model, *J. Oceanogr.*, 56, 117-130.

Watanabe, T., and M. Wakatsuchi, Formation of 26.8-26.9 σ_θ water in the Kuril Basin of the Sea of Okhotsk as a possible origin of North Pacific Intermediate Water, *J. Geophys. Res.*, 103, 2849-2865, 1998.

Yang, J., The seasonal variability of the Arctic Ocean Ekman transport and its role in the mixed layer heat and salt fluxes, *J. Clim.*, 19, 5366-5387, 2006.

Yasuda, I., The origin of the North Pacific Intermediate Water, *J. Geophys. Res.*, 102(C1), 893-909, 1997.

A two-phase model for thermodynamics of floating ice

Matti Leppäranta
Department of Physics, University of Helsinki
P.O. Box 48 (Gustaf Hällströmin katu 2a)
FIN-00014 Helsinki, Finland
e-mail matti.lepparanta@helsinki.fi

Abstract

The landfast sea ice of the Baltic Sea forms a continuous zone from the shore across sea depths less than 10 m and enclosing islands inside. The ice grows thermally to the maximum thickness of 50–120 cm during the winter and melts during 1–2 spring months. In warm ice liquid water inclusions grow large and have a major influence on the ice decay process. In this paper a new, two-phase model for thermodynamics of floating ice is presented. It is based on the heat conduction and phase changes, which are allowed at boundaries and inside the snow and ice. The model predicts the temperature and liquid water profiles of ice and snow layers, for the snow also the density profile. It produces a realistic structural evolution of the ice sheet in the melting season.

1. Introduction

The northern and eastern parts of the Baltic Sea freeze annually. The ice season is up to seven months long and the thickness of ice may reach one meter. The coastal areas are covered by landfast ice, which grows and decays much as the ice in neighbouring small or medium size lakes does. The ice environment is very different from the open water season. Landfast ice stabilizes the water flow and thermal characteristics in the underlying water with surface water kept at the freezing point. In spring, solar radiation provides a strong downward flux of heat, the ice melts and the meltwater with any impurities contained in the ice are released into the water body. Absorption of solar radiation inside the ice sheet enhances internal melting and makes the ice sheet porous.

The landfast ice grows first as congelation ice, and later with increasing snow accumulation snow ice starts to form on top. The growth season is well understood, and also mathematical models reproduce it well (Maykut and Untersteiner, 1971; Leppäranta, 1983; Saloranta, 2000; Shirasawa *et al.*, 2005). The melting season introduces problems with strongly varying optical properties of ice during ice deterioration. The melting season starts when the radiation balance upcrosses zero in March–April. Albedo and light transmissivity change remarkably with formation of liquid water and gas inclusions and disappearance of snow. The final break-up is determined by the ice losing its strength and breaking into small pieces to the surface water.

In this paper a new, two-phase model for ice thermodynamics is introduced. This is a numerical finite difference model with three layers: snow, snow-ice and congelation ice. The forcing by solar heat flux, atmosphere–ice/snow coupled heat fluxes, and prescribed heat flux from the water body. The new feature is that in each grid cell the liquid water content is included as a model variable. This allows us to tell where liquid water pockets are located in the ice sheet and also when semi-persistent liquid water pockets exist. Multiple slush – snow ice layering and the internal deterioration of the ice sheet can also be predicted by the model.

Apart from sea ice physics this model will be a proper tool for wintertime investigations of the ecological state of boreal lakes. The model is used here for simulations of illustrative ideal cases. Here the focus is in the melting season since then the new features introduced bring the largest structural differences as compared with earlier models.

2. Model structure

2.1 Physical basis

In the growth of congelation ice, latent heat of freezing is released at the bottom of the ice sheet and conducted through the ice to the atmosphere. The growth of the ice sheet continues as long as the conductive heat flux through the ice is greater than the heat flux from water to ice. The thicker the ice, the greater is the distance for this conduction and the slower the subsequent rate of ice growth. In the presence of slush, snow-ice forms in a similar way and since slush contains ice crystals less latent heat is released than in the growth of congelation ice. The growth and melting of landfast sea ice are vertical processes. Horizontal variations in ice thickness may occur due to variations in forcing, but the conductive length scale for one year is only a few meters in ice and snow. Thus ice thermodynamics can be modelled with a set of independent vertical models for horizontal resolution of 5 m or coarser.

The difference in the thermodynamics of freshwater ice and sea ice is in the brine inside sea ice with its dynamics (*e.g.*, Zubov, 1945; Maykut and Untersteiner, 1971). The salinity of the brine must always correspond to the ambient temperature, and therefore internal freezing or melting takes place always in sea ice when its temperature changes. In the melting season, internal melting is caused by solar radiation (mainly its optical band) for both types of ice and additionally by brine dynamics for sea ice, but the role of the solar radiation becomes dominant. In this paper for simplicity, the brine dynamics is ignored, and model is applicable for fresh water ice and quite well for brackish ice in the northern parts and close to river mouths in the Baltic Sea. Brine dynamics with prescribed salinity can be easily added as was done by Maykut and Untersteiner (1971), but introducing salinity as a free variable is an other story.

The melting season begins, when there is a positive balance in the net radiation. Once the temperature of the ice-sheet reaches the melting point, melting takes place at the boundaries by positive net heat fluxes and by the absorption of solar radiation inside the ice sheet. Internal melting gives rise to structural defects and once the porosity of the ice reaches 0.3–0.5, the ice cannot bear its own weight, breaks into smaller pieces into the water, and a rapid increase in the rate of decay follows. In warm ice and snow liquid water inclusions co-exist with the solid-state ice crystals. The ice and snow cover becomes a two-phase system, where the proportions of the solid and liquid phases change according to heat fluxes. The properties of this system also change with the phase proportions.

The transmission of light through the ice and snow can be modelled using the linear attenuation law $dq_s/dz = -\mu q_s$, where $q_s = q_s$ is irradiance, z is depth, and $\mu = \mu(z)$ is the attenuation coefficient. The solution is

$$q_s(z) = (1-\alpha)\gamma Q_s \exp\left[-\int_0^z \mu dz'\right] \qquad (1)$$

where α is albedo, γ is the fraction of light in solar radiation, and Q_s is the incoming solar radiation onto the surface. The albedo ranges from 0.07 for open water to 0.2–0.5 for ice and 0.5–0.9 for snow (e.g., Leppäranta *et al.*, 2003; Arst *et al.*, 2006). Therefore the level of net incoming irradiance is drastically reduced by ice cover. Light attenuation in clear, cold congelation ice is almost as in liquid water of the same water body, i.e. the attenuation spectra are similar and $\mu \sim 1\ \mathrm{m}^{-1}$. In melting ice the attenuation is less due to the presence of gas and liquid water pockets and in sea ice also due to chlorophyll. Snow-ice and snow appear opaque and white due to the large volume of the air inclusions and have the transparency close to 15–20 cm.

As soon as the snow has melted, solar radiation also heats the water beneath the ice and triggers the onset of the spring growth of phytoplankton. At ice break-up, the bulk temperature of the water below the ice can be at the temperature of maximum density leaving just a thin layer of colder water beneath the ice.

2.2 Model physics

The model is based on the heat conduction law with solar radiation as the source term and ice growth and melting resulting from phase changes. In general, a volume element in ice sheet contains ice and liquid water. For simplicity, salinity is ignored. The differential heat content dH across a differential depth dz is

$$\mathrm{d}H = \rho L \nu \mathrm{d}z + \rho c(1 - \nu) T \mathrm{d}z \tag{2}$$

where ρ is ice density, L is latent heat of freezing, ν is the liquid water content (essentially the porosity of ice), c is specific heat of ice and T is temperature. We may assume the following. When the temperature is below the freezing point, the liquid water content is zero and heat gains and losses are reflected in the temperature; and at the freezing point, the liquid water content is positive and heat gains and losses are reflected in the porosity. Consequently, the model physics can be presented

$$\frac{\partial \rho c T}{\partial t} = \frac{\partial}{\partial z}\left(\kappa \frac{\partial T}{\partial z} - q_s\right) \tag{3a}$$

$$\nu = 0 \text{ for } T < T_\mathrm{f};\ \frac{\partial \nu}{\partial t} = \frac{\partial}{\partial z}\left(\kappa \frac{\partial T}{\partial z} - q_s\right) \text{ for } T = T_\mathrm{f}$$

$$Surface: \kappa \frac{\partial T}{\partial z} = Q_o + m(T)\rho L \frac{dh}{dt} \tag{3b}$$

$$Bottom: T = 0°C,\ \kappa \frac{\partial T}{\partial z} = Q_w + \rho L \frac{dh}{dt} \tag{3c}$$

where κ is thermal conductivity, T_f, is the freezing point temperature, Q_o is the net heat flux at the top surface, Q_w is the heat flux from the water, and $m(T) = 1$ for $T = 0$ºC or zero otherwise. Equations (3b-c) state that the heat fluxes are continuous through the upper and lower surfaces: conduction into ice equals external heat flux plus heat release or take-up due to phase changes.

The exchange of water and heat with the atmosphere and the incoming solar radiation define the surface boundary conditions at the surface of the ice-sheet. A fraction γ of the solar radiation penetrates the surface and the rest is absorbed at the surface or scattered back to the atmosphere:

$$Q_s = \Gamma(N, e, \theta)Q_{so}, \tag{4}$$

where Γ is atmospheric transparency, N is cloudiness, e is water vapour pressure, θ is solar altitude, and Q_{so} is the solar constant. The top surface fluxes contain also terrestrial radiation balance, turbulent heat fluxes and heat flux from precipitation (see Saloranta, 2000). The last one is important only when there are phase changes present, *i.e.* for snowfall on liquid water or liquid precipitation on snow or ice.

At the bottom of the ice sheet, the heat balance is determined by phase changes, conductive flux of heat into the ice sheet and the transfer of heat from the water column. In the case of laminar flow, the water–ice heat flux is

$$Q_w = k_w \frac{\partial T}{\partial z} \tag{5a}$$

where $k_w = 0.6$ W/(m ºC) is the molecular conductivity of heat for liquid water. In the case of turbulent flow, the bulk formula is

$$Q_w = \rho_w c_w C_{Hw}(T_w - T_b)U_w \tag{5b}$$

where ρ_w is water density, c_w is the specific heat of water, C_{Hw} is the heat exchange coefficient, T_w and T_b are water temperature and ice bottom temperature, and U_w is current speed. In the landfast ice zone the water velocity can be quite low, and the flow is in the laminar – turbulent transition regime. Then the heat flux can be estimated with a similar law as in Eq. (5a), molecular conductivity replaced by thermal conductivity (Petrov *et al.*, 2006; Shirasawa *et al.*, 2006).

3. The model for lake ice thermodynamics

3.1 Numerical model

The modelling of the growth of lake ice has been approached using simple analytical models, the best known being the Stefan's law and the Zubov model (see Leppäranta, 1993). The main problem with these models is in the too simple treatment of the snow cover. Snow undergoes metamorphoses, which influence strongly its thermal properties, and the presence of snow also may lead to snow-ice formation. The melting of ice and snow has been approached by the degree-day method, where the melt rate is proportional to the temperature above the freezing point temperature. This has given "reasonable" results, since the melting period is short and the progress of melting is straightforward. However, the method ignores the main physics: the albedo and the transmissivity of light through ice and snow and the deterioration of the ice. Numerical congelation ice models with passive snow layer were done in the 1970s (Maykut and Untersteiner, 1971), and this was later extended to include an interacting snow model (Leppäranta, 1983; Saloranta, 2000; Shirasawa et al., 2005).

The new feature is that the phase proportions are simulated for each grid cell in addition to the temperature (Figure 1). This approach allows a realistic structural profile with locations of liquid water containing layers. The forcing of the model is due to heat fluxes from air and water and due to mass flux from precipitation. The full model includes primary ice formation, congelation ice growth, snow metamorphosis with slush formation, and snow ice growth. Thus it consists of five types of cells: snow, slush, snow-ice, solid congelation ice and rotten congelation ice. These layers are interacting: snow accumulation creates slush and snow-ice depending on the total thickness of ice, while the growth and decay of congelation ice depends on the snow and slush conditions. Slush and snow-ice may form a multiple layer structure with snow-ice and slush layers in turn. The thickness of snow decreases due to three different reasons: surface melting, compaction, and formation of slush, which further transforms into snow-ice. The snow density change depends mainly on the mass of overlaying snow and temperature, and the thermal conductivity is proportional to the density squared (Yen, 1981).

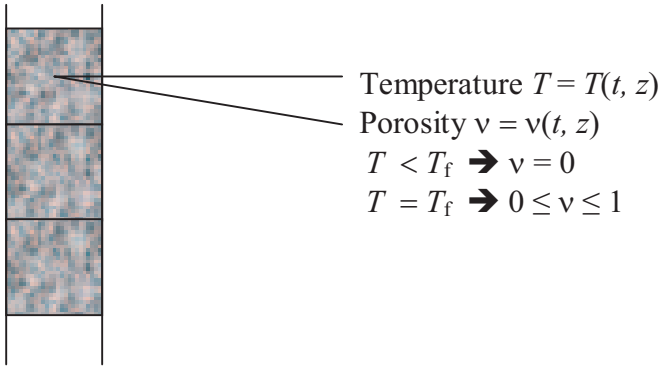

Figure 1. The model grid cells.

The active layer in solar heating equals the attenuation depth μ^{-1}, which is of the order of 1 m for congelation ice and 0.1 m for snow and snow-ice. Thus, as soon as the snow has melted, internal melting takes place all across the ice sheet and also the water beneath the ice warms up. By simple analytic analysis, it is seen that the temperature rise of cold ice and porosity increase of warm ice are

$$\Delta T = (1-\alpha)\frac{\gamma Q_s}{\kappa\mu} \tag{6a}$$

$$\Delta \nu = (1-\alpha)\frac{\gamma Q_s}{\rho L \Delta z} \tag{6b}$$

Increasing of the porosity leads to deterioration and ice breakage, which is not yet included in the model.

The volume of ice is porosity times the thickness of ice $V = \nu h$, the thickness defines as the distance between the upper and lower ice boundaries. The volume change is

$$\frac{dV}{dt} = \nu\frac{dh}{dt} + h\frac{d\nu}{dt} \tag{7}$$

as dictated by internal and boundary melting. Which one term on the right-hand side is stronger, depends on the ratio between internal and surface heating, but the experience so far suggests that the terms are of the same order of magnitude in general.

3.2 A study case

A case study was done used typical weather data for a mild winter in southern Finland. Figure 2 shows a comparison between analytic model and the full model. Analytic model ice grows much faster in the early season and the maximum thickness is much higher than in the full model. Also in the analytic model ice grows or melts when the surface temperature is above or below, respectively, the freezing point. This is sometimes quite biased since the surface temperature is not always a good predictor of the net heat flow. It is seen that the melting period is about one month. The ice thickness decreases first by 10 cm in 20 days and the last 15 cm disappears in five days. This is due the porosity increasing, more porous ice loses thickness more easily.

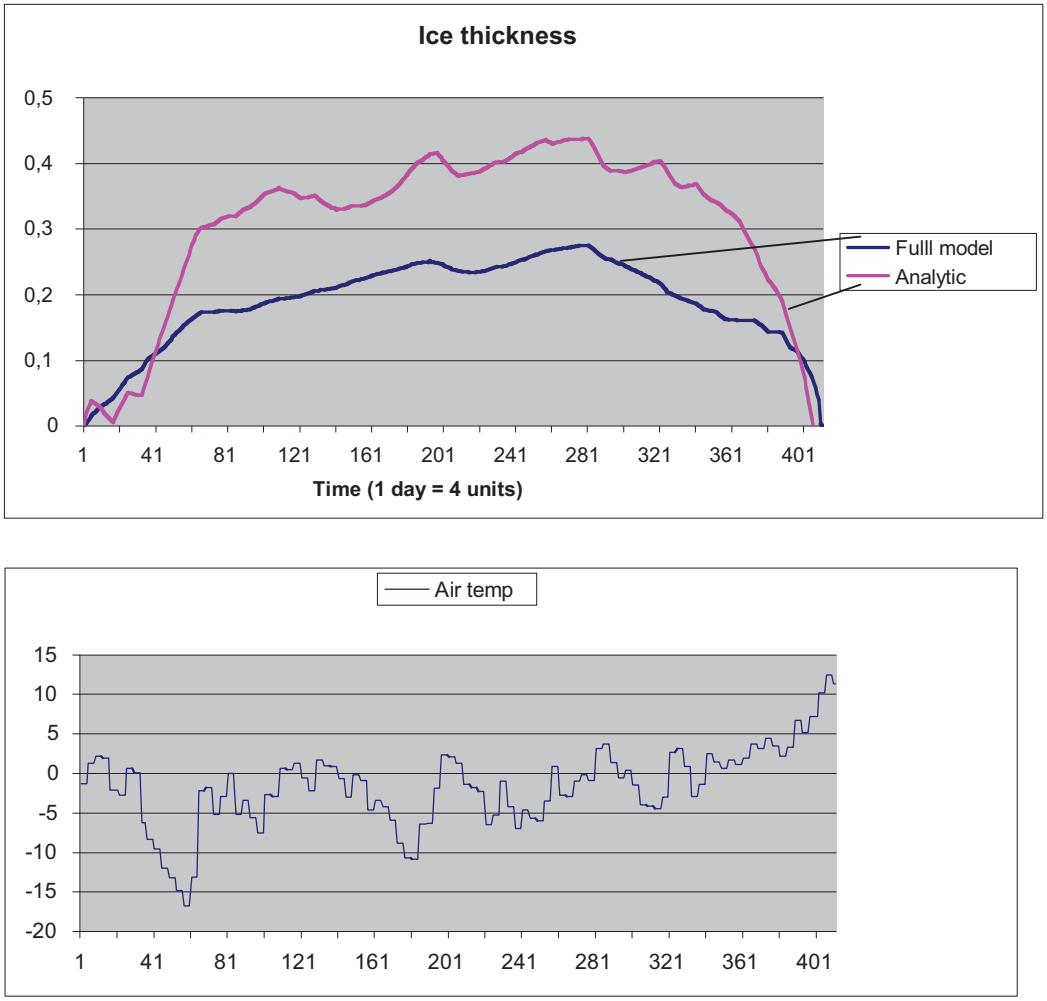

Figure 2. Upper plot: Simulated ice thickness (m) using an analytic model and full model. Lower plot: Air temperature (ºC) In the horizontal axis tic spacing is five days (20 units).

Figure 3 shows the melting season in more detail. The liquid water volume in top layer cells increases up 40% of the grid cells before the their total disappearance due to ice thickness decrease. In the beginning of the melting season, the thickness decrease and internal melting start up at the same time. For most of the melting season the thickness decreases by 0.5 cm/day and voids are added the top cells up to 1mm/day The internal melting decreases the total volume and in the last 10 days the thickness decreases fast, 1.5 cm/day.

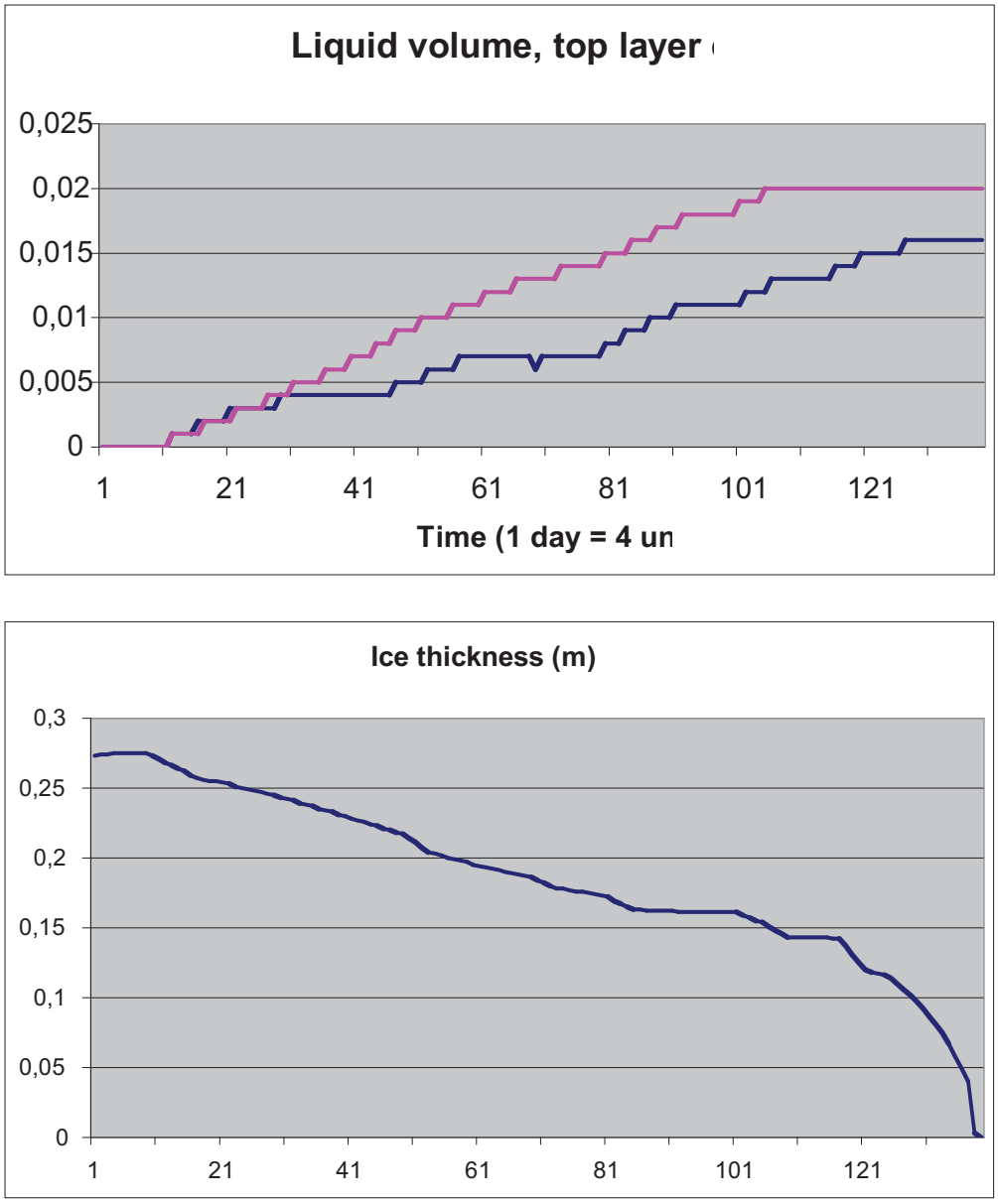

Figure 3. The melting season (40 days). Upper plot: liquid water volume in two top layer cells in equivalent meters (grid size 0.05 m). Lower plot: ice thickness (distance between upper and lower surfaces).

The liquid water volume becomes largest in grid cells 2-4 covering the depths 5–20 cm (Figure 4), with the peak in grid cell 3. In the surface cell the radiation balance keeps negative all time and no internal melting is seen, but deeper internal melting is present in all cells and some of the solar radiation goes through the ice. This distribution is well know from practice.

The top layers of the ice become soft in the melting season and difficult to walk or drive by snow mobile, even though the lower layers still give a significant bearing capacity to the ice.

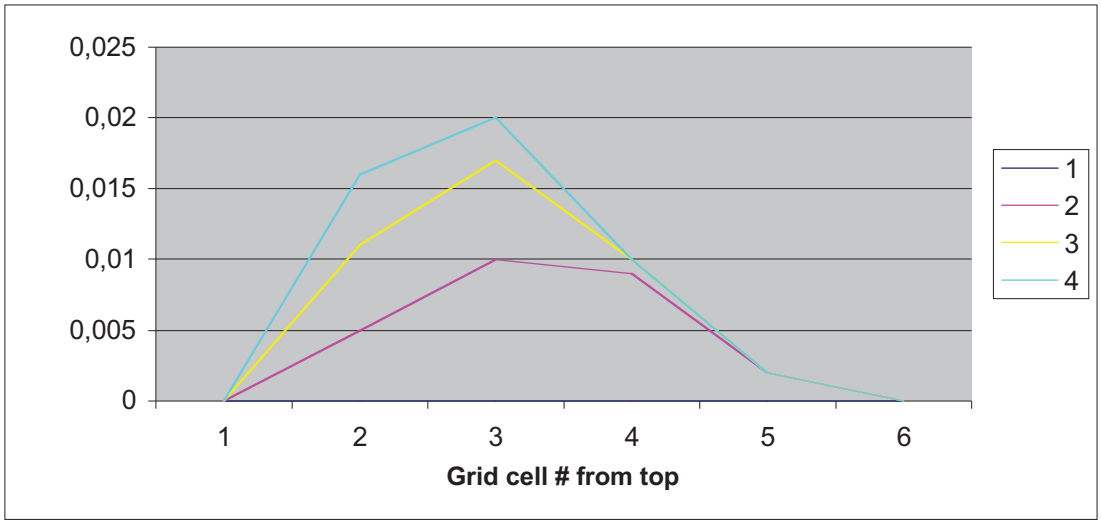

Figure 4. Evolution of the porosity distribution in the six grid cells on top, grid size is 5 cm. The curves show the distribution at 10-day intervals, starting from zero level (1).

4. Concluding remarks

A new thermodynamic model was presented for its structure and a case study example. The novel feature of this model is a two-phase approach where for each grid cell the modelled quantities are temperature and liquid water volume. The liquid water is present any time when slush is formed on in the snow layer, and slush trapped within the ice sheet may persist there long time. In the melting season, the melting takes place at the boundaries and, due to solar radiation, inside the ice sheet. The internal melting is caused by solar radiation, and thus albedo and light attenuation coefficient are critical model parameters.

With the two-phase approach the evolution of the ice structure can be properly modelled. Slush layers are well reproduced and the physical representation of melting ice is realistic. Then better estimate for ice loads and bearing capacity can be made, since ice strength is a function of porosity. Ice break-up comes correctly since this is dictated by achieving the critical porosity where ice has lost its strength. For lake ecology research, realistic locations of biological habitats in the ice sheet can be predicted and with an advance light transfer model the light conditions beneath ice become better understood.

The two-layer model has also been applied by the author for supraglacial lakes in Antarctica, where problem is reverse to ice season modelling, i.e. it is formation of liquid water lake from glacier surface layer ice and freezing the lake back to the glacier. Further testing of the model is now ongoing using cases with detail data available.

Acknowledgements. This work has been supported by the project 'Mesoscale Dynamic-Thermodynamic Modelling of Sea Ice' funded by the Academy of Finland.

5. References

Arst, H., Erm, A. Leppäranta, M. and Reinart, A. (2006) Radiative characteristics of ice-covered fresh- and brackish-water bodies, *Proceedings of the Estonian Academy of Sciences. Geology* **55**, 3–23.

Ashton, G. (ed.) (1986) *River and lake ice engineering*. Water Resources Publications, Littleton, Co.

Leppäranta, M. (1983) A growth model for black ice, snow ice and snow thickness in subarctic basins, *Nordic Hydrology* **14**, 59–70.

Leppäranta, M. (1993) A review of analytical sea ice growth models, *Atmosphere–Ocean* **31**, 123–138.

Leppäranta, M., Reinart, A., Arst, H., Erm, A. Sipelgas, L. and Hussainov, M. (2003) Investigation of ice and water properties and under-ice light fields in fresh and brackish water bodies, *Nordic Hydrology* **34**, 245–266.

Maykut, G.A. and Untersteiner, N. (1971) Some results from a time-dependent, thermodynamic model of sea ice, *Journal of Geophysical Research* **76**, 1550–1575.

Petrov, M.P., Terzhevika, A.Yu., Zdorovennov, R.E. and Zdorovennova, G.E. (2006) The thermal structure of shallow lake in early winter. *Water Research* **33**: 135–143.

Saloranta, T. (2000) Modeling the evolution of snow, snow ice and ice in the Baltic Sea, *Tellus*, **52**A, 93–108.

Shirasawa, K., Leppäranta, M., Saloranta, T., Polomoshnov, A., Surkov, G. and Kawamura, T. (2005) The thickness of landfast ice in the Sea of Okhotsk, *Cold Regions Science and Technology* **42**, 25–40.

Shirasawa, K., Leppäranta, M., Kawamura, T., Ishikawa, M. and Takatsuka, T. (2006) Measurements and modelling of the water–ice heat flux in natural waters, *Proceedings of the 18th IAHR Symposium on Ice*, Hokkaido University, Sapporo, Japan, pp. 85–91.

Yen, Y.-C. (1981) Review of thermal properties of snow, ice and sea ice, CRREL Report 81-10.

Zubov, N.N. (1945) *L'dy Arktiki* [Arctic Ice], Izdatel'stvo Glavsermorputi, Moscow [English translation 1963 by U.S. Naval Oceanographic Office and American Meteorological Society, San Diego]

Evaluation of the Operational HIGHTSI Thermodynamic Ice Model in the Baltic Sea for the Winter 2007–2008

Juha Karvone,n Bin Cheng, Markku Similä
Finnish Institute of Marine Research (FIMR)
email : Firstname.Lastname@fimr.fi

Abstract

A thermodynamic sea ice model named HIGHTSI developed at FIMR was run operationally at Finnish Ice Service for the first time during the winter 2007–2008. Here the modeling results are compared to other existing measurements and the model performance is evaluated and some recommendations for the future winters are given.

1 Introduction

During the winter 2007–2008 the thermodynamic ice model HIGHTSI (HIGH-resolution Thermodynamic Snow/Ice model) [1, 2, 3] was run operationally for the first time at Finnish Ice Service (FIS). Here we show the first evaluation results for the model runs during the winter 2007–2008, and also give some general remarks on the model performance and describe our future plans regarding operational thermodynamic ice modeling at FIS. The main goal was to create a reliable operational version of the model and also to develop an evaluation process and test it for use in the future winters. During the winter 2007–2008 the model was run with 116 hour forcing data from ECMWF (European Centre of Middle-range Weather Forecasts), i.e making five day forecasts possible. Next winter our aim is to use 10-day forcing data and provide 10-day snow and ice forecasts and compare these results with the current operational 10-day forecasts by using freezing degree days (Zubov equation) method applied for harbors in Finland.

2 HIGHTSI Snow/Ice Model

The HIGHTSI snow/ice model was developed at FIMR [1]. The model is targeted for process studies, i.e. to simulate evolution of snow/ice surface temperature, in-snow/ice temperature and snow/ice thickness. Special attention is paid on the penetration of solar radiation in the snow and ice, which makes the model capable to quantitatively calculate sub-surface melting. The parameterizations turbulent surface fluxes are made taking the thermal stratification into account. The model has been validated against several in situ data sets and, in general, yields good results of the surface heat balance, snow/ice mass balance and snow/ice temperature regimes [2, 3]. It has been found that successful simulation of temperature regimes within snow/ice during a melt season with large solar radiation requires a high vertical resolution. Recent developments of HIGHTSI have focused on processes during the melt season, i.e. snow/ice surface and sub-surface melting, refreezing, and superimposed ice formation (ice refrozen from melt water) [3], effects of precipitation, and the impact of surface albedo on snow and ice mass balance [4].

The external forcing were wind speed, air temperature, relative humidity, cloudiness and precipitation yielded by numerical weather forecast models (e.g. ECMWF, HIRLAM). The initial ice thickness and ice edge (ice/open water) were retrieved from operational Ice Charts (IC). The open water classification from SAR data can provide ice and open water area for HIGHTSI independent of IC's. The variation

of snow thickness in HIGHTSI was operationally taken into account, i.e. snow was increased with incoming precipitation and decreased with compactness, surface melting and formation of snow-ice and superimposed ice. A schematic presentation of the model is given in Fig. 2.

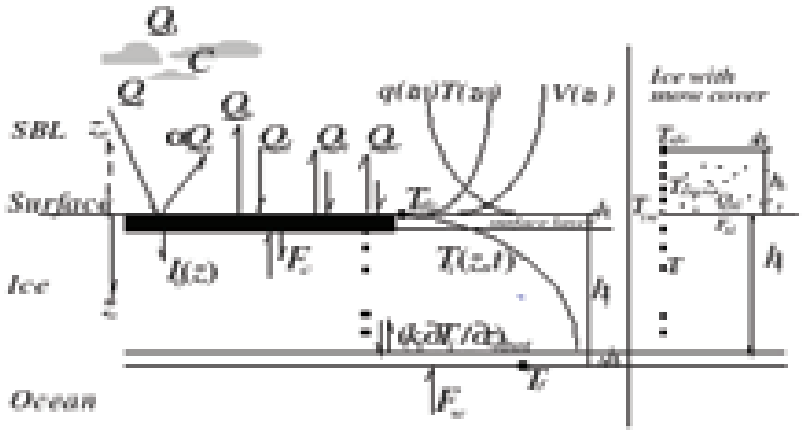

Figure 1: Structure of the HIGHTSI ice model.

The variables taken into account in the model are:

- Q_0, Q_s: global downward solar radiation under clear and cloudy sky condition
- C: total cloudiness factor, between 0 and 1
- α: surface albedo
- Q_d, Q_b: down-welling and surface-emitted long wave radiation
- Q_h, Q_{le}: surface turbulent fluxes of sensible and latent heat
- $I_o(z)$: penetrating solar radiation below surface
- F_c: surface heat conductive flux
- T_{sfc}: surface temperature solved from a surface heat balance equation.
- $T_i(z,t)$ / T_{snow}: vertical temperature distribution within the ice/snow floe solved by a heat conduction equation. The heat flux divergence at ice bottom determines the mass balance
- k_i: heat conductivity of ice
- F_w: the oceanic heat flux assumed to be a function of the ice concentration
- T_f:freezing temperature
- h_s, h_i: snow and ice thickness

HIGHTSI reads IC's daily so the ice edge and thickness were initialized accordingly. The initial snow and ice temperature profiles are generated by letting the model adapt for a five-day period before the actual model run start time, using appropriate forcing data and 24-hour HIGHTSI outputs as inputs of the daily HIGHTSI runs for the adaptation period. Since IC's do not provide any information on the snow thickness, the precipitation from weather forecast model is the sole source for snow accumulation. We applied five days ECMWF forecasts to run HIGHTSI up to 116 hours daily. On each day, the 24-hour snow forecast will be used as the initial snow condition for HIGHTSI run on the next day.

FIS delivers Finnish Maritime Administration (FMA) 10-day ice thickness forecasts for the winter harbors in Finland. These are based on the computation of the Zubov's equation:

$$H^2 + 50H = 8\Phi, \tag{1}$$

where H is the ice thickness, Φ is the number of the freezing degree days (sum of negative daily temperatures). The computation with this formula is started every winter after the ice concentration at a harbor exceeds 80 %. In the future HIGHTSI will be used for this purpose and compared with the current system when 10-day ECMWF forecasts are available (next winter). If the HIGHTSI forecasts are more accurate, HIGHTSI will be used to forecast the harbor ice. Combining HIGHTSI and SAR data is under construction [6, 8], the ice dynamics will be extracted from the SAR data (ice drift from the successive SAR images, SAR backscattering details).

3 Operation of HIGHTSI during the winter 2007–2008

The winter 2007–2008 in the Baltic Sea was extremely mild and the sea ice cover was significantly thinner and covered smaller area than in an average year. The measured daily temperatures (minimum, mean, maximum) starting from December 1st and ending May 27th are shown at two places one in the area of Bay of Bothnia and the other in the area of Gulf of Finland in Fig. 2.

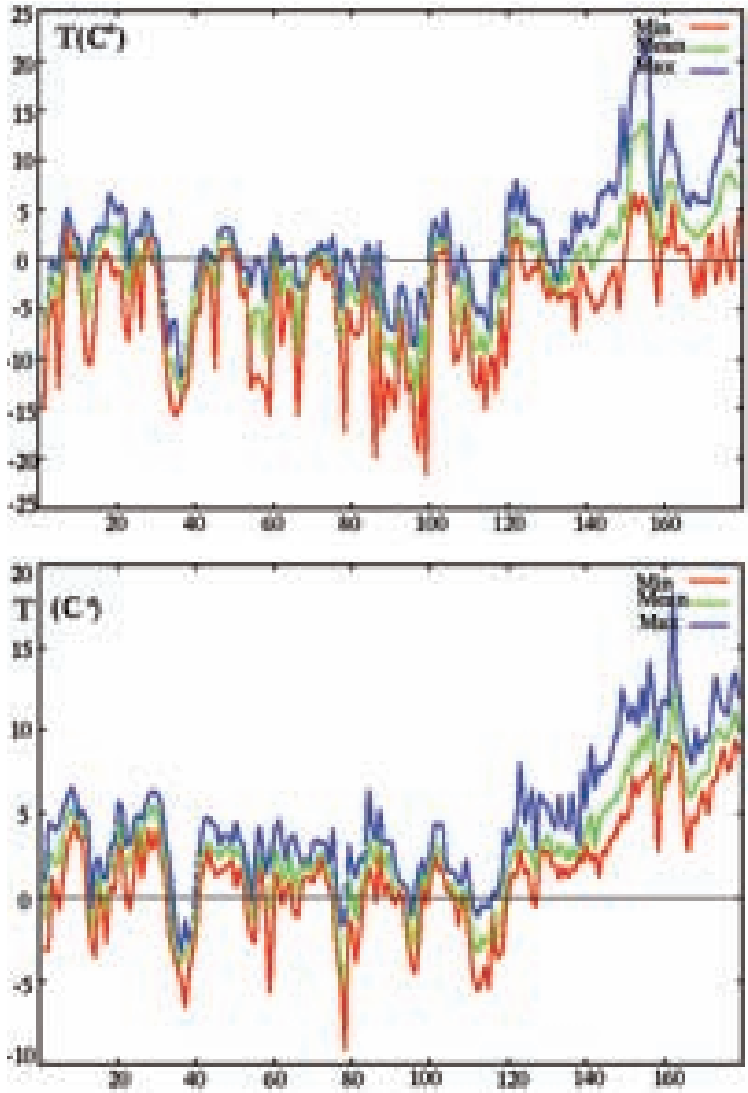

Figure 2: Temperatures at Hailuoto (65^{o}00.50'N, 24^{o}42.92E, upper) and Isosaari (60^{o}06.13'N, 25^{o}03.26'E, lower).

The operational version of the HIGHTSI ice model run was started on January 29th 2008 and the

model was run until May 16th 2008. The model was run daily giving a hourly forecast up to 54 hours. For technical reasons the model output were not generated in 13 days: February 16th, 22-23th, April 1st, 3-4th, 10-11th, 24-24th, 28th and May 7th and 9th.

The HIGHTSI run area covers the whole Baltic Sea (66.0N, 9.0E) → (53.0N, 31.0E). The operational model runs can be turned into numbers (ice thickness and snow thickness) at a given location (latitude, longitude) or into graphics showing the forecasted ice thickness as a colored thematic map, see 3.

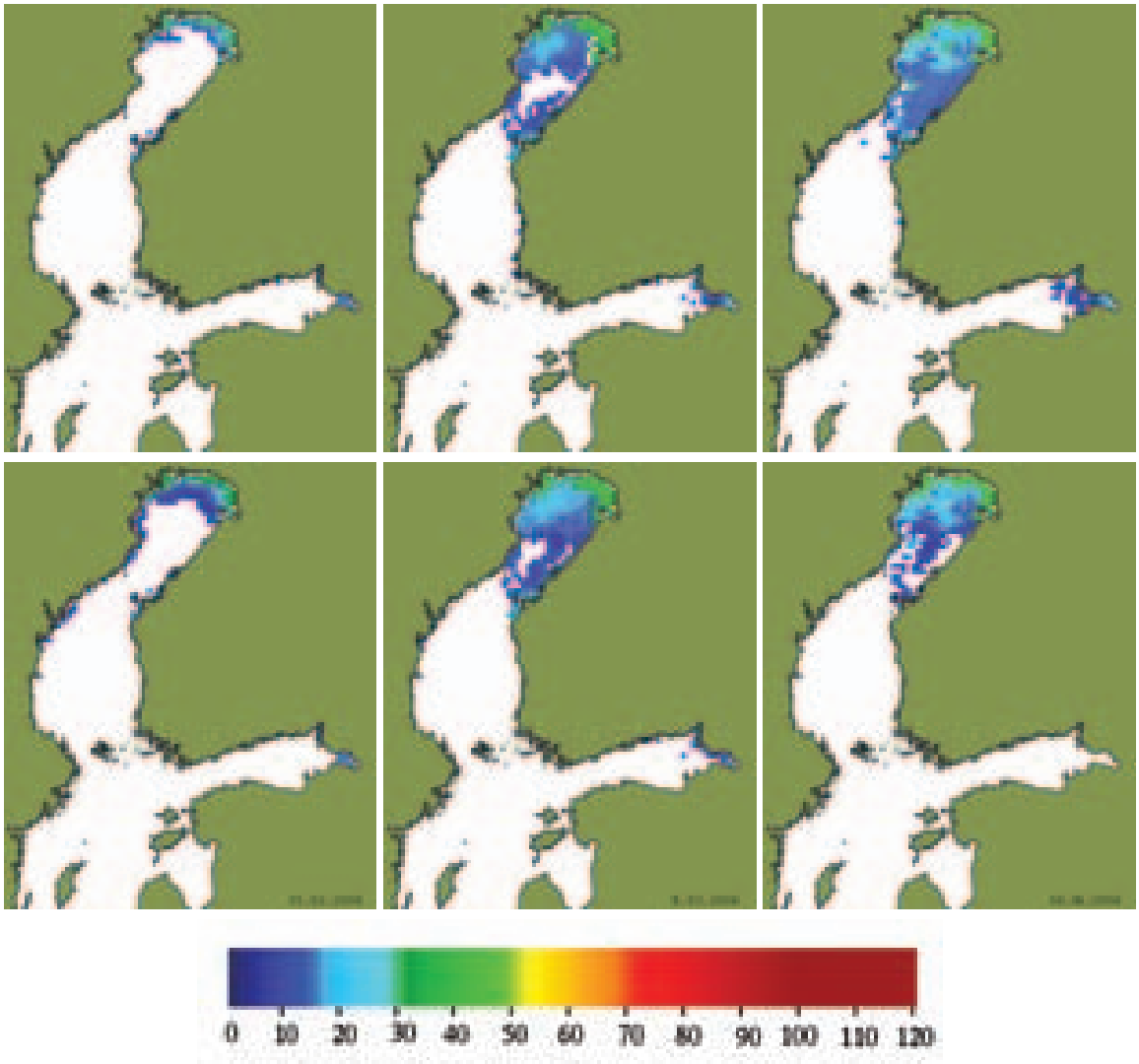

Figure 3: An example of the operational graphics product based on the HIGHTSI model, a five day forecast showing the forecasted ice thickness on February 5th 2008 (left), M;arch 16th 2008 (middle) and April 8th 2008. The initial thicknesses from the ice charts five days before are shown on the upper panel and the five day forecasts on the lower panel. The first date represents the freezing season, the middle data about the annual maximum, and the third the melting season.

4 Evaluation results

The HIGHTSI results of five day forecasts were compared with ice thickness and snow thickness measurement made on ice breakers during the winter 2007–2008 and with the thicknesses of the operational ice thickness charts (ITC's) [5], also publicly available at http://polarview.fimr.fi. The ITC's are based

on Ice Charts (IC's) from FIS and SAR data.

Fourteen point measurements made by the ice breakers were made during the same day of available HIGHTSI two-day forecasts. The ice breaker measurements were made during the period January 31st to April 8th 2008. The L_1 error E_1 between the measurements and HIGHTSI was 12.9 cm and the systematic error E_s ("signed L_1-error") was -11.1 cm, i.e HIGHTSI on average underestimates the ice thickness by this amount. For comparison, we also computed the five-day forecasts using the Zubov's equation, starting from the thickness values given by the ice charts, i.e. the initial value for the frost degree days, Φ_0 is naturally given based on the Zubov's equation:

$$\Phi_0 = \frac{{h_0}^2 + 50h_o}{8}, \tag{2}$$

where h_0 is the ice thickness at the starting moment, and the ice thickness h solved from Eq. 2 is

$$h = \frac{-50 + \sqrt{50^2 + 32\Phi}}{2}. \tag{3}$$

The corresponding error measures for the Zubov method were $L_{1Z} = 16.5cm$ and $E_{sZ} = -15.0cm$. For the snow thickness the corresponding values were E_1=3.5 cm and E_s=1.4 cm. The figures 4 and 6 show the measured thickness values vs. the thickness values estimated by HIGHTSI. Also the ice thicknesses estimated by the Zubov method are shown.

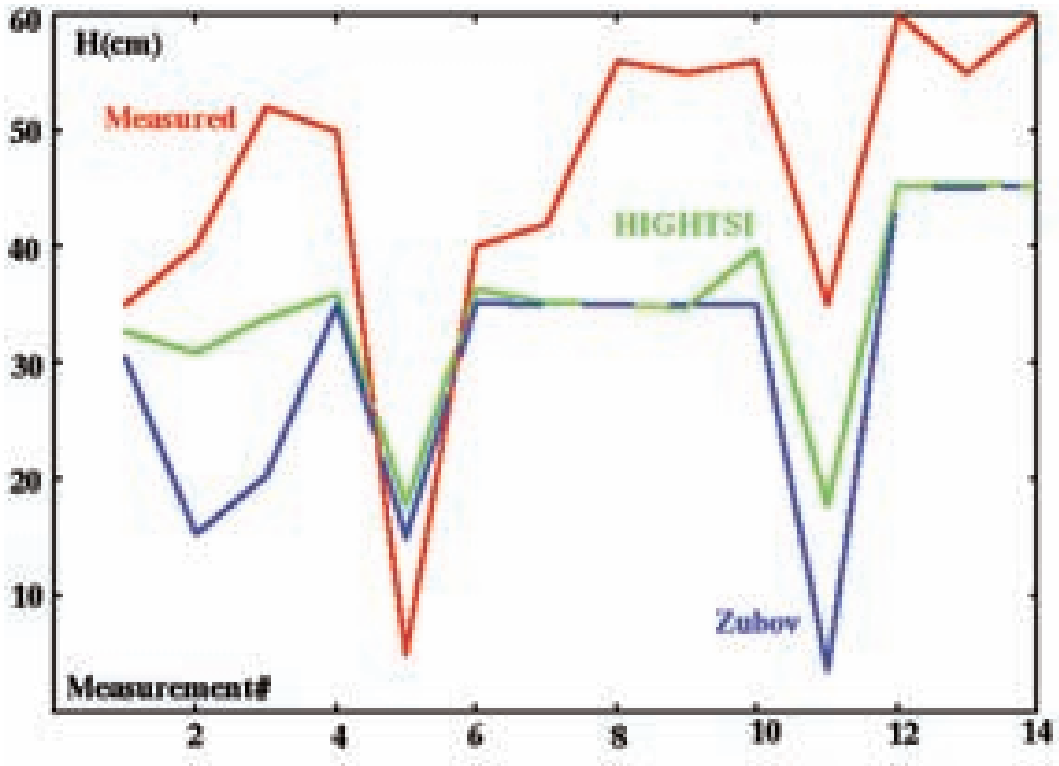

Figure 4: Comparison between point measurements made on ice breakers and 5-day HIGHTSI forecast and Zubov method, ice thickness.

The comparison between operational ITC's was again made for the five-day HIGHTSI forecasts. Totally 75 ice thickness charts were used in the comparison (the day of the ice thickness charts being the same as for the HIGHTSI two-day forecasts). Three measures of similarity were computed for this data set in their overlapping areas: E_1 and E_s. The computed values are shown in Table 1. These values are for ice thickness only, because ice thickness charts only give the ice thickness. It can be seen that again

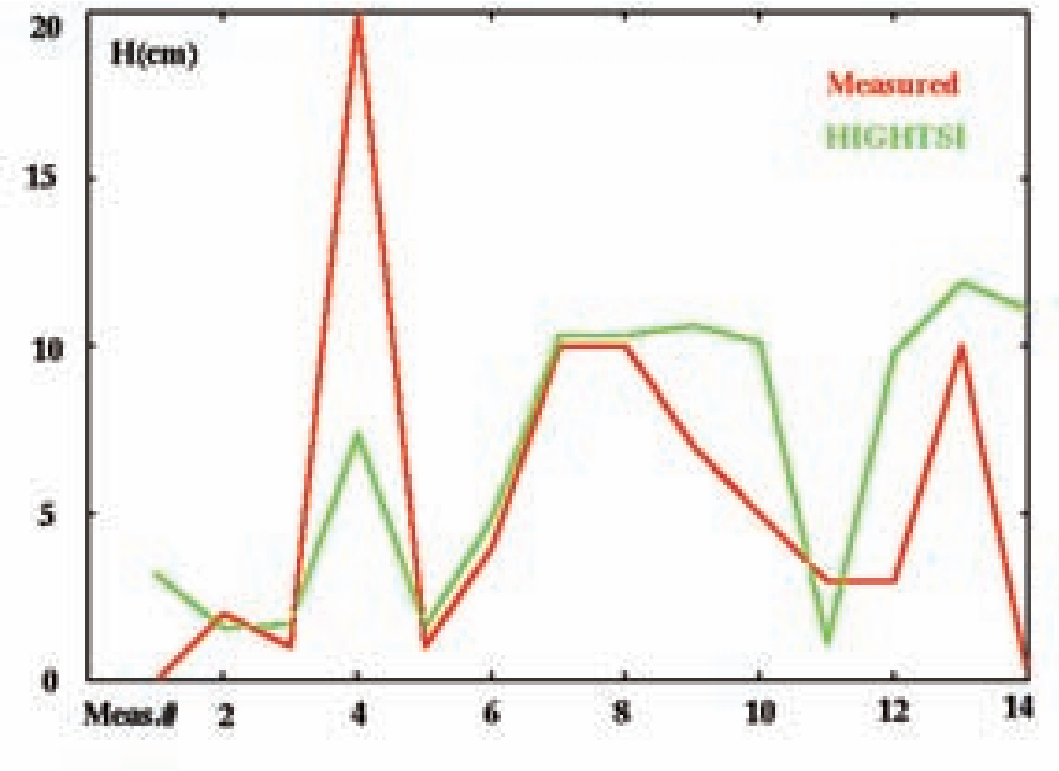

Figure 5: Comparison between point measurements made on ice breakers and 5-day HIGHTSI forecast, snow thickness.

Table 1: Comparison between HIGHTSI ice thickness and the ice thickness of the operational ice thickness charts in numbers.

Measure	Mean	Standard dev.
L1 error	8.7 cm	2.2 cm
Systematic error	-3.2 cm	3.8 cm

HIGHTSI slightly underestimates the ice thickness. We also noticed that cross-correlation values are very high between HIGHTSI results and ITC's. This is natural because both are using the same initial data from IC's.

5 Conclusion and Future Work

The HIGHTSI model results have been validated against field measurements in fast ice areas in several field campaigns where it has yielded consistently accurate snow/ice thickness values. Also our comparisons show that HIGHTSI produces useful sea ice information. However, the initial ice thickness values from the IC's seem to underestimate the ice thickness. In the next winter we are going to run two operational versions of HIGHTSI in parallel with 10-days ECMWF forecasts. One is using the IC ice thickness as its initial information, and the other is run throughout the whole winter without this information, only taking the previous model outputs as its inputs. Additionally the ice edge and ice concentration input information is derived from SAR data. These model versions will be compared to each other and also to the operational model based on Zubov's equation. Additionally we will study the joint use of the parallel HIGHTSI model results.

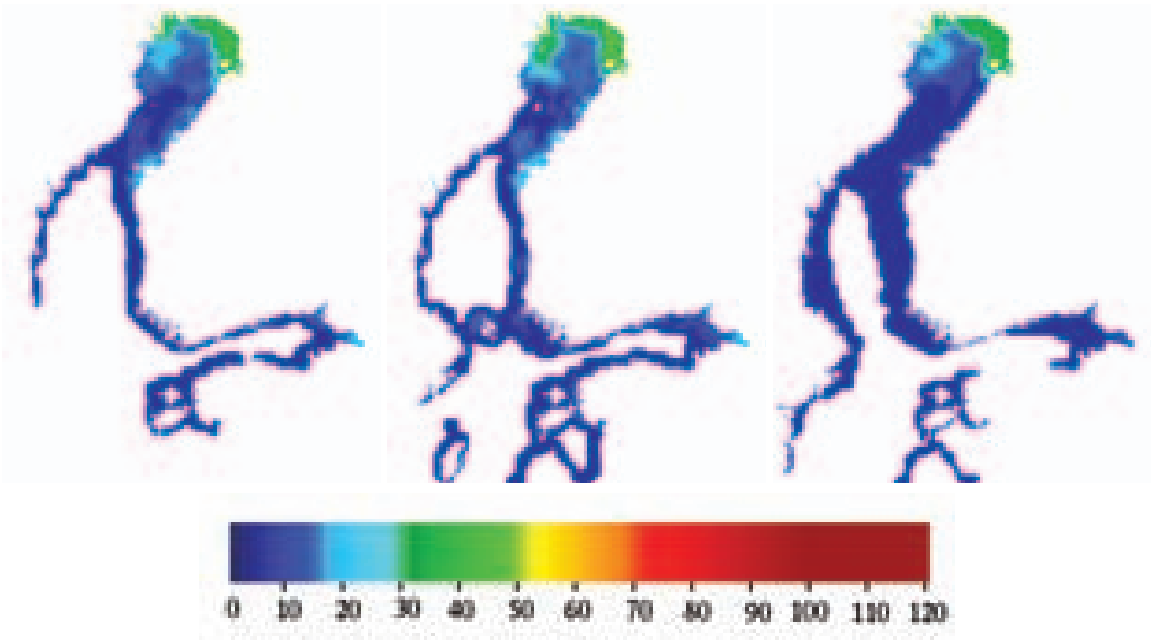

Figure 6: The operational IC on March 13th 2008 (left), the operational ITC (middle, based on most recent SAR data), and the HIGHTSI five-day forecast for the same day (right).

The HIGHTSI snow thickness forecasting seems to give reasonable results. This can be explained by the good quality of weather forecasts (external forcing of HIGHTSI) from ECMWF and by that HIGHTSI models snow melting with a relative good accuracy (a new surface albedo parametrization used). In the future we hope that we can also utilize the snow cover information produced by HIGHTSI in sea ice SAR data interpretation.

Comparison to operational ITC's also provided good results. One natural reason for this is that both HIGHTSI and the ITC's use the same initial information from IC's. However, our evaluation results from earlier winters have clearly shown that ITC's give good estimates of the ice thickness compared to the measured values [7].

We are going to continue the evaluation of HIGHTSI yearly using all possible reference data sets available, the most important ones being the ice thickness measurements made by ice breakers and our operational ITC's. In 2007–2008 the starting of the model was delayed because of technical reasons. There also were some breaks in the service because of computer problems (full hard disk). In general the operational HIGHTSI model setup seems to work reliably and the results are reasonable. The evaluation methods are now ready and tested for the next season and HIGHTSI can be started from the beginning of the ice season, and yearly evaluation reports will be delivered, and HIGHTSI parametrization will be developed and adjusted accordingly.

References

[1] J. Launiainen, B. Cheng, Modeling of ice thermodynamics in natural water Bodies, Cold Reg. Sci Technol., v. 27, n. 3, pp. 153–178, 1998.

[2] B. Cheng, T. Vihma, J. Launiainen, Modeling of the superimposed ice formation and sub-surface melting in the Baltic Sea, Geophysica, v. 39, n. 1-2, pp. 31–50, 2003.

[3] B. Cheng, T. Vihma, R. Pirazzini, M. Granskog, Modeling of superimposed ice formation during spring snowmelt period in the Baltic Sea, Ann. Glaciology, v. 44, pp. 139–146, 2006.

[4] B. Cheng, Z. Zhang, T. Vihma, M. Johansson, L. Bian, Z. Li, H. Wu, Model experiments on snow and ice thermodynamics in the Arctic Ocean with CHINARE 2003 data, J. Geophys. Research, v. 113, 2008.

[5] J. Karvonen, M. Simila, I. Heiler, Ice Thickness Estimation Using SAR Data and Ice Thickness History, Proceedings of the IEEE International Geoscience and Remote Sensing Symposium 2003 (IGARSS'03), v. I, pp. 74-76, 2003.

[6] J. Karvonen, B. Cheng, M. Simila, Baltic Sea Ice Thickness Charts Based on Thermodynamic Ice Model and SAR Data, Proc. of the International Geoscience and Remote Sensing Symposium 2007 (IGARSS'07), pp. 4253-4256, 2007.

[7] J. Karvonen, J. Haapala, J. Lehtiranta, A. Seina, Polarview@FIMR: WWW-based Delivery of Baltic Sea Ice Products to End-Users, Proc. of the International Geoscience and Remote Sensing Symposium 2007 (IGARSS'07), pp. 1242-1245, 2007.

[8] J. Karvonen, B. Cheng, M. Simila, M. Hallikainen, BalticSea Ice Thickness Charts Based on Thermodynamic Snow/Ice Model, C-Band SAR Classification and Ice Motion Detection, Proc. of the International Geoscience and Remote Sensing Symposium 2008 (IGARSS'08).

Freeze fractionation of Dissolved Organic Matter during sea ice formation

Susann Haase
Department of Biological and Environmental Sciences
PL 65 (Viikinkaari 1), 00014 University of Helsinki
susann.haase@helsinki.fi; phone+358-445155646

Abstract

Sea ice plays an important role in heat flux mechanisms of the oceans such as air-ocean interaction, thermohaline mixing and albedo feedback. In addition, the brine channels of sea ice serve as a habitat for various organisms. A main factor controlling the biology of sea ice, but also optical properties, is dissolved organic matter (DOM) which is strongly influenced by the initial freezing process. Therefore, the behavior of DOM during the ice formation needs to be described in detail to allow predictions about the character and concentration of DOM in sea ice.

This study about the freeze fractionation of DOM from the Gulf of Finland used 450 liter tanks to grow sea ice at -5°C. The initial conditions were compared to the ice and under-ice water by measuring the absorption coefficient of chromophoric DOM, fluorescent DOM and the size distribution of DOM. Excitation-Emission Matrices (EEMs) of DOM fluorescence were used for parallel factor analysis (PARAFAC).

In order to investigate the behavior of DOM relative to salts, an enrichment factor was calculated for CDOM and FDOM for the initial water samples and one week after ice formation. The mean enrichment factor was found to be 1.4 in ice whereas 1 in under-ice water which means that enrichment only took place within the ice. The size exclusion chromatography shows a shift in size distribution towards higher molecular size in ice. This change is less obvious for young ice and hence depends on physical processes during the ice formation and growth. The components identified by PARAFAC behave differently during the freeze fractionation, but were always enriched in the ice relative to salts.

The tank experiment leads to the assumption that the freeze fractionation of DOM depends on molecular size, composition of DOM and physical processes such as diffusion and convection.

Maximum Extent of the Baltic Sea Ice Recalculated for the Period 1971-2008

Tuomas Niskanen, Jouni Vainio, Patrick Eriksson, István Heiler

Finnish Institute of Marine Research, Ice Service, E-mails: firstname.lastname@fimr.fi

Abstract

In Finland the publication of operational ice charts of the Baltic Sea was started in 1915. Since 1993, when the ice charting software IceMap was launched, all ice charts have been drawn by computer. Before that the ice charts were hand drawn paper copies.
Since the year 1996 IceMap has had a module that calculates the areas of the different ice area polygons in the chart. By this the area of the maximum ice extent is easy to solve automatically. Before this function was in use, all maximum extent areas were calculated manually by using a planimeter.
During recent years it has become clear that areas calculated using the planimeter don't give the same result as IceMap. Such an error can be caused for example by inaccuracy of old coastlines, map projections or the calibration of the planimeter.

Introduction

When comparing old maximum extent ice charts, it was found that in the winters 1971 (figure 1) and 1999 (figure 2) original numerical values of the ice covered areas were the same (157,000 km^2). Looking at the charts, however, it is easy to see that this cannot be the case. In the year 1971 charts were hand drawn and ice extents were calculated by planimeter. In 1999 the IceMap software was used in order to produce ice charts and also to calculate the maximum extent of the ice cover.

Fig. 1.

Fig. 2.

The examination of the maximum ice extent figures in the frame of the current ice winter severity classification indicates that the classification not always correlates with how the winter navigation has experienced the ice conditions. Using the newly calculated ice extents, a new scale of ice winter severity classification is therefore put under construction.

The reason for the chosen time period (1971 forward) is that it comprises the meteorological 30-year climatological reference period 1971-2000. Another motive is that since that winter the most important harbours (nowadays called winter ports) have not been closed due to ice conditions. This has ensured ice observations reliable enough to allow comparisons to more modern observation techniques.

Recalculation of maximum ice extent charts

In order to decrease error sources, old maximum extent charts from winters 1970-71 to 1991-92 were re-drawn with the ice charting software IceMap. First the old paper charts had to be converted into digital form.

The orientation and shape of the latitude-longitude grids of the old paper charts indicated that they are in some conical map projection but unfortunately all the projection parameters were unknown (Figure 3a). Thus, the paper charts were scanned (FMA, Hydrographic Department) and rectified to mercator projection by using the intersections of the latitude-longitude lines as tie points (Figure 3b). The rectification was performed in two steps: 1) rectification to equirectangular (plate carré) projection by using a 3rd degree polynomial, 2) transformation to mercator projection that is used in the current ice maps. Finally some IceMap required parameters were embedded to the image files of the rectified maps. The first rectification is based on two polynomials that map the source coordinates (x,y) to the destination coordinates (X,Y):

$$X = a[1]*x + a[2]*y + a[3]*x^2 + a[4]*x*y + a[5]*y^2 + a[6]*x^3 + a[7]*x^2*y + a[8]*x*y^2 + a[9]*y^3$$
$$Y = b[1]*x + b[2]*y + b[3]*x^2 + b[4]*x*y + b[5]*y^2 + b[6]*x^3 + b[7]*x^2*y + b[8]*x*y^2 + b[9]*y^3$$

The coefficients a[i] and b[i] were computed by least square fitting. In this case (x,y) were the row- and column indexes of the intersection points of the latitude-longitude lines and (X,Y) the corresponding latitudes and longitudes.

After these procedures the old charts could be opened in IceMap and new charts were drawn according to them (Figure 3c).

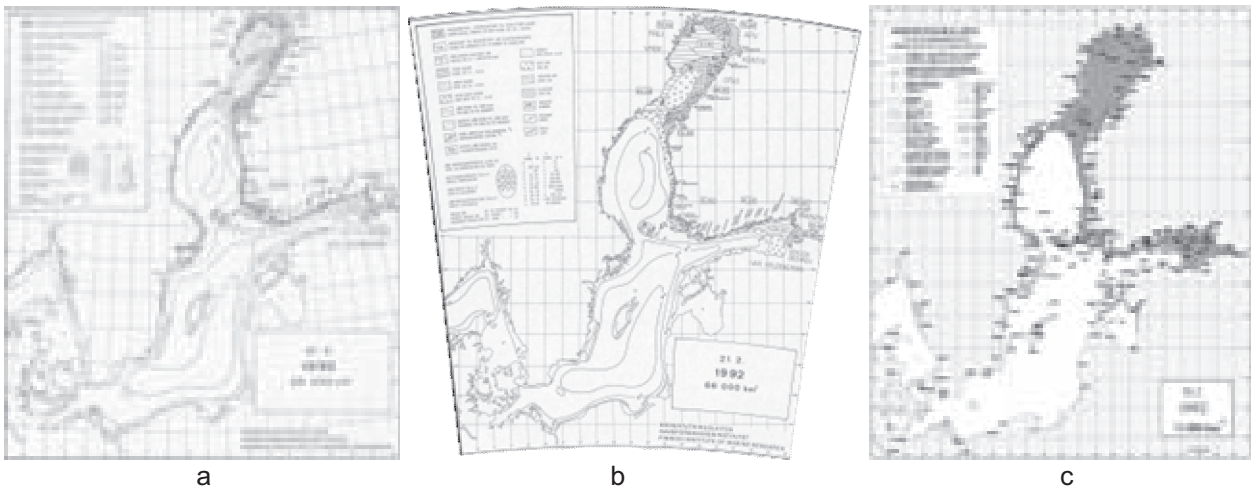

a b c

Fig. 3.

The areal coverage of the re-drawn ice areas were calculated with the ice area calculation tool integrated in the IceMap software (Figure 4).

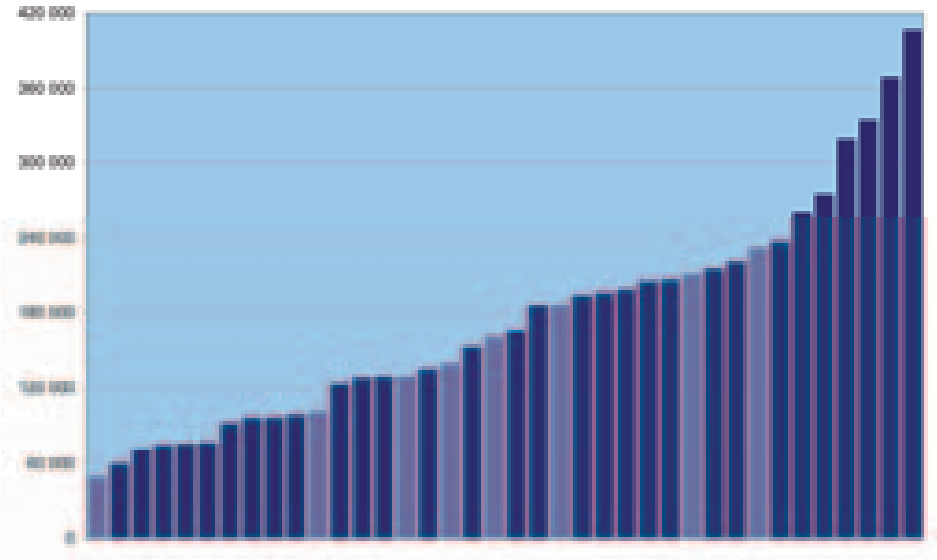

Fig. 4. Maximum ice extents of the Baltic Sea for the winters 1971 to 2008, in the order of magnitude. Dark bars indicate winters 1971-2000, light bars indicate winters 2001-2008.

Results

When comparing the old values of the maximum ice extent with the ones calculated from the new IceMap-drawn maximum charts, significant differences could be noticed (figure 5). At most the differences reached values of about 30,000 km^2. Further examination still has to be carried out to identify the reasons for these differences. Also uncertainty estimates will be made to get a confidence level of the calculated differences.

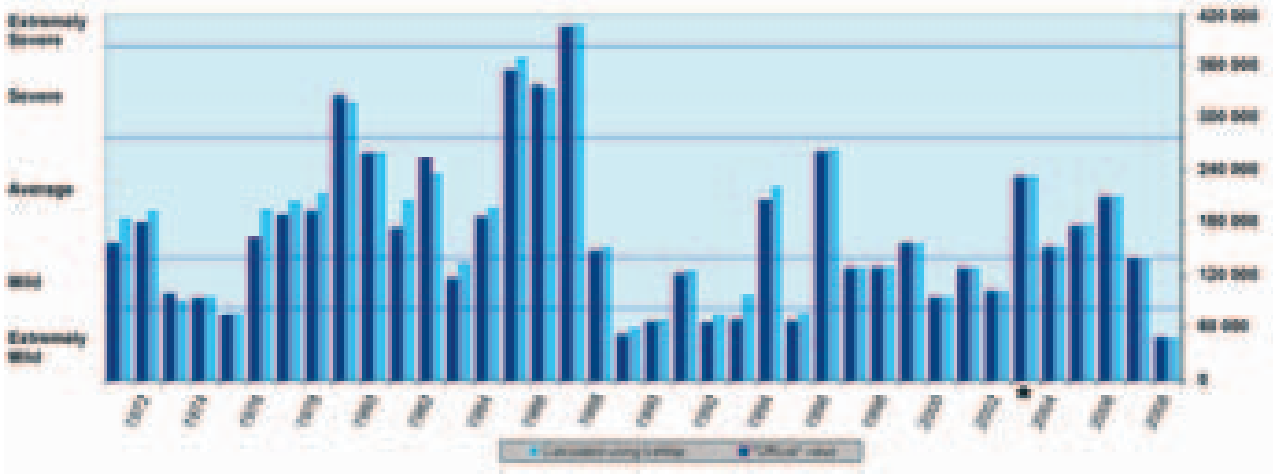

Fig. 5.

Discussion

The current ice winter severity classification has been discussed through the years. The maximum ice extent has, not without reason, been criticised for not giving a realistic picture of the experienced ice winter severity. Not least from the point of view of winter navigation. As an example we may look at the conditions of the winter 2003 (asterisk in figure 5), when the shipping in the northern Baltic Sea encountered ice conditions that could be described as very severe. Average ice extent was reached already at the end of January and especially in the Gulf of Finland ice thickness measurements reached all-time high values. The winter's maximum ice extent reached 232,000 km^2, thus classified as a normal ice winter. If the weather in southern parts of the Baltic Sea would have been cold for a longer period, the result might have looked very different.

The intuitive conclusion of the winter 2003 is, however, that it with respect to navigation conditions in the north, easily could be considered a severe ice winter. As a result efforts are put to build up a new scale of maximum ice extent-based classification that would give a more realistic picture with respect to shipping.

Influence of dissolved and particulate constituents on the optical properties of landfast sea ice

Jari Uusikivi[1], Anssi V Vähätalo[2], Mats A Granskog[3], Ruben Sommaruga[4] and Jonna Piiparinen[5]

[1] Department of Physics, University of Helsinki
[2] Department of Biological and Environmental Sciences, University of Helsinki
[3] Arctic Centre, Rovaniemi
[4] Laboratory of Aquatic Photobiology and Plankton Ecology, Institute of Ecology, University of Innsbruck, Austria
[5] Finnish Institute of Marine Research

Abstract

Ultraviolet radiation (UVR) and photosynthetically available radiation (PAR) were measured in and under coastal fast ice in the Baltic Sea. The measurements included the spectral albedo and transmittance, and spectral attenuation coefficients ($K_{d,\lambda}$) for the entire sea ice thickness and columnar ice layer. Vertical distribution of absorption by particle matter (PM) and colored dissolved organic matter (CDOM) were measured from melted ice samples to quantify their contribution to light attenuation in ice. From PM samples also the concentration of mycosporine-like amino acids (MAAs) in different ice layers was measured.
Spectral absorption coefficients for PM in sea ice revealed significant absorption by MAAs in the 320-345 nm range. MAAs were found in high concentrations (1.37 $\mu g\ l^{-1}$) in the surface layer and concentrations were almost equal to that of chlorophyll-*a* (chl-*a*), resulting in high MAA to chl-*a* ratios. CDOM was found to be the most significant absorber in the UVR (<380nm) with the exception of the surface ice layer where PM and especially MAAs dominated absorption. Absorption by CDOM was the major factor in the ice column affecting UVR intensities and UVR to PAR ratios. CDOM and PM concentrations also affected wavelength of maximum transmittance and minimum attenuation through the whole ice sheet. PM had larger effect to those than CDOM and maximum transmittance shifted from 460 to 580 nm from ice with no PM or CDOM to ice with PM and very high CDOM inclusions, respectively. In the columnar ice layers wavelength of minimum $K_{d,\lambda}$ shifted towards longer wavelengths quite linearly with increasing chl-*a* concentrations in the ice cover, except ice covers where CDOM concentrations were extremely high.

The estimates of ice pile-up intensity and frequency on the eastern Gulf of Finland coasts using the dynamic model

Klyachkin S.V. and Drabkin V.V.

1 Review of existing models and methods of coastal pile-up

Coastal ice piling up is rather typical phenomena occurred at low coasts of freezing seas. Sometimes, coastal ice conglomerations can threaten the facilities located close to shore line. In some cases, ice pile-up destroys the buildings and entire villages.

Rather detailed review of pile-up data in various regions was presented in the paper [Kovacs and Sodhi, 1979]. According to this paper, pile-up height usually does not exceed several meters, but sometimes it can reach 20-30 m. The distance from shore line to pile-up foot rarely exceeds 10 meters, while the width of pile-up can comprise tens and even hundreds of meters.

The main factor making ice pile-up possible is the absence of landfast ice. The presence of even narrow landfast ice practically excludes the possibility of ice piling up; that is why the studies of ice pile-up are closely connected with landfast ice regime.

The factors affecting the geometrical parameters of ice pile-up are speed and direction of wind and sea current, ice thickness, and slope of the coastal beach. The wind-caused fluctuations of the sea level also play very important role. These fluctuations affect, a great extent, the distance between the shore line and pile-up foot. This influence is illustrated by the Table 1 [Drabkin, 1978] characterizing ice conglomeration formed in the Neva Bay at strong flooding in December, 1973.

Table 1 – Distance between the pile-up foot and shore line versus the coast steepness near the town of Sestroretsk (eastern Gulf of Finland, December, 1973, sea level elevation 2.40 m)

Slope steepness, deg.	> 10	5-10	2-5	1-2
Distance from shore line to pile-up foot, m	< 8	8-15	15-40	> 40

Duration of the process of pile-up formation usually does not exceed 30-60 minutes that seems a very important factor.

As the ice pile-up formation is considered as dangerous phenomenon, the elaboration of the model which allows simulating and forecasting this process (including geometrical parameters, forces and energy) seems very urgent.

Some papers related to this problem are known.

In particular, the mentioned above paper [Kovacs and Sodhi, 1979] presents the model calculating the linear load which leads to formation of pile-up of given size. The authors reveal the “primary” stage of pile-up formation, when ice blocks creep on beach surface, and next stages, when ice blocks move up the slope of already formed pile-up. Using the values of ice thickness, steepness of coast and the angle of lateral surface of pile-up measured in the Gulf of Bothnia, the authors obtained quite realistic estimates of the forces ant stresses within ice floe.

The paper [Kheisin, 1989] proposes the method of calculating the wind speed resulting in pile-up formation. The method is based on the principle of energy balance, i.e. the work of external forces of ice pressure is equated with the potential energy of ice pile-up. The main

factor providing the necessary capacity is wind, and author obtains rather simple (from mathematical view point) correlation between wind speed and pile-up size.

The paper [Hopkins, 1997] presents the comparison between the numerical and laboratory models of pile-up formation. The numerical model is based on the principles of classical work [Parmerter and Coon, 1972]. The laboratory experiment is executed as follows: the sloping surface imitating the slope of some offshore structure moves towards the motionless ice floe. The sensors mounted within the sloping surface measure the pressure; the pressure, in turn, is used for estimating the energy of the process including the potential energy of pile-up. Comparison between numerical and laboratory results demonstrated rather good correlation.

The paper [Alexeev and Karulina, 1999] considers the pile-up formation at the sloped surface of an artificial structure. The pile-up body is partly afloat, and the ice floe directly contacting with structure surface is affected by the pile-up keel. When this pressure exceeds the flexural strength of this ice floe, the ice floe is broken. In accordance with authors' opinion, this break means the end of pile-up formation, because the further process can be qualified as ice ridging. As the pressure from pile-up keel depends on its size, the equation system correlating ice thickness (strength) with keel size (pressure on ice floe from below) becomes closed, and the problem can be solved analytically. Besides, using this approach, one can estimate the ice floe size necessary for forming the maximum (at given ice thickness and drift speed) pile-up.

Highly appreciating the advantages of all mentioned papers, to our opinion, the whole complex of ice and wind conditions is taken into account not sufficiently. Besides, there are no works containing the specific calculations of pile-up in the Gulf of Finland applying to North-European Pipeline location.

Some earlier the model of pile-up formation was developed in the AARI, which principally can be used for simulating this phenomenon in any freezing basin.

2 Description of pile-up model

The matter of the model is as follows [Klyachkin, 1998a; Klyachkin, 1998b; Klyachkin et al., 2006].

Under the effect of coastward wind, a massif of compact drifting ice is pressed to coast. The force of ice pressure increases from seaward edge of ice massif to coast, i.e. the ice pressure reaches its maximum at the coast and, respectively, the minimum pressure is observed at the seaward edge of ice massif. If the stress within ice cover exceeds ultimate value (this value can be estimated as ultimate stability of ice plate under longitudinal buckling [Kheisin, 1971]), ice massif would move and be ridged.

During the ridging process, equivalent ice thickness grows while the width of ice massif decreases. These lead to decrease of actual stress and increase of ultimate one, hence, at some moment ice ridging should stop.

Using this approach for calculations of ice ridging, one should accept the condition of impenetrability (i.e. ice can not penetrate through the coastline). However, in real nature this condition is not always satisfied. In such cases ice begins creeping inland, that results in forming the ice pile-up. The possibility of pile-up formation depends on balance of forces affecting ice element in the point of "ice-coast" contact, namely: ice pressure, reaction of coast and projection of gravity on the slope surface. As ice creeps inland, the force which generates the process becomes weaker, while the forces of resistance grow. Finally it results in stopping the process.

In order to determine the pile-up geometry, one should estimate the energetic parameters of the process.

If pressed ice massif did not resist the external forces, every element of ice cover would move free, i.e. the elementary work would be done. It can be interpreted as some kind of analog of potential energy contained in compressed ice massif (like the compressed spring). Indeed, during the processes of (1) ice drift (horizontal motion), (2) ice ridging, (3) creeping inland and (4) piling up, some amount of mechanical work is done. Respectively, this work consists of four principal components: (1) kinetic energy of horizontal motion (ice drift) in the sea, (2) creation of potential energy of ice ridges in the sea, (3) work against the friction of the slope surface and (4) creation of the potential energy of coastal conglomeration. The model of ice ridging described above gives an opportunity to estimate the potential energy of ice massif before and after the process, as well as two first energetic components connected with ridging in the sea. Hence, the sum of the third and fourth components can be calculated easily.

In accordance with [Timokhov, Kheisin, 1987; Kheisin, 1989], the components (3) and (4) have the ratio as ½. This estimate is very approximate, but it can be set more precisely some later using the results of test calculations. Thus, if we (1) know the potential energy of ice conglomeration, (2) accept that the cross section of pile-up body has the triangular shape with known angle of lateral surface, and (3) know the porosity coefficient of pile-up body, we can calculate the main geometrical parameters of pile-up: height and width. Besides, if we know the value of work done against the slope friction, we can estimate the location of ice conglomeration relative to the shore line.

As a rule, pile-up formation is accompanied with sea level elevation. Elevation of the sea level itself, i.e. the presence of vertical component of sea current, does not “create” the pile-up, but affects this process. This effect, to our opinion, consists of two items. First, at higher level, the point of contact between ice and coast is located deeper inland than at normal level, that results in deeper inland location of ice conglomeration. Second, higher sea level facilitates the overcoming of resistance of landfast ice foot which remains unbroken and motionless after general break-up of landfast ice (Figure 1). This effect can play significant role in winter and spring, when landfast ice foot is rather thick and strong. As for pile-up formation in autumn, as a rule, the landfast ice is either absent or too thin, and that is why the role of sea level elevation is not so great.

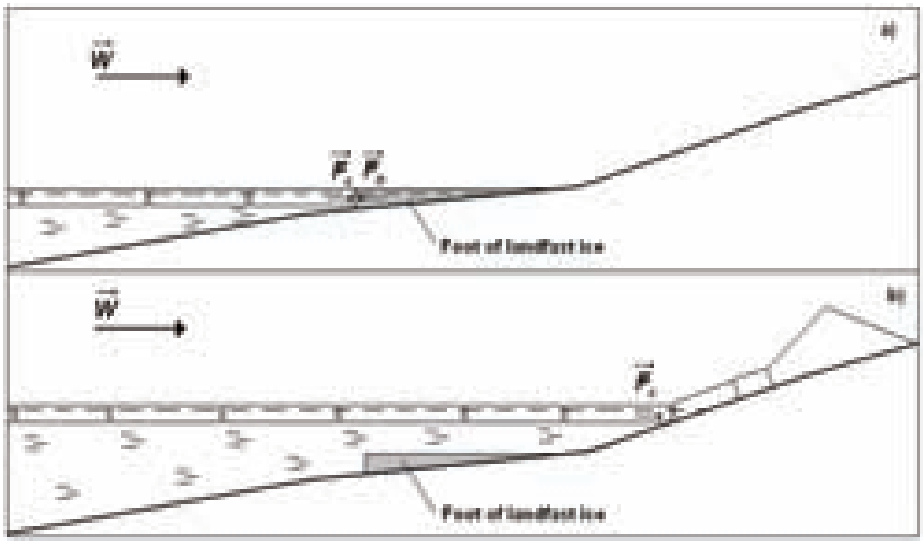

Figure 1 – Principal scheme of sea level influence upon the landfast ice foot resistance
a) normal level, b) high level

Thus, the pile-up formation is regulated by the following factors: (1) presence of contact between drifting ice and coast, (2) width of ice massif pressed to the coast, (3), ice

thickness, (4) speed of coastward wind, (5) sea level elevation, and (6) steepness of coast slope.

This model describes a kind of single case of pile-up formation, though the conditions of piling up can occur several times per ice season. However, as known, pile-up does not grow endlessly, i.e. some ultimate value exists.

As shown in [Klyachkin et al., 2006], in case of repeatable loading of the same value, pile-up grows less and less, and after several cycles the growth stops (Figure 2). To restart the process, the external forces should be larger and larger. But neither wind speed, nor ice thickness, nor ice massif width can grow endlessly, hence, the unlimited growth of ice conglomeration is also impossible. By the way, the same idea is put into base of ice ridging model of Parmerter and Coon [Parmerter and Coon, 1972].

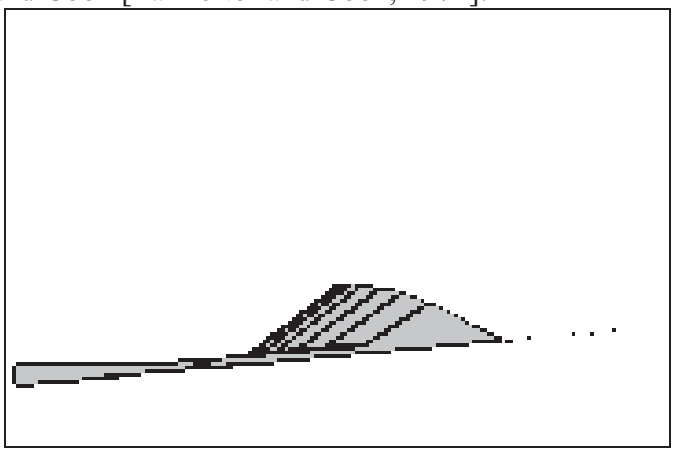

Figure 2 – Principal scheme of ice conglomeration growth after 7 cycles of piling up

3 Analysis of model calculations of piling up and comparison with observation data

3.1 Calibration test

In order to calibrate the model proposed, the special test simulating the real observed pile-up event was carried out. In particular, such case was observed during the most significant winter storm in the eastern Gulf of Finland occurred in December 20, 1973 [Drabkin, 1978].

The sea level elevation reached 240 cm higher than norm. The flooding was accompanied with western and south-western wind of 25-30 m/s. Ice thickness was about 15-30 cm.

The average height and width of ice conglomerations measured accurately by means of air-born photography over some part of Neva Bay coast comprised about 2-2.5 and 30-35 m, respectively. However, the visual observations of pile-up height carried out over the entire coast line of the Neva Bay gave somewhat larger values – up to 3-3.5 m. Thus, we would accept the mean typical value of pile-up height equal to 2,5-3 m.

Using the specific conditions of December 20, 1973, as initial data, the model simulations of piling up were carried out. Results of these tests gave an opportunity to specify some parameters of the model. The observed and calculated geometrical characteristics of ice conglomeration on the coast of the Neva Bay are presented in Table 2.

Table 2 – Geometrical parameters of simulated and observed ice conglomeration on the coast of the Neva Bay in December 20, 1973

Parameter	Observed	Simulated

Height, m	2,5-3,0	3,1
Width, m	30-35	20,2
Inland intrusion of ice conglomeration, m	65-75	65,8

Comparison of the observed and calculated characteristics allows making the following conclusions.

Calculated and observed heights of ice conglomeration are very close to each other. The calculated width is much less than observed one, while the calculated depth of inland intrusion of ice conglomeration (distance between shore line and coastward edge of ice conglomeration) is rather close to the observed one. The difference between the widths seems rather large, but we believe that the most important parameter of piling up is just the distance between shore line and coastward foot, because just this parameter characterizes the danger of piling up.

Thus, one may recognize that the proposed model simulates the natural phenomenon rather satisfactory, and this model may be used for calculating the statistical parameters of piling up on the Gulf of Finland coasts.

3.2 Calculation of the piling up statistics

The calculations of piling up were applied to the point where the North-European Pipeline would enter the Baltic Sea (about 30 km to the west from Vyborg, steepness of coast slope was accepted equal 3 degrees) for 5 months of ice season (from December to April).

The central idea put into base of these calculations is as follows: piling up takes place under the effect of combination of specific factors (ice thickness, wind speed, sea level, etc.). Every factor has its own distribution function, i.e. every value of every factor has specific probability. In turn, pile up formation is the result of the combination of factors.

Formally, any combinations of ice thickness, wind speed, ice massif width, etc., can occur. Hence, the product of probabilities of the individual factors gives the probability of the combination, and, consequently, the probability of pile up corresponding to this combination.

For example, (1) ice massif of width B has the probability P_b; (2) ice thickness T has the probability P_t; (3) wind speed W has the probability P_w; (4) sea level elevation H has probability P_h; (5) absence of landfast ice has the probability P_{nf}. Then, the combination of these factors (and pile up formed by this combination) has the probability P_{comb}:

$$P_{comb} = P_b \times P_t \times P_w \times P_h \times P_{nf}$$

When estimating the probability of factors affecting the pile-up formation, one should take into account that some of them are dependent, namely: wind speed, sea level elevation and landfast ice absence. For example, high elevation of sea level and storm wind lead to decrease of landfast ice probability (especially at the beginning and end of winter), or storm wind increases the probability of high level, etc. Besides, ice massif width and ice thickness are also dependent factors.

Basing on these assumptions and using the well known generalization of ice and hydrometeorological parameters of the Baltic Sea [Project “The Baltic”, 1997; “Atlas…”, 2000], the distribution functions of the basic pile-up forming factors were developed for every month of ice season, taking into account their dependence on each other.

It is obvious that when preparing such distribution functions, one can not but resort to some simplifications. It means that every factor is presented as finite ensemble of discrete values, every value has its specific probability, and the sum of these probabilities equals to 1.

The examples of such distribution functions (ice massif width and wind speed) are presented in Table 3.

Table 3 – Examples of the distribution functions of ice massif width and wind speed in January

Speed of coastward wind		Ice massif width	
Value, m/s	Probability, %	Value, km	Probability, %
0-5	75.12	20	30
10	13.42	50	250
15	8.89	80	25
20	2.32	100	20
25	0.25		

One should mention that interval of wind speed values 0-5 m/s means not only weak winds, but seaward and coast-parallel winds of any speed.

Every combination of factors has its specific probability and results either in pile-up of specific size or in no piling up. If we sum up the probabilities of the combinations resulting in conglomerations of similar sizes, we can obtain the distribution function of the geometrical parameters of ice conglomerations.

3.3 Analysis of pile-up model simulations

The Figures 3-5 illustrate the distribution functions obtained from the generalization of the model simulations.

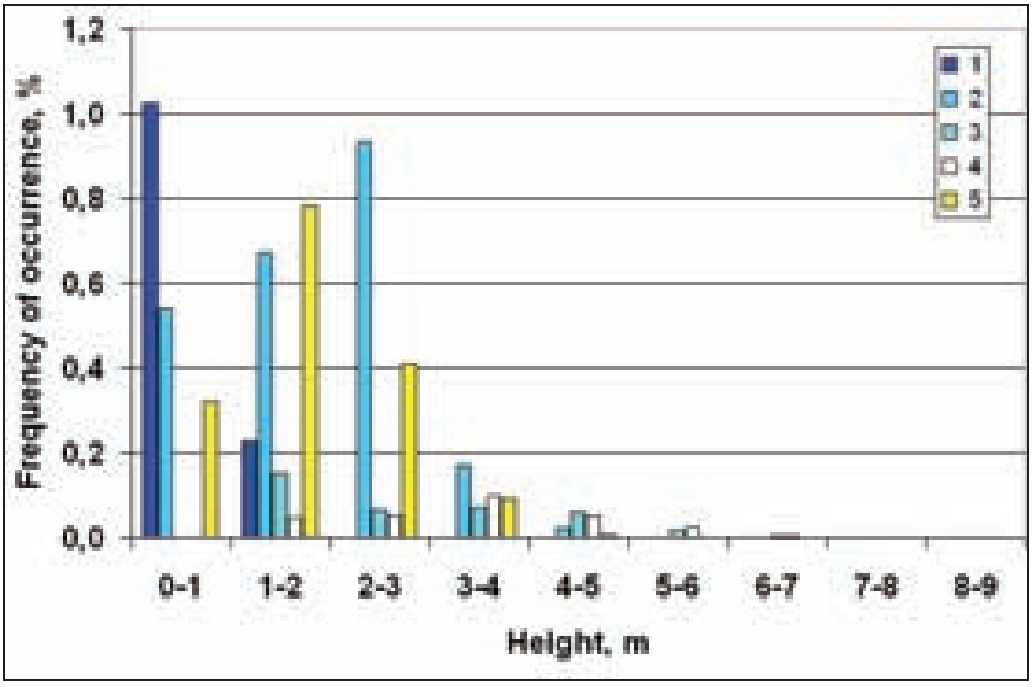

1 – December, 2- January, 3 – February, 4 – March, 5 - April

Figure 3 – Histogram of pile-up height

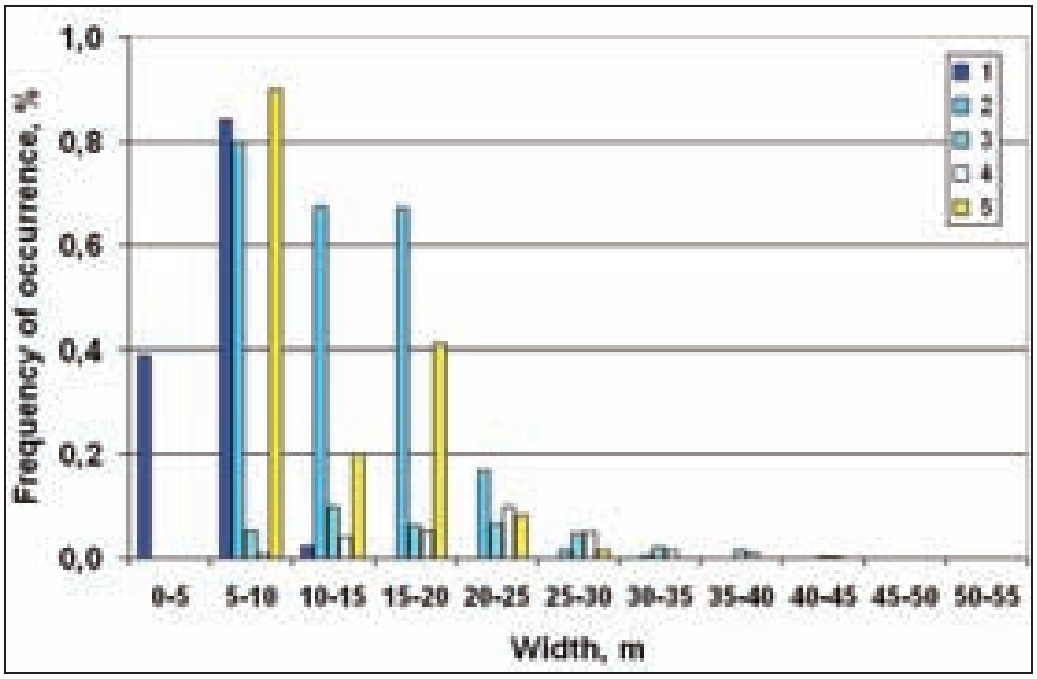

1 – December, 2- January, 3 – February, 4 – March, 5 - April
Figure 4 – Histogram of pile-up width

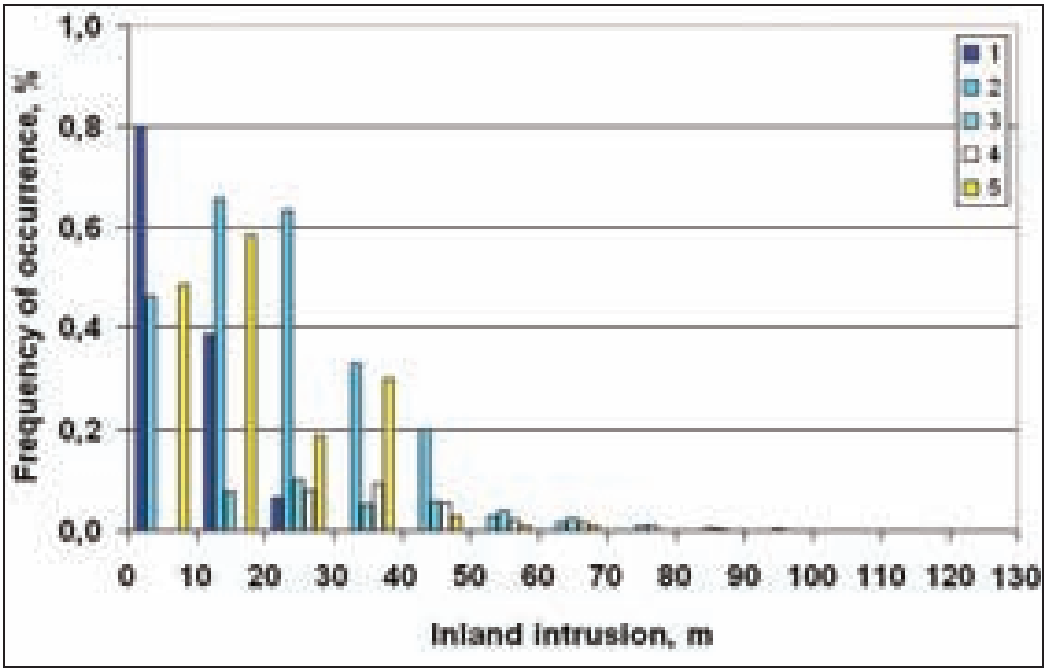

1 – December, 2- January, 3 – February, 4 – March, 5 - April
Figure 5 – Histogram of pile-up inland intrusion

The probability of “zero” pile-up (i.e. “no piling up”) is advisedly not shown on these diagrams, because the probability of “no pile-up” is much greater than that of any pile-up, and it is absolutely impossible to demonstrate the probability of “zero pile-up” on the same diagram in the same scale. For better understanding the histograms, these probabilities are presented in separate table (Table 4).

Table 4 – The probabilities of no piling up

Month	Probability, %
December	98,75
January	97,67
February	99,65
March	99,73
April	98,39

As seen from Figures 3-5 and Table 4, in great majority of cases there is no piling up at all, i.e. the piling up phenomenon seems to be very rare.

The most frequent (0.6-1.0 %) ice conglomerations are not very large: height is not more than 2-3 m, width is about 10-15 m, inland intrusion is about 20-30 m. Larger conglomerations (3-5 m high) have the probability about 0.1-0.2 %. Very large pile-up (5-7 m) occurs in 0.01 % of cases. The giant conglomerations (more than 7 m) have very low probability and it is even not seen on the diagrams in given scale (not more than 0.0002 %).

The distribution of other geometrical parameters has the same character: wide conglomerations deeply intruding inland are very rare.

The temporal evolution of pile-up regime is also rather interesting.

December is characterized with the smallest pile-up – not more than 2 m. This is caused by general lack of ice in this month: ice thickness is not large, and ice edge is located close to the coast. However, due to non-stability of landfast ice, the frequency of occurrence of pile-up is the highest just in December – up to 1 %. It is difficult to evaluate the character of distribution, but it seems close to exponential.

In January, as ice cover grows, the probability of small pile-up decreases while that of larger conglomerations increases, i.e. distribution becomes closer to log-normal. It is caused by ice thickness growth and widening the area occupied by ice, and, hence, increase of the external forces. Hereby, the probability of piling up remains rather high – up to 0.6-0.8 %. In general, January is the period of the most active piling up – both by probability and size.

In February-March the character changes noticeably. First of all, probability of piling up decreases sharply (caused by high stability of landfast ice). However, just in these months ice conglomerations can reach the maximum size – up to 6-8 m (due to maximum ice thickness and ice-covered area), though with very little probability.

At last, in April, i.e. during active melting and landfast ice decay, probability of piling up grows noticeably (in comparison with February-March), and conglomerations can reach significant size – up to 3-4 m.

Rather often, when making applied engineering decisions, one should estimate the probability of natural phenomena (including piling up) not only in per cent, but also in terms like “once per N years”.

Such transformation (from per cent to “once per N years”) can be based on the assumption that not more than 1 event (1 piling up) can take place within 1 day. Then, quantity of events during 5-month ice period would be equal about 150, and the event observed once per ice season (1 case of 150) would have probability $6{,}7 \cdot 10^{-3}$ (or 0,7%); 1 event per 100 years corresponds to $6{,}7 \cdot 10^{-5}$, etc.

Thus, it is easy to present the probability of piling up in terms like “once per N years” (Table 5).

Table 5 – Probability of piling up expressed in terms “once per N years”

Height		Width		Inland intrusion	
0-1 m	1 / 1-2	0-5 m	1 / 8-9	0-10 m	1 / 1-2
1-2 m	1 / 1-2	5-10 m	1 / 1-2	10-20 m	1 / 1-2

2-3 m	1 / 2-3	10-15 m	1 / 3-4	20-30 m	1 / 3-4
3-4 m	1 / 7-8	15-20 m	1 / 2-3	30-40 m	1 / 4-5
4-5 m	1 / 20-25	20-25 m	1 / 8-9	40-50 m	1 / 9-11
5-6 m	1 / 80-90	25-30 m	1 / 25-30	50-60 m	1 / 30-35
6-7 m	1 / 300	30-35 m	1 / 80-90	60-70 m	1 / 50-55
7-8 m	1 / 800	35-40 m	1 / 100-150	70-80 m	1 / 150-200
8-9 m	1 / 2000	40-45 m	1 / 500	80-90 m	1 / 500

As seen from Table 5, coastal ice conglomerations less than 2 m high can be formed practically every year. Inland intrusion less than 20 m is also quite usual phenomenon.

Only very large pile-up (higher than 4 m, wider than 25 m and intruding inland deeper than 50-60 m) can be formed rarely (once per more than 20 years).

Though, taking into account the results of calibration test, the calculated inland intrusion is somewhat larger than the observed one, but in general the results obtained seem to be rather close to reality.

Finalizing, one should note that the model gives average values of the geometrical parameters. In fact, every coastal ice conglomeration has specific spatial variability (in some points the conglomeration can be higher or lower, and wider or narrower). For example, the pile-up formed on the Neva Bay coasts in December 20, 1973, had average height about 2-3 m, while in some points its height reached 8-9 m [Drabkin, 1978]. Besides, Giriatowicz [Giriatowicz, 1975] told about coastal conglomerations reaching 10-12 m in the Gulf of Finland and 15-20 m in the Bothnian Bay, Gulf of Riga and Gulf of Kurshi. It seems probable that all these data related to extreme but not average parameters.

Probably, this variability follows specific regularities, but the lack of observation data does give an opportunity to make any suppositions on this issue.

4 Conclusions

Finalizing, it seems necessary to point out the basic question requiring deeper studies.

First, the case of piling up at steep coast needs to be studied in more details.

Second, ice pressure should be estimated more precisely by taking into account the tangential stress on the lower ice surface generated by under-ice current.

Third, as known, sometimes ice floes creep inland but do not pile up. The reason of this phenomenon is not quite clear. The urgency of this problem may be, in particular, confirmed by the observations described in [Kovacs, Sodhi, 1979]: sometimes ice floes creep up to 100 m inland not forming high conglomeration. Probably, the micro-features of relief of the beach play significant role. In any case, this question is not clear enough and requires further studies and observations.

References

Alexeev Y.N., Karulina M.M. An assessment of pile-up dimensions in front of sloping offshore structures. – Proc. of POAC'99, 1999, Helsinki, Finland, Vol.2, p.396-405.

Atlas of Ice Cover of the Gulf of Finland (ed. by V.V.Drabkin). St. Petersburg, 2000, GUNIO, 160 p.

Drabkin, V.V. Ice ridge and pile-up formation at wind-caused level elevations (on example of the Gulf of Finland). Proc. AARI, 1978, vol.354, p.89-96.

Giriatowicz, J.P. Napor rier lodowych na brzeg Zalewu Szczecinskiego. Czas. Geogr., 1975, 46, N1, p,65-72

Hopkins M.A.. Onshore ice pile-up: a comparison between experiments and simulations Cold Regions Science and Technology, 1997, Volume 26, Issue 3, p.205-214

Kheisin, D.Ye. On generation of ice pressure at hydrodynamic stage of ice drift. Proc. AARI, 1971, vol.303, p.89-97.

Kheisin, D.Ye. Wind-caused ice piling up on the coasts and slopes of the offshore structures. Proc. of the Conference "Sea ice and economic activities in the offshore area", Murmansk, 1989, p.96-98.

Klyachkin, S.V. Dynamic model of ice pile-up formation on the example of the Pechora Sea. Proc. AARI, 1998, vol.437, p.151-161.

Klyachkin, S.V. Dynamic model of formation of coastal pile-up on the example of the Pechora Sea. – Proc. of the 7-th Int. Conference on the Development and Commercial Utilization of Technologies in Polar Regions (POLARTECH'98), Nuuk, Greenland, 1998, p.198-208.

Klyachkin, S.V., Gudkovich, Z.M., Drabkin, V.V., Voyevodin, V.A. Ice conglomerations on the coasts of freezing seas and its modelling. In: Ice features of the Western Arctic seas (ed. by G.K. Zubakin and Yu.A.Gorbunov). St. Petersburg, 2006, AARI Publ., p.248-264.

Kovacs A., Sodhi D.S. Ice pile-up and ride-up on Arctic and subarctic beaches. - Proc. of Int. Conf. POAC-79. - P.127-146.

Parmerter R.R., Coon M. D. Model of pressure ridge formation in sea ice. – J. Geophys. Res., 1972, vol.77, No.33, p.6565-6575.

Project "The Baltic. The problems of studying and mathematical modeling of the ecosystems of the Baltic Sea" (ed. by I.N.Davidan). Iss.5. "The ecosystem model and the assessment of the modern state of the Gulf of Finland", Part 2. St. Petersburg, "Gidrometeoizdat", 1997, 449 p.

Timokhov, L.A., Kheisin, D.Ye. Sea ice dynamics (mathematical models). Leningrad, 1987, "Gidrometeoizdat", 271 p.

The peculiarities of ice condition variations in the Gulf of Finland in connection with the global warming

Lebedev A.A., Mironov Ye.U. and Drabkin V.V.

Arctic and Antarctic Research Institute, St. Petersburg, Russia

The well known report (prepared by the International Commission on Climatic Changes and submitted to the UN Organization) points out that the so-called global warming does not raise doubts. The winter seasons of 2006-2007 and 2007-2008 in the north-west Russia (the warmest winters during the whole history of instrumental observations) appeared especially indicative [1].

It looks interesting to consider the peculiarities of ice conditions in the Baltic Sea and Gulf of Finland in the second half of the 20th century and in the beginning of the 21st century (from 1950 till 2008). The temporal variations of ice cover extent in the Baltic Sea and the length of ice navigation route in the Gulf of Finland were in the focus of the study. The most detailed attention was paid to the most well-studied ice phenomena from the 1980-s of last century.

The multi-year tendencies of inter-annual variations of ice conditions were studied by analyzing the integral characteristics of ice cover extent and length of ice navigation routes (Figure 1a, b). The typical feature of both parameters is their decrease in the 1950-s at climatic warming in the Arctic and increase in the 1960-s at simultaneous climatic cooling. However, the rapid decrease which started in the second half of the 1980-s and continues till 2008, attracts the attention. Hereby, one should mention the brief stop or even increase (in 1995-1996 and 2002-2003) on the general background of integral curves (Figure 1a, b).

The quantitative estimates of ice cover extent and length of ice navigation routes were executed by means of classification of their anomalies (5 gradations) relative to the standard deviation [3]:

1 – negative very large (NVL) anomaly or very late (VL) date: $\leq$-1,2σ;

2 – negative large (NL) anomaly or late (L) date: from -1.2δ to -0.4σ;

3 – close to norm (CN): $\pm$0.4σ;

4 – positive large (PL) anomaly or early (E) date: from 0.4δ to 1.2σ;

5 – positive very large (PVL) anomaly or very early (VE) date: $\geq$1,2σ.

The procedure includes the calculations of anomalies (Δ), normalized anomalies (Δ/σ) and frequency of occurrence of the characteristics within each gradation during the selected decades.

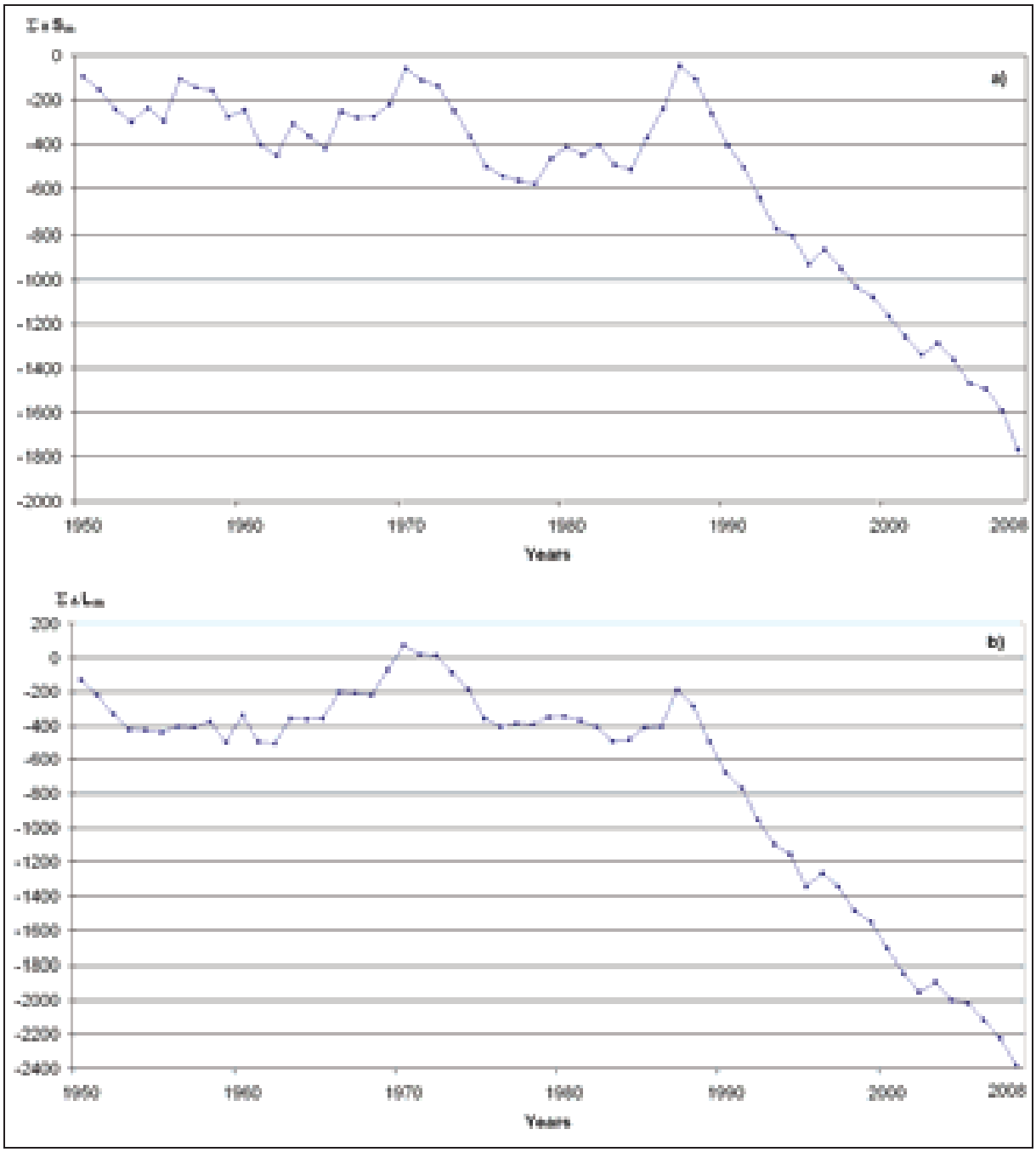

Figure 1 – Integral curves of the inter-annual variability of ice conditions in 1950-2008
a) ice cover extent (10^3 km^2) in the Baltic Sea at to the moment of seasonal maximum $\sum \Delta S_m$
b) length of ice navigation route (nautical miles) in the Gulf of Finland at to the moment of seasonal maximum $\sum \Delta L_m$

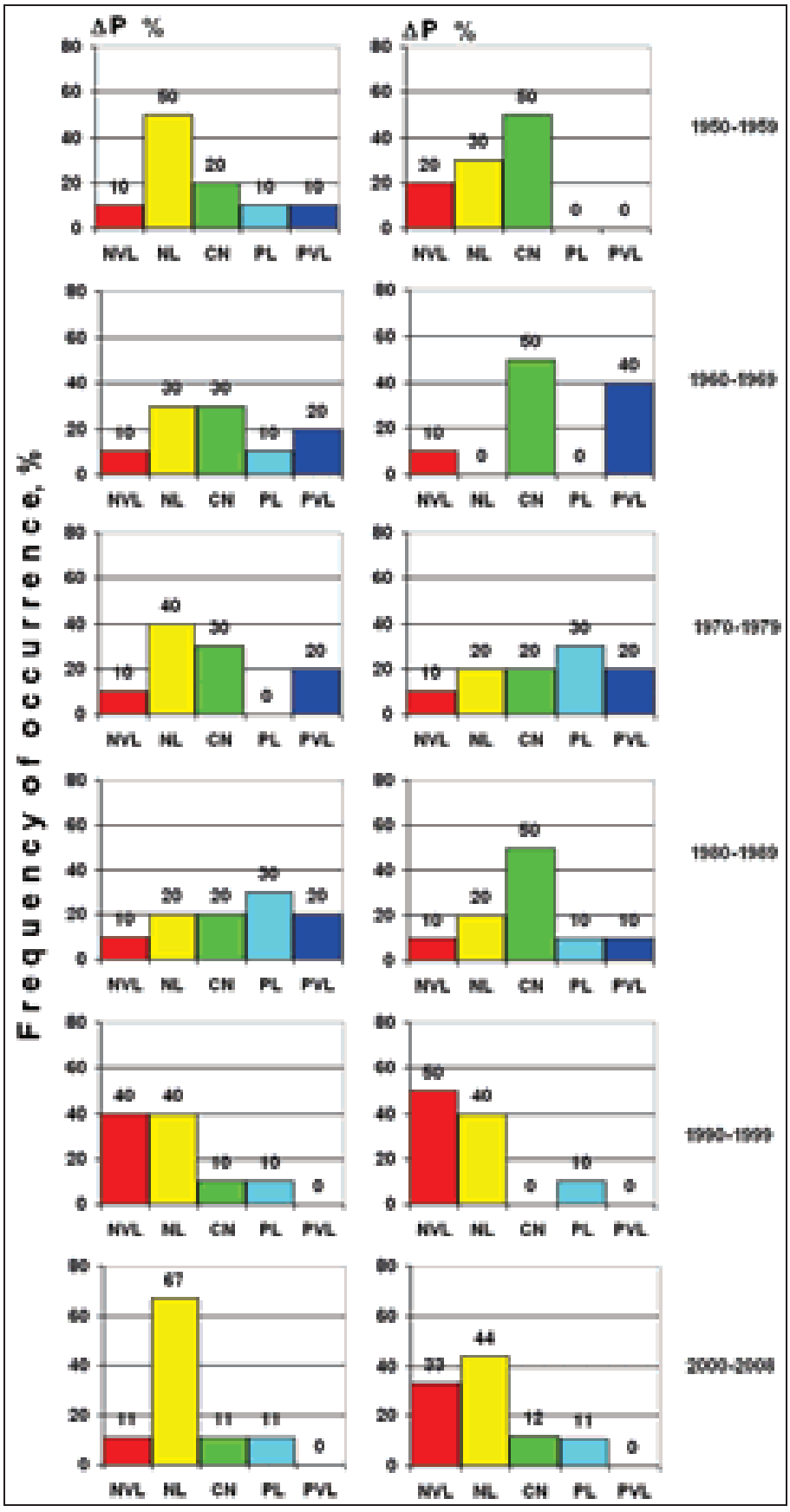

Figure 2 – Frequency of occurrence (%) of the anomaly types:
left – ice cover extent in the Baltic Sea, right – length of ice navigation route

As seen on Figure 2, the total values of NVL and NL anomalies in the 1950-s comprised 50-60%. In the 1960-s it decreased to 10-40%, but in the 1990-s and 2000-s the frequency of NVL and NL anomalies grew sharply up to 77-90%. This growth observed in these latter years resulted in favorable conditions of ice navigation (except winter seasons of 1996-96 and 2002-03). The empirical distributions of ice cover extent and length of ice navigation route are characterized by clear left-side asymmetry, i.e. by higher frequency of NVL and NL anomalies in the 1990-s and 2000-2008 (Figure 2).

In fact, these conclusions, though obtained by somewhat different way, are principally similar to earlier results (Figure 1). Finally, the reliability of the conclusions regarding the extreme anomalous character of ice conditions in the Baltic Sea in late 20th – early 21st century becomes higher.

As known, ice conditions are closely correlated with air temperature. The air temperature anomalies for the same decades are considered at two representative points: Helsinki and St. Petersburg. The histograms of seasonal (December-February) mean air temperature clearly demonstrate, in particular, the predominance of total PVL and PL anomalies (up to 30-50%) in the 1950-s, decrease to 20-30% in the 1960-s and sharp growth in the 1990-s and 2000-2008 (Figure 3).

Comparing the histograms presented on the Figures 2 and 3, one should remember that the predominance of positive anomalies of air temperature, according to physical reasons, should correspond to negative anomalies of ice characteristics (and vice versa). As could be expected, the empirical distributions of air temperature anomalies in Helsinki and St. Petersburg at the end of last century and beginning of current century (Figure 3) are characterized by clear right-side asymmetry (predominance of PL and PVL).

The integral curves of the anomalies of ice season length ("number of days with ice") to the west of the Neva Bay (stations Tolbukhin Lighthouse and Cape Shepelevsky) are of equal interest. The corresponding illustrations are not presented in order to shorten the paper, but it is worth mentioning that the integral curve of the anomalies of number of days with ice at the Cape Shepelevsky decreased sharply since the late 1990-s and during 2000-2008. The only exclusion is moderately severe season of 2002-2003, when the decrease of the curve was slightly damped. The analogous (but not so bright) regularity is seen on the integral curve of ice season length at the Tolbukhin Lighthouse.

At last, it seems important to consider the peculiarities of landfast ice formation at the same stations. The most important seasons are those when the landfast ice was not formed at all. In connection with these considerations, the histograms of the anomalies of landfast ice formation dates were developed using the same five gradations added with the sixth one corresponding to the cases of landfast ice absence (marked at the histogram as NPh which means "No Phenomenon").

As seen, the gradation "No phenomenon" appeared the most typical in recent decades. Its frequency in the 1980-s comprised 40%, in the 1990-s it grew to 50-70%, and in 2000-2008 the probability of landfast ice absence reached almost 80% (Figure 4). The corresponding histograms illustrate that the empirical distributions of landfast ice formation dates (both for the Cape Shepelevsky and Tolbukhin Lighthouse) are characterized by sharp left-side asymmetry: predominance of very late dates and absence of landfast ice (Figure 4).

As a rule, the papers like the present one contain some analysis of ice navigation conditions that promotes the improvement of hydrometeorological support. However, one should not ignore that, in turn, ice navigation can affect, to some extent, the character of ice phenomena. In particular, later dates of landfast ice formation (in comparison with the multi-year norm) or full absence of landfast ice can be correlated with the increase of navigation intensity. Indeed,

the turnover of goods in such Russian ports as Primorsk, Vysotsk, Ust-Luga, etc., grew significantly in comparison with previous years.

Its interesting that the peculiarities of ice conditions in the north-west Russia mentioned above take place simultaneously with air temperature growth, especially, in winter periods. Formation of extremely easy ice conditions, frequent absence of landfast ice or decrease of landfast ice extent are observed on the background of the so-called global warming. As known, the scientific community does not have uniform opinion on this issue [2, 4, 5]. It seems more probable that the global warming is caused by the complex of natural and anthropogenic factors which play their role both in long-range and short-range fluctuations of the atmosphere and ocean. In fact, the structure of climate-forming natural phenomena is characterized by multi-cyclicity. Thus, the study of regularities of the modern ice cover variations in connection with global warming becomes a part of the planetary system research.

The authors express their deep gratitude to the specialists of the North-West Administration of Hydrometeorology Ye.V. Komissarov and P.V. Soloschuk for the submitted ice observations data.

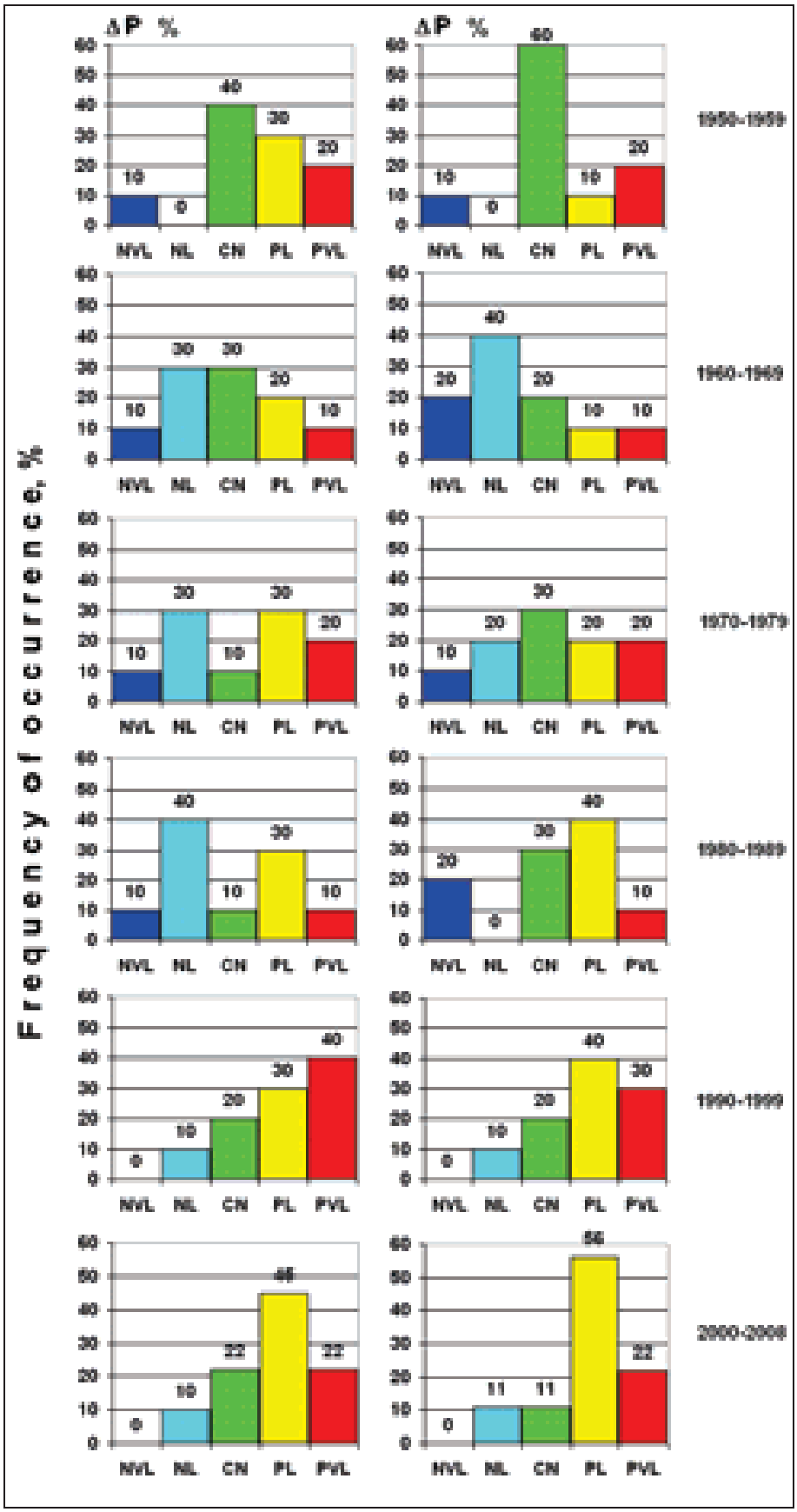

Figure 3 – Frequency of occurrence (%) of anomaly types of seasonal (December-February) mean air temperature, 1950-2008; left – Helsinki, right – St. Petersburg

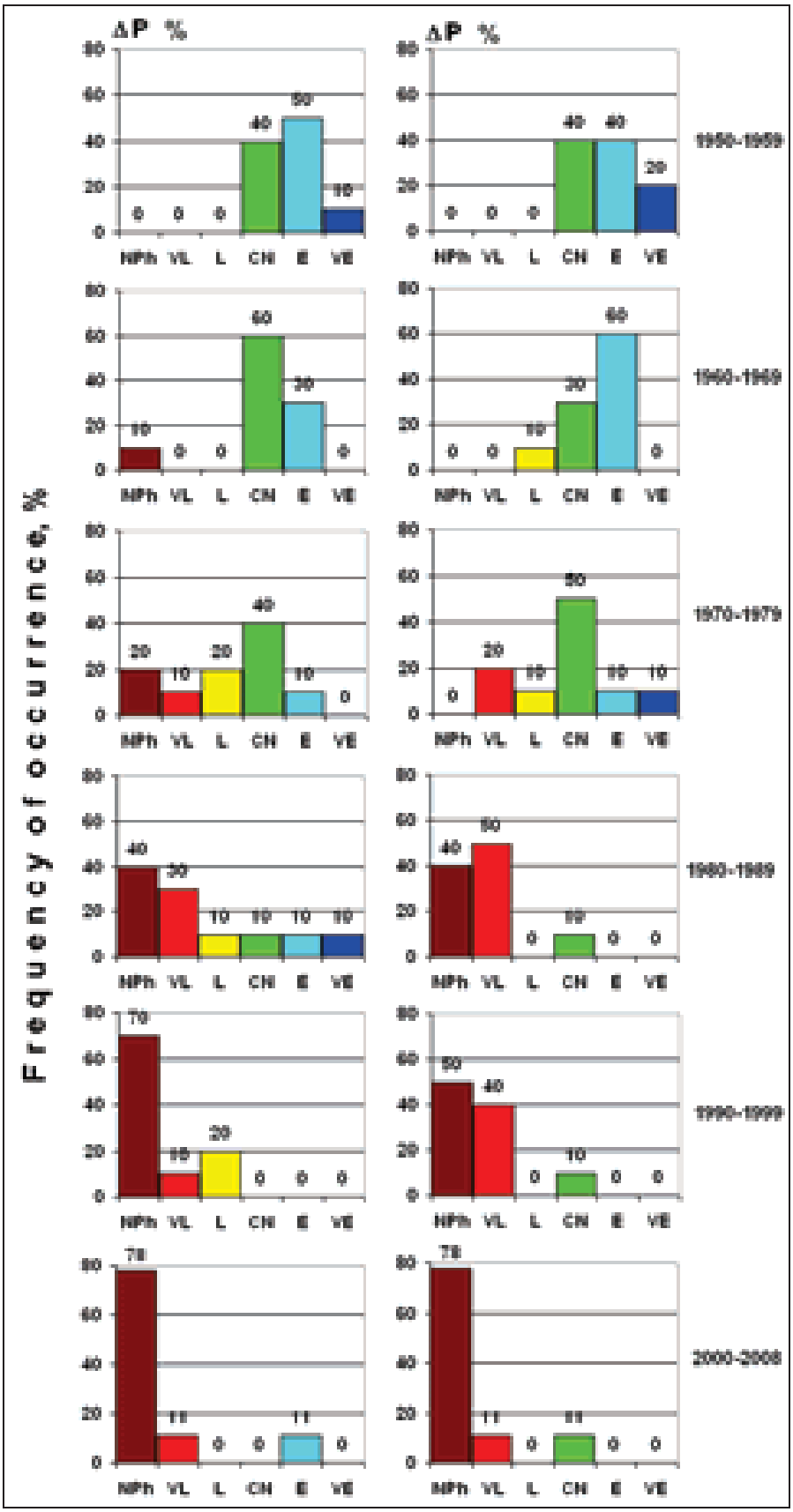

Figure 4 – Frequency of occurrence (%) of anomaly types of landfast formation dates, 1950-2008; left – Cape Shepelevsky, right – Tolbukhin Lighthouse

References

1. Klimenko, V.V. Climatic sensation: “What expects us in the nearest future?” Public lecture, “Polit.ru” Project, February 1, 2006, 27 p., web-site www.polit.ru/lectures/2007/02/15/klimenko.html
2. Frolov, I.Ye., Gudkovich, Z.M., Karklin, V.P., Kovalev, Ye.G., Smolyanitsky, V.M. Scientific researches in the Arctic. Vol.2. Climatic changes of ice cover of the Euro-Asian shelf seas. St. Petersburg, 2007, “Nauka”, 122 p.
3. Lebedev, A.A., Drabkin, V.V. Secular fluctuations of ice cover extent in the Baltic Sea. Proc. AARI, 2001, vol.443, p.13-14.
4. Lebedev, A.A., Drabkin, V.V., Mironov, Ye.U. Climatic variability of ice phenomena in the eastern Gulf of Finland. Report Series in Geophysics, 2002, Helsinki, N 44, p.17-29.
5. Jevrejeva, S., Drabkin, V.V., Kostyukov, J., Lebedev, A.A., Lepparanta, M., Mironov, Ye.U., Schmelzer, N., Sztobryn, M. The Baltic Sea ice seasons in the twentieth century. Climate Research, 2004, Inter-Research, vol.25, p.217-227.

List of Participants

	Denmark
Rasmus T. Tonboe	Technical University of Denmark
	Estonia
Ants Erm	Institute for Marine Systems, Tallinn University of Technology
Ove Pärn	Institute for Marine Systems, Tallinn University of Technology
Jevgeni Rjazin	Institute for Marine Systems, Tallinn University of Technology
	Finland
Patrick Eriksson	Finnish Institute of Marine Research
Susann Haase	Department of Biological and Environmental Sciences, University of Helsinki
Pekka Juuti	Aker Arctic Technology Inc.
Hermanni Kaartokallio	Finnish Institute of Marine Research
Juha Karvonen	Finnish Institute of Marine Research
Matti Leppäranta	Department of Physics, University of Helsinki
Mika Mäkelä	Department of Physics, University of Helsinki
Kai Myrberg	Finnish Institute of Marine Research
Tuomas Niskanen	Finnish Institute of Marine Research
Annu Oikkonen	Department of Physics, University of Helsinki
Hilkka Pellikka	Department of Physics, University of Helsinki
Jari Uusikivi	Department of Physics, University of Helsinki
Anssi Vähätalo	Department of Biological and Environmental Sciences, University of Helsinki
Ilona Välisuo	Department of Physics, University of Helsinki
Juho-Pekka Vehviläinen	Department of Physics, University of Helsinki
	Germany
Andreas Lehmann	Leibniz Institute of Marine Sciences
Nina Maass	University of Hamburg
Natalija Schmelzer	Bundesamt für Seeschifffahrt und Hydrographie
Anke Strübing	
Klaus Strübing	Bundesamt für Seeschifffahrt und Hydrographie
	Japan
Yusuke Kawaguchi	Institute of Low Temperature Science, Hokkaido University
Mrs. Kawaguchi	

Norway

Sönke Maus	Geophysical Institute, University Bergen

Poland

Marzenna Sztobryn	Institute of Meteorology and Water Management, Gdynia

REPORT SERIES IN GEOPHYSICS

(Reports 1 to 25 are listed up to Report No 51)

26. Simojoki, H., 1992: Geofysiikan tulo oppiaineeksi Helsingin yliopistossa (2nd ed.)
27. Leppäranta, M., Haapala, J. (eds.), 1993: Proceedings of the first workshop on the Baltic sea ice climate, Tvärminne, Finland, 22-26 August 1993
28. Vihma, T. (ed.), 1994: Evening sessions of the summer school on physics of ice-covered seas, Savonlinna, Finland, 6-17 June 1994
29. Pulkkinen, K., 1995: STD-12 mini-CTD:n käyttö ja datan kalibrointi (English summary: The use of STD-12 mini-CTD and calibration of data)
30. Pulkkinen, K. (ed.), 1995: Underwater optical measurements made during the first concentrated field effort (CFE 1) of NOPEX - A data report
31. Multala, J., Hautaniemi, H., Oksama, M., Leppäranta, M., Haapala, J., Herlevi, A., Riska, K., Lensu, M., 1995: Airborne electromagnetic surveying of Baltic sea ice
32. Pulkkinen, K. (ed.), 1995: Proceedings of the 2nd Finnish-Estonian seminar on underwater optics with applications, Helsinki, 10-12 April 1995
33. Launiainen, J., Cheng, B., 1995: A simple non-iterative algorithm for calculating turbulent bulk fluxes in diabatic conditions over water, snow/ice and ground surface
34. Stipa, T., 1996: Water renewal and vertical circulation of Pohja Bay
35. Haapala, J., Alenius, P., Dubra, J., Klyachkin, S.V., Kõuts, T., Leppäranta, M., Omstedt, A., Pakstys, L., Schmelzer, N., Schrum, C., Seinä, A., Strübing, K., Sztobryn, M., Zaharchenko, E., 1996: IDA. Ice data bank for Baltic Sea climate studies
36. Leppäranta, M. (ed.), 1996: AISA lake experiment 1993-94. Final Report
37. Haapala, J., Leppäranta, M. (eds.), 1997: ZIP-97 data report
38. Pulkkinen, K. (ed.), 1998: Proceedings of the 4th Finnish-Estonian seminar on underwater optics with applications, Lammi, 22-24 April 1997
39. Saloranta, T.M., 1998: Snow and snow ice in sea ice thermodynamic modelling
40. Leppäranta, M. (ed.), 1998: Downscaling in sea ice geophysics
41. Herlevi, A. (ed.), 1999: The optics ground truth of the Finnish SALMON experiment
42. Haapala, J., 2000: Modelling of the seasonal ice cover of the Baltic sea
43. Zhang, Z., 2000: On modelling ice dynamics of semi-enclosed seasonally ice-covered seas
44. Jevrejeva S., Drabkin, V.V., Kostjukov, J., Lebedev, A.A., Leppäranta, M., Mironov, Ye. U., Schmelzer, N., Sztobryn, M., 2002: Ice time series of the Baltic Sea
45. Herlevi, A., 2002: Inherent and apparent optical properties in relation to water quality in Nordic waters
46. Leppäranta, M. (ed.), 2003, Proceedings of the seminar “Sea Ice Climate and Marine Environments in the Okhotsk and Baltic Seas – The Present Status and Prospects”
47. Rasmus, K., Granberg, H., Kanto, K., Kärkäs, E., Lavoie, C., Leppäranta, M., 2003: Seasonal snow in Antarctica data report
48. Rasmus, S., 2005: Snow pack structure characteristics in Finland – Measurements and modelling
49. Kanto, E., 2006. Snow characteristics in Dronning Maud Land, Antarctica
50. Halkola, K., 2006. The orographic climate factors contributing to the mass balance of small glaciers in North-Iceland
51. Elo, A.-R., 2007. Effects of climate and morphology on temperature conditions of lakes
52. Donadini, F., 2007. Features of the geomagnetic field during the Holocene and Proterozoic
53. Wang, K., 2007. On the mechanical behaviour of compacted pack ice: theoretical and numerical investigation
54. Koistinen, E., 2007. Antarktikan ilmastohistoria
55. Kanto, E., Leppäranta, M. and Mattila, O-P., 2007. Seasonal snow in Antarctica. Data report II
56. Oikkonen, A., 2008. Variability and changes of Arctic sea ice cover, 1975-2000
57. Forsström, S., 2008. Carbonaceous aerosol particles in Svalbard snow
58. Mäkiranta, E., 2009. Observations of atmospheric boundary layer over sea ice in a Svalbard fjord
59. Salminen, J., 2009. Paleomagnetic and rock magnetic study with emphasis on the Precambrian intrusions and impact structures in Fennoscandia and South Africa
60. Kohout, T., 2009. Physical poperties of meteorites and their role in planetology

ISBN 978-952-10-5633-8 (printed version)
ISBN 978-952-10-5634-5 (pdf-version)
ISSN 0355-8630

Helsinki 2009
Yliopistopaino